

UNCLASSIFIED

AD NUMBER

AD863248

LIMITATION CHANGES

TO:

Approved for public release; distribution is unlimited.

FROM:

Distribution authorized to U.S. Gov't. agencies and their contractors; Critical Technology; OCT 1969. Other requests shall be referred to Space and Missile Systems Organization, Norton AFB, CA 92409. This document contains export-controlled technical data.

AUTHORITY

SAMSO ltr, 19 Jan 1972

THIS PAGE IS UNCLASSIFIED

SAMSO TR 69-313 - Vol. I

STRUCTURE—MEDIUM INTERACTION AND DESIGN PROCEDURES STUDY

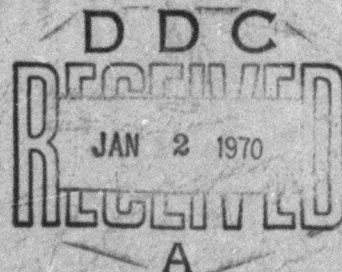
Volume I

Analysis Method, Theory, Verification and Applicability

Mr. H. G. Leistner
Dr. R. E. Jones
Mr. W. J. Walker
et. al.

THE **BOEING** COMPANY

October 1969



This document is subject to special export controls and each transmittal to foreign Governments or foreign nationals may be made only with prior approval of SAMSO (SAMS). The distribution of this report is limited because it contains technology restricted by mutual securities acts.

Reproduced by the
CLEARINGHOUSE
for Federal Scientific & Technical
Information Springfield Va. 22151

Prepared under Contract No. F04694-67-C-0084 for

THE DEPARTMENT OF THE AIR FORCE
SPACE AND MISSILE SYSTEMS ORGANIZATION
AIR FORCE SYSTEMS COMMAND
NORTON AIR FORCE BASE CALIFORNIA

AD 863248

245

STRUCTURE - MEDIUM INTERACTION
AND DESIGN PROCEDURES STUDY

Volume I,
Analysis Method, Theory, Verification and Applicability

Mr. H. G. Leistner
Dr. R. E. Jones
Mr. W. J. Walker
et. al.

THE **BOEING** COMPANY

October 1969

Prepared under Contract No. F04694-67-C-0084

This document is subject to special export controls and each transmittal to foreign Governments or foreign nationals may be made only with prior approval of SAMSO (SAMSOC). The distribution of this report is limited because it contains technology restricted by mutual securities acts.

SAMSO/SMSD
L 7A. AFS. CALIF 90045

FOREWORD

This report describes research performed by The Boeing Company under direction of Mr. P. E. Grafton, Deputy Technical Director for Research and Development, Aerospace Systems Division. The Boeing Company personnel who made significant contributions to this study include: Dr. S. L. Strack (Program Management), Mr. H. G. Leistner (Technical Management), Dr. R. E. Jones (Technology Development), W. J. Walker, R. D. Caudle, S. A. Shipley, Dr. G. C. Chang, J. vanDerlinden, G. Fair, and J. Urban.

This research study was performed from 16 May 1967 to 15 October 1969 under Contract No. F04694-67-C-0084 for the Department of the Air Force, Space and Missile Systems Organization (AFSC), Norton Air Force Base, California 92409. The SAMSO project officers were Captain U. L. Barnwell, Lt. R. G. Tart and Captain R. H. Waters. The Aerospace Corporation provided technical direction through Mr. N. F. Kfoury and Dr. T. L. Alley.

Information contained in this document is also released as Boeing Document D2-121409.

This technical report has been reviewed and approved.


G. S. Christensen, Lt. Col., USAF
Chief, Facilities Development Branch
Hard Rock Silo Development Division


Ronald H. Waters, Capt., USAF
Project Officer, Technology Section
Facilities Development Branch

ABSTRACT

This report contains a detailed description of the analysis method developed for this structure - medium interaction study. The material properties representation and the structure modeling concepts used in the analysis models are presented. Results of analyses performed for verification of the method and compilations of typical earth media and construction material physical properties are included.

A summary section presents a description of capabilities of the FEAT computer codes developed for the analysis of structure - medium interaction. It also includes discussion of the application of the analysis method to the development of design information for advanced, hardened missile facilities. Recommended uses for the method are presented, together with suggested extensions for the enhancement of its capabilities.

INTRODUCTION

The purpose of this study was to develop an analysis method for the computation of loads and motions of buried structures subject to nuclear attack, and to utilize this method for the development of design information for such facilities. The achievement of this objective required the accomplishment of several interrelated tasks. These included the development of the numerical analysis technique, the verification of the analysis technique's capability to perform the required computations, the demonstration of the analysis method for a set of realistic problems, and the development of design information for hardened missile facilities.

It is recognized that the problem of structure - medium interaction is truly three-dimensional. The current state of the art, however, does not include adequate techniques or computational facilities for such analyses in three dimensions. Recognition of these facts at the outset of this study led to an approach which uses basic two-dimensional analyses coupled together to represent the most important features of the three-dimensional wave diffraction problem for blast loaded silo structures. The direct stiffness version of the finite element analysis technique (FEAT) is used to construct the analysis models for structure - medium interaction. These analysis models are representations of realistic structures and earth media. Consideration of a wide variety of structural configurations is possible with nominal code modification.

The interaction of structure and earth media is a local phenomenon, whose effects dissipate with distance from the structure. This allows that a finite region of earth material surrounding the structure is adequate for the interaction analysis. All analysis models developed for this study take advantage of this fact and use finite regions of earth media. The boundaries of the finite region considered are loaded by imposed motions or forces which are either determined analytically, obtained from test data, or from computations by other numerical techniques. In this study all three of these boundary loading types were used. For the demonstration cases of four attack conditions on a missile silo the data were generated during computation of free field responses by ATI-AJA under SAMSO Contract FO4694-67-C-0120.

This report is presented in four volumes. The first volume is subdivided in three parts which address the subjects of: the analysis method development (Part I), the verification of the analysis method (Part II), and the summary and design procedure discussion (Part III).

The entire report consists of the following documents:

Volume I - Analysis Method, Theory, Verification and Applicability

Volume II - Method Demonstration (Secret)

Volume III - Modifications to the Method (Secret)

Volume IV - FEAT Code User's Guide

Volume III is the result of work done subsequent to completion of the basic study. Certain modifications in the technique were identified which would enhance the capability of the method. These were incorporated into the code and demonstrated by additional calculations, and the results are reported in the third volume. The FEAT Code User's Guide provides necessary information to those who wish to employ the codes.

TABLE OF CONTENTS

VOLUME I.

	PAGE
FOREWORD	ii
ABSTRACT	iii
INTRODUCTION	iv
PART I, Analysis Method Development	1
PART II, Verification of the Analysis Method	118
PART III, Summary and Design Procedure Discussion	212
REFERENCES	233

PART I.

Analysis Method Development

TABLE OF CONTENTS

PART I.

	PAGE
1.0 INTRODUCTION	6
1.1 Objective	6
1.2 General Method	6
1.3 Finite Element Analysis Technique	7
2.0 FINITE ELEMENT FORMULATION	9
2.1 Basic Concepts	9
2.2 Stiffness Matrix and Generalized Loads	9
2.3 The Plane Strain Problem	13
2.4 The Axisymmetric Problem	13
2.5 Computation Procedure	14
2.6 Computer Requirements	16
3.0 EARTH MEDIA REPRESENTATION	24
3.1 Basic Concepts	24
3.2 Non-linear Elastic and Compacting Relations	24
3.3 Incremental Plastic Relations	27
3.4 Tensile Cracking of Earth Media	30
4.0 STRUCTURE REPRESENTATION	32
4.1 Basic Concepts of Axisymmetric Model	32
4.2 The Overlay Model	37
4.3 The Horizontal Plane Strain Model	44
4.4 Synthesis of Axisymmetric and Plane Models	48

TABLE OF CONTENTS (Continued)

PART I.

	PAGE
5.0 DEBONDING AND SLIP	52
5.1 Basic Concepts	52
5.2 Interface Force Determination	53
5.3 Physical State Determination	56
5.4 Integration Procedure	59
5.5 Displacement and Velocity Tests	60
6.0 SUSPENSION SYSTEM	68
6.1 Introduction	68
6.2 Equations of Motion	68
6.3 Suspension Element Forces	76
7.0 LOADING CONDITIONS	83
7.1 Basic Concepts	83
7.2 Free Field Input	83
7.3 Air Blast Input	85

APPENDICES

A.	Trapezoidal Plane Strain Element	86
B.	Triangular Plane Strain Element	96
C.	Beam Element	101
D.	Rectangular Axisymmetric Element	103
E.	Triangular Axisymmetric Element	110

LIST OF ILLUSTRATIONS

PART I.

FIGURE	TITLE	PAGE
2-1	The Plane Strain Model, Global Coordinates	18
2-2	The Plane Strain Elements, Local Coordinates	18
2-3	The Axisymmetric Problem	19
2-4	The Axisymmetric Element	19
2-5	Flow Chart for Axisymmetric "Soil Island" Version of FEAT Interaction Analysis Code	20
2-6	Vertical Velocity Results for Two Time Steps	22
2-7	Finite Element Idealization of Structure Region (Silo Representation)	23
3-1	A Typical Hydrostat	26
3-2	Transition from Drucker-Prager to Von Mises Criteria	28
4-1	Axisymmetric Model	32
4-2	Structure Model	33
4-3	Ring Deformation	35
4-4	Ring Loading	35
4-5	Stress State	36
4-6	Unlined Cavity Model	38
4-7	Overlay Model	39
4-8	Overlay Paths	39
4-9	Overlay Spring Effect	41
4-10	Typical Overlay Spring Region	42
4-11	Horizontal Section Model	45
4-12	Plane Strain Ring Model	47
4-13	Trapezoidal Element	47
4-14	Axisymmetric and Plane Strain Comparison Models	49

LIST OF ILLUSTRATIONS (Continued)

PART I.

FIGURE	TITLE	PAGE
5-1	Displacement States	54
5-2	Velocity Band	64
5-3	Corner Node Debonding (Example for Upstream Corner)	66
5-4	Corner Node Slipping	67
6-1	Suspension System to be Modeled	69
6-2	Generalized Suspension System Model	70
6-3	Geometry for General and Extension Suspension Elements	71
6-4	Geometry for Compression Suspension Elements	72
6-5	Force Calculation - Compression Suspension Elements	73
7-1	Soil Island Layout	84
A-1	A Trapezoidal Plane Strain Element	86
B-1	A Triangular Plane Strain Element	96
C-1	A Beam Element	101
D-1	An Axisymmetric Ring Element of Rectangular Cross Section	103
E-1	An Axisymmetric Ring Element of Triangular Cross Section	110

INTRODUCTION

1.1 Objective

The objective of this study is to produce an operational computer code which will model the response of a buried structure to a nuclear burst. This code will then be used to generate data for the establishment of realistic design procedures and criteria. This volume describes the analysis method used to develop the computer code. Results and methods for obtaining design procedures will be given in subsequent reports.

1.2 General Method

The approach to the basic task of code construction has been to model the structure and its suspended contents in a large section of the free-field medium (a "soil-island") using a finite element technique. Time histories of stress and motion in the structure and surrounding media are calculated using previously derived free-field motions as forcing functions applied to the boundaries of the soil-island.

Since the use of three-dimensional models for the analysis of structure-medium interaction problems is not practical with current computers, a combination of two-dimensional axisymmetric and horizontal plane analyses is used to solve the general problem. In the case of vertical cylindrical structures, air-blast and ground transmitted loadings result in axial stress and bending of the structures as beams, as well as gross motions of the structure. These responses are determined from the axisymmetric analysis, using orthotropic and overlay elements to model the structure and the stress paths as correctly as possible in a two-dimensional model. The forces acting between the medium and structure also result in deformation of the structure cross-section. A horizontal plane analysis is used to determine the response of the cylinder cross section. This analysis is also used to determine orthotropic material properties for the axisymmetric overlay model.

In several respects the earth-structure models provide a significant advance over current two dimensional codes. First, both models provide a complete two-dimensional diffraction behavior by considering the earth and the structure together as an inhomogeneous medium. In addition, the axisymmetrical model provides an approximation to three dimensional behavior through the use of overlay elements. Second, the earth and structure media are permitted to move relative to one another, that is, to undergo debonding and slip at the interface surfaces, subject to the appropriate stress and motion conditions. Third, earth medium properties are permitted realistic representations, including

plastic behavior, compaction, tensile stress limitation (cracking), non-linear (pressure dependent) elastic properties, and appropriate post-cracking modifications in mechanical properties. Finally, the response of flexible contents supported within the structure can be computed during the earth-structure interaction calculations, and the resulting dynamic forces can be included in the calculations, so that the code provides an earth-structure-contents interaction capability.

In order to establish the credibility of the method, several comparisons have been made with analytical and test data. These results are presented in Part II of this report.

1.3 Finite Element Analysis Technique

The basic premise of the finite element analysis technique is that the behavior of complex two- and three-dimensional media can be approximated by the behavior of an "equivalent" assemblage of small pieces, called elements. In the application of the technique, the actual medium is replaced by a finite number of small, interconnected elements. If the behavior approximated is dynamic in nature, inertia forces are included in the analysis and the response is determined incrementally at discrete time intervals. The response is computed at a set of points called nodal points which are the intersections of the boundaries of the elements.

The finite character of the idealization permits the response to be analyzed by means of simultaneous difference equations at discrete points in time. The concept of finite parameter analysis and availability of large digital computers make it feasible to consider very complex dynamics problems which can not readily be handled by classical methods of analysis.

Finite element methods can be separated into two categories - the force methods and the displacement methods. In general, it has been found (Ref.1) that the displacement methods are more readily formulated and programmed for solution on digital computers. In this study a version of the displacement method, the so-called direct stiffness method, is utilized.

The direct stiffness method was developed originally in the aircraft industry as a tool for analyzing the dynamic behavior of complex airframe structures (Ref.2). During the past 15 years many papers have been written on the development and applications of the method both in the aeronautical engineering and civil engineering fields (Ref.3). The method is an application of the method of Ritz or Kantorovich to obtain an approximate solution to the variational calculus formulation of the field equations of continuum theory. The variational formulation is identical to the stationary potential energy principle. The method is used to solve elastic-plastic problems through a step-by-step or incremental procedure (Ref.4).

The direct application of the variational principle leads to a finite system of equations in the nodal incremental displacements.

$$\begin{bmatrix} M \end{bmatrix} \{ \Delta \ddot{u}_i \} + \begin{bmatrix} K \end{bmatrix} \{ \Delta u_i \} = \{ \Delta F_{ex} \} \quad 1-1$$

where $[M]$ is the mass matrix, $[K]$ is the stiffness matrix, $\{ \Delta u_i \}$ is the matrix of nodal incremental displacements, $\{ \Delta \ddot{u}_i \}$ is the matrix of nodal incremental accelerations, and $\{ \Delta F_{ex} \}$ is the matrix of externally applied loads in incremental form. If the mass is assumed lumped at the nodes, the mass matrix is diagonalized. Such an assumption, which greatly simplifies computational requirements, has been found to yield satisfactory results (Ref. 5).

The logic for numerical implementation of this technique is developed in sections which follow. The computer code has been given the acronym "FEAT" for Finite Element Analysis Technique.

II

FINITE ELEMENT FORMULATION

2.1 Basic Concepts

The fundamental equation of the direct stiffness method gives the nodal forces of an element in terms of its nodal displacements, in incremental form,

$$(\Delta \text{ Nodal Forces}) = (\text{Stiffness}) \times (\Delta \text{ Nodal Displacements})$$

The incremental form of the basic equation permits step-by-step solution of nonlinear and dynamic response problems.

In the sections which follow, the method of derivation of the stiffness matrix is given, together with a brief discussion of the elements used to model the geometry of the buried structure problem. Detailed derivations of the element matrices are given in the Appendices. Final sections describe the integration procedure and computational details.

2.2 Stiffness Matrix and Generalized Loads

The formulation of the stiffness matrix $[K]$ for an individual element is carried out as follows (Ref. 3):

1. The displacement field $\{u_1(x_1, x_2); u_2(x_1, x_2)\}$ is represented in the form of a matrix of assumed displacement functions, $[C]$, with amplitude defined by a set of generalized coordinates, $\{q\}$:

$$\{u_1, u_2\} = [C] \{q\} \quad 2-1$$

Here x_1 and x_2 are the spatial coordinates and u_1, u_2 are the displacements in the x_1 and x_2 directions, respectively. The matrix $[C]$ has two rows, one for each of u_1 and u_2 and defines the displacement field $u_{in}(x_1, x_2)$ for a unit amplitude of the n th generalized coordinate; q_n . The displacements u_1 and u_2 are permitted to occur independently of one another, so that the matrix $[C]$ has the form:

$$[C] = \begin{bmatrix} U_{11} & U_{12} & \cdot & \cdot & \cdot & U_{1n} & 0 & 0 & \cdot & \cdot & \cdot & 0 \\ 0 & 0 & \cdot & \cdot & \cdot & 0 & U_{21} & U_{22} & \cdot & \cdot & \cdot & U_{2m} \end{bmatrix}$$

2. The nodal point displacements are expressed in terms of the generalized coordinates:

$$\{u_i\}_{\text{Nodes}} = [A] \{q\} \quad 2-2$$

Elements of the matrix $[A]$ are obtained by substitution of the nodal point coordinates into the matrix of assumed displacement functions, $[C]$. The number of rows in $[A]$ is twice the number of nodes of the element, and the number of columns is the same as for $[C]$.

3. It is specified for most applications that $[A]$ is a square nonsingular matrix; i.e., the total number of q_n is twice the number of nodes of the element. Then by inversion of $[A]$,

$$\{q\} = [A^{-1}] \{u_i\}_{\text{Nodes}} \quad 2-3$$

At this point the displacements are considered in incremental form, so that

$$\left\{ \frac{d}{dt} q \right\} = [A^{-1}] \left\{ \frac{d}{dt} u_i \right\}_{\text{Nodes}}$$

or

$$\{\Delta q\} = [A^{-1}] \{\Delta u_i\}_{\text{Nodes}}$$

where the increments are those which take place during a single time interval of a stepwise response calculation. Corresponding to Δq and Δu_i are increments in the displacement fields themselves, $\{\Delta u_1(x_1, x_2); \Delta u_2(x_1, x_2)\}$ and

$$\{\Delta u_1, \Delta u_2\} = [C] [A^{-1}] \{\Delta u_1, \Delta u_2\}_{\text{Nodes}} \quad 2-4$$

4. The incremental strain field is expressed in terms of the incremental generalized coordinates:

$$\{\Delta \epsilon\} = [B] \{\Delta q\} \quad 2-5$$

The matrix $[B]$ is obtained from the matrix $[C]$ by appropriate operations performed on the assumed displacement functions with respect to the spatial coordinates. For rectangular cartesian coordinates, for example,

$$\Delta \epsilon_{ij} = \frac{1}{2} \left(\frac{\partial \Delta u_i}{\partial x_j} + \frac{\partial \Delta u_j}{\partial x_i} \right) \quad 2-6$$

5. The incremental stresses $\{\Delta \sigma\}$ are determined by means of a stress-strain matrix $[D]$,

$$\{\Delta \sigma\} = [D] \{\Delta \epsilon\} = [D] [B] \{\Delta q\} \quad 2-7$$

The characteristics of the matrix $[D]$ may reflect elastic, plastic, elastic-plastic or any other specified material properties with specified spatial orientation, i.e., isotropic or orthotropic, etc.

6. The accumulated strain energy of a differential volume of material within an element is obtained by integrating with respect to time, starting from a state of zero stress, strain, and energy.

$$dW_I = dV \int_0^t \left\{ \sigma \right\}^T \left\{ \frac{d\epsilon}{d\eta} \right\} d\eta \quad 2-8$$

where η is a dummy variable of integration. The stresses at time $t = \eta$ are

$$\left\{ \sigma \right\} = \int_0^\eta [D] [B] \left\{ \frac{dq}{d\tau} \right\} d\tau \quad 2-9$$

where τ is also a dummy variable of integration. Substituting 2-9, 2-5 into 2-8,

$$dW_I = dV \int_0^t \left\{ \int_0^\eta [D] [B] \left\{ \frac{dq}{d\tau} \right\} d\tau \right\}^T [B] \left\{ \frac{dq}{d\eta} \right\} d\eta \quad 2-10$$

For the entire volume of the element,

$$W_I = \int_V \left[\int_0^t \left\{ \int_0^\eta \left\{ \frac{dq}{d\tau} \right\}^T [B]^T [D]^T d\tau \right\} [B] \left\{ \frac{dq}{d\eta} \right\} d\eta \right] dV \quad 2-11$$

The rate of change of the strain energy of the element with respect to time is

$$\frac{dW_I}{dt} = \int_V \left\{ \int_0^t \left\{ \frac{dq}{d\tau} \right\}^T [B]^T [D]^T d\tau \right\} [B] \left\{ \frac{dq}{dt} \right\} dV \quad 2-12$$

Interchanging the order of integration

$$\frac{dW_I}{dt} = \int_0^t \left\{ \frac{dq}{d\tau} \right\}^T \left[\int_V [B]^T [D]^T [B] dV \right] d\tau \left\{ \frac{dq}{dt} \right\} \quad 2-13$$

The stiffness matrix is defined to be the transpose of the bracketted quantity, i.e.,

$$[\bar{k}] \equiv \int_V [B]^T [D] [B] dV \quad 2-14$$

It is seen that $[\bar{k}]$ provides a relationship between generalized displacements $\{q\}$ and the corresponding generalized loads, which are called $\{\bar{Q}\}$. The relationship parallels equation 2-9, and for a single element is

$$\left\{ \frac{d\bar{Q}}{dt} \right\} \equiv [\bar{k}] \left\{ \frac{dq}{dt} \right\} \quad 2-15$$

The correspondence between $\{\bar{Q}\}$ and $\{q\}$ is that for the element

$$\frac{dW_I}{dt} = \{\bar{Q}\}^T \left\{ \frac{dq}{dt} \right\} \quad 2-16$$

from which

$$\frac{dW_I}{dt} = \int_0^t \left\{ \frac{dq}{d\tau} \right\}^T [\bar{k}]^T d\tau \frac{dq}{dt} \quad 2-17$$

from which follows the definition of $[\bar{k}]$, equation 2-14.

The manner in which the stiffness matrix is used in the computer code is indicated by the form of equation 2-15.

The total nodal forces, $\{\bar{Q}\}$, are obtained by summing, cumulatively, the increments of the form

$$\Sigma \{\Delta q\}^T \left[\int_V [B]^T [D]^T [B] dV \right] d\tau$$

and retaining the accumulated value as the total nodal force applied by the element to the nodal mass.

7. The time rate of change of external virtual work $\frac{dW_E}{dt}$ associated with the generalized displacements $\{q\}$ is given by:

$$\frac{dW_E}{dt} = \left\{ \frac{dq}{dt} \right\}^T \{\beta\} \quad 2-18$$

where $\{\beta\}$ represents the generalized forces corresponding to the generalized coordinates $\{q\}$.

8. The element stiffness matrix $[K]$, in terms of the nodal displacements, is obtained as follows:

$$[k] = [A^{-1}]^T [\bar{k}] [A^{-1}] \quad 2-19$$

This operation is merely a coordinate transformation from the generalized coordinates $\{q\}$ to the nodal point coordinates as defined by equations 2-2 and 2-3. The transformation of the generalized loads is given by

$$[Q] = [A^{-1}]^T \{\beta\} \quad 2-20$$

where $\{Q\}$ is the matrix of generalized loads corresponding to the nodal displacements.

This standard procedure is a straightforward process, except perhaps for the definition of the stress-strain matrix $[D]$ for elastic-plastic or variable moduli materials. This will be discussed in Section 3.0 and the appropriate Appendices.

2.3 The Plane Strain Problem

In order to compare computer results with analytical and test results, (Part II) and to assist in interpreting results from a vertical section analysis of the buried structures, two plane strain versions of the FEAT code have been developed. One of these is rectangular in form, and hence can readily be loaded at a boundary by a plane wave. This version is used to obtain numerical solutions to the analytical problems of plane elastic waves impinging on buried horizontal cylinders. The other version has been formulated in a fan-shaped geometry (using trapezoidal elements) in order to model cylindrical waves. This version will be used as a horizontal slice out of the axisymmetric model to provide ring deformations and stresses for different cross-sections of a buried vertical cylinder. Rectangular, trapezoidal and triangular elements of unit thickness are used in these codes to represent the free field and the buried structure.

A schematic representation is given in Figure 2-1. The triangular elements are constant strain elements, but the rectangular and trapezoidal ones are linear strain elements. All elements have displacement fields such that compatible displacements are maintained along each boundary. Full details of the elements including derivations, are given in the Appendices.

For the rectangular element shown in Figure 2-2 the incremental strain tensor $\Delta \epsilon_{ij}$ is

$$\Delta \epsilon_{ij} = \begin{pmatrix} \Delta \epsilon_x & \frac{\Delta \gamma_{xy}}{2} & 0 \\ \frac{\Delta \gamma_{xy}}{2} & \Delta \epsilon_y & 0 \\ 0 & 0 & 0 \end{pmatrix} \quad 2-21$$

and the corresponding incremental stress tensor is:

$$\Delta \sigma_{ij} = \begin{pmatrix} \Delta \sigma_x & \Delta \tau_{xy} & 0 \\ \Delta \tau_{xy} & \Delta \sigma_y & 0 \\ 0 & 0 & \Delta \sigma_z \end{pmatrix} \quad 2-22$$

2.4 The Axisymmetric Problem

Another version of the FEAT computer codes is the "axisymmetric" program. A schematic illustration is shown in Figure 2-3.

In this code, ring elements of both rectangular and triangular cross sections have been used (See Figure 2-3). In addition, orthotropic elements and

overlay-elements are used to simulate the structure and medium in the region of the structure. These are discussed in Section 4.

For the axisymmetric problems, the incremental strain tensor for the element shown in Figure 2-4 is as follows:

$$\Delta \epsilon_{ij} = \begin{pmatrix} \Delta \epsilon_x & \frac{\Delta \gamma_{xr}}{2} & 0 \\ \frac{\Delta \gamma_{xr}}{2} & \Delta \epsilon_x & 0 \\ 0 & 0 & \Delta \epsilon_\theta \end{pmatrix} \quad 2-23$$

and the corresponding incremental stress tensor is:

$$\Delta \sigma_{ij} = \begin{pmatrix} \Delta \sigma_x & \Delta \tau_{xr} & 0 \\ \Delta \tau_{xr} & \Delta \sigma_r & 0 \\ 0 & 0 & \Delta \sigma_\theta \end{pmatrix} \quad 2-24$$

2.5 Computation Procedure

2.5.1 Integration Process

Before describing the technique for marching the complete calculations forward in time, it is necessary to describe how the displacements are obtained at each time step.

The displacement-increment matrix, $\{\Delta u_i\}$, is found by an integration technique called the acceleration-pulse method (Ref. 6). It yields displacements for given accelerations:

$$u = 2 u' - u'' + \frac{F}{m} (\Delta t)^2 \quad 2-25$$

where u , u' , u'' = displacements corresponding to time, t , $t - \Delta t$ and $t - 2\Delta t$, respectively, and

Δt = time increment

F = total force acting on the mass at the node in the direction corresponding to u at time $t - \Delta t$

m = mass at the node

The above equation can be rewritten as follows:

$$\Delta u = u - u' = u' - u'' + \frac{F}{M} (\Delta t)^2 \quad 2-26$$

which is the quantity desired for computation of $\{\Delta u_i\}$.

With displacements, stresses, and material properties known for all nodes and elements at the current and previous times, the increments of strain and stress can be computed for the next time interval. The sequence of the computations used in the axisymmetric "soil island" version of the FEAT interaction analysis code is shown in the flow chart on Figure 2-5.

2.5.2 Selection of Time Steps

In a numerical procedure for wave motions, time steps must be chosen in such a way that they satisfy requirements for stable, accurate calculations and satisfactory representation of applied pulses. In addition, computing economy is also an important consideration. However, there are no exact criteria which can be used for the selection of a unique "best" time step. It is known, however, that the time step for wave motions should be smaller than the smallest element transit time in the spatial domain of interest.

A practical approach toward the selection problem is numerical experimentation. For a given problem a time step of, say, fifty to sixty percent of the transit time can be used. Numerical results are then carefully examined for possible computational instability. Through a series of trials it is possible to find a proper time step. Experience indicates that a proper time step is sixty percent of the smallest transit time for multi-dimensional problems.

An example of computation with two significantly different time steps is given in Figure 2-6. The dilatational wave speed in this medium was about 15,000 fps, and with the 20' square elements used, transit time was 1.33 msec. Taking 60% of the value gave 0.8 msec as a suggested computation time interval. Another solution was run using 0.2 msec for the computation time, with comparable results. Based on these and other similar results a time step of 60% of transit time is used.

The wave motions of the free field, which drive the structure region, are the result of propagation through the free field mesh. They contain frequencies which are governed by the element size and the integration time step. Consequently, the computed response of the structure region is limited in frequency content to the character of the free field motion. Since, however, the structure region contains smaller elements, Figure 2-7, than the free field, it requires a smaller integration time step for stability of the calculation. To avoid the need for smaller time steps over the whole model a procedure was developed by which several time step computations can be executed in the structure region for each free field time step.

In the Figure 2-7 the shaded region represents the structure region requiring smaller integration steps. Nodes on the boundary between the free field and the structure region (A in the Figure), together with all nodes in the structure region (e.g., C in the Figure), have their motions computed with the smaller integration step. All free field nodes, other than those on the interface between the regions, (e.g., B in the Figure) have their motions computed at the larger, free field time step.

Node B, therefore, undergoes motions consistent with its velocity and the forces applied to it by all adjacent elements at time t_i , throughout the time step t_i to t_{i+1} . Nodes A and C on the other hand undergo motions during the time step t_i to $t_{i+1/n}$, where n is an integer governed by the time step requirements in the structure region. The forces and velocities of nodes such as A and C are updated to the values which are present at the time $t_{i+1/n}$, prior to computations for time step $t_{i+1/n}$ to $t_{i+2/n}$. This process is continued to the time $t_{i+n/n} = t_{i+1}$, at which point the entire field step-wise calculation is begun again.

The forces on the boundary nodes, such as node A, which come from elements outside the structure region are not updated to times subsequent to t_i ; they are kept at the values which they had at t_i . This detail amounts, approximately, to an effective prorated updating of the displacements of nodes such as node B during t_i to t_{i+1} , to the time points $t_{i+1/n}$, $t_{i+2/n}$, etc. It is needed in order to prevent unrealistic strains to develop in these elements during the small Δt calculations. For interior nodes such as node C, updated forces from all connected elements at all of the small Δt calculations are used.

2.6 Computer Requirements

Several computer programs have been written to apply the finite element method to wave motion calculations, including problems of plane strain and axisymmetry. Each program was written as a separate unit to take advantage of the characteristics in the problem that it was describing. In this way efficient computer codes, utilizing a minimum of computer time, could be constructed.

All programs were written in FORTRAN IV (Univac) language and are designed to run on the Univac 1108 digital computer at The Boeing Company in Seattle. Although these programs use many of the common hardware and software capabilities, they do require several items not usually needed by computer programs used for engineering applications.

The first of these items is the amount of computer core required for the storage of program instructions. This amount is unusually high because each program is several thousand cards in length. To store sufficient program instructions and permit some data storage in core, nearly all of the available storage unit is required. In addition, several chain links are needed for the pre- and post-processing of data.

The second item is the amount of out-of-core storage used. To minimize dispersion effects and to delay reflections from boundaries of the finite element model, a large number of degrees-of-freedom is desirable for each model. To save the necessary data for the model, vast regions of drum and/or magnetic tape storage are used. While the present facilities would permit as many as 250,000 degrees-of-freedom, computer run times dictate a much smaller number, in the range of 10,000 to 20,000 degrees-of-freedom. Even with this limited number, 4 to 7 tapes, each 2,400 feet long and of density 800 bits per inch, and a drum storage of 1.5 million words are required.

Because of the large amount of data constantly being input, calculated and output, a special input/output routine is used. This routine permits simultaneous input/output and calculations. As a result, the program can be simultaneously outputting data already calculated, calculating the present data in core, and inputting the data necessary for the next calculation.

Another aspect of the computation is the long run times encountered, since many time steps have to be used to describe a satisfactory solution to a given problem, although the average computing time is of the order of milliseconds per degree-of-freedom per time-step computation. This time step requirement, together with the number of degrees-of-freedom required, dictates computer run times of the order of 30 minutes to several hours. Even to obtain these run times, numerous time-saving devices have been included in the program. In addition, a safety measure has been added to guard against computer hardware failure. Each program is equipped with the capability to stop at any time, saving all pertinent information on magnetic tapes. The solution can then be examined in detail and at a later date restarted on the computer. In this way no program need be on the computer for more than, say 30 minutes at a time.

Finally, because of the large quantity of digital output possible, some systematic method for displaying the results of the solution is essential. To facilitate this display, each program has several output capabilities:

- (1) Print motions and stresses for selected nodes and elements at each time step.
- (2) Plot via automatic plotting machine the time histories of motions and stresses for selected nodes and elements.
- (3) At each time step print a "motion map" indicating, through the use of various print characters, the magnitude of the velocity or acceleration vector for each node of the finite element model.
- (4) At each time step print a "state of stress map" indicating the condition of each element of the model, i.e., elastic, plastic, loading, unloading, cracked, or recompressed, etc.

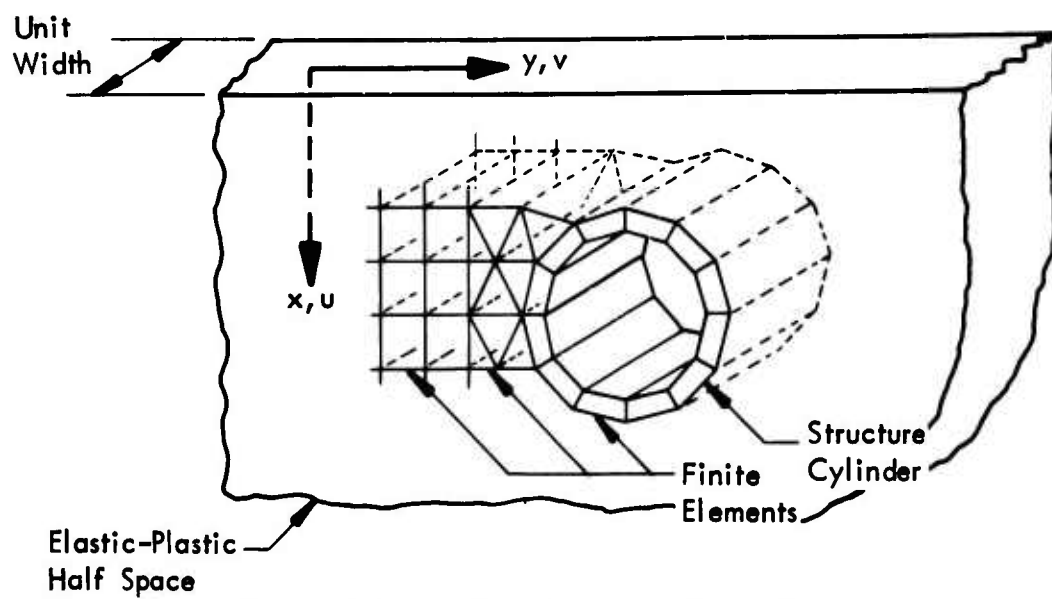


Figure 2-1: THE PLANE STRAIN MODEL
Global Coordinates

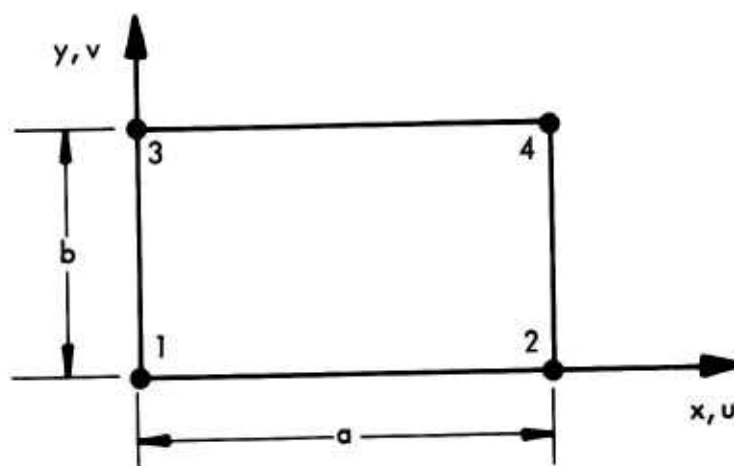


Figure 2-2: THE PLANE STRAIN ELEMENT
Local Coordinates

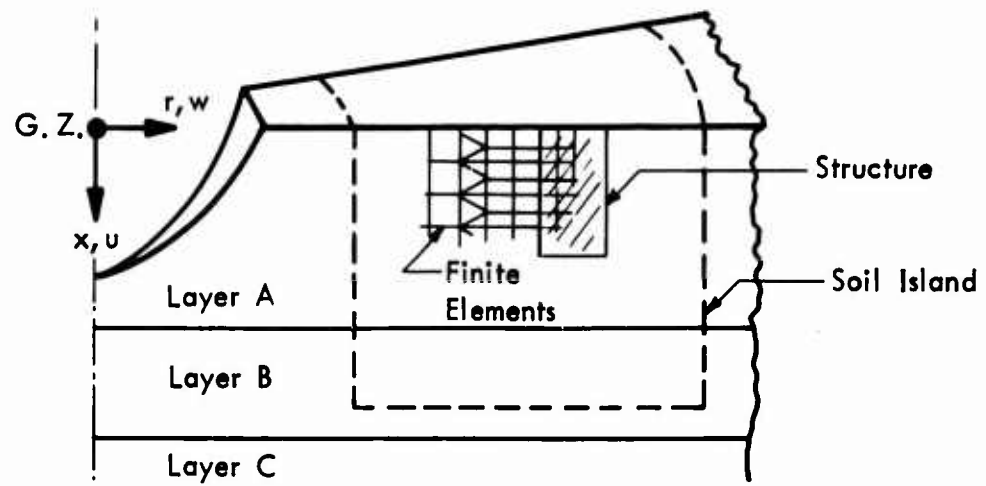


Figure 2-3: THE AXISYMMETRIC PROBLEM

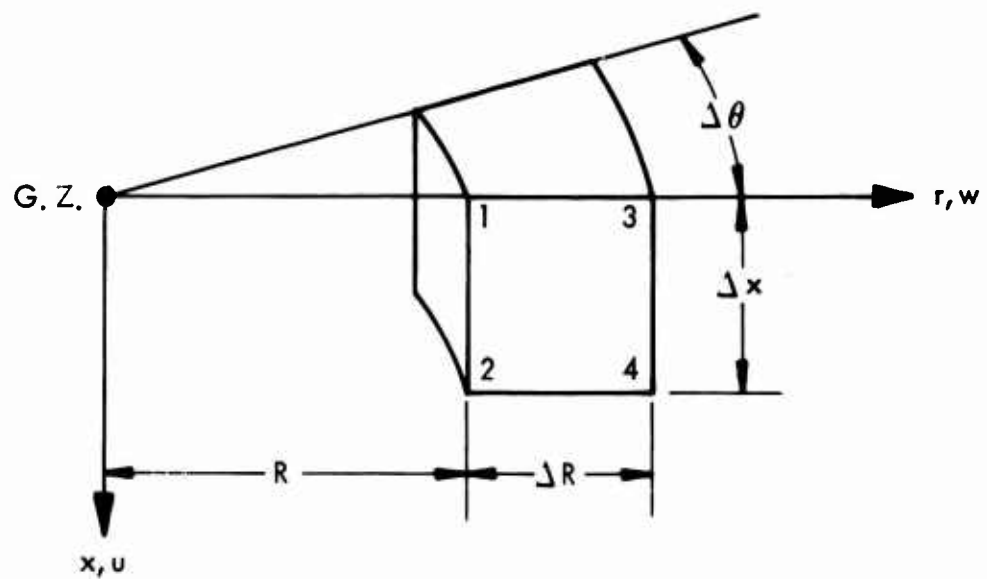
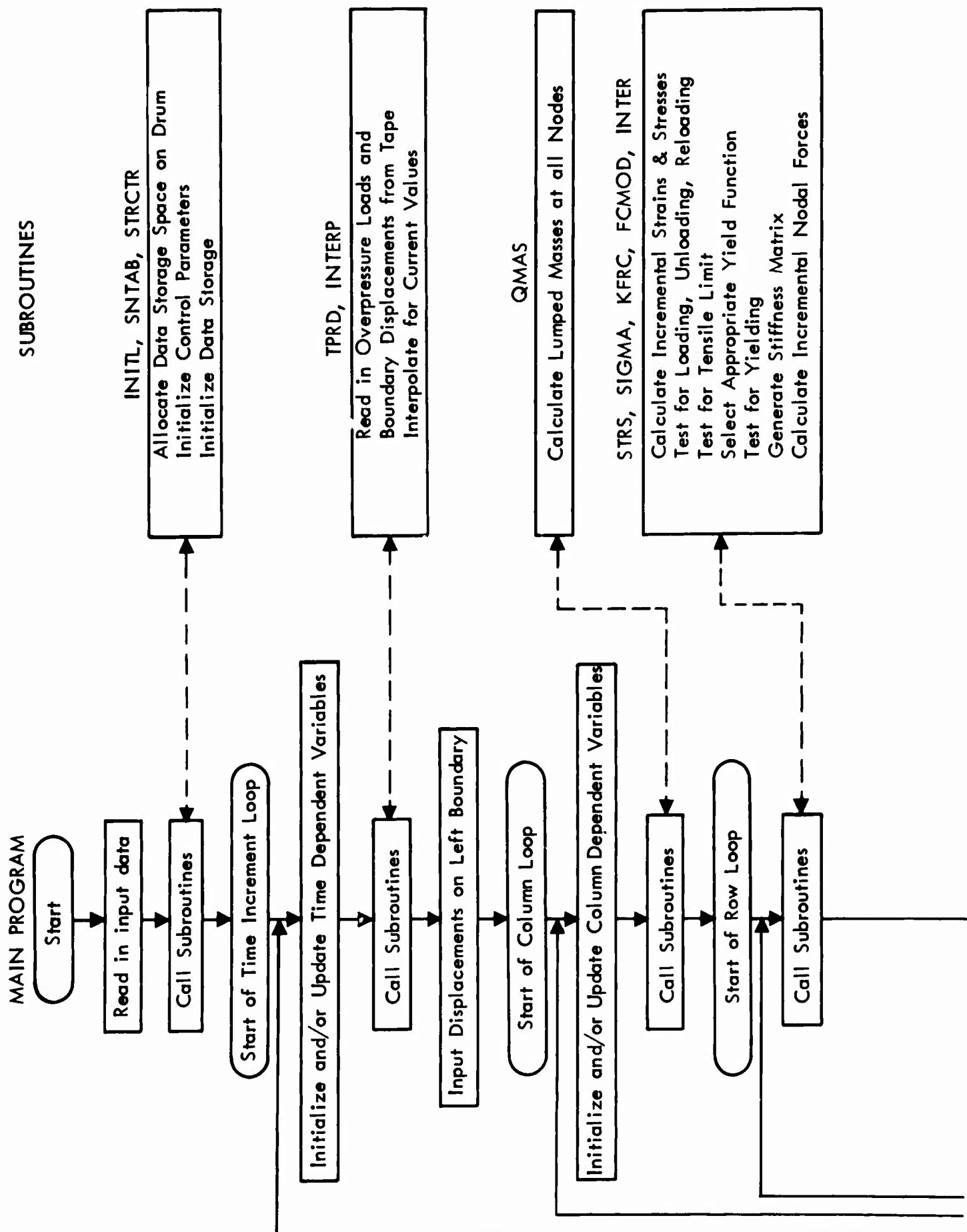


Figure 2-4: THE AXISYMMETRIC ELEMENT



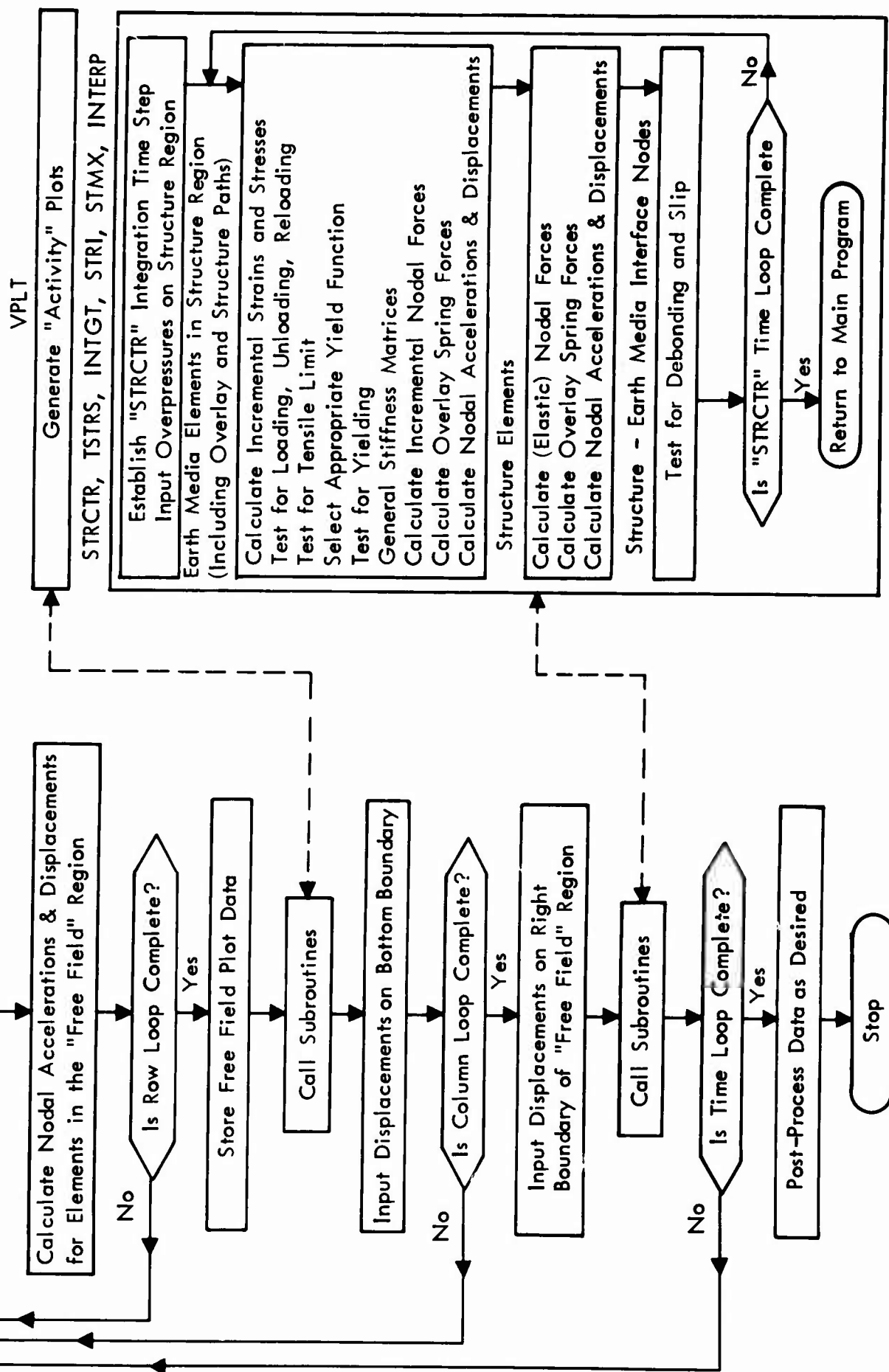
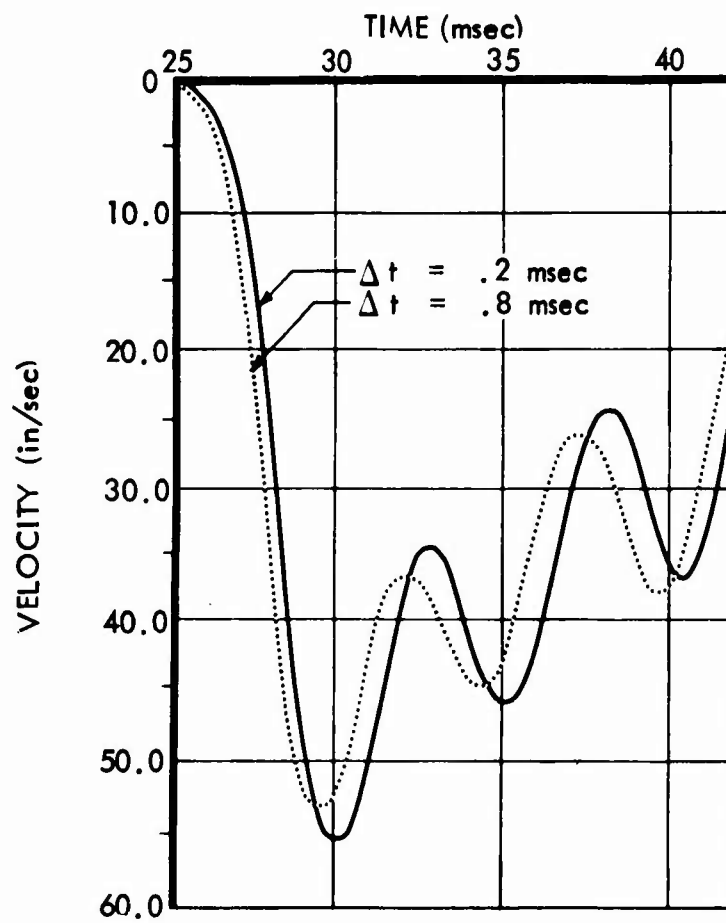


FIGURE 2-5: FLOW CHART FOR AXISYMMETRIC "SOIL ISLAND" VERSION OF FEAT INTERACTION ANALYSIS CODE



- a - Prescribed displacements as input
- b - Air over pressure as input

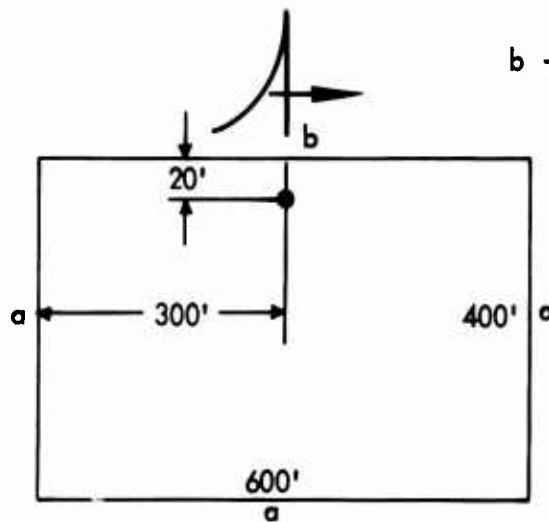
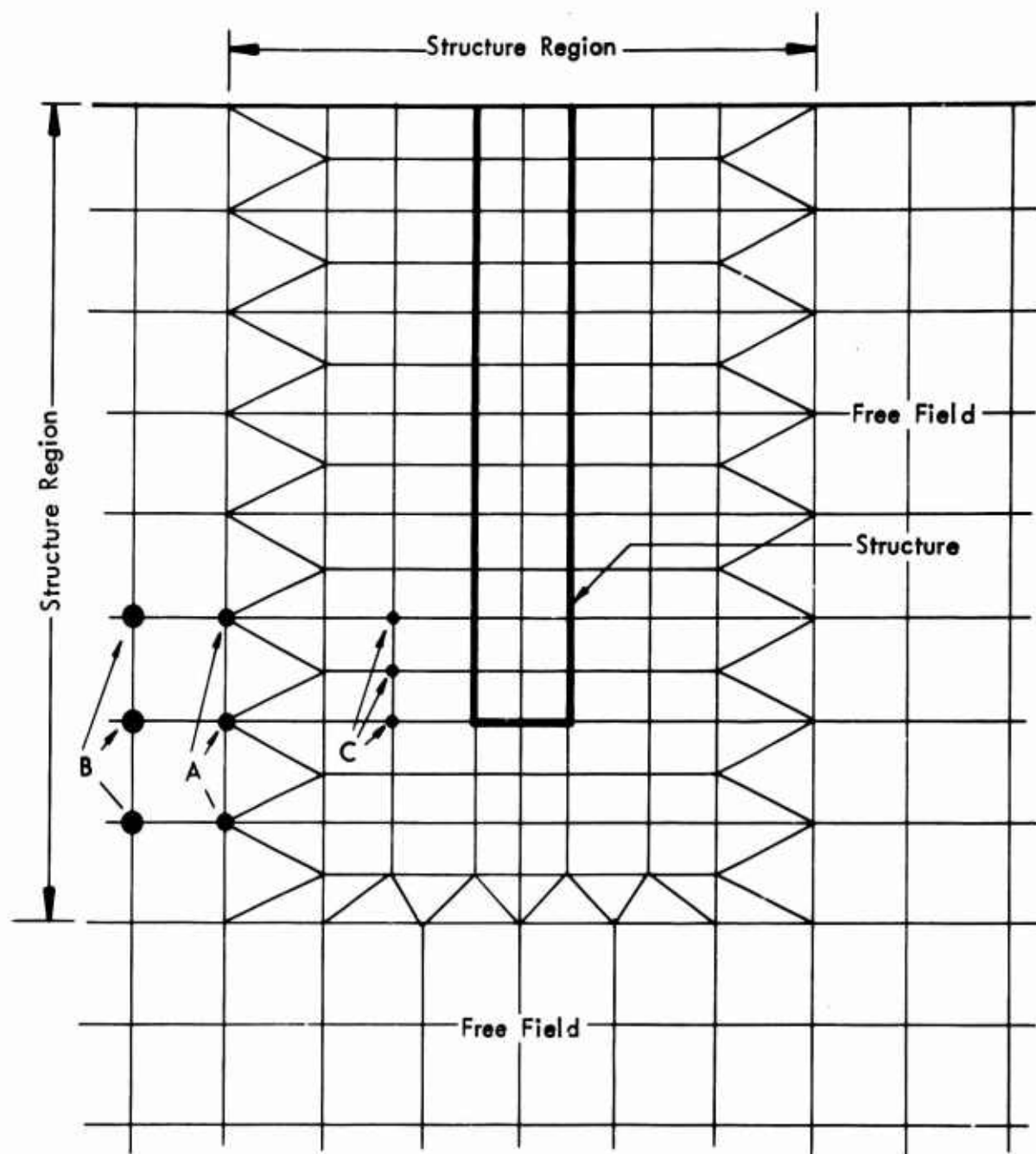


Figure 2-6: VERTICAL VELOCITY RESULTS FOR TWO TIME STEPS



A, B, C, - TYPICAL NODE POINTS

Figure 2-7: FINITE ELEMENT IDEALIZATION OF STRUCTURE REGION
(SILO REPRESENTATION)

III

EARTH MEDIA REPRESENTATION

3.1 Basic Concepts

Studies and tests of earth media* behavior under a variety of loading conditions have shown that these media will experience recoverable and non-recoverable deformations during loads imposed by nuclear blasts. The recoverable portion of the deformations is the result of elastic response which for many earth materials will involve a nonlinear relation between stress and strain. The nonrecoverable deformations are either due to the compactive nature of the material or due to plastic flow. In addition to these characteristics, which describe earth media under compressive loads, it can readily be seen that tensile strength of these materials is extremely limited. The FEAT code has been designed to take into account these material characteristics. The following sections describe in detail how this is accomplished.

Past work with earlier versions of the FEAT code had considered a material model incorporating linear elasticity and a Mohr-Coulomb type of plasticity. The requirements imposed by this contract included a model capable of considering a Young's Modulus dependent upon the state of hydrostatic stress. In the preparation of the necessary changes to the code to provide this capability, investigation showed that current developments in soil testing and material model concepts are aiming towards the use of the basic elastic parameters of bulk and shear modulus, rather than Young's Modulus and Poisson's ratio. The revision of the FEAT code was undertaken to provide the facility to prescribe bulk and shear moduli as independent functions of the state of hydrostatic stress. This extends the usefulness of this analysis technique to take advantage of advances in material property determination.

3.2 Non-linear Elastic and Compacting Relations

3.2.1 Fundamental Relations

The behavior of earth materials in the lower pressure regions can be represented by an elastic model for certain soils and rocks, while for some materials, usually the more porous types, portions of the displacements are not recovered after loading is removed. This occurs because the material unloads with a different modulus. In this section these two types of material models, the elastic and the compacting, will be discussed.

* Solid matter of this planet.

In the FEAT computer code this type of material behavior is represented by a variable moduli model in an incremental manner. An excellent discussion of the use of variable moduli models was presented at the DASA Long Range Planning Meeting, January 1968, by Nelson and Baron in their paper "Development of Non-linear Hysteretic Material Models." (Ref. 7)

In indicial notation the stress-strain relations can be written as:

$$d\sigma_{ij} = 2Gd\epsilon'_{ij} + K\delta_{ij} d\epsilon_{kk} \quad 3-1$$

where K = Bulk Modulus

G = Shear Modulus

$d\sigma_{ij}$ = the differential stress tensor

$$= \begin{pmatrix} d\sigma_{11} & d\sigma_{12} & d\sigma_{13} \\ d\sigma_{21} & d\sigma_{22} & d\sigma_{23} \\ d\sigma_{31} & d\sigma_{32} & d\sigma_{33} \end{pmatrix} \quad 3-2$$

and $d\sigma_{ij} = d\sigma_{ji}$

$d\epsilon_{ij}$ = the differential strain tensor

$$= \begin{pmatrix} d\epsilon_{11} & d\epsilon_{12} & d\epsilon_{13} \\ d\epsilon_{21} & d\epsilon_{22} & d\epsilon_{23} \\ d\epsilon_{31} & d\epsilon_{32} & d\epsilon_{33} \end{pmatrix} \quad \text{and } d\epsilon_{ij} = d\epsilon_{ji} \quad 3-3$$

$d\epsilon'_{ij}$ = the deviatoric differential strain tensor

= $d\epsilon_{ij} - 1/3 \delta_{ij} d\epsilon_{kk}$

δ_{ij} = Kronecker delta

The moduli K and G to be used in the stress-strain relationship 3-1 can be obtained from uniaxial strain and triaxial compression tests. However, for the calculations to be performed under this contract, the material property data were given in the form of hydrostats, i.e., a proportional relationship between hydrostatic stress and volumetric strain together with a specified Poisson's ratio. The bulk and shear moduli can be derived from the hydrostat and the value of Poisson's ratio.

The hydrostat can be represented as

$$dP = -K \frac{dV}{V} \quad 3-4$$

or

$$dP = K \frac{1}{(1+\mu)} d\mu \quad 3-5$$

where μ = excess compression

$$= \frac{\rho}{\rho_0} - 1$$

Other parameters are

V = the specific volume
 dV = the differential of V
 P = the mean pressure = $\frac{-1}{3} \sigma_{ii}$
 dP = the differential of P
 σ_{ii} = the sum of normal stress components
 ρ_0 = reference density
 ρ = density

A typical hydrostat for a compacting medium is shown in Figure 3-1. A set of moduli can be derived for the loading and the unloading hydrostat.

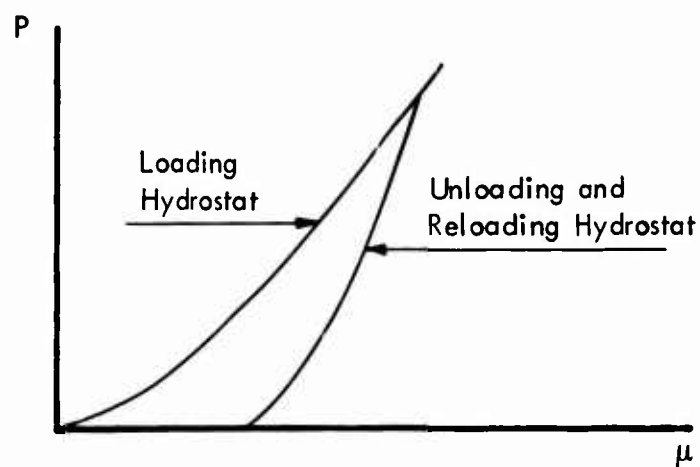


Figure 3-1: A TYPICAL HYDROSTAT

3.2.2 Loading and Unloading Moduli

In order to accommodate the various forms of material behavior anticipated for analysis by FEAT it was necessary to write the stress-strain relationships in terms of variable moduli. In this manner it is feasible to handle nonlinearly elastic response as well as the phenomenon of compaction. At the same time the code is in a position to use the variable moduli models now under study by various researchers.

The input to the FEAT code includes the bulk and shear moduli as functions of mean pressure P . The moduli are described in the input to the program as piecewise linear approximations.

The state of stress is monitored constantly in each element so that for each incremental calculation the correct values of $K(P)$ and $G(P)$ will be used. At the same time the program monitors the increment of pressure dP to determine whether the element is loading or unloading. As long as dP remains positive the loading moduli are used. When dP becomes negative, the current value of mean pressure P is stored and further calculations are made using the unloading $K(P)$ and $G(P)$ until such a time that the mean pressure exceeds the highest previous value. If this occurs the program switches to the loading moduli, using them until another unloading cycle begins, at which time again the current P is stored. The degree to which the "Compaction" phenomenon occurs in the shear modulus, $G(P)$, depends on information not contained in the hydrostat. The FEAT code can accept any data which may be suggested by test results. The current calculations use a constant value of Poisson's ratio, as specified for this contract, with the result that $G(P)$ and $K(P)$ have identical compaction behavior.

3.3 Incremental Plastic Relations

3.3.1 Preliminary Remarks

In Section 3.1, two causes of nonrecoverable deformations were described. The permanent deformations due to compaction of the medium were considered under the description of non-linear elastic relationships. Another source of nonrecoverable deformations arises from plastic flow in the medium. The constitutive relations used for this study are based on the incremental plasticity theory with a non-strain hardening material. A brief account of the theory as well as formulas applicable to the present study are given in the next several sections.

3.3.2 The Yield Criterion

For this study the material is assumed to obey the Drucker-Prager yield criterion which is a generalization of the Mohr-Coulomb law for solid media exhibiting internal friction, (Refs. 8 and 9). This yield criterion is considered to be valid when the state of hydrostatic stress lies below a certain level. Above this level the shear strength of the material is assumed not to increase further with increasing hydrostatic stress. At this point the Drucker-Prager criterion is specialized to the von Mises criterion by changing the parameters in the following equations. The complete yield criterion is shown in Figure 3-2. The criterion can be written in the form

$$\begin{aligned}
 f &= \alpha J_1 + \sqrt{J_2'} = k, \quad J_1 > J_{1v} \\
 \text{or } f &= \sqrt{J_2'} = k_v, \quad J_1 < J_{1v}
 \end{aligned}
 \tag{3-6}$$

where $J_1 = \sigma_{kk}$; $J_2' = 1/2 \sigma_{ij}' \sigma_{ij}'$

σ_{ij}' = deviatoric stress tensor

The parameters α , k , k_v and J_{1v} serve to characterize material behavior.

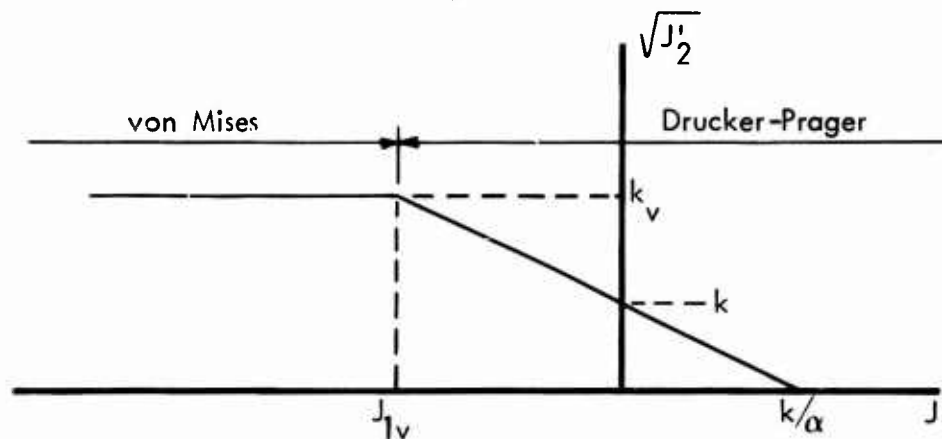


Figure 3-2: TRANSITION FROM DRUCKER-PRAGER TO VON MISES CRITERIA

Since the computation procedure involves finite time steps and finite mesh sizes, it is unavoidable that small errors will be introduced into the numerical results. As a consequence, the plastic state of stress cannot satisfy the yield criterion exactly at all time steps and, thus, the yield criterion must be examined by means of a tolerance control factor. The following formula is used:

$$[f - k] \leq e_t k \tag{3-7}$$

where e_t is a small number used for the tolerance control. A typical value is $e_t = 0.02$. The state is plastic when Equation 3-7 is satisfied.

It will occur occasionally that the stress point will pass outside the upper tolerance limit, that is,

$$f > k + e_t k$$

When this happens, the state of stress will be returned to the yield surface by a correction procedure exercised on the deviatoric component of the stress state (Ref. 10). The following are the corrected stresses:

$$\begin{aligned}
\sigma_x^c &= \frac{1}{3} (3-2\eta) \sigma_x + \frac{1}{3} \eta \sigma_y + \frac{1}{3} \eta \sigma_z \\
\sigma_y^c &= \frac{1}{3} \eta \sigma_x + \frac{1}{3} (3-2\eta) \sigma_y + \frac{1}{3} \eta \sigma_z \\
\sigma_z^c &= \frac{1}{3} \eta \sigma_x + \frac{1}{3} \eta \sigma_y + \frac{1}{3} (3-2\eta) \sigma_z \\
\tau_{xy}^c &= (1 - \eta) \tau_{xy} \\
\tau_{yz}^c &= (1 - \eta) \tau_{yz} \\
\tau_{zx}^c &= (1 - \eta) \tau_{zx}
\end{aligned} \tag{3-8}$$

where the stresses with a superscript "c" refer to corrected values, the ones without the superscript are the uncorrected values, and

$$\eta = 1 - \frac{k - \alpha J_1}{\sqrt{J_2}}$$

This procedure leaves J_1 unchanged.

3.3.3 Plastic Flow Rule

The post yielding behavior of the material is described by the plastic flow rule on an incremental basis (Ref. 11). The flow rule can be derived in accordance with the theory of plastic potential (Ref. 12). This leads to:

$$\Delta \epsilon_{ij} = \frac{1}{2G} \Delta \sigma'_{ij} + \frac{1}{9K} \delta_{ij} \Delta \sigma_{kk} + h \frac{\delta f}{\delta \sigma_{ij}} d\epsilon \tag{3-9}$$

The last term above represents the plastic strain increment, and h is a scalar function of stress invariants. In the absence of strain hardening $h \rightarrow \infty$, but hdf remains finite.

The equation can be inverted to give:

$$\Delta \sigma_{ij} = 2G \Delta \epsilon_{ij} + (K - 2/3 G) \delta_{ij} \Delta \epsilon_{kk} - Q H_{ij} H_{mn} \Delta \epsilon_{mn} \tag{3-10}$$

where

$$\begin{aligned}
Q &= \xi 2G \left\{ \frac{1}{2} + \frac{9K}{2G} \alpha^2 \right\}^{-1} \\
H_{ij} &= \frac{1}{2} \frac{\sigma_{ij}}{\sqrt{J_2}} + \left(\frac{3K}{2G} \alpha - \frac{1}{6} \frac{\sigma_{kk}}{\sqrt{J_2}} \right) \delta_{ij} \\
\xi &= 0, \quad (\text{elastic}) \\
\xi &= 1, \quad (\text{plastic})
\end{aligned}$$

3.3.4 Cycles of Plastic Flow

Unloading from plastic flow commences when the stress state falls below the tolerance envelope about the yield surface, i.e., when

$$f < k(1 - e_f) \quad 3-11$$

Continuation of the non-plastic state is guaranteed as long as equation 3-11 is satisfied.

Re-occurrence of plastic flow may take place, as governed by equation 3-6

3.3.5 Plastic Volumetric Expansion

When the Drucker-Prager yield criterion is used in the Prandtl-Reuss flow rule, there results plastic volumetric expansion.

$$d\epsilon_{kk}^p = d\lambda \frac{\delta f}{\delta \sigma_{kk}} = 3\alpha d\lambda \quad 3-12$$

Where $d\lambda = h df$ is a positive scalar function of stress and stress rates.

The plastic volume increment is given by

$$d\epsilon_{kk}^p = d\epsilon_{kk} - \frac{1}{3K} d\sigma_{kk} \quad 3-13$$

where $d\epsilon_{kk} =$ total volumetric strain.

The quantity $d\epsilon_{kk}^p$ is calculated and printed out, as desired. Thus the amount of plastic volumetric strain calculated can be compared with observed data.

3.4 Tensile Cracking of Earth Media

Earth materials have limited tensile resistance. Consequently, provisions are made to take that into account in this study. It is accomplished by specification of a state of hydrostatic stress below which the material is assumed to experience a complete cracking in tension.

3.4.1 Criterion for Tensile Cracking

When the sum of normal stress components becomes equal to or greater than a specified number, the material is said to experience excessive tension and is to crack. Thus, the criterion for tensile cracking is

$$\sigma_{kk} \geq -3 P_{lt} \quad 3-14$$

where P_{lt} is a prescribed number. For convenience, the above criterion can be written as follows:

$$P - P_{lt} \leq 0 \quad 3-15$$

The prescribed number P_{lt} reflects the tensile resistance of the material under consideration.

Equation 3-15 is the primary criterion for tensile cracking. It is used for material which has never cracked before. For material which has experienced tensile cracking in its histories of loading, the criterion is taken as

$$P - P_{lt}^* \leq 0 \quad 3-16$$

Since the material is relatively weak and is capable of sustaining reduced tension $|P_{lt}^*|$ will generally be less than $|P_{lt}|$.

When an element cracks it no longer contributes forces to its adjoining nodes. In fact, the entire past history of nodal forces contributed by that element is erased. To accomplish this, the program has storage arrays for nodal forces for every element in the analysis model, so that the appropriate forces can be set to zero, when an element has cracked.

3.4.2 Recovery and Post-Cracking Behavior

At the instant an element cracks a reference value of volumetric strain is computed for that element and stored. This value is taken to be the volumetric strain which existed in the element when its state of hydrostatic stress was $P=0$ just prior to cracking. Subsequently the volumetric strain of the cracked element is monitored. A cracked element is defined to have recovered its strength (reloading moduli) when it has recompressed to the reference volumetric strain.

It is recognized that the process of cracking will modify the material properties of the region. Therefore, the FEAT codes have separate arrays for material property parameters for pre-cracked and post-cracked conditions. After an element has once cracked, it will forever after utilize its prescribed post-cracked properties.

IV

STRUCTURE REPRESENTATION

The buried structure representations discussed in this section provide a means of approximating three dimensional buried-structure response to blast through the use of state-of-the-art two dimensional computations. In order to accomplish this, two models are used: One is a horizontal plane strain slice in which a vertical silo appears as a circular ring. This model is used to determine cross-sectional deformations and stresses. The other is a bomb-centered axisymmetric model in which, in a vertical section view, a vertical silo appears as a rectangular form. This model is used primarily to determine the bending, shearing, and vertical compressing of the silo.

The axisymmetric model actually has somewhat more than a two dimensional capability. A first order consideration of the effect of arching of the stress wave around the structure is included. This provides that model with an approximation to three dimensional diffraction phenomena and with a realistic determination of the cross-sectional squashing of the structure.

The following three subsections describe the models in detail. Section 4.4 describes the combined use of the horizontal plane and axisymmetrical models.

4.1 Basic Concepts of Axisymmetric Model

The bomb-centered axisymmetric model is illustrated in a vertical section view by Figure 4-1.

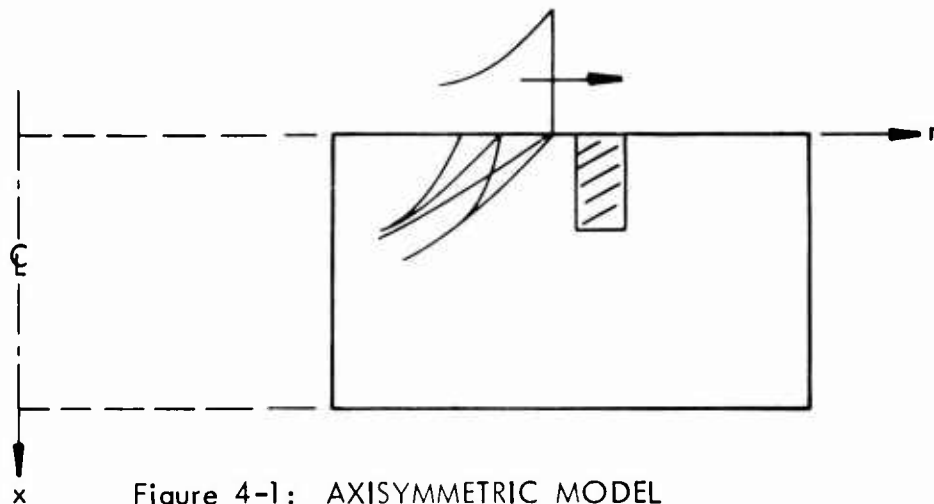


Figure 4-1: AXISYMMETRIC MODEL

In this model the structure is actually a large diameter ring of material with appropriate mechanical properties centered on the model axis. The axisymmetry of the structure itself necessitates the refinements of the model which are used

to obtain realistic results. Though the details of this are discussed in the next section, two items must be mentioned here. First, the circumferential stiffness of the large diameter structure ring is avoided through setting to zero the appropriate stiffness coefficients. Second, the ability of stress waves to propagate around as well as through the structure is provided through the use of alternative axisymmetric paths, one in the earth and one in the structure, both occupying the structure region shown shaded in the figure. With these features included the structure behavior is that of a vertical beam which deforms in bending, shear, vertical compression, and cross-sectional squashing.

The basic conditions of the determination of the structural model are that the above-mentioned beam stiffnesses match those of the actual structure. Hence we have:

- | | | |
|-------------------------|---------------------------|-----|
| (1) Bending stiffness, | $(EI)_S = (EI)_M$ | |
| (2) Crushing stiffness, | $(EA)_S = (EA)_M$ | |
| (3) Total mass, | $(\rho A)_S = (\rho A)_M$ | 4-1 |
| (4) Shearing stiffness, | $(GA')_S = (GA')_M$ | |
| (5) Rotatory inertia | $(\rho I)_S = (\rho I)_M$ | |

in which customary definitions of symbols are employed and the subscripts S and M refer to the actual structure and to the model of the structure, respectively. Item (4) employs primed area quantities consistent with the fact that, in beam shearing, the actual cross-sectional area is not the appropriate measure of shearing stiffness. Items (2) and (3) together provide the proper vertical wave speed in the structural model. In combined material sections, such as reinforced or steel lined concrete, the above refer to the appropriate composite section quantities according to customary procedures. The result of this modeling approach is to obtain correct gross motions and beam-column deformations and stresses of the buried structure.

The cross-section of the structure model is represented as shown in Figure 4-2.

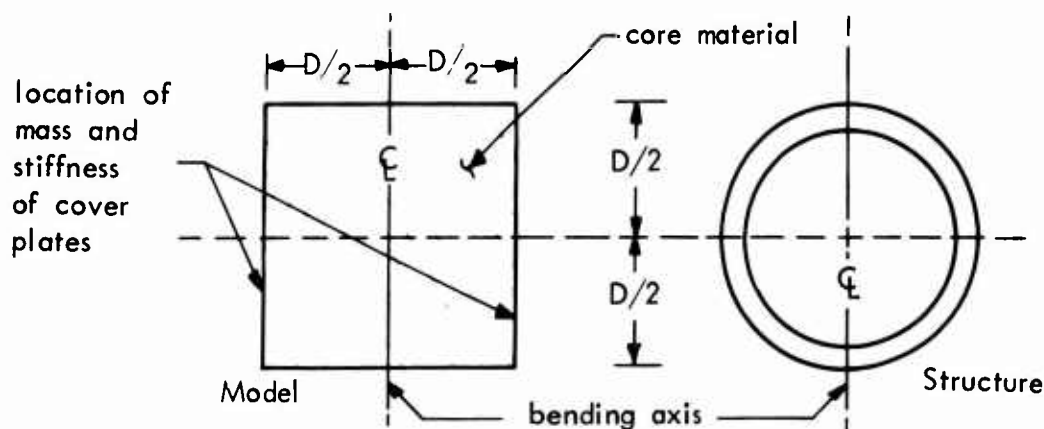


Figure 4-2: STRUCTURE MODEL

The model is composed of a core which carries all types of stresses and cover plates which carry only vertical stress. The core material is represented by two elements (shown cross-hatched) in order to obtain accurate beam bending and shearing behavior. The cover plates are present in the model only through their mass and stiffness. In the calculations the cover plates thus do not experience transverse wave propagation and do not give rise to difficulties of spurious oscillations or short integration step requirements.

Application of the equations 4-1 yields values of the moduli E and G of the core elements, which resist vertical compression and shear strain in the r - x plane, respectively. In addition the stiffnesses of the cover plates are determined along with E , since they contribute to the values of $(EI)_M$ and $(EA)_M$. The pertinent equations are:

$$(EI)_M = E_x \frac{D^4}{12} + 2 \left(\frac{D}{2} \right)^2 (AE)_c \quad 4-2$$

where E_x refers to the core, and $(AE)_c$ is the stiffness of the cover plate elements,

$$(EA)_M = D^2 E_x + 2 (AE)_c \quad 4-3$$

$$(\rho A)_M = \rho D^2 + 2 (\rho A)_c \quad 4-4$$

where ρ refers to the core and $(\rho A)_c$ is the mass per unit length of each cover plate,

$$(GA')_M = G_{rx} D^2 \quad 4-5$$

where G_{rx} is the shear stiffness of the core elements in the r - x plane. Together with the formula for $(\rho A)_M$ goes the following relation, which has the effect of modeling in addition the mass moment of inertia of the structure.

$$\rho \frac{D^4}{12} + 2 \left(\frac{D}{2} \right)^2 (\rho A)_c = (\rho I)_M \quad 4-6$$

where $(\rho I)_M$ is the mass moments of inertia of the model.

The equations given suffice to determine the quantities E_x , G_{rx} , ρ , and $(\rho A)_c$, $(AE)_c$.

In the determination of G_{rx} , the value of $(GA')_S$ has been put at half the value obtained using the total composite cross-section, in recognition of the shear stress distribution through the circular cross section. For the model, however, $(GA')_M$ is seen to be based on the total core area, in recognition of the effect of the cover plates in producing a nearly constant shear strain

through the core region. It is understood that these are approximate values; the degree of approximation is acceptable within the accuracy of the modeling process.

The wave propagation through the structure takes place in the two core elements. Associated with this wave response is a radial strain of the structure cross-section. The radial strain of the two core elements must match an effective strain of the actual structure determined on the basis of the squashing of its cross section. The amount of ring squashing depends on the pressure distribution around the circumference of the ring, which varies during the time history of any one event. The radial stiffness of the core elements is chosen to give a time history of squashing behavior which approximates that of the actual structure.

As a first approximation to the radial stiffness, E_r , of the model structure, the lateral deformation of the two element core, due to stress σ_r is equated to the actual structure deformation of quantity, δ_s :

$$\delta_s = \delta_M = \frac{\sigma_r}{E_r} D \quad 4-7$$

δ_s is determined as follows. It is assumed that the ring deformation takes place in the shape of the second mode, as shown in Figure 4-3.

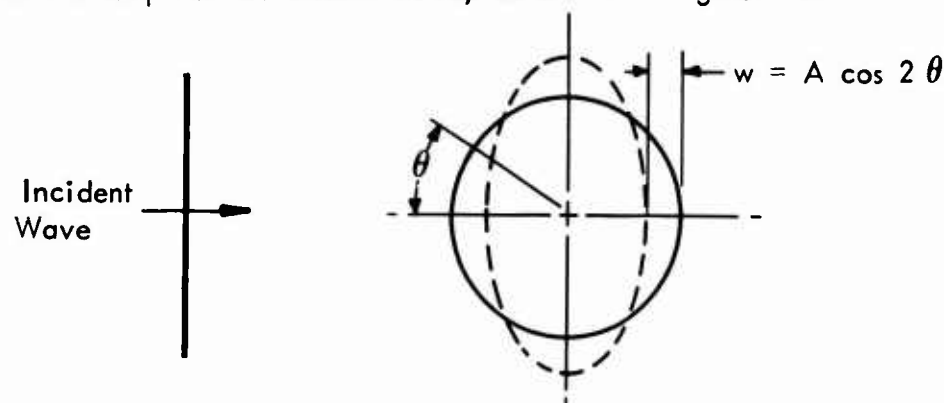


Figure 4-3: RING DEFORMATION

The total ring crushing in this mode, is determined for the loading below by means of the Rayleigh procedure, as shown in Figure 4-4.

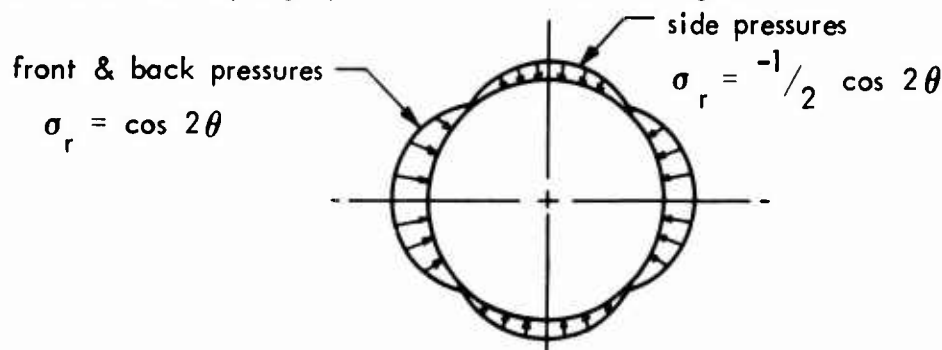


Figure 4-4: RING LOADING

The result is

$$\delta_s = \frac{2 (\sigma_r)_{\max} (R_{NA})^4}{36 (EI)_w} \quad 4-8$$

where $(EI)_w$ is the ring wall bending stiffness and (R_{NA}) is the ring radius measured to the neutral bending surface of the structural wall. From the equation 4-7, $\delta_s = \delta_M$, E_r is determined.

The higher modes, $\cos n\theta$, $n > 2$, will participate in the ring response and will cause stresses of importance. However, the associated displacements will not be significant relative to the matter of wave propagation through the structure. Therefore, by determining E_r in the manner described the gross structural squashing will be predicted accurately. The determination of E_r will be refined, if the need to do so is indicated by the procedure given in Section 4.4.

In the axisymmetric model the E_θ of the structure cannot take a value corresponding to the actual structural stiffness. There exists a stress, called σ_θ^* in Figure 4-5,

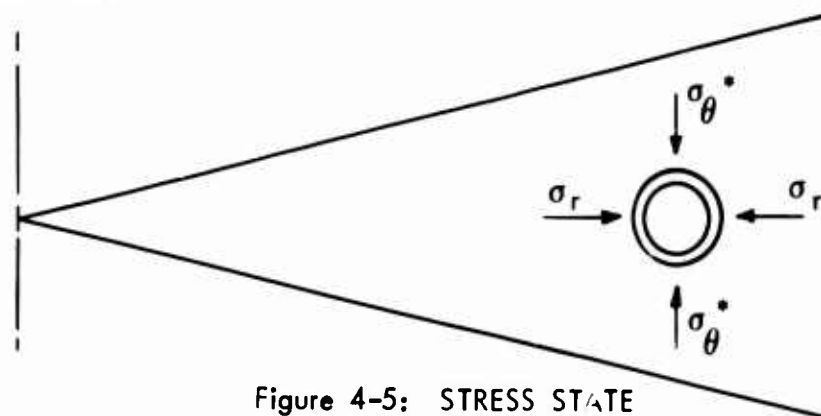


Figure 4-5: STRESS STATE

which resists the θ -direction displacement due to squashing of the ring. It is unreasonable to assume that this stress is a circumferential one, having the associated effect of a circumferential stress on radial equilibrium. It is to avoid this radial equilibrium effect that in the axisymmetric model E_θ is in fact set to zero, rather than some reduced value corresponding to an earth medium property. The resulting loss of σ_θ has an influence, through Poisson's ratio, on the radial strain of the model structure. For this reason E_r of the model is a nonphysical value which must yield a correct strain ϵ_r due to the presence of only the stress σ_r .

The foregoing has provided, for model structure core elements, the moduli E_x , E_r , G_{rx} , and $E_\theta = 0$. The Poisson's ratio values which have been used are

$$\nu_{rx} = \nu_{\text{concrete}}, \quad 4-9$$

where ν_{rx} is defined as used in the formula

$$\epsilon_r = \frac{\sigma_r}{E_r} - \frac{\nu_{rx} \sigma_x}{E_x} \quad 4-10$$

The value of ν_{xr} , as defined by

$$\epsilon_x = \frac{\sigma_x}{E_x} - \frac{\nu_{xr} \sigma_r}{E_r} \quad 4-11$$

is taken in the form required for symmetry of the stress-strain matrix,

$$\nu_{xr} = \nu_{\text{concrete}} \left(\frac{E_r}{E_x} \right) \quad 4-12$$

The effect of this is to prevent large ϵ_x from resulting due to the softness of the structure in horizontal squashing.

The final form of the orthotropic stress-strain matrix of the core elements is

$$\begin{Bmatrix} \sigma_x \\ \sigma_r \\ \tau_{xr} \\ \sigma_\theta \end{Bmatrix} = \begin{bmatrix} \frac{E_x}{1 - \nu_{xr} \nu_{rx}} & \frac{\nu_{rx} E_x}{1 - \nu_{xr} \nu_{rx}} & 0 & 0 \\ \frac{\nu_{xr} E_r}{1 - \nu_{xr} \nu_{rx}} & \frac{E_r}{1 - \nu_{xr} \nu_{rx}} & 0 & 0 \\ 0 & 0 & G_{rx} & 0 \\ 0 & 0 & 0 & 0 \end{bmatrix} \begin{Bmatrix} \epsilon_x \\ \epsilon_r \\ \gamma_{xr} \\ \epsilon_\theta \end{Bmatrix} \quad 4-13$$

4.2 The Overlay Model

The overlay model provides a parallel wave propagation path through the structure region. The need for this extension is illustrated by Figure 4-5, in

which the structure is an unlined cavity, having essentially zero values of E_r and E_x as well as E_θ .

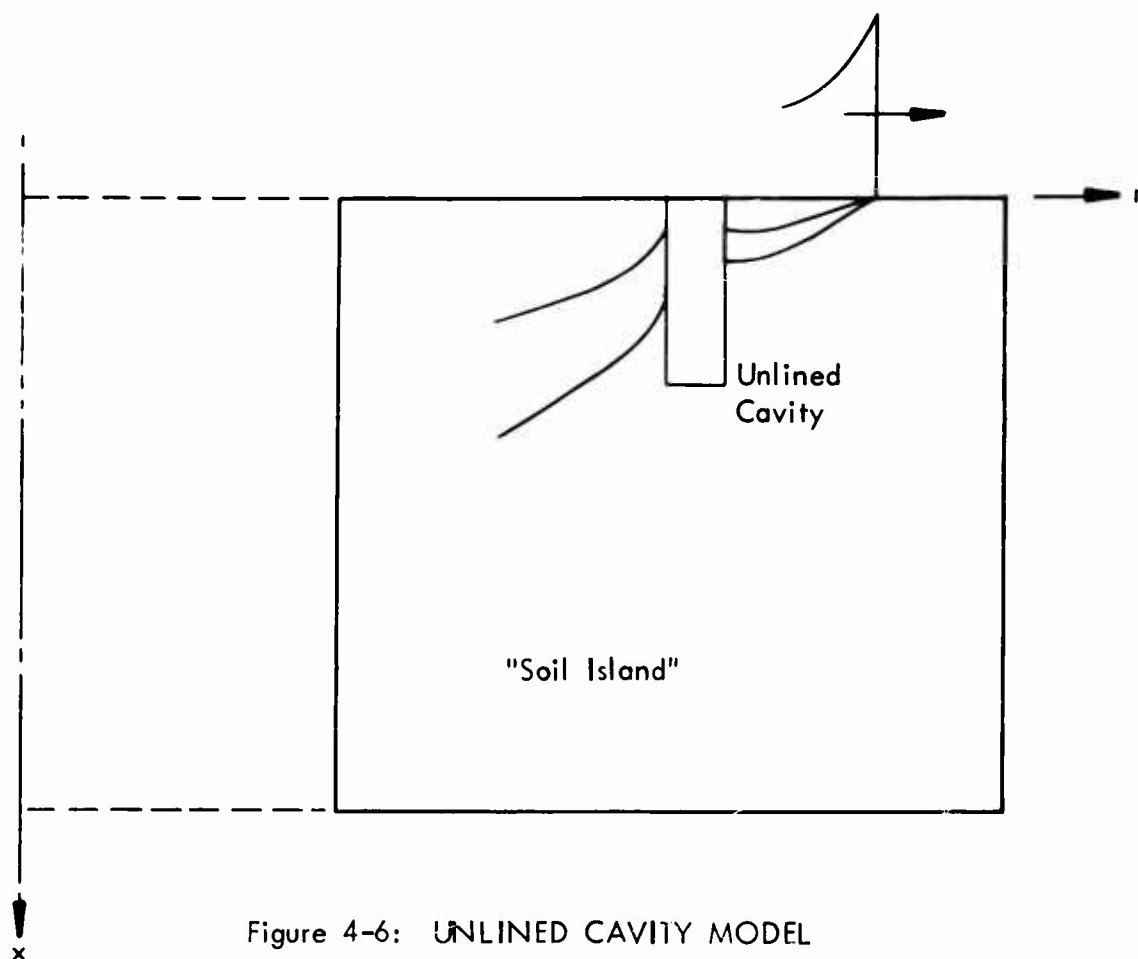


Figure 4-6: UNLINED CAVITY MODEL

The inability of the wave fronts to propagate through the cavity is apparent, particularly in the case of the direct transmitted waves. This occurs because in the axisymmetrical model the structural cavity is in reality a trench centered on ground zero. What is needed is a parallel path in the structure region, by means of which the incident waves can by-pass the structure in an earth medium route. In order to provide this capability the structure region is provided with both a structure path and an earth medium path which is called an overlay path. In this region there are two sets of nodes, one set in each path, and two sets of material properties, one appropriate to earth media and one having the orthotropic representation which was outlined above for the modeling of the structure. First approximation procedures for the determination of model parameters are given here. The model parameters will be refined by the procedures of Section 4.4.

The overlay model is derived on the basis of Figure 4-7.

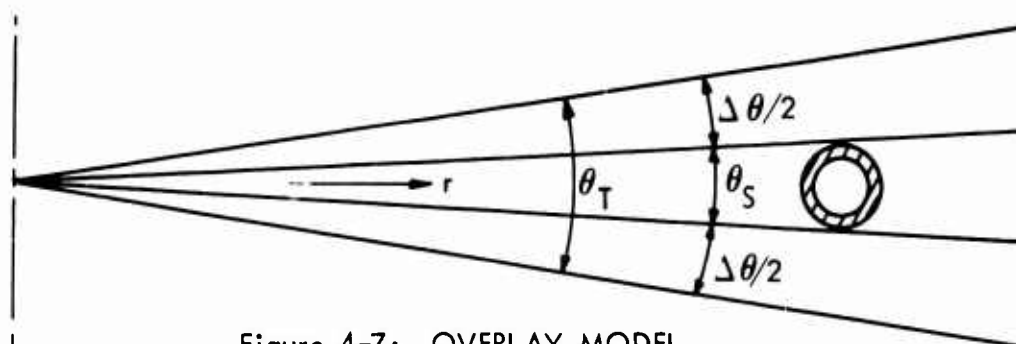


Figure 4-7: OVERLAY MODEL

An incident wave will diffract around the structure in a manner dependent on the relative properties of the structure and the earth medium. For example, a flexible structural ring may refuse to carry large radial stresses, in which case the associated forces must be carried by earth material adjacent to the structure. In the overlay model these participating earth regions adjacent to the structure are given the included angles $\Delta\theta/2$. The quantity $\Delta\theta$ is a parameter of the model. The angle θ_S includes the structural ring, and is determined by the ring diameter and the range. The total angle is designated by $\theta_T = \theta_S + \Delta\theta$.

The region in which parallel paths exist is arbitrarily chosen to extend about one ring diameter upstream and downstream of the structure. This is indicated schematically in Figure 4-8. The incident wave pattern splits into the structure path and the

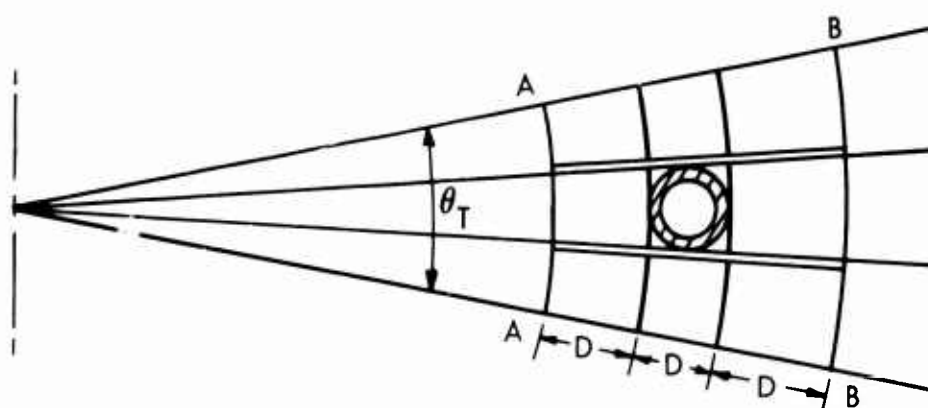


Figure 4-8: OVERLAY PATHS

overlay paths at location A-A above, and is re-united at location B-B. It is noted that due to symmetry the two overlay paths experience the same response and that therefore the use of two overlay paths is redundant. This fact is used later to compose a two path model for actual calculations. However, for the present conceptual treatment, the three path model is helpful and will be retained.

Consider a particular case in which the structure is an unlined cavity. The incident wave will propagate equally in all paths of the above figure until the free surface of the cavity is reached in the structure path. A tensile reflection will occur, with increased particle velocities, and will propagate back to A-A. The interaction at A-A will result in increased stresses and particle velocities in the overlay paths. The resulting stress increase in the overlay paths represents the tendency toward dynamic arching and stress concentration behavior. The assumption of load by the overlay paths, results in a prevention of total collapse of the cavity and represents the effect of the surrounding medium in supporting the cavity. Finally, the arrival at location B-B of a modified stress wave represents the actual ability of the earth medium to propagate stress waves into the shadow region behind the structure by means of diffraction phenomena.

The behavior described above is deficient in that the elapsed time for the reflected tensile wave to return to A-A and subsequently to effect a parallel path response will alter the shape of the transmitted pulse in a way which is dependent on the distance between A-A and the structure. The actual behavior involves relative shearing of the overlay and structural paths, with a continuously distributed shear stress transmitted between them. That is, the parallel path behavior is affected all along the interface between the paths rather than only at locations A-A and B-B. The overlay model represents this behavior by means of flexible connections between the paths. The connections are called overlay springs and provide radial forces between the paths dependent on their relative radial displacements. These springs exist at all nodes of the overlay region, connecting nodes which in the undeformed state are adjacent to one another. It is noted, referring to the above figure, that each path behaves in an axisymmetric way, i.e., the overlay springs do not cause shearing deformations of the paths. They simply provide a coupling which interrelates the magnitudes of the axisymmetric motions of the separate paths. The overlay springs are parameters of the overlay model.

This brief discussion indicates the basic mechanical behavior of the overlay model. It is clearly not a three-dimensional model in a wave diffraction sense. However, in a behavioral sense it displays in a reasonable physical manner characteristics of stress and motion which occur in the three dimensional problem.

The making of the overlay model of the figure into an axisymmetrical model is discussed next. In order to accomplish this, the overlay paths of angles $\Delta\theta/2$ are merged into a single path of angle $\Delta\theta$ and then the properties attributed to this merged path are altered so that it will provide unchanged behavior if its angle is increased to θ_T . Similarly, the properties of the structure path are altered so that its behavior is unchanged with its angle increased from θ_S to θ_T . The result is two alternate paths each having the included angle θ_T . Each path occupies the same spatial location but

but responds independently of the other except for the coupling effects of the overlay springs. This is accomplished in the following manner. The earth material properties in the overlay path, are multiplied by the ratio $\Delta\theta/\theta_T$ while the properties of the earth material of the structure elements in the structure path, are multiplied by the ratio θ_S/θ_T . The Poisson's ratios of all media are unaffected by the transformation to the included angle θ_T .

The airblast loads must be modified as follows:

$$\begin{aligned} \left(\begin{array}{c} \text{Air Blast} \\ \text{pressure intensity} \end{array} \right)_{\text{Overlay Path}} &= \left(\begin{array}{c} \text{Air Blast} \\ \text{pressure intensity} \end{array} \right) \frac{\Delta\theta}{\theta_T} \\ \left(\begin{array}{c} \text{Air Blast Load} \\ \text{pressure intensity} \end{array} \right)_{\text{Structure Path}} &= \left(\begin{array}{c} \text{Air Blast} \\ \text{pressure intensity} \end{array} \right) \frac{\theta_S}{\theta_T} \end{aligned} \quad 4-14$$

This calculation distributes the air blast load between the paths in the correct proportions and retains the correct total load.

First approximation values for these parameters $\Delta\theta$ and the overlay spring stiffnesses are discussed below. $\Delta\theta/2$ defines the angular extent of the regions on each side of the structural cross section which participate in the dynamic arching and stress concentration behavior. Based on data obtained from elastic plane strain solutions which have been calculated to date, $\Delta\theta/2$ is set equal to θ_S . The overlay springs represent the shearing action of the earth medium in the region between the structure path and the overlay paths. In Figure 4-9

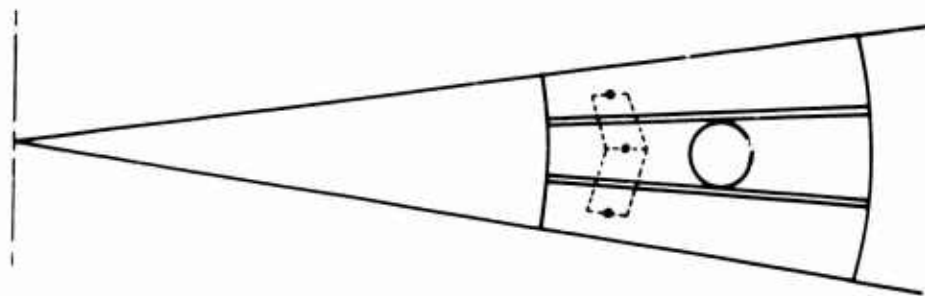


Figure 4-9: OVERLAY SPRING EFFECT

this shearing action is illustrated by dashed lines.

Figure 4-10 shows the region of material considered to contribute to the stiffness of an overlay spring (one side only) which is to represent the shearing

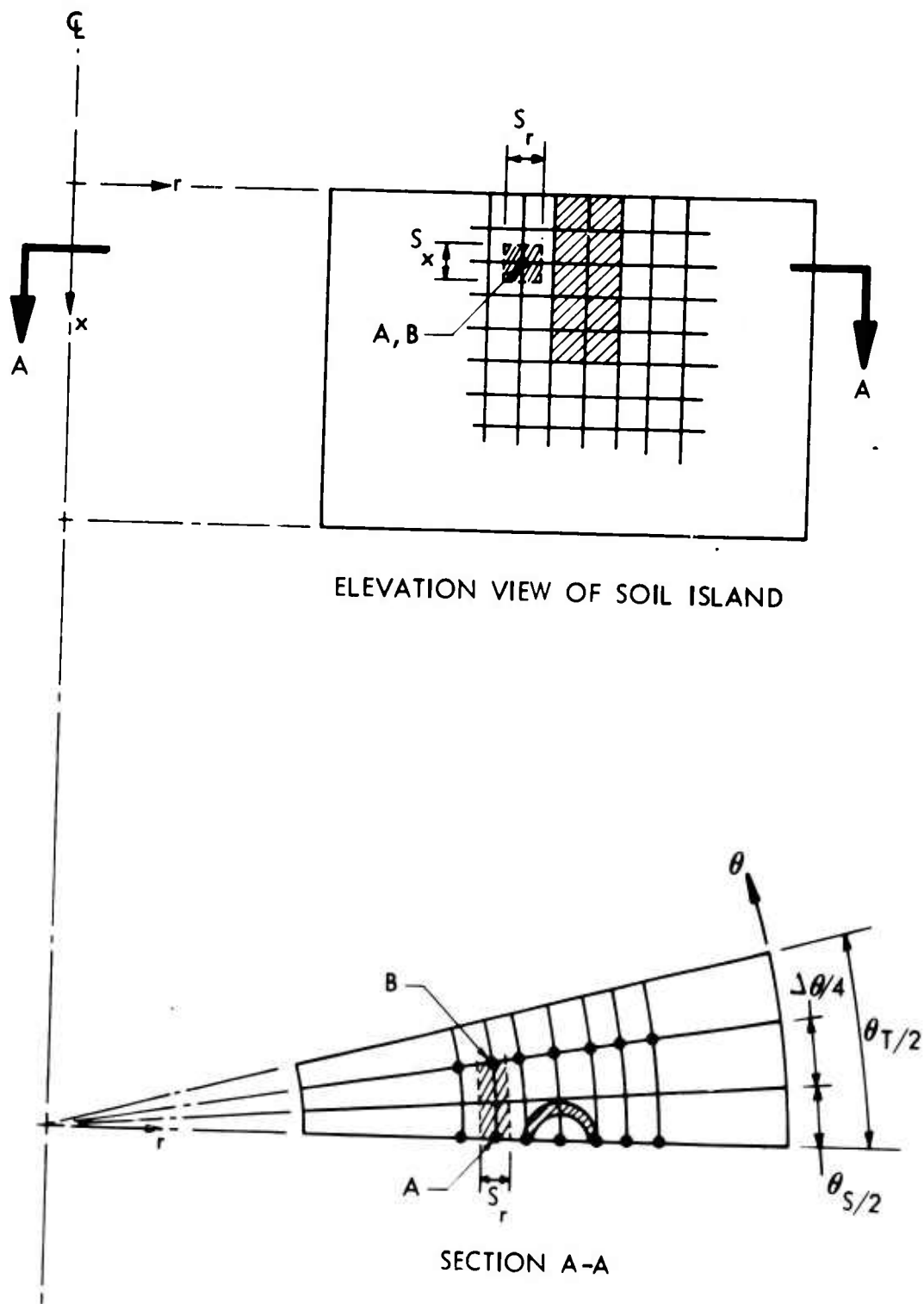


Figure 4-10: TYPICAL OVERLAY SPRING REGION

action between the structure path node A and the overlay path node B.

It is seen that this volume of material involves eight elements, four in the structure path and four in the overlay path. The nodes are assumed to take central positions in the paths, with the result that the circumferential extent of the sheared material includes the angle $(\theta_{S/2} + \Delta\theta/4)$. The radial dimension of the sheared material is the sum of the half element sizes on either side of the nodes in question (A and B), and the same is true of the vertical dimension of the volume of sheared material. Defining

S_r = sum of half element sizes on either side of node
 S_x = sum of half element sizes above and below node and using
 R to represent the radial distance to the nodes in question, the volume of the sheared material is

$$R (\theta_{S/2} + \Delta\theta/4) S_r S_x \quad 4-15$$

The shearing displacement between the nodes, taken positive when the displacement of the structure path exceeds that of the overlay path, is, with radial displacement designated by w ,

$$(w_{SP} - w_{OP}) \quad 4-16$$

and the shear strain becomes

$$\frac{(w_{SP} - w_{OP})}{R (\theta_{S/2} + \Delta\theta/4)} \quad 4-17$$

The elastic shear strain energy is

$$\frac{1}{2} \frac{(w_{SP} - w_{OP})^2}{R^2 (\theta_{S/2} + \Delta\theta/4)^2} R (\theta_{S/2} + \Delta\theta/4) S_r S_x G \quad 4-18$$

where G is the elastic shear modulus of the earth medium. The overlay spring stiffness is obtained as the second derivative of the above with respect to $(w_{SP} - w_{OP})$, multiplied subsequently by 2 in order to account for the presence of overlay paths on either side of the structure path. The result is

$$K_{\theta_T \text{ overlay spring}} = \frac{2 S_r S_x G}{R (\theta_{S/2} + \Delta\theta/4)} \quad 4-19$$

where the subscript θ_T designates the fact that this value applies to a model of angular extent θ_T . For the 1 radian model used in calculations, the value is

$$K_{\text{overlay spring}} = \frac{1}{\theta_T} K_{\theta_T \text{ overlay spring}} \quad 4-20$$

There are several simple exceptions to the above formulas which involve modified dimensions of the sheared volume material. First, for elements at the top surface of the model, S_x must be modified to

$$(S_x)_{\text{Top Node}} = \text{half element size below the node} \quad 4-21$$

Second, for the overlay springs which connect nodes in the overlay paths with the nodes on the sides of the structure, the angular extent of the participating material no longer contains the component angle $\theta S/2$, since the material in question is entirely within the overlay path. The result is, for nodes not on the top surface of the model,

$$K_{\theta_T \text{ overlay spring}} = \frac{2 S_x S_r G}{R \Delta \theta / 4} \quad 4-22$$

and

$$K_{\text{overlay spring}} = \frac{1}{\theta_T} K_{\theta_T \text{ overlay spring}} \quad 4-23$$

The above discussions of the overlay springs and derivations of their stiffnesses have considered only the relative displacements of the paths in the radial direction. The paths will also experience relative motions vertically, and the overlay springs will provide stiffnesses in the vertical direction. All of the considerations given apply equally to the two coordinate directions, and the overlay springs are given stiffnesses of equal magnitudes in the x and r directions.

The above derivations constitute a first approximation. They are to be checked and refined if necessary by the procedure outlined in section 4.4. The use of overlay springs within the computer code is restricted to the use of an elastic, constant earth medium shear modulus.

4.3 The Horizontal Plane Strain Model

The horizontal plane strain model provides an approximation to the response which takes place in a horizontal slice of earth and structure media. The deformation of the structural ring cross section is the principal item of importance in the calculations. The model provides a correct two dimensional wave diffraction behavior around the structural cross section. For the free field, it propagates only cylindrical dilatational waves.

Limitations of the horizontal plane model are discussed with reference to the Figure 4-11. The numbered waves will be discussed individually.

The airblast induced P wave, labeled (1) has a ratio of horizontal particle velocity to horizontal stress which is about 20% higher than that of cylindrical waves. The horizontal velocity of the wave is that of the airblast rather than C_p , the P wave speed which will occur in the horizontal plane model. The rate of envelopment of the structural ring by the advancing airblast P wave is thus much greater in the actual event than it will be in the plane model.

The airblast induced S wave, labeled (2), has a very large particle velocity to horizontal stress ratio, amounting to several times the value which will occur in the horizontal plane model for the same stress. As in the case of the P wave, the horizontal wave speed is again incorrectly represented in the plane model, being there C_p rather than V .

For both of these airblast responses, the change of pulse shape with range is governed by the airblast wave itself, whereas in the horizontal plane model the characteristic geometrical dispersion of cylindrical waves will force an incorrect change of pulse magnitude and shape with range.

The direct induced P wave, labeled (3), is well represented by the horizontal model. The wave speed, particle velocity and stress have correct values, and the dispersion effects are correctly modeled. It is this wave response and the resulting structural ring action which can be determined accurately by the horizontal plane model.

The head wave, labeled (4) has essentially the same particle velocity versus stress character as wave (2), since it is a shear wave. It does have the P wave speed, C_p , which will occur in the horizontal model.

The direct induced shear wave, labeled (5), has no adequate representation in the horizontal model. Aside from the difficulties of the other waves mentioned above, this wave has essentially vertical rather than horizontal particle velocities, at the depths of present interest, and gives rise to interaction phenomena which are completely outside the scope of the horizontal model.

Finally, in the horizontal model, all diffraction phenomena at the structural cross-section take place as governed by a wave front to structure incidence angle which in the vertical plane is 0° . In the actual event, however, the incident waves are in several cases oblique relative to the structure. The oblique incidence will produce reflection effects which are grossly different from those which will occur in the horizontal model. The previously mentioned difficulty regarding the direction of the particle velocity has a related effect to that of oblique incidence. The resulting inaccuracies of the horizontal model will occur in the cases of all waves except the direct induced P wave.

This discussion should make clear the deficiencies of the horizontal plane model relative to use for incident waves other than the direct P wave. In addition to using the model for this important case, however, it is also applied to the analysis of other loading cases, as described in the following section. Its ability to handle the complete horizontal diffraction phenomenon, including effects of plasticity, non-linear elastic behavior, compaction, tensile cracking, and debonding and slip constitutes a significant advance in the current state-of-the-art in interaction calculations.

The model of the structural ring for thick walled structures makes use of trapezoidal elements in plane strain, as shown in Figure 4-12.

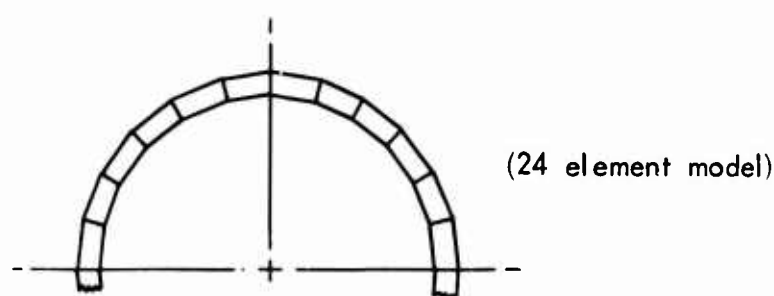


Figure 4-12: PLANE STRAIN RING MODEL

Calculations, the results of which are reported in Part II of this report, have shown this representation to yield results for wall stresses within a few percent of analytical solutions for elastic wave problems. The material properties of the trapezoidal structural elements are chosen in such a way that the bending and compression stiffnesses of the wall and the total mass are properly modeled with the total wall thickness of the model equal to that of the actual ring. For cases in which the actual structural wall is of a single material, it suffices to make the model trapezoidal elements of the same thickness and the same material properties as the actual structural wall. For reinforced or lined structural rings, whose stiffnesses are those of appropriate composite sections, the trapezoidal elements are supplemented by cover plate elements, as in Figure 4-13.

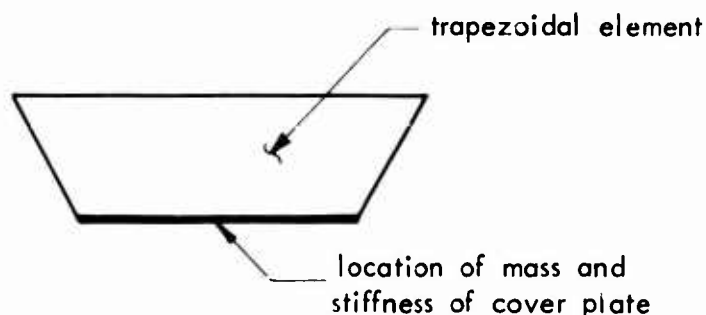


Figure 4-13: TRAPEZOIDAL ELEMENT

Such coverplates are represented in the model only by their mass and stiffness.

For thin walled structures, the model of the ring uses beam elements.

4.4 Synthesis of Axisymmetric and Plane Models

Each of the models described in the previous sections has the capability to represent certain aspects of the three dimensional wave propagation, diffraction, and structural response problem. In total capability they consider all important aspects of the posed interaction problem. The means by which these models are used to solve the three dimensional problem involves solving with each model the problem of structural response to cylindrical wave loading. The responses obtained with each model are compared. This comparison provides a parameter selection for the axisymmetric model and a method of determining peak structural ring wall stress. The present subsection describes the procedure which is used as shown in Figure 4-14.

The axisymmetric model is supported on the top and bottom against displacement normal to the boundary, and the structure extends completely through its vertical dimension. Hence its behavior will be in accordance with plane strain theory; i.e., ϵ_z will be zero throughout. If the structures were omitted in both the models of the figures, their responses to the same applied stress would be identical. With the structures in place, the differences between the two responses result entirely from differences in the behavior of the overlay region of the axisymmetric model and the correct two-dimensional diffraction behavior of the plane model. These differences are made as small as possible.

To accomplish this, the following items are computed and compared between the two models. The comparisons are made on the basis of time histories of the listed quantities.

- (1) gross, or average, radial motion of the structure
- (2) gross, or average, squashing of the structure
- (3) σ_r and σ_θ stress intensities at the front and back surfaces of the structure
- (4) σ_r and σ_θ stress intensities in the overlay path of the axisymmetrical model and in the earth medium adjacent to the structure in the plane model (shaded region)
- (5) radial motion of the overlay paths in the axisymmetrical model and in the shaded region of the plane model
- (6) the shear stress $\tau_{r\theta}$ in the earth medium adjacent to the structure in the plane model and the forces in the overlay springs of the axisymmetrical model

The above six items are listed in the order of their priority regarding the matching of response between the two models. Items (1) and (2) and (3) have

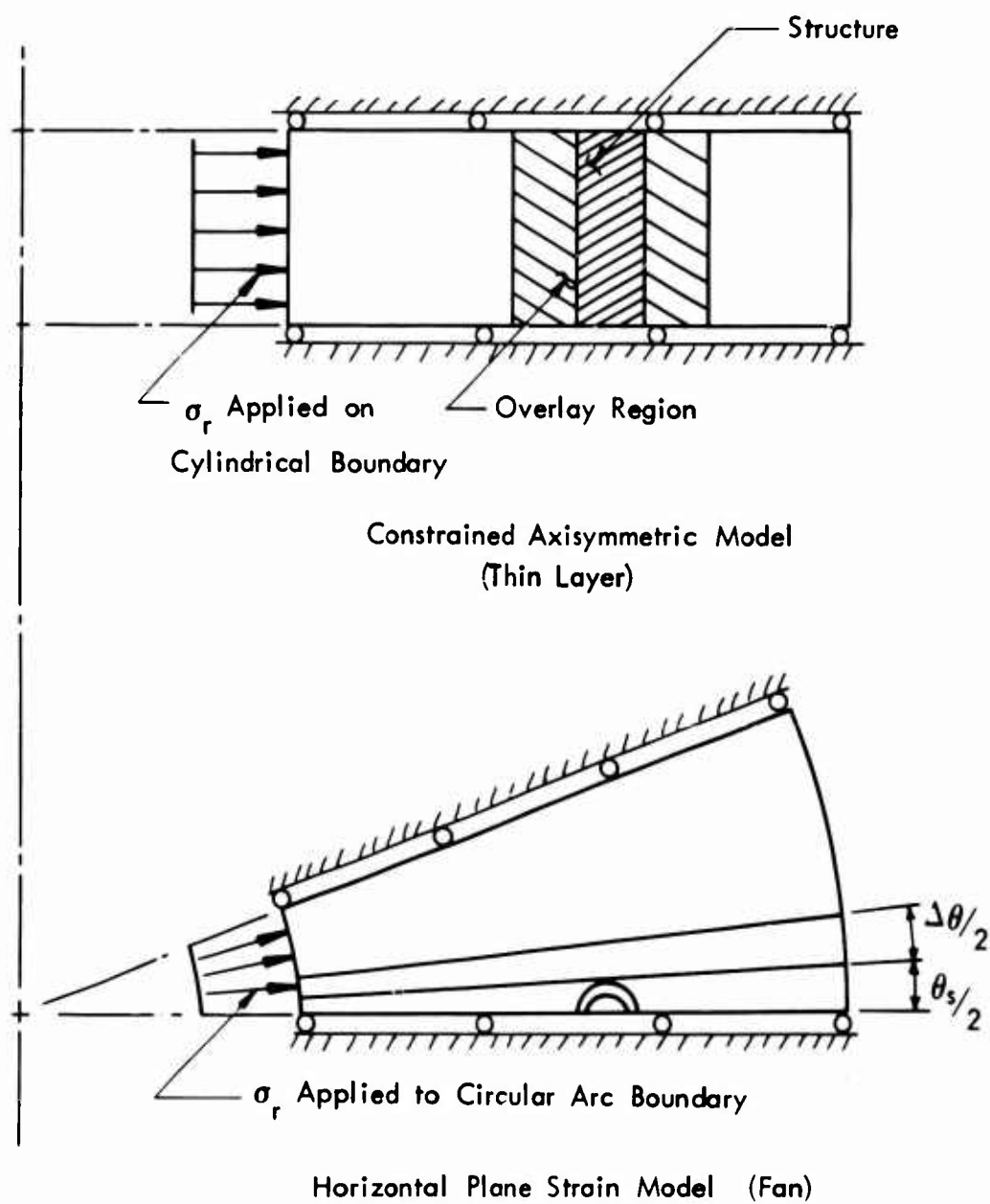


Figure 4-14: AXISYMMETRIC AND PLANE STRAIN COMPARISON MODELS

a governing effect on the selection of the overlay model parameters $\Delta\theta$ and (E) Structure. Items (4), (5), and (6) are included to aid in determining overlay spring stiffnesses, relative to which they have a direct applicability.

The procedure is to exercise the overlay model with the first approximation parameter values given in subsection 4.2, to compare the results with the plane model response, and modify the parameters in the directions implicated by the comparisons. The overlay model response is then recomputed and the parameters remodified until a correspondence between the two models is obtained adhering to the order of priority given above. For the first few problem types attempted there may be required a number of computer runs to accomplish the optimization. However, after experience is gained the procedure should be carried out with relatively little effort and expense.

The prediction of peak structural ring wall stress is accomplished by means of the procedure described below. The horizontal plane model is used to compute the following

- (1) the distribution of displacements of the structural ring normal to its circular boundary, with the gross motion term removed from the response
- (2) the distribution of ring outer and inner surface wall stresses around the circumference of the ring.

Item (2) identifies the maximum ring wall stress and its location. Item (1) provides the gross ring squashing. This will be taken as the average of the displacements over the angles $345^\circ \leq \theta \leq 15^\circ$ and $165^\circ < \theta < 195^\circ$. The ratio of the maximum wall stress to the gross squashing, with the latter designated by δ , i.e.,

$$\frac{(\sigma_{\text{wall}})_{\text{max}}}{\delta}$$

is obtained as a function of time. The ratio is used to infer ring wall stress peak values from gross squashing amplitudes obtained from the axisymmetrical model. The procedure is

$$(\sigma_{\text{wall}})_{\text{max}} \approx \left[\frac{(\sigma_{\text{wall}})_{\text{max}}}{\delta} \right]_{\text{Plane}} \delta_{\text{Axisymmetric}} \quad 4-24$$

in which the bracketed term takes values appropriate to the parameters of the problem being solved and appropriate to the time range (early or late times) under consideration.

Through this procedure the horizontal plane model calculation of ring bending stresses can be applied to other cases than the direct induced P wave. As discussed in Section 4.3, the model is not truly applicable to other types of

loading. The described procedure therefore represents an extrapolation of the usefulness of the model. The justification for this extrapolation is the lack of any other means of solving the overall problem.

DEBONDING AND SLIP

5.1 Basic Concepts

The transfer of loading from the surrounding medium to the buried structure is, to a large extent, affected by the condition of the interface between them. It is quite possible, as a result of construction processes or by predetermined procedures, that very limited shear and tension bonds will exist between the structure and the surrounding earth. To investigate the effects of these conditions provisions have been made for consideration of debonding and slip in this interaction analysis.

Debonding and slip in the FEAT code occur at the interface between elements of the structure and of the surrounding medium. At each of the interface nodes debonding is defined as the separation of the two regions, normal to the interface surface, while slip is defined as the relative motion between the two regions, parallel to the interface. A node point on the interface is considered to have two partial masses associated with it; one from the free field and one from the structure. The two mass particles of a node can be considered as separate nodes when in a state of debonding or slip.

In the fan model, the interface surface is defined in cylindrical polar coordinates; therefore, references to perpendicular and parallel displacements are the radial and tangential displacements for this model. In the axisymmetric model the perpendicular and parallel displacements are horizontal and vertical. In the axisymmetric model the corner nodes require special treatment, and the subsequent discussion of corner nodes refer only to the axisymmetric model.

The various displacement relations that may exist between the partial masses are called the "Physical State" of the node point. To identify the physical state of a node, in a given time increment, a quantity called "Key" is generated, which has a specific numerical value that corresponds to a particular displacement configuration of the interface partial masses.

For a non-corner node, the key values define the following states:

- Key = 1: Node with partial masses moving in unison
- Key = 2: Node with partial masses separated (debonded)
- Key = 3: Node with partial masses have relative motion parallel to interface surface (slip), while the motions perpendicular to the interface are identical.

For a corner node the key values of 1 and 2 define the same nodal state as above. The only special cases arise when slip is considered and is as follows:

Key = 31: Node which has slip in horizontal direction and the vertical interface surfaces have debonded

Key = 32: Node which has slip in vertical direction and the horizontal interface surfaces have debonded.

Shown in Figure 5-1 is a diagram of the displacement configuration for each key value.

The physical state or key values for the displacement conditions above are determined by a series of interface surface force tests. The debonding of the surfaces is predicted by the existence of a tension state between the interface partial masses. Similarly, slip between the partial masses is due to high shear forces on the interface surface. These conditions are determined by examining the interface forces perpendicular and parallel to the interface surface. The termination of a debonded or slip state is based upon the relative displacement and relative velocity respectively between interface partial masses.

In the sections below the details of the sequence of operations for the debonding and slip subroutine in the code are discussed. Briefly, the sequence flow is as follows:

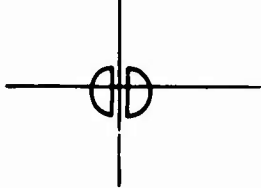
At a given time the displacements, velocities and key values are known. Next, the partial forces in each element are computed and used to determine the current interface force. That force is then tested to update a node's key value. Based on this value, the proper method of integration is performed on each node predicting a new set of displacements. The velocities are then computed and both displacements and velocities are used to examine the validity of the current key value. These key values are revised if necessary. The required information is then ready for the next cycle of computations.

5.2 Interface Force Determination

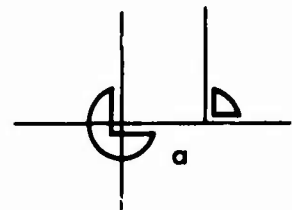
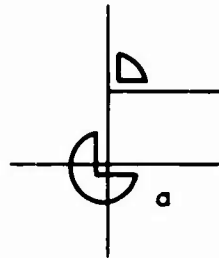
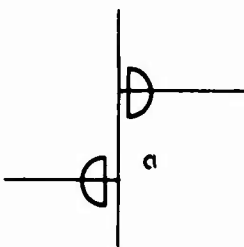
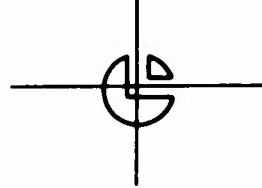
The total force at an interface node, i.e., between the structure and the free field media, is determined from the element stiffness matrices and displacement states of the elements adjacent to the node under consideration. Hence, the partial force, the force in each element, on each side of the node is known. However, the definition of the true interface force remains in question.

To define the interface force for a non-corner node, consider the following model:

Non-Corner Node

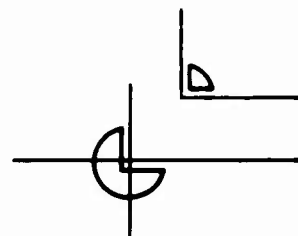
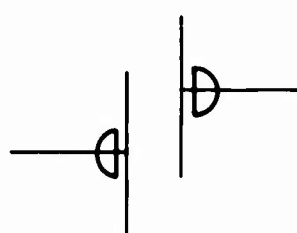


Corner Node

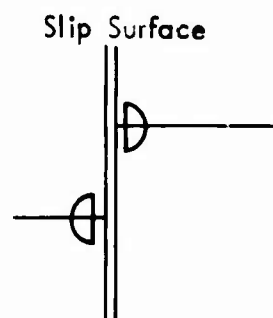


(Note: Condition "a" Indicates Prior History of Debonding or Slip)

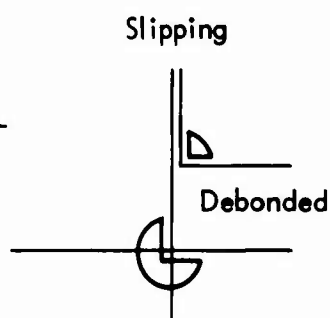
Key = 1 Partial Masses Move in Unison



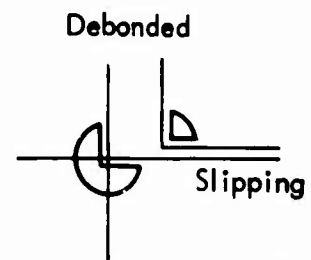
Key = 2 Partial Masses Debonding



Key = 3



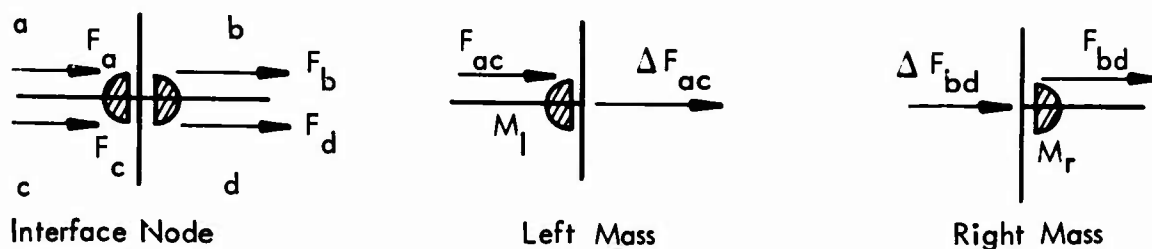
Key = 32



Key = 31

Partial Mass Slip States

Figure 5-1: DISPLACEMENT STATES



Where F_a , F_c and M_l are the free field nodal forces and mass; and F_b , F_d and M_r are the structural nodal forces and mass. Now, on M_l acts the force $F_a + F_c = F_{ac}$, on M_r acts the force $F_b + F_d = F_{bd}$, and on $M_l + M_r$ acts the force

$$F_a + F_c + F_b + F_d = F_{ac} + F_{bd} = F_{abcd} \quad 5-1$$

For the accelerations of M_l and of M_r to be identical and the same as the acceleration of $M_l + M_r$, a portion of the force F_{ac} must act on M_r and a portion of the force F_{bd} must, in turn, act on M_l .

Expressing this fact in terms of Newton's 2nd law of motion for $(M_l + M_r)$, M_r and M_l the following equations are obtained:

$$F_{abcd} = (M_l + M_r) A_{abcd} \quad 5-2$$

$$F_{bd} + \Delta F_{bd} = M_r A_{bd} \quad 5-3$$

$$F_{ac} + \Delta F_{ac} = M_l A_{ac} \quad 5-4$$

If the accelerations are to be equal; i.e., $A_{abcd} = A_{bd} = A_{ac}$, ΔF_{ac} and ΔF_{bd} can be defined as:

$$\Delta F_{bd} = \frac{M_r}{M_r + M_l} (F_{abcd}) - F_{bd} \quad 5-5$$

$$\Delta F_{ac} = \frac{M_l}{M_r + M_l} (F_{abcd}) - F_{ac} \quad 5-6$$

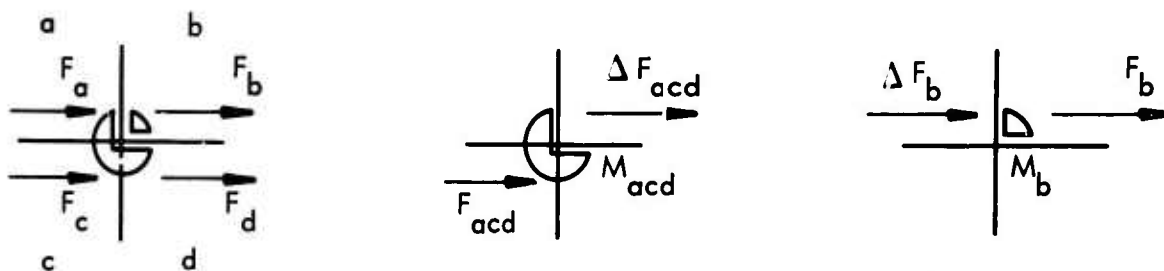
Therefore, ΔF_{bd} and ΔF_{ac} are the interface forces and are defined by the two equations above. Also note that ΔF_{ac} and ΔF_{bd} satisfy Newton's 3rd law; i.e., $\Delta F_{bd} = -\Delta F_{ac}$. This definition of the interface force is valid for both the components of the partial forces; i.e., parallel and perpendicular to the interface surface.

In the subsequent sections the forces used in the tests to define a debonded or slip state are the ΔF 's defined above. Accordingly, the following notation is adopted for the interface force components:

ΔF_{\perp} = the interface force perpendicular to the interface surface, and

ΔF_{\parallel} = the interface force parallel to the interface surface.

For a corner node the definition of the interface force proceeds in similar manner to the above. Consider the node shown below.



Again, from the acceleration consideration for M_b , M_{acd} and M_{abcd} , the interface forces ΔF_{acd} and ΔF_b are defined as:

$$\Delta F_b = \frac{M_b}{M_{acd} + M_b} (F_{abcd}) - F_b \quad 5-7$$

$$\Delta F_{acd} = \frac{M_{acd}}{M_{acd} + M_b} (F_{abcd}) - F_{acd} \quad 5-8$$

by means of Newton's 2nd law.

In the force tests for the corner node used to establish the debonded or slip state, the following notation is adopted for each component or force:

ΔF_{\rightarrow} = the horizontal interface force

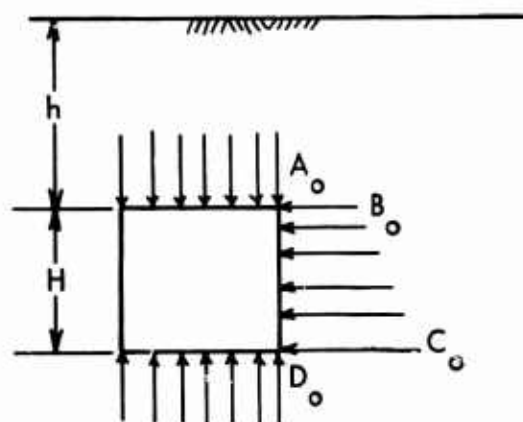
ΔF_{\uparrow} = the vertical interface force.

5.3 Physical State Determination

The physical state of the partial masses at a node is determined by an examination of the interface forces. The "physical state" identifies if the partial masses; (a) displace as a unit, (b) move separately-debonded, or (c) slide relative to each other-slip. The force tests necessary for this determination are categorized according to node type; i.e., non-corner node or corner node and then are distinguished as to a debonding or slip.

5.3.1 Non-Corner Node

Debonding -- A debonded state for a non-corner node is established through a consideration of the normal interface surface force (ΔF_{\perp}) and the static overburden applied to the structure (F_{ST}). For the FEAT code the static overburden is defined as shown:



Where

$$A_o = \gamma h$$

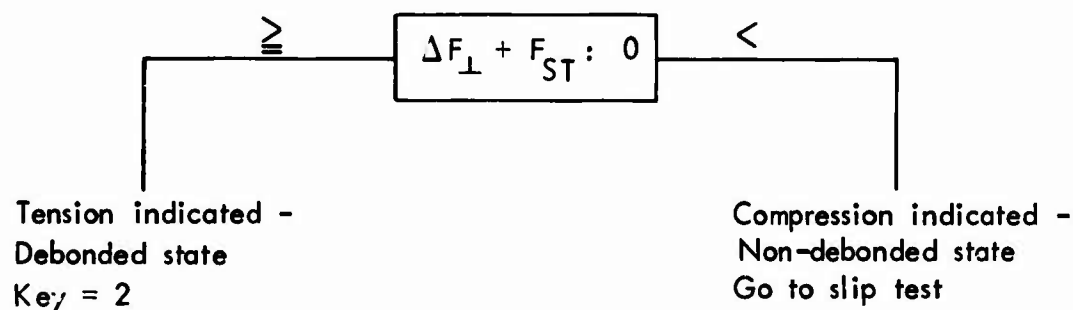
$$B_o = \gamma h K_o$$

$$C_o = \gamma(h + H)K_o$$

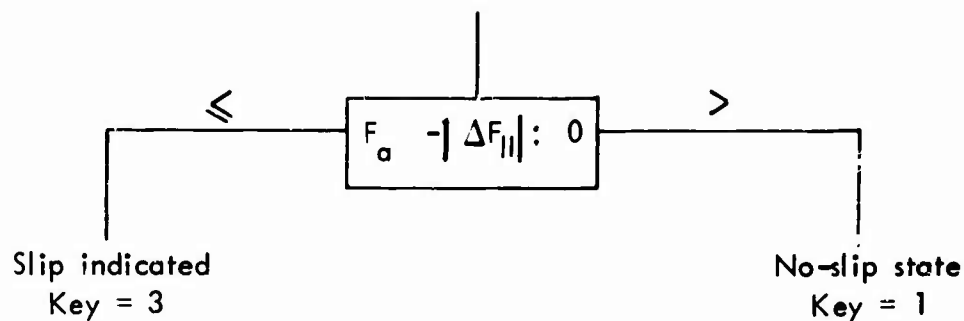
$$D_o = \gamma(h + H)$$

γ = density of medium
 K_o = coefficient of lateral earth pressure

For a node, the corresponding static overburden force and the interface force normal to surface are summed. If this sum indicates tension, a debonded state is predicted and a key value of 2 is assigned for the node. If the sum indicates compression, no change in key value results. The debonding force test is schematically shown below:



Slip -- The slip state for a non-corner node is established through an examination of the interface surface force, parallel to the surface, ΔF_{\parallel} , in relation to a defined allowable value for the force. This allowable force is composed of two parts; (1) a cohesive force, provided no prior history of slip or debonding is recorded, and (2) a static coulomb friction force. The allowable force can be expressed as $F_a = F_c + \mu |\Delta F_{\perp} + F_{ST}|$ where F_c and μ are positive input quantities to the codes. Also note that the term ($\Delta F_{\perp} + F_{ST}$) must indicate compression to be used in F_a . If the interface force is greater than the allowable force, slip is indicated. The slip force test is schematically shown below:



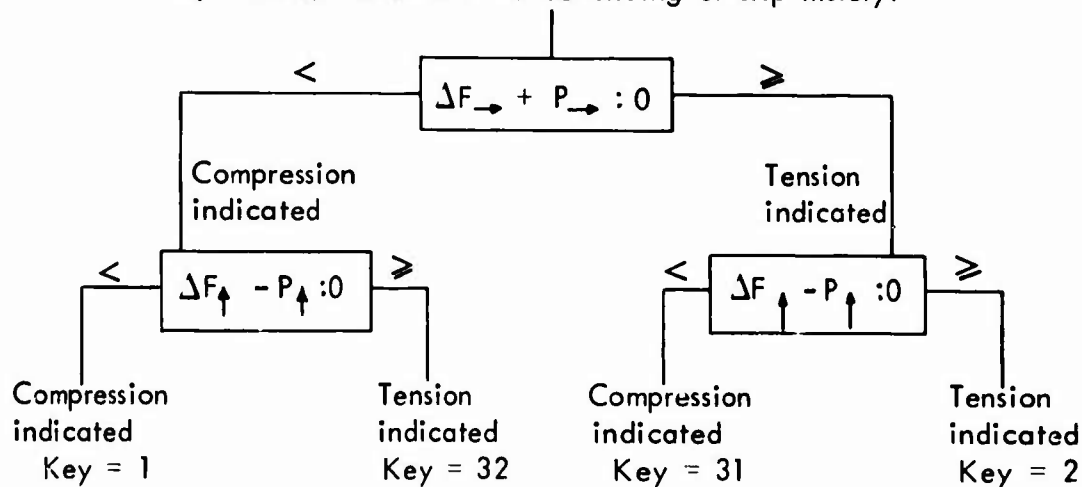
5.3.2 Corner Node

Debonding with Slip -- The force tests for the partial masses at a corner node are defined in a manner dependent on the displacement history of the node. Three possible partial mass displacement configurations exist for these nodes which involve slip and debonding. These configurations are:

1. Complete separation of the partial masses (Key = 2).
2. Debonding on vertical surface and slip on horizontal surface (Key = 31).
3. Debonding on horizontal surface and slip on vertical surface (Key = 32).

To determine which of the above states a node may enter, account must be taken of any previous debonding or slip history. To do this, the following force tests are established:

1. Corner node with no debonding or slip history:

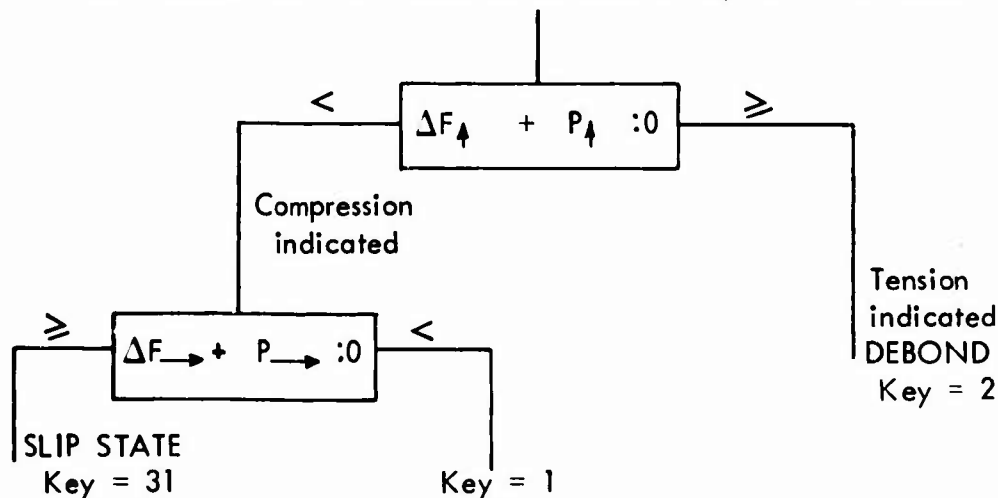


$$\text{Where } P_{\rightarrow} = F_{a\rightarrow} + F_{ST\rightarrow} \text{ and } F_{a\rightarrow} = F_c + \mu (\Delta F_{\uparrow})$$

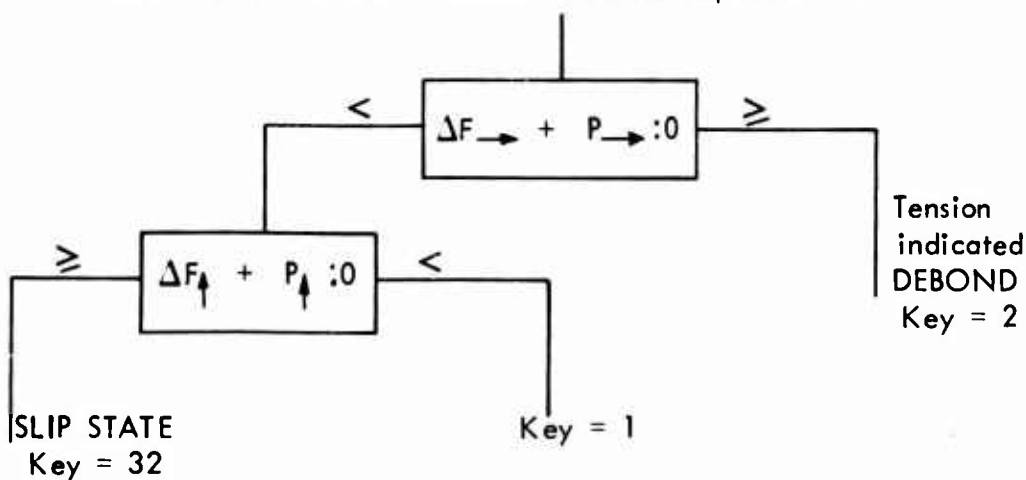
$$\text{and } P_{\uparrow} = F_{a\uparrow} + F_{ST\uparrow} \text{ and } F_{a\uparrow} = F_c + \mu (\Delta F_{\rightarrow})$$

The static overburden force F_{ST} is determined as shown in Section 5.3.1. If a node has a prior history of debonding or slipping, the F_C force above will be zero. In addition ΔF_{\uparrow} and ΔF_{\rightarrow} must indicate compression to be included in $F_{a\uparrow}$ and $F_{a\rightarrow}$.

2. Corner node with relative horizontal displacements; i.e.:



3. Corner node with relative vertical displacement:



5.4 Integration Procedure

In Section 2.5 the integration procedure by which the nodal displacement time histories are obtained is presented. In this section the necessary alterations to that procedure when considering the debonding and slip phenomena at an interface node are discussed. Recall the possible states of displacement for an interface node as set forth in Section 5.1. See Figure 5-1. Accordingly, for each key value a different type of integration equation is necessary. However, this difference results in the alteration of the numerical value of the mass and force terms in the equation rather than a new form of equations.

For a key = 1 node type, the partial masses have the same incremental displacement; i.e., the nodal mass is the sum of the partial masses while the total force on the mass is the sum of the element stiffness forces. The total partial mass displacement is obtained by summing the incremental displacements. This procedure being identical with Section 2.5. However, when a node has had a history of slip or debonding, the total displacements for the partial masses may be different. As a result, each partial mass has a distinct displacement time history.

For a key = 2 node type, the partial masses have separate integration equations. In each equation only the stiffness forces which correspond to the partial mass are considered; i.e., free field or structure. In this case different incremental displacements are obtained for all degrees of freedom of the partial masses.

For a key = 3, 31, or 32 node type, a special consideration is necessary to determine the motion of the partial masses. Normal to the slip plane an integration procedure is used as if the key were 1. That is, the mass and force in this degree of freedom are the sum of the partial quantities. For the degrees of freedom parallel to the slip plane the partial masses act independently, as in the case of key = 2. The corresponding stiffness forces act on the partial mass and, in addition, a Coulomb friction force is incorporated parallel to slip plane such that it opposes the relative motion between the partial masses. This friction force is defined as:

$$F_F = N \sum F_N \quad 5-9$$

$$\text{where } \sum F_N = \mu (\Delta F_{\perp} + (\Delta F_{ST})_{\perp}) \quad 5-10$$

and $N = \pm 1$ such that F_F opposes the relative motion of the masses.

When the slip state is initiated the value for N is obtained from the instantaneous accelerations between the partial masses. When the slip state is continuous the value for N is obtained from the relative velocity between the partial masses.

5.5 Displacement and Velocity Tests

The displacement and velocity tests are used after the integration of an interface node when a key value is different than one. For a non-corner node, these tests establish for:

- Key = 2, a) If the partial masses have overlapped during the current time increment, and

- b) If the relative velocity parallel to the interface surface is sufficient to cause slip.

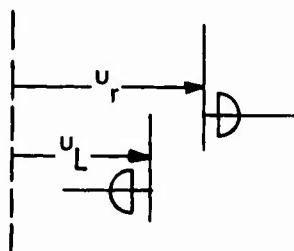
Key = 3, If the relative velocity between the partial masses is sufficient to maintain slip.

For a corner node the displacement and velocity tests are identical with the non-corner node. But, due to the debonding and slip states occurring in a unique manner at the corners, the test sequence and results may differ.

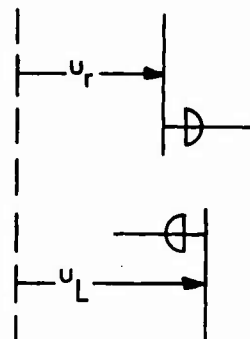
If it is found from the displacement tests that the partial masses have joined, it is necessary to insure that each partial mass has a consistent velocity and displacement. This is achieved by considering displacement compatibility and conservation of linear momentum between the integrated (overlap) and joined (compatible) positions of the partial masses.

Presented below are the schematic diagrams of these tests and the governing equations. The tests are listed according to node type; non-corner or corner, and key value 2, 3, 31 or 32. For these tests, let "u" denote the displacement perpendicular to the interface surface and "v" the displacement parallel to the interface surface.

For a non-corner node with a key value of 2, consider the following displacement model:

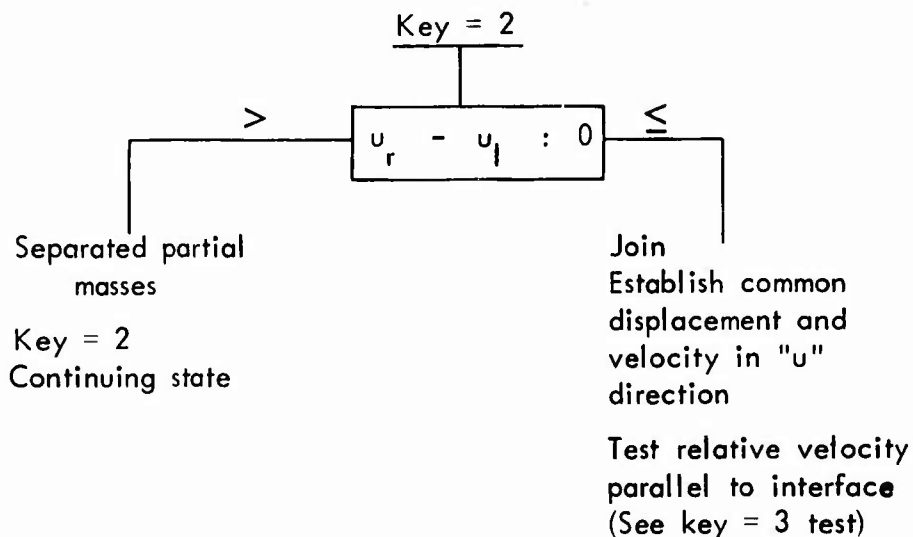


At time $t - \Delta t$



At time t

The displacement test at time t then is:



The join conditions are as follows:

Given the current displacements and velocities for the right and left partial masses, u_r , \dot{u}_r , u_l and \dot{u}_l .

Let $u_r - u_l = -K$ where K is positive.

This condition indicates an overlapping of the masses. Assuming that the current velocities were constant over the past time increment, solve for the position where the masses cross, designated U_{rn} and U_{ln} :

$$u_{rn} = u_r + K \left\{ \frac{\dot{u}_r}{\dot{u}_r - \dot{u}_l} \right\} \quad \text{and} \quad 5-11$$

$$u_{ln} = u_l + K \left\{ \frac{\dot{u}_l}{\dot{u}_r - \dot{u}_l} \right\} \quad 5-12$$

These equations yield the common displacement position for both partial masses. However, for the masses to be together they must also have a common velocity.

The common velocity is determined by considering the conservation of linear momentum between the overlap position and the compatible displacement position.

Let \dot{u}_t be this common velocity, expressed as:

$$\dot{u}_t = (M_r \dot{u}_r + M_l \dot{u}_l) / (M_r + M_l) \quad 5-13$$

The common displacement and velocity, now known for the partial masses, are used in the integration for the next time step, i.e., from t to $t + \Delta t$. Since the integration equation does not use velocity directly the correct increment in displacement must be determined for the interval $t - \Delta t$ to t . This increment is obtained by considering the definition of velocity as follows,

$$\Delta u = \Delta t \dot{u}_t \quad \text{or} \quad 5-14$$

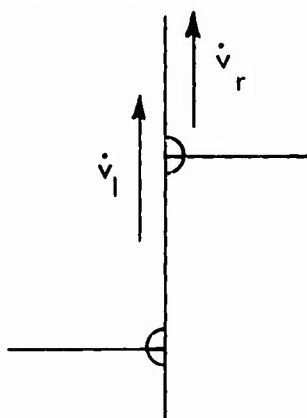
$$u(t - \Delta t) = u_{rn}(t) - \Delta t \dot{u}_t \quad 5-15$$

which are the values used in the subsequent integration for the node.

Also, note that these considerations imply a perfectly plastic impact with coefficient of restitution equalling zero.

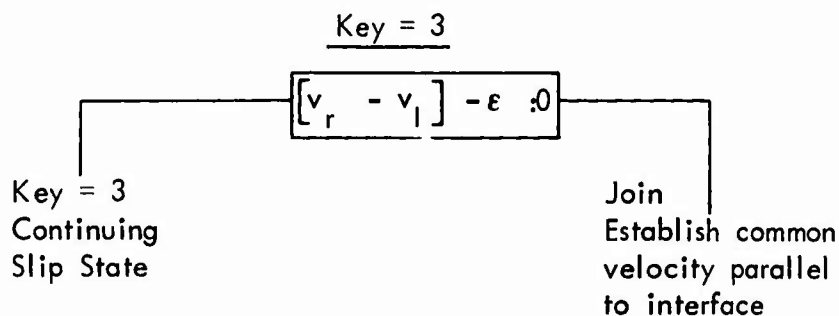
For a non-corner node with key value of three (3):

Consider the model:



Where \dot{v}_r and \dot{v}_l are the current velocities parallel to the interface surface for right and left partial masses.

For the slip state to cease, theoretically the relative velocity must be zero. Within the numerical operation of the code, zero is difficult if not impossible to achieve exactly; for example 10^{-6} in relation to one may be considered sufficiently close to zero. In addition other factors may in the judgment of the code user affect the termination of the slip state, e.g., the adhesion characteristics of the interface surface. To facilitate these conditions in the code, the following slip test has been defined where the parameter " ϵ ", an input quantity, is termed a velocity band and further discussed below.



The velocity band defines a region centered on the time axis of the velocity versus time diagram for an interface node. See Figure 5-2.

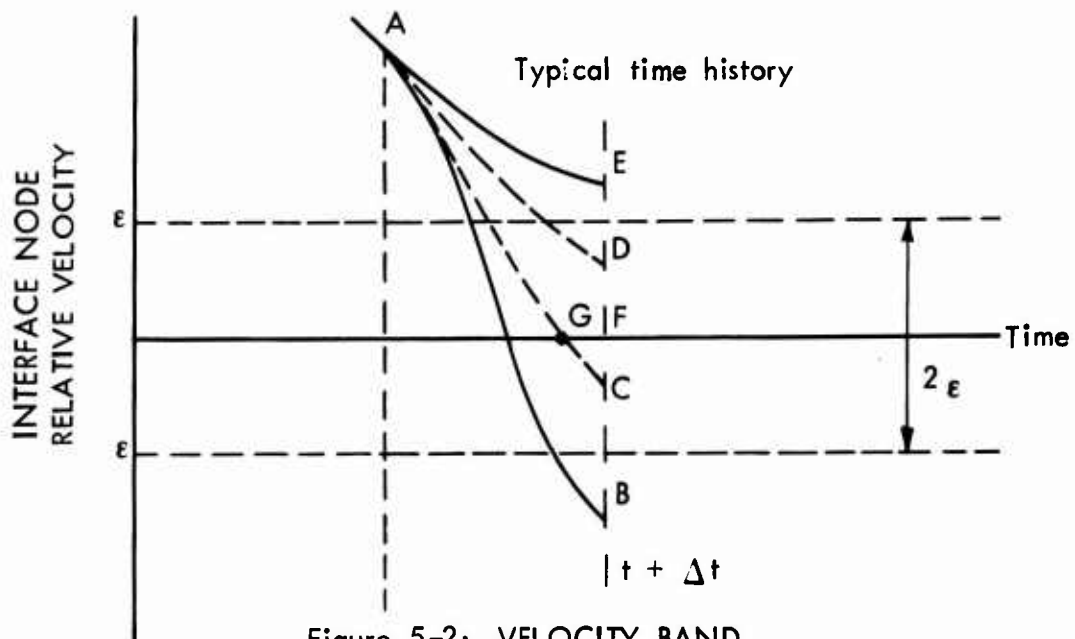


Figure 5-2: VELOCITY BAND

Assume at time " t " a velocity shown at point A. At a time " $t + \Delta t$ " four possible velocity values are shown. Two are outside the velocity band and two inside. Points B and E will have a continuing slip state predicted by the above test. Point E shows a relative velocity in the same direction as at A, while point B shows that the partial masses are moving relative to each other in an opposite manner to point A. This would be due to radical force change from t to $t + \Delta t$ and the continued state of slip would be justified.

The points D and C, however, are within the velocity band and from the slip test a join condition is specified. Point C shows a change in sign in the relative velocity as does point B, but the magnitude indicates insufficient relative velocity to continue slip. This means that at the point G, the slip state should have ended but due to the time increment Δt , point C was reached. To correct this condition the joining conditions are imposed and point F is specified.

The point D shows a small relative velocity but with same sign as point A. It is felt from the nature of the structure media interface surface that enough friction exists that cannot theoretically be predicted, that to continue slip from point D would be erroneous. Hence, the join conditions specify the point F as the proper relative velocity at this time; i.e. ($t = \Delta t$).

The join condition for this case is again based on linear momentum being conserved between the computed velocity state and the common velocity state such that:

$$\dot{v}_t = \left\{ M_r \dot{v}_r + M_l \dot{v}_l \right\} / (M_r + M_l) \quad 5-16$$

Where \dot{v}_t is the assumed common velocity for the partial masses. Note that no restriction is being placed on the current displacement of M_r and M_l ; i.e., v_r and v_l ; only the incremental values over the time increment are different; i.e., based on \dot{v}_t

$$\Delta v = \Delta t \dot{v}_t = v(t) - v(t - \Delta t) \quad 5-17$$

for both right and left masses.

The different, $v_r - v_l$ is assumed to be small in relation to the element size and, hence, will not affect the nodal equilibrium equations. This is a consistent assumption with the small displacement theory used in deriving the element stiffness matrices.

Corner Nodes -- The type of displacements and velocity tests used for corner nodes are identical with the above. The sequence of the test is different, however, because slip and debonding exist in combinations not as an either/or state. Also, the establishment of the common displacements and velocities is carried out in the manner indicated above.

Hence, only the schematic diagrams indicating the check procedure are shown. The subscript "M" indicates the medium mass and the subscript "S" indicates the structure mass, while "u" and "v" indicate horizontal and vertical motions. The sequence of necessary tests for corner nodes is shown in Figures 5-3 and 5-4.

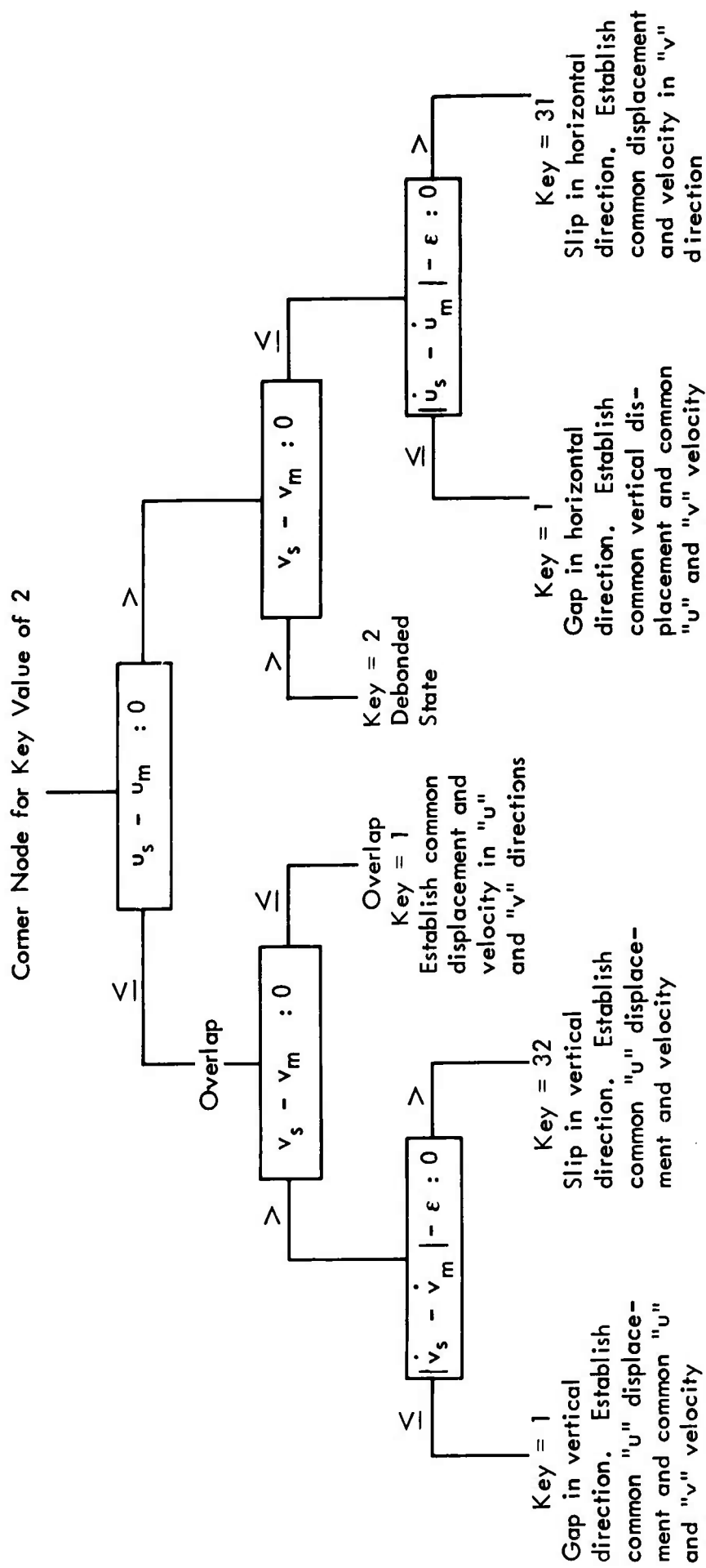


Figure 5-3: CORNER NODE DEBONDING
(EXAMPLE FOR UPSTREAM CORNER)

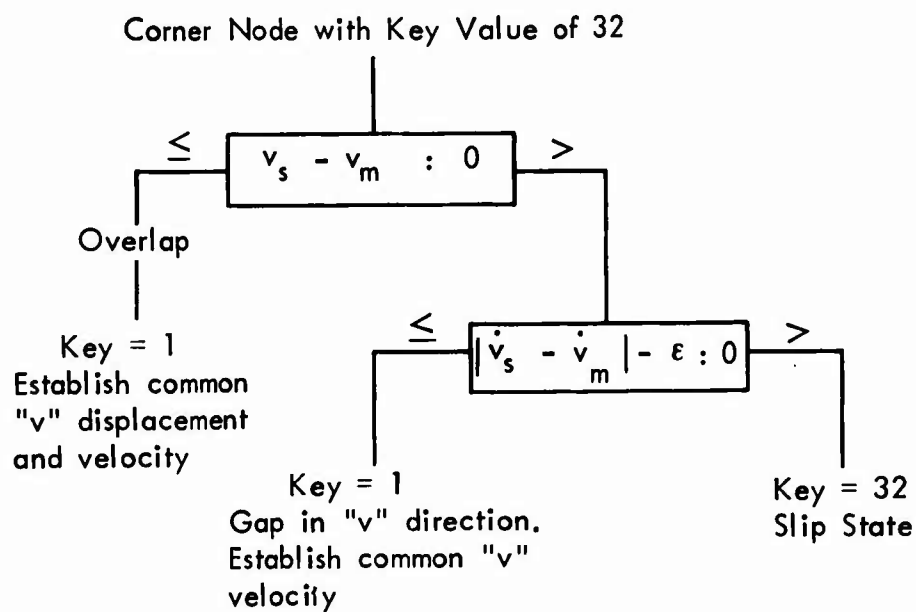
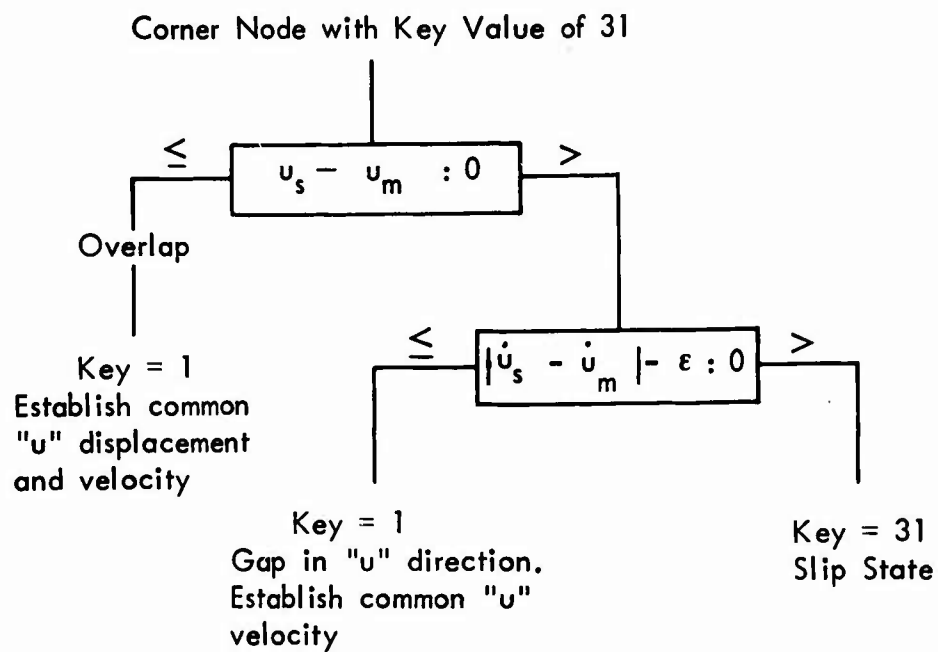


Figure 5-4: CORNER NODE SLIPPING

VI

SUSPENSION SYSTEM

6.1 Introduction

The objectives for including a representation of a suspension system model and in-structure elements in the interaction analysis are to: (1) assess their contribution to the interaction of the facility with the free field, (2) determine loads induced in the structure by the suspension system connections, and (3) evaluate the response of suspended contents as a result of structure motions.

The two suspension system/in-structure contents configurations to be represented in this study are shown in Figure 6-1. The model included in the FEAT program, Figure 6-2, is a generalization of these two configurations. Note that this model reduces to either one of the configurations of Figure 6-1 by appropriate selection of suspension system element parameters. In addition, this model can be used to simulate other configurations, such as concepts incorporating inclined suspension system elements.

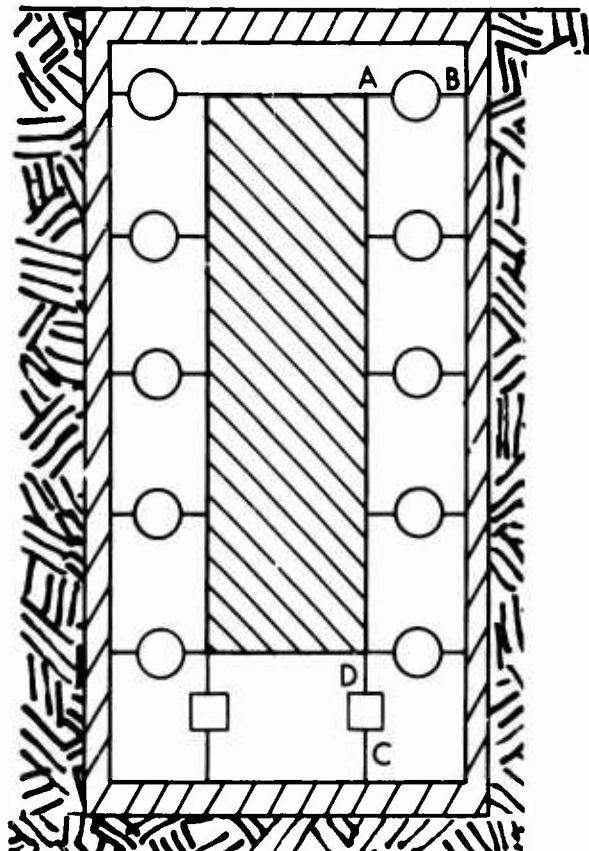
The in-structure contents are represented by a single flexible body with three rigid degrees of freedom in the plane of the structure motions (horizontal and vertical translation, and pitch) and one lateral bending degree of freedom.

Figure 6-3 summarizes model geometry conventions when suspension elements are selected capable of both extension and compression, or extension only. Figure 6-4 summarizes geometry assumed when suspension elements are selected capable of compression only.

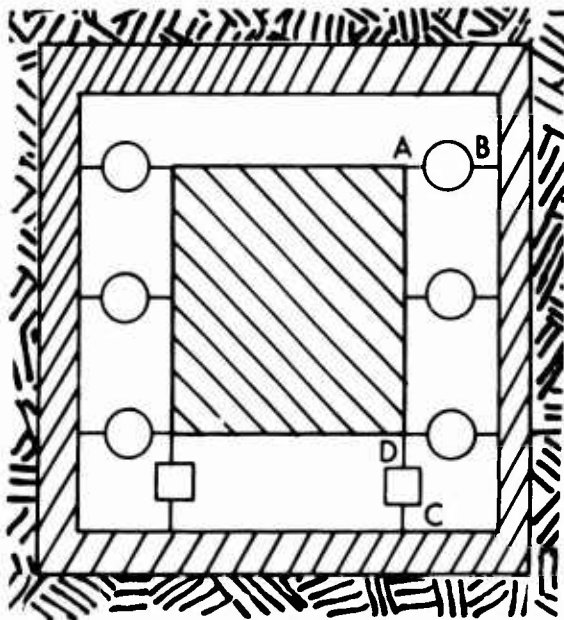
6.2 Equations of Motion

The equations of motion of the in-structure contents were obtained using Lagrange's equations. The coordinate system associated with the contents can be assumed fixed in space at any arbitrary point. The coordinates of the contents are assumed equal to zero when the contents body axes are centered on the coordinate axes. In terms of generalized forces the equations of motion are

$$\begin{aligned} M\ddot{w}_c &= Q_R \\ M\ddot{u}_c &= Q_X + Mg \\ I\ddot{\gamma}_c &= Q_\gamma \\ M_q \ddot{q}_c &= Q_q - M_q \omega^2 q_c \end{aligned} \quad (6-1)$$

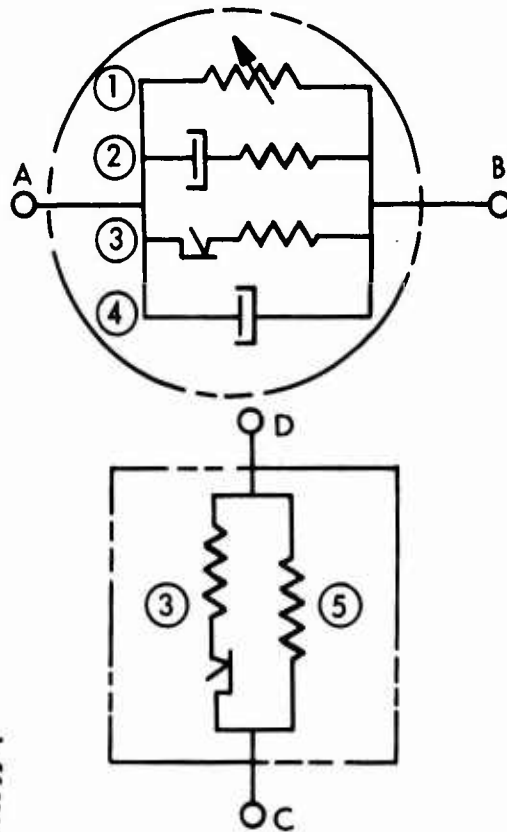


LF

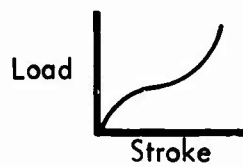


LCF

SUSPENSION SYSTEM ELEMENTS

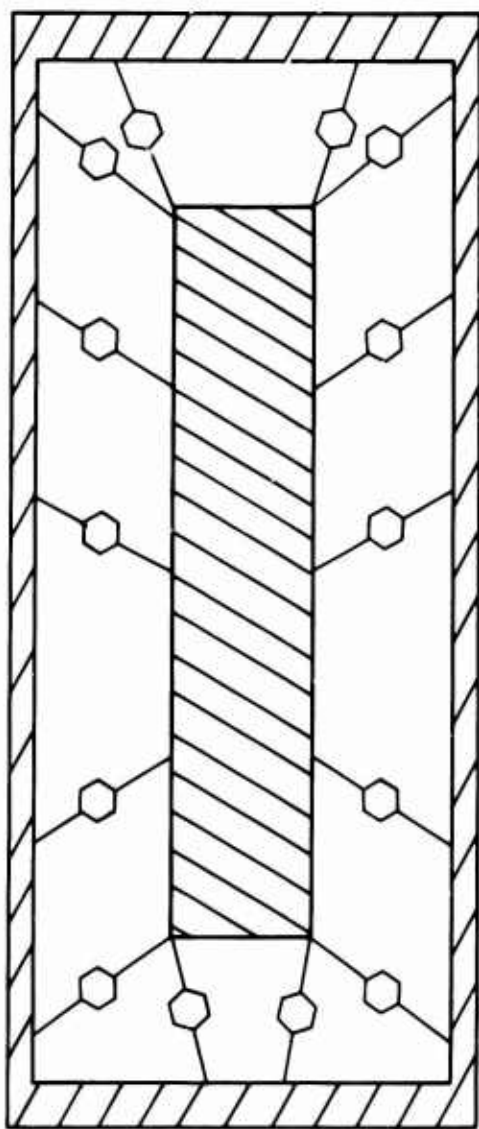


- ① Non-linear elastic spring

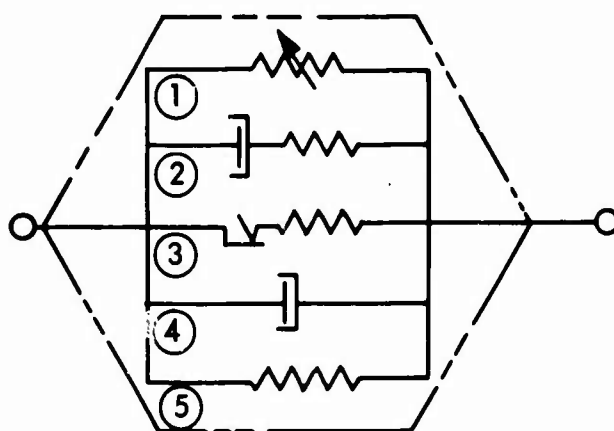


- ② Maxwell element
- ③ Coulomb damper & linear spring
- ④ Velocity proportional damper
- ⑤ Linear spring

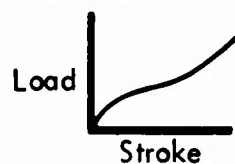
Figure 6-1: SUSPENSION SYSTEM TO BE MODELED



SUSPENSION SYSTEM ELEMENTS



- ① Non-linear elastic spring



- ② Maxwell element
- ③ Coulomb damper & linear spring
- ④ Velocity proportional damper
- ⑤ Linear spring

NOTES: Structures attachments of suspension elements are made at structure element nodes. Individual suspension elements may contain any or all of the numbered components.

Figure 6-2: GENERALIZED SUSPENSION SYSTEM MODEL

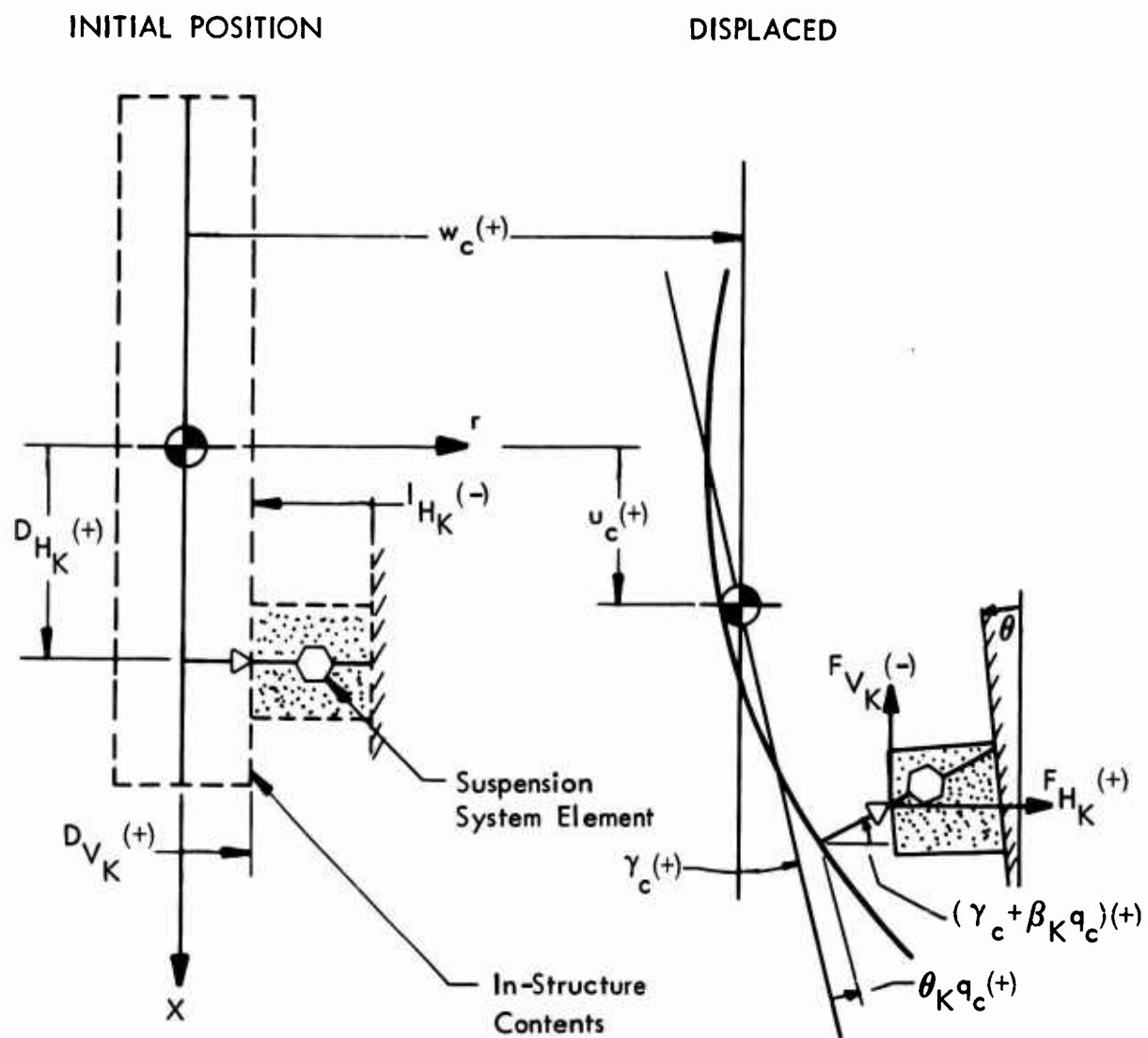


Figure 6-4: GEOMETRY FOR COMPRESSION SUSPENSION ELEMENTS

Where:

M = The sprung mass

I = The pitch moment of inertia of the sprung mass

M_q = The generalized mass of the lateral bending mode

w_c, u_c, γ_c and q_c = Degrees of freedom of the contents

ω = The frequency of the bending mode

Q_R, Q_X, Q_Y and Q_q = Generalized forces

g = Acceleration of gravity.

The generalized forces are defined using the principle of virtual work. Optionally, suspension elements may be capable of extension only, compression only, or both extension and compression. Extension and general (extension and compression) elements are assumed pin-ended, as shown in Figure 6-3. Compression elements can not support shear (slide) at the contents attachment point, as shown in Figure 6-4. Rigid body rotations and flexible body deformations are assumed to be sufficiently small for small angle approximation. The distances from the C.G. of the in-structure contents to the point of attachment of the k^{th} suspension system element on the contents, D_{HK} and D_{VK} are used in calculating displacements of the attachment points. The senses of these lengths are positive if they are the same sense as the positive directions of their respective axes.

The horizontal and vertical displacements of the suspended contents of the k^{th} suspension element are given by:

$$\begin{aligned} w_k &= w_c + D_{HK} \sin \gamma_c + \phi_K \cos \gamma_c q_c - D_{VK} [1 - \cos (\gamma_c + \beta_K q_c)] \\ u_k &= u_c - D_{HK} (1 - \cos \gamma_c) - \phi_K \sin \gamma_c q_c - D_{VK} [\sin \gamma_c \cos (\beta_K q_c) \\ &\quad + \cos \gamma_c \sin (\beta_K q_c)] \end{aligned} \quad (6-2)$$

Where:

ϕ_K = The nodal displacement at the k^{th} element

β_K = The nodal bending rotation of the k^{th} element

The virtual displacements of the suspended contents of the k^{th} suspension element become:

$$\delta w_K = \delta w_c + D_{HK} \cos \gamma_c \delta \gamma_c - \phi_K \sin \gamma_c q_c \delta \gamma_c + \phi_K \cos \gamma_c \delta q_c \quad (6-3)$$

$$\begin{aligned}
& - D_{VK} \sin \gamma_c \cos(\beta_K q_c) \delta \gamma_c - D_{VK} \beta_K \cos \gamma_c \sin(\beta_K q_c) \delta q_c \\
& - D_{VK} \cos \gamma_c \sin(\beta_K q_c) \delta \gamma_c - D_{VK} \beta_K \sin \gamma_c \cos(\beta_K q_c) \delta q_c \\
& \approx \delta w_c + [D_{HK} - \phi_K \gamma_c q_c - D_{VK} (\gamma_c + \beta_K q_c)] \delta \gamma_c + \\
& [\phi_K - D_{VK} \beta_K (\gamma_c + \beta_K q_c)] \delta q_c
\end{aligned}$$

$$\begin{aligned}
\delta u_k &= \delta u_c - D_{HK} \sin \gamma_c \delta \gamma_c - \phi_K \cos \gamma_c q_c \delta \gamma_c - \phi_K \sin \gamma_c \delta q_c \quad (6-4) \\
& - D_{VK} \cos \gamma_c \cos(\beta_K q_c) \delta \gamma_c + D_{VK} \beta_K \sin \gamma_c \sin(\beta_K q_c) \delta q_c \\
& + D_{VK} \sin \gamma_c \sin(\beta_K q_c) \delta \gamma_c - D_{VK} \beta_K \cos \gamma_c \cos(\beta_K q_c) \delta q_c \\
& \approx \delta u_c - (D_{HK} \gamma_c + \phi_K q_c + D_{VK}) \delta \gamma_c - (\phi_K \gamma_c + D_{VK} \beta_K) \delta q_c
\end{aligned}$$

The virtual work performed by the horizontal and vertical forces from the k^{th} suspension element on the suspended contents is given by:

$$\begin{aligned}
\delta \bar{W}_E &= F_{HK} \left\{ \delta w_c + [D_{HK} - \phi_K \gamma_c q_c - D_{VK} (\gamma_c + \beta_K q_c)] \delta \gamma_c + [\phi_K - \right. \quad (6-5) \\
& D_{VK} \beta_K (\gamma_c + \beta_K q_c)] \delta q_c \left. \right\} + F_{VK} \left\{ \delta u_c - (D_{HK} \gamma_c + \right. \\
& \phi_K q_c + D_{VK}) \delta \gamma_c - (\phi_K \gamma_c + D_{VK} \beta_K) \delta q_c \left. \right\}
\end{aligned}$$

The total virtual work performed on the suspended contents is obtained by summing that performed by all S suspension elements:

$$\begin{aligned}
\delta \bar{W}_{\text{Total}} &= \sum_{K=1}^S \left\langle F_{HK} \left\{ \delta w_c + [D_{HK} - \phi_K \gamma_c q_c - D_{VK} (\gamma_c + \beta_K q_c)] \delta \gamma_c \right. \right. \quad (6-6) \\
& + [\phi_K - D_{VK} \beta_K (\gamma_c + \beta_K q_c)] \delta q_c \left. \right\} + F_{VK} \left\{ \delta u_c \right. \\
& - (D_{HK} \gamma_c + \phi_K q_c + D_{VK}) \delta \gamma_c - (\phi_K \gamma_c + D_{VK} \beta_K) \delta q_c \left. \right\} \rangle
\end{aligned}$$

The virtual work may be expressed in terms of the generalized forces as:

$$\begin{aligned}
\delta \bar{W}_{\text{Total}} &= \left(\sum_{K=1}^S F_{HK} \right) \delta w_c + \left\langle \sum_{K=1}^S \left\{ F_{HK} [D_{HK} - \phi_K \gamma_c q_c - D_{VK} (\gamma_c + \right. \right. \\
& \beta_K q_c)] - F_{VK} (D_{HK} \gamma_c + \phi_K q_c + D_{VK}) \left. \right\} \delta \gamma_c \\
& + \left(\sum_{K=1}^S F_{VK} \right) \delta u_c = \left\langle \sum_{K=1}^S \left\{ F_{HK} [\phi_K - D_{VK} \beta_K (\gamma_c + \right. \right. \\
& \beta_K q_c)] - F_{VK} (\phi_K \gamma_c + D_{VK} \beta_K) \left. \right\} \delta q_c \right. \quad (6-7)
\end{aligned}$$

Thus the generalized forces are given by:

$$\begin{aligned} Q_R &= \sum_{K=1}^S F_{HK} ; & Q_x &= \sum_{K=1}^S F_{VK} \\ Q_\gamma &= \sum_{K=1}^S \left\{ F_{HK} [D_{HK} - \phi_K \gamma_c q_c - D_{VK} (\gamma_c + \beta_K q_c)] - F_{VK} (D_{HK} \gamma_c + \phi_K q_c + D_{VK}) \right\} \quad (6-8) \\ Q_q &= \sum_{K=1}^S \left\{ F_{HK} [\phi_K - D_{VK} \beta_K (\gamma_c + \beta_K q_c)] - F_{VK} (\phi_K \gamma_c + D_{VK} \beta_K) \right\} \end{aligned}$$

6.3 Suspension Element Forces

The forces in the k^{th} suspension element are determined in the following manner. The vertical and horizontal projections of the length of the element when the contents are at coordinates origin are input to the program as l_{HK} and l_{VK} . Note that these need not be equal to either the unstressed or the statically loaded element projections. If the element is capable of compression only, then the vertical projection is equal to zero, as shown in Figure 6-4. The projections are measured from the structure attachment point to the in-structure contents attachment point. Their senses are positive if they are the same sense as the positive direction of their respective coordinate axis. If an element is extended or compressed in the zero coordinates position, the unstressed length of the element l_K must be input. Otherwise, the unstressed length of the k^{th} element is calculated as:

$$l_K = (l_{HK}^2 + l_{VK}^2)^{1/2} \quad (6-9)$$

The motion of the structure wall at the k^{th} suspension element attachment point is input from the main FEAT program as $u(i,j)_k$, $\dot{u}(i,j)_k$, $w(i,j)_k$ and $\dot{w}(i,j)_k$. The indices i and j refer to the row and column of the node from the finite element representation of the structure where the suspension element is attached.

The changes in the horizontal and vertical projections of the distance between the k^{th} element attachment points are

$$\Delta l_{HK} = (w_{ij})_k - w_k \quad (6-10)$$

$$\Delta l_{VK} = (u_{ij})_k - u_k \quad (6-11)$$

In the case of a general or extension element (pin-ended) the instantaneous projections of the distance between attachment points are:

$$l'_{HK} = l_{HK} - \Delta l_{HK} \quad (6-12)$$

$$l'_{VK} = l_{VK} - \Delta l_{VK} \quad (6-13)$$

For a compression element (sliding) shown in Figure 6-4 the instantaneous projections of the distance between contents and structure, at the k^{th} element, are given by

$$l'_{HK} = l_{HK} - \Delta l_{HK} + \Delta l_{VK} \theta_K \quad (6-14)$$

$$l'_{VK} = - l'_{HK} (\gamma_c + \beta_K q_c) \quad (6-15)$$

where:

θ_K = The slope of the structure at the element attachment point

The instantaneous distance between contents and structure is

$$l'_K = (l'^2_{HK} + l'^2_{VK})^{1/2} \quad (6-16)$$

The difference between the unstrained length of the k^{th} element and the instantaneous distance between contents and structure is

$$\Delta l_K^* = l_K - l'_K \quad (6-17)$$

The rate of change of this difference is approximated by

$$\dot{\Delta l}_K^* = (\Delta l_K^* - \Delta l_{Kp}^*) / \Delta t \quad (6-18)$$

Where:

Δl_{Kp}^* = difference from previous time step

Δt = compute time increment.

If the element is capable of extension and compression, the deformation and rate of deformation of the element are simply

$$\Delta l_K = \Delta l_K^* \quad (6-19)$$

$$\dot{\Delta l}_K = \dot{\Delta l}_K^* \quad (6-20)$$

If options are chosen which limit suspension element capability to support extension or compression only, the calculation of element deformation is more complex. The behavior of a compression element will be used as an example. Calculation of forces and deflections in such an element are outlined in Figure 6-5. The procedure is identical for a tension element with the exception that all signs are reversed. The program offers the additional choice of removing an element's capability of supporting compression (tension) forces as well as its capability to compress (extend). If this option is not selected,

element force and deflection are set to zero only when the distance between contents and structure exceeds the free length of the element ($\Delta l_K^* < 0$) as shown in path ①→②→⑭ of the figure. If $\Delta l_K^* \geq 0$, the deformation and its rate for an element are determined by Equations (6-19) and (6-20) as shown by path ①→②→⑥.

The force limit option provides a means of describing the behavior of suspension system elements, such as a foam ring, whose rate of recovery from deformation may be less than the rate which the gap between structure and contents increases at some time in the time history of loading. If the force option is selected the program models all possible loading conditions: (1) The force developed during the last time step was positive and the silo to contents gap is less than the spring free length. (The element is transmitting load normally.) The deformation and its rate for an element, Δl_K , and $\dot{\Delta l}_K$ are given by Equations (6-19) and (6-20) as shown by ①→③→⑤→⑥; (2) The force from the last time step was zero and the gap is greater than instantaneous element length from the last time step. (Separation of element and contents has occurred and is continuing.) Then the Δl_K and $\dot{\Delta l}_K$ are given by the following equations as shown by ①→③→④→⑦:

$$\Delta l_K = \Delta l_{KP} \quad (6-21)$$

$$\dot{\Delta l}_K = \dot{\Delta l}_{KP} \quad (6-22)$$

Where:

Δl_{KP} = the element deformation from the previous time step

$\dot{\Delta l}_{KP}$ = the element rate of deformation from the previous time step

(3) The force from the last time step was zero and the gap is less than the instantaneous element length from the last time step. (Contact of the suspension element and the contents is commencing.) Then Δl_K and $\dot{\Delta l}_K$ are given by Equations (6-19) and (6-20) as shown by ①→③→④→⑥; and

(4) The force from the last time step was positive but the gap is larger than the free length of the element. (Separation of element and contents occurred when the instantaneous length of the element approximately equaled the free length. Positive force was due to nonlinear element components.) Then Δl_K and $\dot{\Delta l}_K$ are given by Equations (6-21) and (6-22) as shown by ①→③→⑤→⑦.

Time histories of Δl_K and $\dot{\Delta l}_K$ provided by Equations (6-19) and (6-20) or (6-21) and (6-22) are sufficient to define the force developed in the k^{th} suspension element as shown by ⑥→⑧ or ⑦→⑧. The force in the generalized k^{th} element is given by

$$F_K = F_{1K} + F_{2K} + F_{3K} = F_{4K} + F_{5K} \quad (6-23)$$

Each of the component forces is contributed by one of the components of the suspension element model (Figure 6-5). If a specific element can be modeled without using all components, forces in extraneous components are reduced to zero by input of the appropriate component parameters.

F_{1K} is a nonlinear monotonic function of the change in length of the k^{th} element, input as a table of force versus change in length.

$$F_{1K} = f(\Delta l_K) \quad (6-24)$$

F_{2K} is the force developed in the Maxwell Element, defined by

$$\dot{\Delta l}_{mK} = \frac{K_{mK}}{C_{mK}} (\Delta l_K - \Delta l_{mK}) \quad (6-25)$$

$$F_{2K} = K_{mK} (\Delta l_K - \Delta l_{mK}) \quad (6-26)$$

F_{3K} is the force developed in the Coulomb damper-linear spring series, defined by

$$\left. \begin{aligned} F_{3K} &= -F_{SK} \\ L_{CK} &= \Delta l_K + F_{SK}/K_{FK} \end{aligned} \right\} \Delta l_K < L_{CK} - F_{SK}/K_{FK} \quad (6-27)$$

$$F_{3K} = K_{FK} (\Delta l_K - L_{CK}); L_{CK} - F_{SK}/K_{FK} \leq \Delta l_K \leq L_{CK} + F_{SK}/K_{FK} \quad (6-28)$$

$$\left. \begin{aligned} F_{3K} &= F_{SK} \\ L_{CK} &= \Delta l_K - F_{SK}/K_{FK} \end{aligned} \right\} L_{CK} + F_{SK}/K_{FK} < \Delta l_K \quad (6-29)$$

where L_{CK} = position of the Coulomb damper

F_{4K} is the force developed in the viscous damper, defined by

$$F_{4K} = C_{VK} \dot{\Delta l}_K \quad (6-30)$$

F_{5K} is the force developed in the linear elastic spring, defined by

$$F_{5K} = K_{LK} \Delta l_K \quad (6-31)$$

After forces have been calculated, the program checks again against the options selected. If force limiting was not specified, the forces and element deflections are retained as calculated above, as shown by ⑧→⑨→⑮.

If force limiting was specified the loading conditions are again checked:

(1) If the force calculated is positive and the gap is equal to the instantaneous length of the element, the element is transmitting load normally. Forces and deflections are retained as calculated above, as shown by $\textcircled{8} \rightarrow \textcircled{9} \rightarrow \textcircled{10} \rightarrow \textcircled{11} \rightarrow \textcircled{15}$; (2) If the force calculated is negative or zero, separation of the element and contents have occurred. In this event the element may contract if it was unrealistically extended in this time step. Assuming that the effective mass of an element is $0.1 \text{ lb sec.}^2 / \text{in.}$, the element deflection and rate of deflection are given by

$$\Delta l_K = \Delta l_K \textcircled{8} + \iint (F_K / 0.1) dt dt \quad (6-32)$$

$$\dot{\Delta l}_K = (\Delta l_K - \Delta l_K \textcircled{8}) / \Delta t \quad (6-33)$$

Where $\Delta l_K \textcircled{8}$ = the element deflection calculated in $\textcircled{8}$.

F_K is then set to zero. If Δl_K from (6-32) is less than zero, the element is extending and Δl_K is set to zero as shown by $\textcircled{8} \rightarrow \textcircled{9} \rightarrow \textcircled{10} \rightarrow \textcircled{12} \rightarrow \textcircled{13} \rightarrow \textcircled{14}$. If Δl_K from (6-32) is greater than or equal to zero, the element is contracting and Δl_K is retained as shown by $\textcircled{8} \rightarrow \textcircled{9} \rightarrow \textcircled{10} \rightarrow \textcircled{12} \rightarrow \textcircled{13} \rightarrow \textcircled{16}$; (3) If the force is positive, but the gap is more than the instantaneous length of the element, separation of the element and contents have occurred. The element is expanding toward its free length. Element deflection and forces are calculated using the procedure of (2) above starting with Equations (6-32) and (6-33) as shown by $\textcircled{8} \rightarrow \textcircled{9} \rightarrow \textcircled{10} \rightarrow \textcircled{11} \rightarrow \textcircled{12} \rightarrow \textcircled{13} \rightarrow \textcircled{14}$ or by $\textcircled{8} \rightarrow \textcircled{9} \rightarrow \textcircled{10} \rightarrow \textcircled{11} \rightarrow \textcircled{12} \rightarrow \textcircled{13} \rightarrow \textcircled{16}$. The element forces specified by $\textcircled{14}$, $\textcircled{15}$ or $\textcircled{16}$ are used in obtaining force components and in the element load condition tests for the following time point. The instantaneous element length is also retained for the following time point.

The horizontal and vertical forces at the i^{th} attachment to the contents which appear in the generalized forces become:

$$F_{HK} = \frac{l'_{HK}}{l'_K} F_K \quad (6-34)$$

$$F_{VK} = \frac{l'_{VK}}{l'_K} F_K \quad (6-35)$$

Structure Loads

The forces acting on the structure wall at the k^{th} suspension element attachment point are

(6-36)

$$(F_{Hi})_K = -F_{HK} ; (F_{Vi})_K = -F_{VK} \quad (6-37)$$

In-Structure Responses

The in-structure contents responses are output in the form of accelerations and displacements. In addition to the rigid body motions, u , \ddot{u} , w and \ddot{w} , the lateral accelerations and displacements of the top and bottom of the contents are obtained from Equation

$$\ddot{w}_K = \ddot{w}_c + D_{HK} \ddot{\gamma}_c + \phi_K \ddot{q}_c \quad (6-38)$$

Where the index K is set to the value of a suspension element at the top or bottom of the contents. In addition, suspension element forces are output.

Static Equilibrium Position

The static equilibrium position of the suspension system is established within the program. The equilibrium position, in terms of the contents generalized coordinates, is related to the generalized forces acting on the contents by the equations

$$\begin{bmatrix} K_o \end{bmatrix} \begin{Bmatrix} w_{c_o} \\ u_{c_o} \\ \gamma_{c_o} \\ q_{c_o} \end{Bmatrix} = \begin{Bmatrix} 0 \\ -Mg \\ 0 \\ 0 \end{Bmatrix} \quad (6-39)$$

where

$$\begin{bmatrix} K_o \end{bmatrix} = \text{A generalized stiffness matrix (generalized force/ generalized displacement)}$$

The generalized coordinates for an arbitrary position are related to the generalized forces in that arbitrary position by

$$\begin{bmatrix} K_p \end{bmatrix} \begin{Bmatrix} w_{c_p} \\ u_{c_p} \\ \gamma_{c_p} \\ q_{c_p} \end{Bmatrix} = \begin{Bmatrix} Q_{R_p} \\ Q_{X_p} \\ Q_{Y_p} \\ Q_{q_p} - M_q \omega^2 q_c \end{Bmatrix} \quad (6-40)$$

If the arbitrary position is sufficiently close, the static position can be expressed in terms of the arbitrary position plus an incremental correction to the arbitrary position.

$$\begin{Bmatrix} w_{c0} \\ u_{c0} \\ \gamma_{c0} \\ q_{c0} \end{Bmatrix} = \begin{Bmatrix} w_{cp} \\ u_{cp} \\ \gamma_{cp} \\ q_{cp} \end{Bmatrix} + \begin{Bmatrix} \Delta w_c \\ \Delta u_c \\ \Delta \gamma_c \\ \Delta q_c \end{Bmatrix} \quad (6-41)$$

If it is assumed that $[K_p] \approx [K_o]$, substituting (6-41) into (6-39), subtracting (6-40) from (6-39), and solving for the correction to the arbitrary position to obtain equilibrium gives:

$$\begin{Bmatrix} \Delta w_c \\ \Delta u_c \\ \Delta \gamma_c \\ \Delta q_c \end{Bmatrix} = [K_p^{-1}] \begin{Bmatrix} -Q_{Rp} \\ -Q_{Xp} - Mg \\ -Q_{\gamma p} \\ -Q_{qp} + M_q \omega^2 q_c \end{Bmatrix} \quad (6-42)$$

If $[K_p]$ were constant, the static position would be uniquely defined by (6-41) and (6-42). Since this is not true for the present problem, an iterative technique is employed. An initial position is input for the contents for which all pertinent coordinates are non-zero. The forces $-Q_{Rp}$, $-Q_{Xp} - Mg$, $-Q_{\gamma p}$ and $-Q_{qp} + M_q \omega^2 q_c$ are calculated. The change in the forces with a δ change in each of the coordinates are calculated in turn to derive the $[K_p]$ matrix.

For example

$$K_{11} = \frac{\delta Q_{Rp}}{\delta w_c} ; K_{21} = \frac{\delta Q_{Xp}}{\delta w_c} ; K_{31} = \frac{\delta Q_{\gamma p}}{\delta w_c} ; K_{41} = \frac{\delta Q_{qp}}{\delta w_c}$$

The changes required to the arbitrary position, Δw_c , Δu_c , $\Delta \gamma_c$ and Δq_c are calculated. These changes are multiplied by 0.25 and applied as corrections to the arbitrary position to obtain a new position closer to equilibrium. The multiplier which is used in the first four iterations improves iteration convergence when $[K]$ is highly nonlinear. On the fifth iteration the multiplier is eliminated and the corrections are equal to the changes calculated. This procedure is repeated until the change in generalized coordinates from iteration to iteration cycle is very small. Coulomb and viscous damping suspension element components are disconnected during the equilibrium search. They are reconnected, with the equilibrium position as their neutral point after equilibrium is attained.

VII

LOADING CONDITIONS

7.1 Basic Concepts

The finite element models discussed in this report are prepared to accept initial conditions as well as boundary loading. The problems of ground motion analysis must be prepared to consider two separate types of loadings; i.e., the surface loading by airblast and the direct loading by stress waves propagating through the ground. Only for certain sites and low overpressure levels is it possible to ignore the direct loading portion.

The FEAT Code was not designed for hydrodynamic analysis and is therefore always dependent on some form of input for the direct loading which was calculated by another analysis technique. This requires the capability of accepting boundary loading in addition to the airblast input. In order to give the required detail to the buried structure interaction analysis it is necessary to limit the extent of the free field computations to the absolute minimum. For this study the decision was made to use the so-called "soil island" concept. This means that the buried structure is considered to be surrounded by a finite region of earth material. It is clear that reflections from the soil island boundaries will cause interference with the interaction response. However, limits to the size of the model to be considered are at this time dictated by computer run time. An adequate compromise was achieved between model size and reflection interference.

7.2 Free Field Input

For the purpose of this structure-media interaction study it was prescribed that the soil island boundary input, except for air blast loading, was to be calculated in a separate study. That work is accomplished by a joint venture of Applied Theory, Incorporated and Agbabian, Jacobsen and Associates (ATI-AJA). Specific soil island boundaries for various yields to be considered were agreed upon. These are shown in Figure 7-1. There is one soil island for each overpressure range for each yield.

The boundary input could be accomplished in several ways. It could be applied as stress-time histories at the boundary nodes, or as particle velocities or displacements. Since any numerical analysis method superimposes its own characteristic oscillations upon any signal it calculates, it was decided that the problem of transferring these oscillations from the ATI-AJA results to FEAT calculations would be minimized if particle displacement-time histories would be used as input.

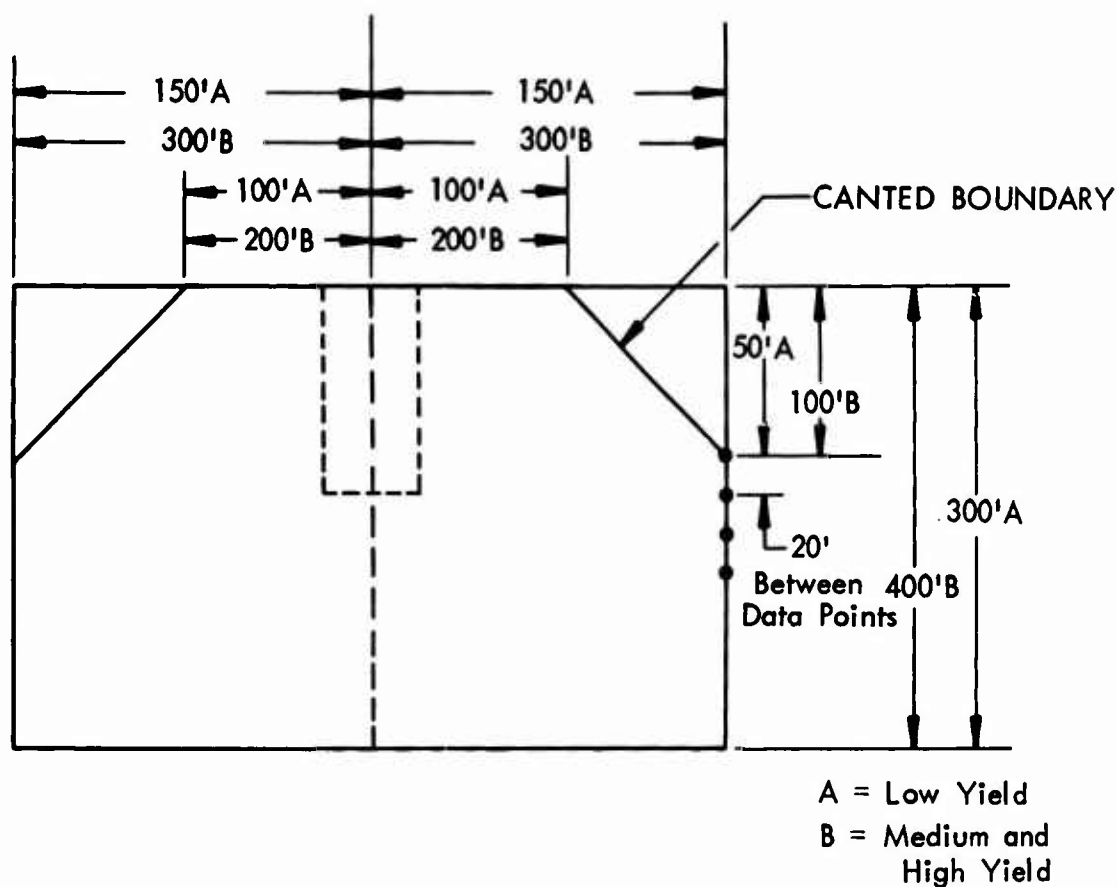


Figure 7-1: SOIL ISLAND LAYOUT

A concept for minimizing interfering boundary reflections was considered. The introduction of canted boundaries near the surface on the upstream sides of the soil island was conceived for the purpose of scattering the waves of interaction emanating from the buried structure response. Attempts to use these canted boundaries were, however, not successful. Interpolation of input data and the construction of these inclined boundaries in the FEAT model apparently require much further study before this scheme can be utilized effectively. The boundaries were generating interference in the solution. Since the use of canted boundaries was not considered essential in this study, further investigations into their application were deferred. Vertical side boundaries have been used throughout this study.

The free field calculations by ATI-AJA produce displacement-time histories along all soil island boundaries at 10 foot space intervals and .5 msec. time intervals. These data are recorded on magnetic tapes which, in turn, are read by The Boeing Company's computer system and re-arranged as required for use of the individual soil island analyses. It is recognized that in generating these time histories at specified points some interpolations in space had to be made by ATI-AJA, while in the use of the data for FEAT calculations

interpolations in time will be necessary since the data time points do not always correspond to the integration step used in FEAT.

The calculations made so far with this type of input data have been reasonably successful. The results are very sensitive to the two individual analyses. Slight incompatibilities of the signal propagated through the FEAT model to the back or bottom boundary with the motion prescribed there by the input will generate undesired reflections. This imposes very strict accuracy requirements on both analysis methods.

7.3 Airblast Input

The principal characteristics of the airblast resulting from a nuclear explosion are the time of arrival, the peak overpressure, the duration of the positive phase, and the time history of the overpressure. In this study these four characteristics are defined by a set of equations which are derived empirically on the basis of a "least squares" fit of experimental data (ref. 13), supplied by Aerospace Corporation.

Three ranges of peak overpressure were fitted separately, and each of the four characteristics is defined by a different equation in each range. The equations include the scaling factors necessary to account for weapons of different yields. Studies performed at The Boeing Company indicate that airblast phenomena obtained from these equations are in good agreement with the corresponding phenomena obtained from other theoretical calculations.

At each discrete point in time ($t = t_0 + n\Delta t$) the position of the wave front is determined, and the overpressure behind the wave front is determined as a function of range. The distance between each pair of node points in the idealized model is divided into many small increments, and the airblast force on each increment is determined by multiplying the average overpressure within that increment by the surface area of the increment. Each of these forces is distributed to the nodal points under the assumption that it is applied to a weightless beam which is simply supported at the node points on either side of the increment.

APPENDIX "A"

Derivations of Trapezoidal Plane Strain Element

The Stiffness Matrix

The trapezoidal plane strain element under consideration is shown in Figure A-1.

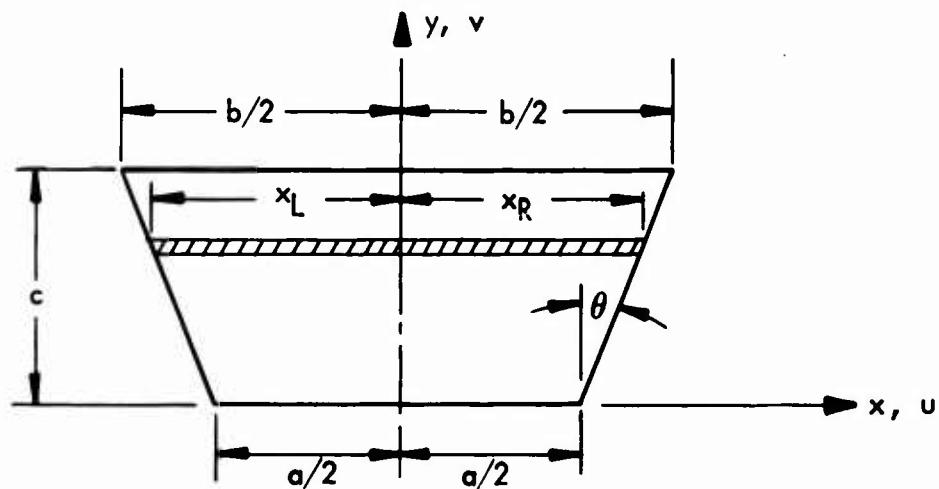


FIGURE A-1 -- A TRAPEZOIDAL PLANE STRAIN ELEMENT

Since there are four nodal points, the assumed displacement functions must contain eight independent degrees of freedom. Let these displacement functions be given by:

$$\begin{bmatrix} \Delta u \\ \Delta v \end{bmatrix} = \begin{bmatrix} 1 & xH & y & xyH & 0 & 0 & 0 & 0 \\ 0 & 0 & 0 & 0 & 1 & xH & y & xyH \end{bmatrix} \begin{Bmatrix} \Delta q_1 \\ \Delta q_2 \\ \vdots \\ \Delta q_8 \end{Bmatrix} \quad (A-1)$$

where

$$H = \frac{1}{a/2 + y \tan \theta}$$

$$\tan \theta = (b-a)/2c$$

Note that according to these displacement functions the edges of the elements are displaced as straight lines, and hence compatibility of displacements across inter-element boundaries is assured.

The incremental nodal point displacement components are:

$$\begin{Bmatrix} \Delta u_1 \\ \Delta u_2 \\ \Delta u_3 \\ \Delta u_4 \\ \Delta v_1 \\ \Delta v_2 \\ \Delta v_3 \\ \Delta v_4 \end{Bmatrix} = [A] \begin{Bmatrix} \Delta q_1 \\ \Delta q_2 \\ \Delta q_3 \\ \Delta q_4 \\ \Delta q_5 \\ \Delta q_6 \\ \Delta q_7 \\ \Delta q_8 \end{Bmatrix} \quad (A-2)$$

where

$$[A] = \left[\begin{array}{cccc|cccc} 1 & -1 & 0 & 0 & & & & \\ 1 & 1 & 0 & 0 & & & & \\ 1 & -1 & c & -c & & & & \\ 1 & 1 & c & c & & & & \\ \hline & & & & 1 & -1 & 0 & 0 \\ & & & & 1 & 1 & 0 & 0 \\ & 0 & & & 1 & -1 & c & -c \\ & & & & 1 & 1 & c & c \end{array} \right] \quad (A-3)$$

The incremental generalized coordinates are now expressed in terms of the incremental nodal point displacements:

$$\begin{Bmatrix} \Delta q_1 \\ \Delta q_2 \\ \vdots \\ \Delta q_8 \end{Bmatrix} = [A^{-1}] \begin{Bmatrix} \Delta u_1 \\ \Delta u_2 \\ \vdots \\ \Delta v_4 \end{Bmatrix} \quad (A-4)$$

where

$$[A]^{-1} = \frac{1}{2c} \begin{bmatrix} c & c & 0 & 0 & 0 \\ -c & c & 0 & 0 & 0 \\ -1 & -1 & 1 & 1 & 0 \\ 1 & -1 & -1 & 1 & 0 \\ 0 & 0 & c & c & 0 & 0 \\ 0 & 0 & -c & c & 0 & 0 \\ 0 & 0 & -1 & -1 & 1 & 1 \\ 0 & 0 & 1 & -1 & -1 & 1 \end{bmatrix} \quad (A-5)$$

The incremental strains are related to the incremental generalized coordinates by the matrix $[B]$ in the following $\{\Delta E\} = [B] \{\Delta q\}$:

$$\begin{Bmatrix} \Delta \epsilon_x \\ \Delta \epsilon_y \\ \Delta \gamma_{xy} \\ \Delta \epsilon_z \end{Bmatrix} = \begin{bmatrix} 0 & H & 0 & H_y & 0 & 0 & 0 & 0 \\ 0 & 0 & 0 & 0 & 0 & -xH^2 \tan \theta & 1 & xH\Gamma \\ 0 & -xH^2 \tan \theta & 1 & xH\Gamma & 0 & H & 0 & H_y \\ 0 & 0 & 0 & 0 & 0 & 0 & 0 & 0 \end{bmatrix} \begin{Bmatrix} \Delta q_1 \\ \Delta q_2 \\ \vdots \\ \Delta q_8 \end{Bmatrix} \quad (A-6)$$

where $\Gamma = 1 - yH \tan \theta$

The elements of the matrix $[B]$ in equations (A-6) are obtained by means of differentiation of equations (A-4).

The generalized coordinate stiffness matrix $[\bar{k}]$ is found by integrating over the volume $(1/2)(a+b)c$

$$[\bar{k}] = \int_V [B]^T [D] [B] dV \quad (A-7)$$

where $dV = dx dy$, $[B]$ is the matrix in equation (A-6), and $[D]$ is the stress-strain matrix

$$[D] = \begin{bmatrix} K+(4/3)G & -QH_{11}^2 & K-(2/3)G & -QH_{11}H_{22} & -QH_{11}H_{12} & K-(2/3)G & -QH_{11}H_{33} \\ -QH_{11}^2 & K+(4/3)G & -QH_{11}H_{22} & -QH_{11}H_{12} & -QH_{12}H_{22} & K-(2/3)G & -QH_{22}H_{33} \\ \text{Symmetric} & & -QH_{22}^2 & G-QH_{12}^2 & -QH_{12}H_{22} & -QH_{12}H_{33} & -QH_{12}H_{33} \\ & & & & G-QH_{12}^2 & -QH_{12}H_{33} & -QH_{12}H_{33} \\ & & & & & K+(4/3)G & -QH_{33}^2 \\ & & & & & -QH_{33}^2 & K+(4/3)G \end{bmatrix} \quad (A-8)$$

The matrix $[k]$ can be written as follows:

$$[k] = [k_{ij}] \quad (A-9)$$

where the elements of the (diagonally symmetric) matrix $[k_{ij}]$ are:

$$k_{1i} = k_{5i} = k_{i1} = k_{i5} = 0$$

$$\text{for } i = 1 \text{ to } 8, j = 1 \text{ to } 8$$

(A-10)

$$k_{22} = (K+(4/3)G - QH_{11}^2) I_3 - 2 \tan \theta (-QH_{11}H_{12}) I_9 \\ + (G - QH_{12}^2) \tan^2 \theta I_8$$

$$k_{23} = (-QH_{11}H_{12}) I_2 - (G - QH_{12}^2) I_7 \tan \theta$$

$$k_{24} = (K+(4/3)G - QH_{11}^2) I_5 + (-QH_{11}H_{12}) (I_7 - 2 \tan \theta I_{11}) \\ - (G - QH_{12}^2) (I_{14} - \tan \theta) I_{17} \tan \theta$$

$$k_{26} = (-QH_{11}H_{12}) I_3 - (K+(1/3)G - QH_{11}H_{22} - QH_{12}^2) I_9 \tan \theta \\ + \tan^2 \theta (-QH_{12}H_{22}) I_8$$

$$k_{27} = (K-(2/3)G - QH_{11}H_{22}) I_2 - I_7 (-QH_{22}H_{12}) \tan \theta$$

$$k_{28} = (K-(2/3)G - QH_{11}H_{22}) (I_7 - I_{11} \tan \theta) + I_5 (-QH_{11}H_{12}) \\ - (I_{14} \tan \theta - I_{17} \tan^2 \theta) (-QH_{12}H_{22}) - I_{11} \tan \theta (G - QH_{12}^2)$$

$$k_{33} = (G - QH_{12}^2) I_1$$

$$k_{34} = (-QH_{11}H_{12}) I_4 + (G - QH_{12}^2) (I_{12} - I_{10} \tan \theta)$$

$$k_{36} = (G - QH_{12}^2) I_2 - I_7 (-QH_{22}H_{12}) \tan \theta$$

$$\begin{aligned}
k_{37} &= I_1 (-QH_{22}H_{12}) \\
k_{38} &= (I_{12}-I_{10} \tan \theta) (-QH_{22}H_{12}) + I_4 (G-QH_{12}^2) \\
k_{44} &= (G-QH_{12}^2) (I_{13}-2 I_{15} \tan \theta + I_{16} \tan^2 \theta) \\
&\quad + 2(I_{10}-I_{18} \tan \theta) (-QH_{11}H_{12}) + I_6(K+4/3)G-QH_{11}^2 \\
k_{46} &= (I_7-I_{11} \tan \theta) (G-QH_{12}^2) + (-QH_{11}H_{12}) I_5 \\
&\quad + QH_{22}H_{12} (I_{14}-I_{17} \tan \theta) \tan \theta - I_{11}(K-(2/3)G-QH_{11}H_{22}) \tan \theta \\
k_{47} &= -QH_{22}H_{12} (I_{12}-I_{10} \tan \theta) + I_4 (K-(2/3)G-QH_{11}H_{22}) \\
k_{48} &= -QH_{22}H_{12} (I_{13}-2 I_{15} \tan \theta + I_{16} \tan^2 \theta) + I_6 (-QH_{11}H_{12}) \\
&\quad + (I_{10}-I_{18} \tan \theta) (K+(1/3)G-QH_{12}^2 - QH_{11}H_{22}) \\
k_{66} &= (G-QH_{12}^2) I_3 + (QH_{22}H_{12}) (2 I_9 \tan \theta) \\
&\quad + (K+(4/3)G-QH_{22}^2) (I_8 \tan^2 \theta) \\
k_{67} &= (-QH_{22}H_{12}) I_2 - (K+(4/3)G-QH_{22}^2) I_7 \tan \theta \\
k_{68} &= (-QH_{22}H_{12}) (I_7-2 I_{11} \tan \theta) + (G-QH_{12}^2) I_5 \\
&\quad - (K+(4/3)G-QH_{22}^2) (I_{14}-I_{17} \tan \theta) \tan \theta \\
k_{77} &= I_1 (K+(4/3)G-QH_{22}^2) \\
k_{78} &= -QH_{22}H_{12} I_4 + (I_{12}-I_{10} \tan \theta) (K+(4/3)G-QH_{22}^2) \\
k_{88} &= (K+(4/3)G-QH_{22}^2) (I_{13}-2 I_{15} \tan \theta + I_{16} \tan^2 \theta) \\
&\quad - 2 QH_{22}H_{12} (I_{10}-I_{18} \tan \theta) + (G-QH_{12}^2) I_6
\end{aligned}$$

where

$$I_1 = \int_0^c \int_{x_L}^{x_R} (1) dx dy = (C/2)(a+b) \quad (A-11)$$

$$I_2 = \int_0^c \int_{x_L}^{x_R} (H) dx dy = 2C$$

$$I_3 = \int_0^c \int_{x_L}^{x_R} (H^2) \, dx dy = \frac{2 \ln \left(\frac{b}{a} \right)}{\tan \theta}$$

$$I_4 = \int_0^c \int_{x_L}^{x_R} (Hy) \, dx dy = C^2$$

$$I_5 = \int_0^c \int_{x_L}^{x_R} (H^2 y) \, dx dy = \frac{2}{\tan^2 \theta} \left(C \tan \theta - \frac{a}{2} \ln \left(\frac{b}{a} \right) \right)$$

$$I_6 = \int_0^c \int_{x_L}^{x_R} (H^2 y^2) \, dx dy = \frac{2}{\tan^3 \theta} \left[\frac{b^2 - a^2}{8} - ac \tan \theta + \frac{a^2}{4} \ln \left(\frac{b}{a} \right) \right]$$

$$I_7 = \int_0^c \int_{x_L}^{x_R} (H^2 x) \, dx dy = 0$$

$$I_8 = \int_0^c \int_{x_L}^{x_R} (H^4 x^2) \, dx dy = \frac{2 \ln \left(\frac{b}{a} \right)}{3 \tan \theta}$$

$$I_9 = \int_0^c \int_{x_L}^{x_R} (H^3 x) \, dx dy = 0$$

$$I_{10} = \int_0^c \int_{x_L}^{x_R} (xy H^2) \, dx dy = 0$$

$$I_{11} = \int_0^c \int_{x_L}^{x_R} (xy H^3) \, dx dy = 0$$

$$I_{12} = \int_0^c \int_{x_L}^{x_R} (Hx) \, dx dy = 0$$

$$I_{13} = \int_0^c \int_{x_L}^{x_R} (H^2 x^2) \, dx dy = \frac{C}{6} (a+b)$$

$$I_{14} = \int_0^c \int_{x_L}^{x_R} (H^3 x^2) dx dy = \frac{2C}{3}$$

$$I_{15} = \int_0^c \int_{x_L}^{x_R} (H^3 x^2 y) dx dy = \frac{C^2}{3}$$

$$I_{16} = \int_0^c \int_{x_L}^{x_R} (H^4 x^2 y^2) dx dy = \frac{I_6}{3}$$

$$I_{17} = \int_0^c \int_{x_L}^{x_R} (H^4 x^2 y) dx dy = \frac{I_5}{3}$$

$$I_{18} = \int_0^c \int_{x_L}^{x_R} (xy^2 H^3) dx dy = 0$$

Finally, the element stiffness matrix is found according to equation (2-13).

$$[k] = [A^{-1}]^T [\bar{k}] [A^{-1}]$$

where $[A^{-1}]$ is given by equations (A-5), and $[\bar{k}]$ is given by equations (A-9), (A-10), and (A-11).

The Mass Matrix

The mass matrix $[M]$ in the equation of motion (1-1) is diagonalized by lumping the mass of the trapezoidal element of the four nodes.

The mass at node 1 or 2 is:

$$m_1 = m_2 = \rho \left[\frac{ac}{4} + \frac{c}{12} (b-a) \right] \quad (A-12)$$

The mass at node 3 or 4 is:

$$m_3 = m_4 = \rho \left[\frac{ac}{4} + \frac{c}{6} (b-a) \right] \quad (A-13)$$

where ρ is the mass density.

The Stress Computation

The stress increments are computed according to the following equation:

$$\{\Delta\sigma\} = [D] [B] [A^{-1}] \{\Delta u\} \quad (A-14)$$

where

$$\{\Delta\sigma\} = \{\Delta\sigma_x, \Delta\sigma_y, \Delta\tau_{xy}, \Delta\sigma_z\}$$
$$\{\Delta u\} = \{\Delta u_1, \Delta u_2, \Delta u_3, \Delta u_4, \Delta v_1, \Delta v_2, \Delta v_3, \Delta v_4\}$$

$[D]$ = The 4x4 matrix given by equation (A-8).

$[A^{-1}]$ = The matrix given by equation (A-5).

$[B]$ = The 4x8 matrix given by (A-6).

It is noted that matrices $[D]$ and $[A]$ are constant. But matrix $[B]$ is a function of x and y , in addition to other constants such as a , b , and c . Thus, the stress field within the trapezoidal element is a varying one. To obtain the magnitude of an average stress in the element, the Mean-Value theorem is invoked as the basis for the averaging process. In this manner, the average stress for the trapezoidal element will be defined at a point where $x = 0$ and $y = c/2$, which is very close to the centroid of the element.

The matrices $[D]$, $[B]$ and $[A]$ are now defined for calculations of the average stress increment based on a given vector of nodal incremental displacement. The stress computation requires adoption of the matrix operations given in Equation (A-14). The total current stresses are obtained by addition. These stresses serve as the basis for determination of the current values of the bulk and shear moduli, which are considered as functions of the mean pressure.

Reduction of the Trapezoidal Element to a Rectangular Element

In the rectangular plain strain analysis of the FEAT code, the element stiffness matrices were obtained from the above trapezoidal element. By allowing the dimensions " b " and " a ", as shown in Figure A-1, to become identical, a rectangular region is obtained. The only difficulty encountered in this process occurs in equations (A-11).

In these equations, the $\log(b/a)$ divided by $\tan \theta$ and similar terms appear. As " b " approaches " a ", this results in the indeterminate form $\log 1 / \tan \theta$. The limit of such terms is investigated by allowing " b " to have the form:

$$b = a (1 + \epsilon)$$

and then let ϵ approach zero. This is required for I_3 , I_5 , I_6 and I_8 of equation A-11.

Carrying out this process, it is found that a finite limit exists for each of these terms.

The limits are:

$$\lim_{\epsilon \rightarrow 0} I_3 = \frac{4c}{a}$$

$$\lim_{\epsilon \rightarrow 0} I_5 = \frac{2c^2}{a}$$

$$\lim_{\epsilon \rightarrow 0} I_6 = \frac{4c^3}{3a}$$

$$\lim_{\epsilon \rightarrow 0} I_8 = \frac{4c}{3a}$$

By making this substitution in the terms of the stiffness matrix (A-10) and recognizing that $\tan \theta = 0$, the stiffness matrix for a rectangular element is obtained.

The incremental stresses for the rectangle are obtained by altering the $[B]$ matrix in equation (A-6). This is achieved without difficulty because $H \rightarrow \frac{2}{3}a$ as $b \rightarrow a$ and $\tan \theta = 0$.

The nodal masses given in equations (A-12) and (A-13) reduce to:

$$m_1 = m_2 = m_3 = m_4 = (ac/4) \rho$$

It is noted that matrices $[D]$ and $[A^{-1}]$ are constant. But matrix $[B]$ is a function of the coordinates, x and y . This is so because of the fact that quadratic displacement functions have been used. Since the displacement function leads to a linear variation in the strain (and, therefore, stress) field, an average state of stress is logically desired. For this purpose, the Mean-Value theorem is invoked to serve as the basis for the averaging process. For the rectangular plane strain element, therefore, the average stresses are defined at the centroid. This is done by substituting $x = a/2$ and $y = c/2$ in the matrix $[B]$.

Having matrices $[D]$, $[B]$ and $[A^{-1}]$ properly defined for the element, the stress increments for the element are obtained by a series of matrix operations, according to equation (A-14), for a given vector of nodal incremental displacements. Finally, the total (current) stress components are obtained by addition. These stresses serve as the base for successive computations in the determination of the current values for the bulk and shear moduli, which are considered as functions of the mean pressure.

APPENDIX "B"

Derivations of Triangular Plane Strain Element

The Stiffness Matrix

In Figure B-1 the triangular plane strain element under consideration is shown.

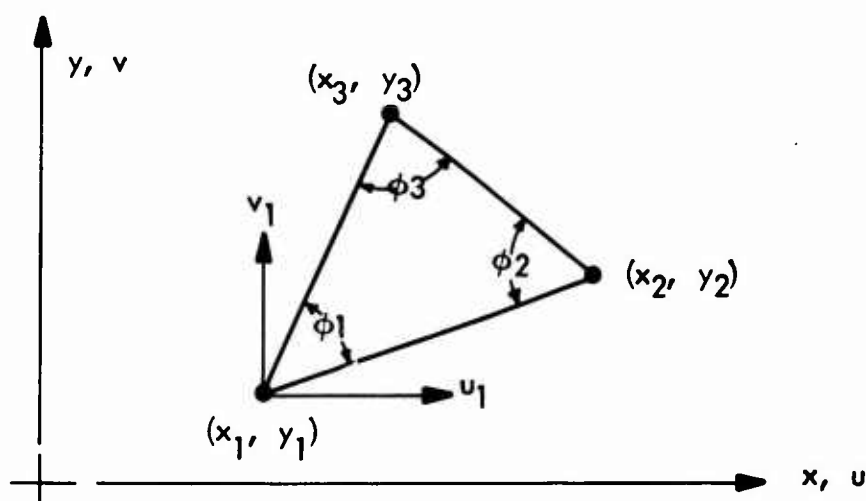


Figure B-1: A TRIANGULAR PLANE STRAIN ELEMENT

Since there are three nodal points, the assumed displacement functions must contain six independent degrees of freedom. Let these displacement functions be given by:

$$\begin{Bmatrix} \Delta u \\ \Delta v \end{Bmatrix} = \begin{bmatrix} 1 & x & y & 0 & 0 & 0 \\ 0 & 0 & 0 & 1 & x & y \end{bmatrix} \begin{Bmatrix} \Delta q_1 \\ \Delta q_2 \\ \Delta q_3 \\ \Delta q_4 \\ \Delta q_5 \\ \Delta q_6 \end{Bmatrix} \quad (B-1)$$

Note that according to these displacement functions the edges of the elements are displaced as straight lines, and hence compatibility of displacements across inter-element boundaries is assured.

The incremental nodal point displacement components are:

$$\begin{Bmatrix} \Delta u_1 \\ \Delta u_2 \\ \Delta u_3 \\ \Delta v_1 \\ \Delta v_2 \\ \Delta v_3 \end{Bmatrix} = [A] \begin{Bmatrix} \Delta q_1 \\ \Delta q_2 \\ \Delta q_3 \\ \Delta q_4 \\ \Delta q_5 \\ \Delta q_6 \end{Bmatrix} \quad (B-2)$$

where

$$[A] = \left[\begin{array}{ccc|ccc} 1 & x_1 & y_1 & & & \\ & 1 & x_2 & y_2 & & 0 \\ & & 1 & x_3 & y_3 & \\ \hline & & & & 1 & x_1 & y_1 \\ & 0 & & & 1 & x_2 & y_2 \\ & & & & 1 & x_3 & y_3 \end{array} \right] \quad (B-3)$$

The incremental generalized coordinates are now expressed in terms of the incremental nodal point displacements:

$$\begin{Bmatrix} \Delta q_1 \\ \Delta q_2 \\ \Delta q_3 \\ \Delta q_4 \\ \Delta q_5 \\ \Delta q_6 \end{Bmatrix} = [A^{-1}] \begin{Bmatrix} \Delta u_1 \\ \Delta u_2 \\ \Delta u_3 \\ \Delta v_1 \\ \Delta v_2 \\ \Delta v_3 \end{Bmatrix} \quad (B-4)$$

where

$$[A^{-1}] = \frac{1}{2S_t} \left[\begin{array}{ccc|ccc} (x_2 y_3 - x_3 y_2) & (x_3 y_1 - x_1 y_3) & (x_1 y_2 - x_2 y_1) & & & 0 \\ (y_2 - y_3) & (y_3 - y_1) & (y_1 - y_2) & & & \\ (x_3 - x_2) & (x_1 - x_3) & (x_2 - x_1) & & & \\ \hline & & & 0 & (x_2 y_3 - x_3 y_2) & (x_3 y_1 - x_1 y_3) & (x_1 y_2 - x_2 y_1) \\ & & & & (y_2 - y_3) & (y_3 - y_1) & (y_1 - y_2) \\ & & & & (x_3 - x_2) & (x_1 - x_3) & (x_2 - x_1) \end{array} \right] \quad (B-5)$$

where

S_t = Area of triangular element

$$= 1/2 [x_1 (y_2 - y_3) + x_2 (y_3 - y_1) + x_3 (y_1 - y_2)]$$

The incremental strains are related to the incremental generalized coordinates by the matrix $[B]$:

$$\begin{Bmatrix} \Delta \epsilon_x \\ \Delta \epsilon_y \\ \Delta \gamma_{xy} \\ \Delta \epsilon_z \end{Bmatrix} = [B] \begin{Bmatrix} \Delta q_1 \\ \Delta q_2 \\ \Delta q_3 \\ \Delta q_4 \\ \Delta q_5 \\ \Delta q_6 \end{Bmatrix} \quad (B-6)$$

where

$$[B] = \begin{bmatrix} 0 & 1 & 0 & 0 & 0 & 0 \\ 0 & 0 & 0 & 0 & 0 & 1 \\ 0 & 0 & 1 & 0 & 1 & 0 \\ 0 & 0 & 0 & 0 & 0 & 0 \end{bmatrix} \quad (B-7)$$

The generalized coordinate stiffness matrix $[\bar{k}]$ is found by integrating over the volume $I \cdot S_t$

$$[\bar{k}] = \int_{Vol.} [B]^T [D] [B] dv \quad (B-8)$$

This matrix can readily be integrated since $dv = I \cdot dx dy$

$$\begin{aligned} [\bar{k}] &= S_t [B]^T [D] [B] \\ &= S_t [k_{ij}] \end{aligned} \quad (B-9)$$

where

$$[D] = \begin{bmatrix} K+(4/3)G & -QH_{11}^2 & K-(2/3)G & -QH_{11}H_{22} & -QH_{11}H_{12} & K-(2/3)G & -QH_{11}H_{33} \\ & K+(4/3)G & -QH_{11}H_{22} & -QH_{12}H_{22} & -QH_{12}H_{22} & K-(2/3)G & -QH_{22}H_{33} \\ & & -QH_{22}^2 & G-QH_{12}^2 & -QH_{12}H_{33} & -QH_{22}H_{33} & K+(4/3)G \\ \text{Symmetric} & & & & & & -QH_{33}^2 \end{bmatrix} \quad (B-10)$$

and $k_{ij} = k_{ji} \quad i = 1, 6; j = 1, 6$

$$k_{1j} = 0, \quad j = 1, 6; \quad k_{i4} = 0, \quad i = 1, 6$$

$$k_{22} = K + (4/3) G - QH_{11}^2$$

$$k_{23} = k_{25} = -QH_{11}H_{12}$$

$$k_{26} = K - (2/3) G - QH_{11}H_{22} \quad (B-11)$$

$$k_{33} = k_{35} = G - QH_{12}^2$$

$$k_{36} = k_{56} = -QH_{12}H_{22}$$

$$k_{55} = G - QH_{12}^2$$

$$k_{66} = K + (4/3) G - QH_{22}^2$$

Finally, the element stiffness matrix is found by:

$$[k] = [A^{-1}]^T [\bar{k}] [A^{-1}] \quad (B-12)$$

where $[A^{-1}]$ is given by equation (B-5), $[A^{-1}]^T$ is the transpose of $[A^{-1}]$, and $[\bar{k}]$ is given by equation (B-9).

The Mass Matrix

The mass matrix $[M]$ in the equation of motion (1-1) is diagonalized by lumping the mass of the triangular element at the nodes. The process is straightforward. Given the included angles of a triangle, ϕ_1, ϕ_2, ϕ_3 , the elements of the mass matrix are

$$M_1 = M_T (\phi_1/\pi); \quad M_2 = M_T (\phi_2/\pi)$$

$$M_3 = M_T (\phi_3/\pi); \quad \text{where } M_T \text{ is the total mass of the triangle.}$$

The Stress Computation

The stress increments are computed according to the following equation:

$$\{\Delta\sigma\} = [D] [B] [A^{-1}] \{\Delta u\} \quad (B-13)$$

where

$$\{\Delta\sigma\} = \{\Delta\sigma_x, \Delta\sigma_y, \Delta\tau_{xy}, \Delta\sigma_z\}$$

$$\{\Delta u\} = \{\Delta u_1, \Delta u_2, \Delta u_3, \Delta v_1, \Delta v_2, \Delta v_3\}$$

$$[D] = \text{The } 4 \times 4 \text{ matrix given by equation (B-10)}$$

$$[A^{-1}] = \text{The matrix given by equation (B - 5)}$$

$$[B] = \text{The } 4 \times 6 \text{ matrix given by equation (B - 7)}$$

It should be noted that the matrix $[B]$ is constant. Thus a constant stress field exists within a triangular element. The total current stresses are obtained by addition. These stresses serve as the basis for determination of the current values of the bulk and shear moduli, which are considered as functions of the mean pressure.

APPENDIX "C"

Derivations of Beam Element

The Stiffness Matrix

The stiffness matrix for a beam element which is shown in Figure (C-1) has been well documented. It is given here for the sake of completeness. (Ref. 14).

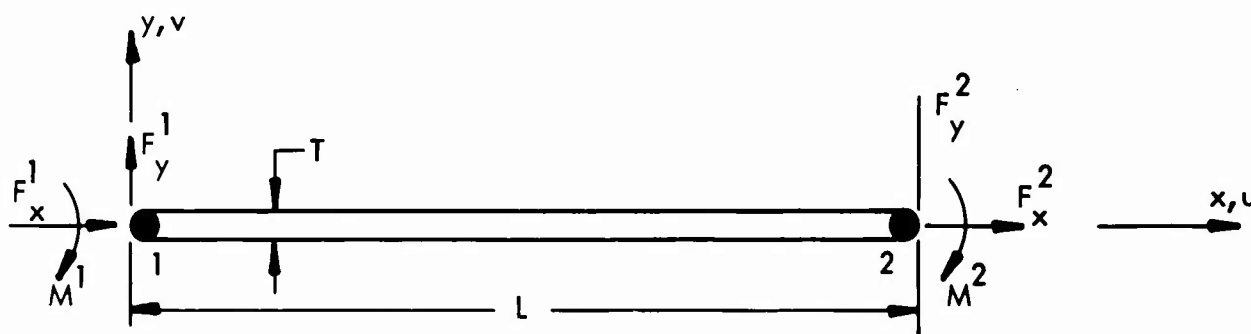


Figure C-1: A BEAM ELEMENT

The stiffness matrix for the element is:

$$\begin{Bmatrix} F_{x1}^1 \\ F_{y1}^1 \\ M_1^1 \\ F_{x2}^2 \\ F_{y2}^2 \\ M_2^2 \end{Bmatrix} = E^m \begin{bmatrix} A/L & 0 & 0 & -A/L & 0 & 0 \\ 0 & 12 I/L^3 & -6 I/L^2 & 0 & -12 I/L^3 & -6 I/L^2 \\ 0 & -6 I/L^2 & 4 I/L & 0 & 6 I/L^2 & 2 I/L \\ -A/L & 0 & 0 & A/L & 0 & 0 \\ 0 & -12 I/L^3 & 6 I/L^2 & 0 & 12 I/L^3 & 6 I/L^2 \\ 0 & -6 I/L^2 & 2 I/L & 0 & 6 I/L^2 & 4 I/L \end{bmatrix} \begin{Bmatrix} u_1 \\ v_1 \\ \theta_1 \\ u_2 \\ v_2 \\ \theta_2 \end{Bmatrix} \quad (C-1)$$

where

- $E^m = E/(1-\nu^2) = 4G(3K+G)/(3K+4G)$
- $A =$ Cross-sectional area of element
- $I =$ Moment of inertia
- $L =$ Length of element
- $F_x^1 =$ Force at node "1" in x-direction
- $F_y^1 =$ Force at node "1" in y-direction
- $M_1^1 =$ Moment at node "1"

- U_1 = Component of displacement at node "1" in the x-direction
 V_1 = Component of displacement at node "1" in the y-direction
 θ_1 = Rotation at node "1"

Similar quantities at node "2" have sub-or superscript "2"

The Mass Matrix

The mass matrix $[M]$ in the equation of motion is diagonalized by lumping the mass of the element at the two nodes.

Thus:

$$m_1 = m_2 = 1/2 \rho AL \quad (C-2)$$

The Stress Computation

The axial force, as well as the shear and the moment, can be obtained by carrying out the computations of equation (C-1) when the six nodal deformation components are known. The stress is then obtained by the customary formula,

$$\sigma_{\max} = \frac{P}{A} + \frac{M}{Z}$$

where P = axial force, M = moment, and A and Z are, respectively, the cross sectional area and the section modulus.

APPENDIX "D"

Derivations of Axisymmetric Ring Element of Rectangular Cross Section

The derivations for an axisymmetric ring element of elastic-plastic behavior are presented below. The element, of which a segment is shown in Figure D-1, has a rectangular cross section. Discussed below are details of the stiffness matrix, the mass matrix, and the stress computation.

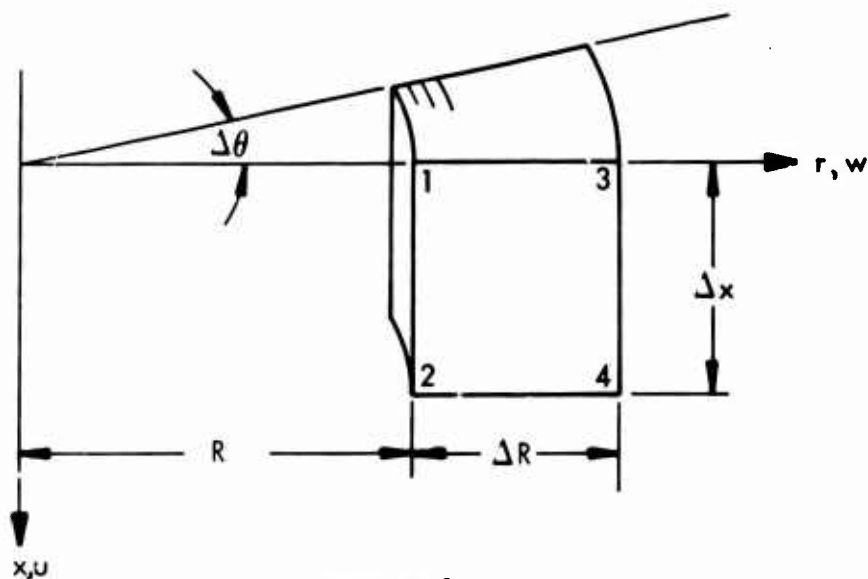


Figure D-1:

AN AXISYMMETRIC RING ELEMENT OF RECTANGULAR CROSS SECTION

The Stiffness Matrix

Referring to Figure (D-1) there are four nodal points, each with two degrees of freedom. Hence, the assumed displacement functions must contain 8 independent degrees of freedom. Let these displacement functions be as shown in equation (D-1).

$$\begin{Bmatrix} \Delta u \\ \Delta w \end{Bmatrix} = \begin{bmatrix} 1 & x & r & xr & 0 & 0 & 0 & 0 \\ 0 & 0 & 0 & 0 & 1 & x & r & xr \end{bmatrix} \begin{Bmatrix} \Delta q_1 \\ \Delta q_2 \\ \Delta q_3 \\ \Delta q_4 \\ \Delta q_5 \\ \Delta q_6 \\ \Delta q_7 \\ \Delta q_8 \end{Bmatrix} \quad (D-1)$$

Note that according to these displacement functions the edges of the element are displaced as straight lines and, hence, compatibility of displacements is assured across element boundaries.

The incremental nodal point displacement components are expressed in terms of the incremental generalized coordinates.

$$\begin{Bmatrix} \Delta u_1 \\ \Delta u_2 \\ \Delta u_3 \\ \Delta u_4 \\ \Delta w_1 \\ \Delta w_2 \\ \Delta w_3 \\ \Delta w_4 \end{Bmatrix} = [A] \begin{Bmatrix} \Delta q_1 \\ \Delta q_2 \\ \Delta q_3 \\ \Delta q_4 \\ \Delta q_5 \\ \Delta q_6 \\ \Delta q_7 \\ \Delta q_8 \end{Bmatrix} \quad (D-2)$$

where:

$$[A] = \left[\begin{array}{cccc|cccc} 1 & 0 & R & 0 & & & & \\ 1 & \Delta x & R & R \Delta x & & & & \\ 1 & 0 & (R + \Delta R) & 0 & & & & \\ 1 & \Delta x & (R + \Delta R) & (R + \Delta R) \Delta x & & & & \\ \hline & & & & 1 & 0 & R & 0 \\ & & & & 1 & \Delta x & R & R \Delta x \\ & & & & 1 & 0 & (R + \Delta R) & 0 \\ & & & & 1 & \Delta x & (R + \Delta R) & (R + \Delta R) \Delta x \end{array} \right] \quad (D-3)$$

The increment generalized coordinates are now expressed in terms of the incremental nodal point displacements.

$$\begin{Bmatrix} \Delta q_1 \\ \Delta q_2 \\ \Delta q_3 \\ \Delta q_4 \\ \Delta q_5 \\ \Delta q_6 \\ \Delta q_7 \\ \Delta q_8 \end{Bmatrix} = [A^{-1}] \begin{Bmatrix} \Delta u_1 \\ \Delta u_2 \\ \Delta u_3 \\ \Delta u_4 \\ \Delta w_1 \\ \Delta w_2 \\ \Delta w_3 \\ \Delta w_4 \end{Bmatrix} \quad (D-4)$$

where

$$[A^{-1}] = \frac{-1}{\Delta R \Delta x} \left[\begin{array}{cccc|cccc} -(R+\Delta R) \Delta x & 0 & R \Delta x & 0 & -(R+\Delta R) \Delta x & 0 & R \Delta x & 0 \\ (R+\Delta R) & -(R+\Delta R) & -R & R & (R+\Delta R) & -(R+\Delta R) & -R & R \\ \Delta x & 0 & -\Delta x & 0 & \Delta x & 0 & -\Delta x & 0 \\ -1 & 1 & 1 & -1 & -1 & 1 & 1 & -1 \end{array} \right] \quad (D-5)$$

The incremental strains are related to the incremental generalized coordinates by the matrix $[B]$ in the following ($\{\Delta \epsilon\} = [B] \{\Delta q\}$)

$$\begin{Bmatrix} \Delta \epsilon_x \\ \Delta \epsilon_r \\ \Delta \gamma_{xr} \\ \Delta \epsilon_\theta \end{Bmatrix} = \begin{bmatrix} 0 & 1 & 0 & r & 0 & 0 & 0 & 0 \\ 0 & 0 & 0 & 0 & 0 & 0 & 1 & x \\ 0 & 0 & 1 & x & 0 & 1 & 0 & r \\ 0 & 0 & 0 & 0 & 1/r & x/r & 1 & x \end{bmatrix} \begin{Bmatrix} \Delta q_1 \\ \Delta q_2 \\ \Delta q_3 \\ \Delta q_4 \\ \Delta q_5 \\ \Delta q_6 \\ \Delta q_7 \\ \Delta q_8 \end{Bmatrix} \quad (D-6)$$

The elements of the matrix $[B]$ in equations (D-6) are obtained by means of differentiation of equations (D-1).

The generalized coordinate stiffness matrix $[\bar{k}]$ is found by integrating over the volume $\Delta x \Delta R (R + \Delta R/2) \Delta \theta$

$$[\bar{k}] = \int_{vol} [B]^T [D] [B] dV \quad (D-7)$$

where $dV = R d\theta dx dr$, $[B]$ is the rectangular matrix in equations (D-6), and $[D]$ is the stress-strain matrix

$$[D] = \begin{bmatrix} K+(4/3)G & K-(2/3)G & -QH_{11}H_{12} & K-(2/3)G & -QH_{11}H_{33} \\ -QH_{11}^2 & -QH_{11}H_{22} & -QH_{11}H_{12} & -QH_{11}H_{33} & -QH_{11}H_{33} \\ K+(4/3)G & -QH_{12}H_{22} & K-(2/3)G & -QH_{22}H_{33} \\ -QH_{22}^2 & G-QH_{12}^2 & -QH_{12}H_{33} & K+(4/3)G & -QH_{33}^2 \\ \text{Symmetric} & & & & \end{bmatrix} \quad (D-8)$$

The matrix $[\bar{k}]$ may be written as: $[\bar{k}] = [k_{ij}]$ where the elements of the (diagonally symmetric) $[k_{ij}]$ matrix for the case $\Delta\theta = 1$ radian are as follows:

$$\begin{aligned} k_{1i} &= k_{i1} = 0 \quad \text{For } i = 1, 8; j = 1, 8 \\ k_{22} &= (K+(4/3)G - QH_{11}^2) I_1 \\ k_{33} &= (G - QH_{12}^2) I_1 \\ k_{44} &= (K+(4/3)G - QH_{11}^2) I_5 + (G - QH_{12}^2) I_4 - 2QH_{11}H_{12}I_8 \\ k_{55} &= (K+(4/3)G - QH_{33}^2) I_{10} \\ k_{66} &= (K+(4/3)G - QH_{33}^2) I_{22} + (G - QH_{12}^2) I_1 - 2QH_{12}H_{33}I_7 \\ k_{77} &= (4K+4G/3 - QH_{22}^2 - 2QH_{22}H_{33} - QH_{33}^2) I_1 \\ k_{88} &= (4K+4G/3 - Q(H_{22}+H_{33})^2) I_4 + (G - QH_{12}^2) I_5 \\ &\quad - 2QH_{12}(H_{22}+H_{33}) I_8 \\ k_{23} &= -QH_{11}H_{12}I_1 \\ k_{24} &= (K+(4/3)G - QH_{11}^2) I_2 - QH_{11}H_{12}I_3 \\ k_{25} &= (K-(2/3)G - QH_{11}H_{33}) I_6 \\ k_{26} &= -QH_{11}H_{12}I_1 + (K-(2/3)G - QH_{11}H_{33}) I_7 \\ k_{27} &= (2K-(4/3)G - QH_{11}H_{22} - QH_{11}H_{33}) I_1 \\ k_{28} &= (2K-(4/3)G - QH_{11}H_{22} - QH_{11}H_{33}) I_3 - QH_{11}H_{12}I_2 \\ k_{34} &= -QH_{11}H_{12}I_2 + (G - QH_{12}^2) I_3 \\ k_{35} &= -QH_{33}H_{12}I_6 \\ k_{36} &= (G - QH_{12}^2) I_1 - QH_{12}H_{33}I_7 \end{aligned}$$

$$k_{37} = -QH_{12} (H_{22}+H_{33}) I_1$$

$$k_{38} = (G-QH_{12}^2) I_2 - QH_{12}(H_{22}+H_{33}) I_3$$

$$k_{45} = (K-2G/3 -QH_{11}H_{33}) I_1 - QH_{12}H_{33}I_7$$

$$k_{46} = QH_{11}H_{12}I_2 + (K+G/3 -QH_{11}H_{33}-QH_{12}^2) I_3 -QH_{12}H_{33}I_9$$

$$k_{47} = (2K-(4/3)G -QH_{11}H_{22} -QH_{11}H_{33}) I_2 -QH_{12} (H_{22}+H_{33}) I_3$$

$$k_{48} = -QH_{12}(H_{22}+H_{33})I_4 -QH_{11}H_{12}I_5 + (2K-(1/3)G -QH_{11}H_{33} -QH_{11}H_{22} -QH_{12}^2)I_8$$

$$k_{56} = -QH_{12}H_{33}I_6 + (K+(4/3)G -QH_{33}^2) I_{11}$$

$$k_{57} = (2K+(2/3)G -QH_{33}H_{22} -QH_{33}^2) I_6$$

$$k_{58} = -QH_{12}H_{33}I_1 + (2K+2G/3 -QH_{33}H_{22} -QH_{33}^2) I_7$$

$$k_{67} = -QH_{12}(H_{22}+H_{33}) I_1 + (2K+(2/3)G -QH_{33}H_{22} -QH_{33}^2) I_7$$

$$k_{68} = (G-QH_{12}^2) I_2 -QH_{12}(H_{22}+H_{33}) I_3 + (2K+(2/3)G -QH_{22}H_{33} -QH_{33}^2) I_9$$

$$k_{78} = -QH_{12}(H_{22}+H_{33}) I_2 + (4K+4G/3 -QH_{22}^2 -2QH_{22}H_{33} -QH_{33}^2) I_3$$

In equations (D-9), the following identities are used:

$$I_1 = \int_V (1) dv = A/2 (2R + \Delta R)$$

$$I_2 = \int_V (r) dv = (A/3) [(R + \Delta R)^2 + R(R + \Delta R) + R^2]$$

$$I_3 = \int_V (x) dv = (A/4) (2R + \Delta R) \Delta x$$

$$I_4 = \int_V (x^2) dv = (A/6) (2R + \Delta R) (\Delta x)^2$$

$$I_5 = \int_V (r^2) dv = (A/4) [(R + \Delta R)^2 + R^2] (2R + \Delta R) \quad (D-10)$$

$$I_6 = \int_V (1/r) dv = A$$

$$I_7 = \int_V (x/r) dv = (A/2) \Delta x$$

$$I_8 = \int_V (x/r^3) dv = (A/6) [(R + \Delta R)^2 + R(R + \Delta R) + R^2] \Delta x$$

$$I_9 = \int_V (x^2/r) dv = (A/3) (\Delta x)^2$$

$$I_{10} \int_V (1/r^2) dv = \Delta x \log_e (1 + \Delta R/R)$$

$$I_{11} \int_V (x/r^2) dv = [\Delta x^2/2] \log_e (1 + \Delta R/R)$$

$$I_{12} \int_V (x^2/r^2) dv = [\Delta x^3/3] \log_e (1 + \Delta R/R)$$

where $A = \Delta x \Delta R$

Finally, the element stiffness matrix is found:

$$[k] = [A^{-1}]^T [\bar{k}] [A^{-1}]$$

where $[A^{-1}]$ is given by equation (D-5) and $[\bar{k}]$ is given by equations (D-8), (D-9), and (D-10).

The Mass Matrix

The treatment of the mass matrix for the axisymmetric element is the same as that of the plane strain element discussed in Appendix A.

The lumped nodal masses are found by the following equations:

$$\begin{aligned} 2 m_1 R + 2 m_3 (R + \Delta R) &= R_c m \\ 2 m_1 + 2 m_3 &= m \\ m_1 &= m_2 \\ m_3 &= m_4 \end{aligned} \tag{D-11}$$

where m is the total mass of the ring element of $\Delta \theta = 1$, and R_c is the location of the centroid. They are found as follows:

$$m = \int_{vol.} dm = \int \rho dV = \rho (R + \Delta R/2) \Delta x \Delta R \tag{D-12}$$

$$R_c = R + (1 + 2 \Delta R/3R) \Delta R / (2 + \Delta R/R)$$

Equations (D-11) and (D-12) lead to:

$$\begin{aligned} m_1 &= (m/2) [1 - (R_c - R) / \Delta R] \\ m_3 &= (m/2) [(R_c - R) / \Delta R] \end{aligned} \tag{D-13}$$

These lumped masses are used in the calculations of the axisymmetric problems.

The Stress Computation

The stress computation for the axisymmetric element is performed in much the same way as that of the plane strain case.

First, the stress increments are computed according to the following equation.

$$\{\Delta \sigma\} = [D] [B] [A^{-1}] \{\Delta u\} \quad (D-14)$$

where

$\{\Delta \sigma\}$ = The 4x1 vector of stress increments

$$= \{\Delta \sigma_x, \Delta \sigma_r, \Delta \tau_{xr}, \Delta \sigma_\theta\}$$

$\{\Delta u\}$ = The 8x1 vector of incremental nodal displacements

$$= \{\Delta u_1, \Delta u_2, \Delta u_3, \Delta u_4, \Delta w_1, \Delta w_2, \Delta w_3, \Delta w_4\}$$

$[D]$ = The 4x4 matrix of the elastic-plastic stress-strain law used in equations (D-7) and (D-8); i.e., equation (B-10)

$[A^{-1}]$ = The 8x8 matrix given by equation (D-5)

$[B]$ = The 4x8 matrix given by equation (D-6).

Following the reasoning given in Appendix A for plain strain elements, the stress increments are calculated at the centroid of the cross section. This is most effectively done by substituting $x = \Delta x/2$, $r = (r_1 + r_3)/2$ in the matrix $[B]$. Having matrices $[D]$, $[B]$, and $[A^{-1}]$ properly defined for the element, the stress increments can be computed. Finally, the total current stress components are obtained by adding the stress increments to the corresponding stress components at the last time level. As for the plane strain case, this element will exhibit linear variations of stress and strain, and again a mean value of stress is determined for use in calculations.

APPENDIX "E"

Derivations of Axisymmetric Ring Element of Triangular Cross Section

The derivations for an axisymmetric ring element of triangular cross section are presented in this appendix. A segment of the element is shown in Figure E-1.

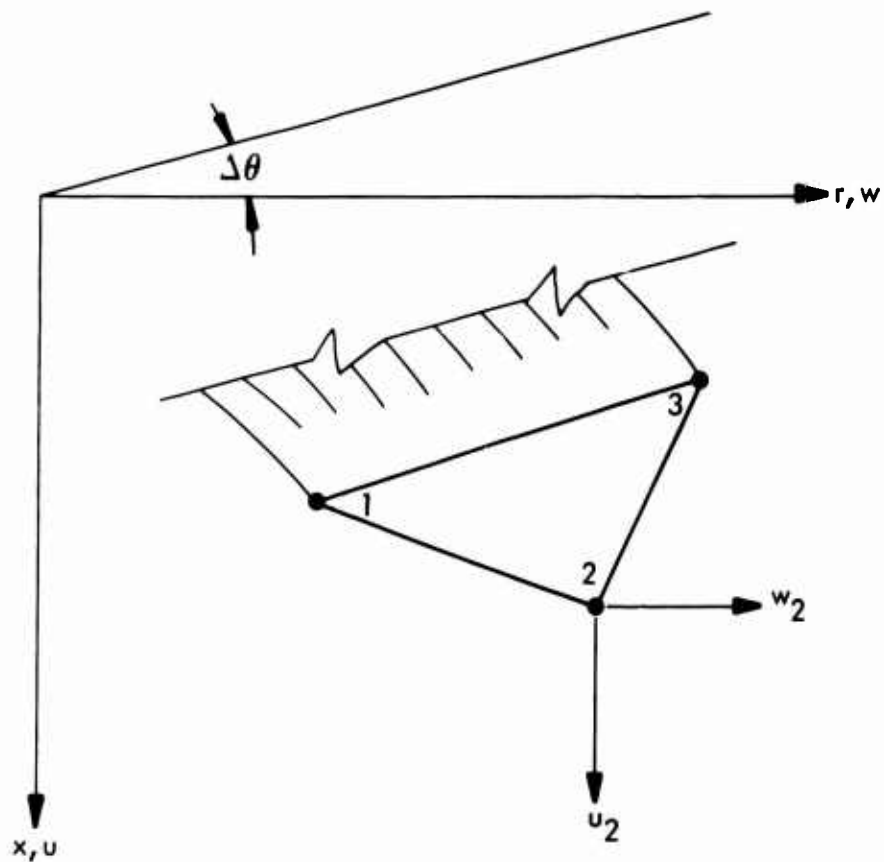


Figure E-1: AN AXISYMMETRIC RING ELEMENT OF
TRIANGULAR CROSS SECTION

The Stiffness Matrix

The assumed displacement functions must contain six independent degrees of freedom, since there are three nodal points in the element as shown in Figure E-1. Let the displacement functions be:

$$\begin{Bmatrix} \Delta u \\ \Delta w \end{Bmatrix} = \begin{bmatrix} x & r & 1 & 0 & 0 & 0 \\ 0 & 0 & 0 & x & r & 1 \end{bmatrix} \begin{Bmatrix} \Delta q_1 \\ \Delta q_2 \\ \Delta q_3 \\ \Delta q_4 \\ \Delta q_5 \\ \Delta q_6 \end{Bmatrix} \quad (E-1)$$

Note that according to these displacement functions the edges of the element are displaced as straight lines and, hence, compatibility of displacements is assured across element boundaries.

The incremental nodal point displacement components are expressed in terms of the incremental generalized coordinates.

$$\begin{Bmatrix} \Delta u_1 \\ \Delta u_2 \\ \Delta u_3 \\ \Delta w_1 \\ \Delta w_2 \\ \Delta w_3 \end{Bmatrix} = [A] \begin{Bmatrix} \Delta q_1 \\ \Delta q_2 \\ \Delta q_3 \\ \Delta q_4 \\ \Delta q_5 \\ \Delta q_6 \end{Bmatrix} \quad (E-2)$$

where

$$[A] = \left[\begin{array}{ccc|ccc} x_1 & r_1 & 1 & & & \\ x_2 & r_2 & 1 & & & 0 \\ x_3 & r_3 & 1 & & & \\ \hline & & & x_1 & r_1 & 1 \\ & & & x_2 & r_2 & 1 \\ & & & x_3 & r_3 & 1 \end{array} \right] \quad (E-3)$$

The incremental generalized coordinates are now expressed in terms of the incremental nodal point displacements.

$$\begin{Bmatrix} \Delta q_1 \\ \Delta q_2 \\ \Delta q_3 \\ \Delta q_4 \\ \Delta q_5 \\ \Delta q_6 \end{Bmatrix} = [A^{-1}] \begin{Bmatrix} \Delta u_1 \\ \Delta u_2 \\ \Delta u_3 \\ \Delta w_1 \\ \Delta w_2 \\ \Delta w_3 \end{Bmatrix} \quad (E-4)$$

where

$$[A^{-1}] = \frac{1}{2S_f} \left[\begin{array}{ccc|ccc} (r_2-r_3) & (r_3-r_1) & (r_1-r_2) & & & \\ (x_3-x_2) & (x_1-x_3) & (x_2-x_1) & & & \\ (x_2r_3-x_3r_2) & (x_3r_1-x_1r_3) & (x_1r_2-x_2r_1) & & & \\ \hline & & & (r_2-r_3) & (r_3-r_1) & (r_1-r_2) \\ & & & (x_3-x_2) & (x_1-x_3) & (x_2-x_1) \\ & & & (x_2r_3-x_3r_2) & (x_3r_1-x_1r_3) & (x_1r_2-x_2r_1) \end{array} \right] \quad (E-5)$$

S_f = Area of the triangle

$$= (1/2) [x_1 (r_2-r_3) + x_2(r_3-r_1) + x_3 (r_1-r_2)]$$

The incremental strains are related to the incremental generalized coordinates by the matrix $[B]$ in the following ($\{\Delta \epsilon\} = [B] \{\Delta q\}$)

$$\begin{Bmatrix} \Delta \epsilon_x \\ \Delta \epsilon_r \\ \Delta \gamma_{xr} \\ \Delta \epsilon_\theta \end{Bmatrix} = \begin{bmatrix} 1 & 0 & 0 & 0 & 0 & 0 \\ 0 & 0 & 0 & 0 & 1 & 0 \\ 0 & 1 & 0 & 1 & 0 & 0 \\ 0 & 0 & 0 & x/r & 1 & 1/r \end{bmatrix} \begin{Bmatrix} \Delta q_1 \\ \Delta q_2 \\ \Delta q_3 \\ \Delta q_4 \\ \Delta q_5 \\ \Delta q_6 \end{Bmatrix} \quad (E-6)$$

The elements of matrix $[B]$ in equations (E-6) are obtained by means of differentiation of equations (E-1).

The generalized coordinate stiffness matrix $[\bar{k}]$ is found by integrating over the volume S_f .

$$[\bar{k}] = \int_{vol.} [B]^T [D] [B] dV \quad (E-7)$$

where $dV = r d\theta dx dr$, $[B]$ is the matrix given by equation (E-6), and $[D]$ is the stress-strain matrix

$$[D] = \begin{bmatrix} K+(4/3)G & -QH_{11}^2 & K-(2/3)G & -QH_{11}H_{12} & K-(2/3)G & -QH_{11}H_{33} \\ & & -QH_{11}H_{22} & & & \\ K-(4/3)G & & -QH_{22}^2 & -QH_{12}H_{22} & K-(2/3)G & -QH_{22}H_{33} \\ & & & & & \\ \text{Symmetric} & & & G-QH_{12}^2 & & -QH_{12}H_{33} \\ & & & & K-(4/3)G & -QH_{33}^2 \end{bmatrix}$$

The matrix $[\bar{k}]$ may be written in the form:

$$[\bar{k}] = [k_{ij}] \quad (E-9)$$

where the elements of the (diagonally symmetric) $[k_{ij}]$ matrix for the case $\Delta\theta = 1$ radian are found as follows:

$$k_{11} = (K+(4/3)G - QH_{11}^2) I_1 \quad (E-10)$$

$$k_{12} = QH_{11}H_{12}I_1$$

$$k_{13} = 0 = k_{23} = k_{33} = k_{34} = k_{35} = k_{36}$$

$$k_{14} = (-QH_{11}H_{12}) I_1 + (K-(2/3)G - QH_{11}H_{33}) I_2$$

$$k_{15} = [2K-(4/3)G - QH_{11}(H_{22}+H_{33})] I_1$$

$$k_{16} = (K - 2G/3 - QH_{11}H_{33}) I_3$$

$$k_{22} = (G - QH_{12}^2) I_1$$

$$k_{24} = (G - QH_{12}^2) I_1 + (-QH_{12}H_{33}) I_2$$

$$k_{25} = [-QH_{12}(H_{22} + H_{33})] I_1$$

$$k_{26} = (-QH_{12}H_{33}) I_3$$

$$k_{44} = (G - QH_{12}^2) I_1 + (-2QH_{12}H_{33}) I_2 \\ + (K + 4G/3 - QH_{33}^2) I_4$$

$$k_{45} = [-QH_{12}(H_{22}+H_{33})] I_1 + \\ [2K + 2G/3 - QH_{33}(H_{22}+H_{33})] I_2$$

$$k_{46} = (-QH_{12}H_{33}) I_3 + (K + 4G/3 - QH_{33}^2) I_5$$

$$k_{55} = [2(2K+2G/3) - Q(H_{22}+H_{33})^2] I_1$$

$$k_{56} = [(2K+2G/3) - QH_{33} (H_{22}+H_{33})] I_3$$

$$k_{66} = [(K+4G/3) - QH_{33}^2] I_6$$

In the above equations the following have been used:

$$\begin{aligned} I_1 &= \iint_{\text{vol.}} (1) r dr dx \\ &= (1/6) [x_{31} (r_3^2 + r_3 r_1 + r_1^2) + \\ &\quad x_{12} (r_1^2 + r_1 r_2 + r_2^2) + \\ &\quad x_{23} (r_2^2 + r_2 r_3 + r_3^2)] \end{aligned} \quad (E-11)$$

$$\begin{aligned} I_2 &= \iint_{\text{vol.}} (x/r) r dr dx \\ &= (1/2) [(r_1 x_{31} - r_3 x_1) (x_3 + x_1) + \\ &\quad (r_2 x_{12} - r_1 x_2) (x_1 + x_2) + \\ &\quad (r_2 x_{23} - r_{23} x_2) (x_2 + x_3)] \\ &\quad + (1/3) [r_{31} (x_3^2 + x_3 x_1 + x_1^2) + \\ &\quad r_{12} (x_1^2 + x_1 x_2 + x_2^2) + \\ &\quad r_{23} (x_2^2 + x_2 x_3 + x_3^2)] \end{aligned}$$

$$\begin{aligned} I_3 &= \iint_{\text{vol.}} (1/r) r dr dx \\ &= (1/2) [x_{31} (r_3 + r_1) + x_{12} (r_1 + r_2) + x_{23} (r_2 + r_3)] \end{aligned}$$

$$\begin{aligned} I_4 &= \iint_{\text{vol.}} (x^2/r^2) r dr dx \\ &= (1/3r_m) [(r_1 x_{31} - r_3 x_1) (x_3^2 + x_3 x_1 + x_1^2) + \\ &\quad (r_2 x_{23} - r_{23} x_2) (x_2^2 + x_2 x_3 + x_3^2) + \\ &\quad (r_2 x_{12} - r_{12} x_2) (x_1^2 + x_1 x_2 + x_2^2)] \\ &\quad + (1/4r_m) [r_{31} (x_3 + x_1) (x_3^2 + x_1^2) + \end{aligned}$$

$$r_{23} (x_2 + x_3) (x_2^2 + x_3^2) + \\ r_{12} (x_1 + x_2) (x_1^2 + x_2^2)]$$

$$I_5 = I_2 / r_m$$

$$I_6 = I_3 / r_m$$

where $r_m = (r_1 + r_2 + r_3) / 3$

$$x_{ij} = x_i - x_j \quad \text{for } i = 1, 2, 3$$

$$r_{ij} = r_i - r_j \quad i = 1, 2, 3$$

Examples are:

$$x_{12} = x_1 - x_2$$

$$= -x_{21}$$

$$r_{23} = r_2 - r_3$$

$$= -r_{32}$$

Finally, the element stiffness matrix is found by carrying out a series of matrix operations:

$$[k] = [A^{-1}]^T [\bar{k}] [A^{-1}]$$

Where $[A^{-1}]$ is given by equation (E-5) and $[\bar{k}]$ is given by equations (E-9), (E-10), and (E-11).

The Mass Matrix

The Mass Matrix for the axisymmetric triangular element is developed from the following three conditions:

1. Conservation of mass,

$$m_1 + m_2 + m_3 = \int_V \rho dv$$

2. The static moment of mass about the r -axis,

$$m_1 r_1 + m_2 r_2 + m_3 r_3 = \int_V r \rho dv$$

3. The static moment of mass about the x-axis,

$$m_1 x_1 + m_2 x_2 + m_3 x_3 = \int_V x \rho \, dv$$

Performing the integration indicated above yields

$$m_1 + m_2 + m_3 = \rho l_1$$

$$m_1 r_1 + m_2 r_2 + m_3 r_3 = \rho l_1 r_m$$

$$m_1 x_1 + m_2 x_2 + m_3 x_3 = \rho l_1 x_m$$

where

$r_m = (1/3)(r_1 + r_2 + r_3)$ and $x_m = (1/3)(x_1 + x_2 + x_3)$ and l_1 is given in equations E-11.

The lumped masses, m_1 , m_2 and m_3 , are used in the calculations of the axisymmetric problems.

The Stress Computation

The stress increments are computed according to the following equation:

$$\{\Delta\sigma\} = [D] [B] [A^{-1}] \{\Delta u\} \quad (E-12)$$

where

$\{\Delta\sigma\}$ = The 4x1 matrix vector of stress increments

$$= \{\Delta\sigma_x, \Delta\sigma_r, \Delta\tau_{xr}, \Delta\sigma_\theta\}$$

$\{\Delta u\}$ = The 6x1 vector of incremental nodal displacements

$$= \{\Delta u_1, \Delta u_2, \Delta u_3, \Delta w_1, \Delta w_2, \Delta w_3\}$$

$[D]$ = The 4x4 matrix of the elastic-plastic stress-strain law of equation (E-8)

$[A^{-1}]$ = The 6x6 matrix given by equation (E-5)

$[B]$ = The 4x6 matrix given by equation (E-6)

Following the reasoning given in Appendix A for plane-strain elements, the stress increments are calculated at the centroid of the cross section. This is most effectively done by substituting $x = (1/3)(x_1 + x_2 + x_3)$ and $r = (1/3)(r_1 + r_2 + r_3)$ in the matrix $[B]$ of equation (E-6).

Having matrices $[D]$, $[B]$ and $[A^{-1}]$ properly defined for the element, the stress increments can be computed for a given $\{\Delta u\}$. Finally, the total current stress components are obtained by adding the stress increments to the corresponding stress components at the last time level.

PART II.

Verification of the Analysis Method

TABLE OF CONTENTS

PART II.

	PAGE
1.0 INTRODUCTION	125
1.1 Code Description	125
1.2 Code Verification Plan	125
1.3 Material Properties	126
2.0 COMPARISON WITH ANALYTICAL SOLUTIONS	127
2.1 Interaction of Plane Stress Waves with a Cylindrical Cavity	127
2.2 Interaction of Plane Stress Waves with a Thin-Walled Cylinder	128
2.3 Interaction of Plane Stress Waves with a Thick-Walled Cylinder	130
2.4 Conclusions	131
3.0 COMPARISON WITH FIELD TESTS	141
3.1 Hard Hat	142
3.2 Distant Plain 6	152
4.0 AXISYMMETRIC PROGRAM	153
4.1 Free Field Runs	153
4.2 Structure Region Verification	161
5.0 SUSPENSION SYSTEM TEST CASE	165
5.1 Problem Description	165
5.2 Results	170
5.3 Discussion	170

TABLE OF CONTENTS (Continued)
PART II.

	PAGE
6.0 DEBONDING AND SLIP TEST RUN	175
6.1 Pilot Program	175
6.2 "Cork Problem"	175
6.3 Results	177
7.0 COMPILATION OF MATERIAL PROPERTIES	187
7.1 Earth Media	187
7.2 Construction Materials	196
7.3 Isolation Materials (Backpacking)	202
7.4 Debonding & Slip	206
APPENDIX Energy Implications of Inter-Related Bulk and Shear Moduli	209

LIST OF ILLUSTRATIONS
PART II.

FIGURE	TITLE	PAGE
2-1	Overall Layout - Free-Field Idealization	132
2-2	Horizontal Section Idealization "A" (Thin Liner)	133
2-3	Comparison of Solutions for Unlined Cavity, $\theta = 45^\circ$	134
2-4	Comparison of Solutions for Unlined Cavity, $\theta = 90^\circ$	134
2-5	Comparison of Solutions for Unlined Cavity, $\theta = 0^\circ$	134
2-6	Horizontal Section Idealization "B" (Thin-Liner)	135
2-7	Comparison of Solutions as a Function of θ for an Unlined Cavity	136
2-8	Comparison of Solutions for Thin Liner, $\theta = 90^\circ$	137
2-9	Dispersion of Pulse with Depth in Finite Element Mesh	137
2-10	12 Element Idealization Section (Thick Liner)	138
2-11	24 Element Idealization Thick Lined Cavity	139
2-12	Comparison of Solutions for Thick Liner, $\theta = 90^\circ$	140
2-13	Comparison of Solutions for Thick Liner, $\theta = 90^\circ$	140
2-14	Comparison of Solutions for Thick Liner, $\theta = 90^\circ$	140
3-1	Test Site Layout	143
3-2	Overall Layout - Free-Field Idealization	145
3-3	Structure Region Idealization	146
3-4	Radial Displacement at 396 Ft.	148
3-5	Radial Velocity at 396 Ft.	148
3-6	Radial Stress at 396 Ft.	148
3-7	Radial Displacement at 505 Ft.	147
3-8	Radial Velocity at 505 Ft.	147
3-9	Computed Radial Stress at 505 Ft.	147

LIST OF ILLUSTRATIONS (Continued)

PART II.

FIGURE	TITLE	PAGE
4-1	Vertical Displacement, GRAN-M Low Overpressure, Free-Field Run	154
4-2	Horizontal Displacement, GRAN-M Low Overpressure, Free-Field Run	154
4-3	Vertical Particle Velocity, GRAN-M Low Overpressure, Free-Field Run	155
4-4	Horizontal Particle Velocity, GRAN-M Low Overpressure, Free-Field Run	155
4-5	Horizontal Stress, GRAN-M Low Overpressure, Free-Field Run	156
4-6	Vertical Displacement Lime-M, Low Overpressure, Free-Field Run	156
4-7	Horizontal Displacement, Lime-M, Low Overpressure Free-Field Run	157
4-8(a)	FEAT Results, Vertical Particle Velocity, Lime-M Low Overpressure, Free-Field Run	158
4-8(b)	ATI-AJA Results, Vertical Particle Velocity, Lime-M Low Overpressure, Free-Field Run	158
4-9(a)	FEAT Results, Horizontal Particle Velocity, Lime-M Low Overpressure, Free-Field Run	159
4-9(b)	ATI-AJA Results, Horizontal Particle Velocity, Lime-M Low Overpressure, Free-Field Run	159
4-10(a)	FEAT Results, Horizontal Stress, Lime-M, Low Overpressure, Free-Field Run	160
4-10(b)	ATI-AJA Results, Horizontal Stress, Lime-M, Low Overpressure, Free-Field Run	160
4-11	Vertical Displacement - Structure and Overlay Paths vs. Free-Field	162
4-12	Horizontal Displacement - Structure and Overlay Paths vs. Free-Field	162
4-13	Vertical Particle Velocity - Structure and Overlay Paths vs. Free-Field	163

LIST OF ILLUSTRATIONS (Continued)

PART II.

FIGURE	TITLE	PAGE
4-14	Horizontal Particle Velocity - Structure and Overlay Paths vs. Free-Field	163
4-15	Horizontal Stress - Overlay Paths vs. Free-Field	164
5-1	Suspension System Subroutine, Sample Problem Layout	166
5-2	Suspension System Check Case, Vertical Displacement of C.G.	168
5-3	Horizontal Displacement and Pitch Displacement of Suspended Contents	168
5-4	Vertical Acceleration of C.G.	171
5-5	Horizontal Acceleration of C.G.	171
5-6	Force in Suspension Element (1)	172
5-7	Force in Suspension Element (3)	172
5-8	Force in Suspension Element (4)	173
6-1	Pilot Program Model	176
6-2	Horizontal Displacement - Surface Node	178
6-3	Vertical Displacement - Surface Node	179
6-4	Horizontal Displacement - Mid-Point Node	180
6-5	Vertical Displacement - Mid-Point Node	181
6-6	Horizontal Displacement - Corner Node	182
6-7	Vertical Displacement - Corner Node	183
6-8	Horizontal Stress in Free-Field Element (4, 18)	184
6-9	Horizontal Stress in Structural Element (4, 1)	184
6-10	Vertical Stress in Free-Field Element (4, 18)	185
6-11	Vertical Stress in Structural Element (4, 1)	185
6-12	Shear Stress in Free-Field Element (4, 18)	186
6-13	Shear Stress in Structural Element (4, 1)	186

LIST OF ILLUSTRATIONS (Continued)

PART II.

FIGURE	TITLE	PAGE
7-1	Elastic - Plastic Yield Paths	193
7-2	Drucker - Prager Parameters for Rocks	194
7-3	Lateral - Axial Stress Plots for 1-D Strain	195
7-4	Compressive Strength versus Young's Modulus	200
7-5	Dynamic Increase Factor for Compressive Strength of Concrete	203
7-6	Dynamic Increase in Yield Stress for Steel	203
7-7	Typical Stress-Strain Curve for Polyurethane Foam	206
A-1	Typical Pressure - Volume Relation	209
A-2	Shear Modulus vs. Pressure for Bi-Linear Medium	210
A-3	Load History for Bi-Linear Medium	210
A-4	History of Shear Stress vs. Shear Strain (Bi-Linear Medium)	211
A-5	Load History for Compacting Medium	212
A-6	History of Shear Stress vs. Shear Strain (Compacting Medium)	212
A-7	Surface Deformation from Air Blast	213
A-8	Surface Node Forces	213

INTRODUCTION

1.1 Code Description

The analysis used to develop the FEAT code (Finite Element Analysis Technique) for structure-medium interaction problems, has been described in Part I of this Report. This code has been written in two basic versions--a plane strain and an axisymmetric form. Both versions use finite elements to model the free-field and the structural region. The medium can be represented as a non-linear, compacting, elastic-plastic material with specified tensile capability. Cylindrical buried structures of circular cross-section have been modeled in both horizontal and vertical sections by two-dimensional representations. In addition, the code considers debonding and slip at the structure-medium interface, and calculates the response of suspended contents in the structure.

1.2 Code Verification Plan

This volume presents comparisons of the results of computer code calculations with theoretical solutions and test data. Good correlation between the various solutions does not necessarily imply that the computer code will give realistic results for all types of structure-medium interaction problems but it does give confidence in the method.

The choice of test cases for method verification is limited by the fact that available analytical solutions are not realistic enough to fully test the capabilities of the numerical code, while the field and lab tests are very complex. That is, analytical solutions exist for simple material representations and loading conditions only, while the test data are for real media, with loading conditions and material properties poorly defined. A verification program has been designed, extending from simulation of simple analyses to complex tests which gives confidence in the ability of this computer code to give realistic results for soil-structure interaction problems.

Prior to this study, the codes (plane strain and axisymmetric) were checked against analytic solutions for elastic wave propagation in homogeneous media (Ref.15). The results of this check were very satisfactory and verified that all the equations (including boundary and initial conditions) were correctly derived and programmed. They also provided insight into the degree of symmetry, the roundoff error, and dispersion effects that could be expected for the particular idealizations used.

For the structure-medium interaction code, it was necessary to verify the structure modeling concepts of the code. Consequently, for the plane strain version of the code a series of analytic solutions were used for an elastic wave impinging on a circular cavity (unlined and lined) (Section 2.0). In addition, two test cases have been chosen to test the code (Section 3.0). Both cases are for circular cylinders, the first was a buried nuclear shot (Hard Hat) and the second, a high explosive surface burst. Details of the structural idealization, the material properties, and load pulse, and a detailed comparison of computed data with the test results for the Hard Hat Test are presented in a classified appendix to Volume II of this report.

A fundamental inconsistency in currently used material representations was discovered during attempts to execute the high explosive and buried nuclear shot cases. A large effort was expended on these calculations and in the diagnosis of the difficulty. Because of this and due to the inconclusiveness which now surrounds the material property question, the calculations for the high explosive case were terminated. The inconsistency of this representation is discussed in the Appendix.

Analytic solutions were not available for comparison with the axisymmetric (vertical cross-section) version of the code. A test was derived to check the internal consistency of the program (Section 4.0). All structural elements were given the properties of the surrounding medium, and the boundary loading and air overpressure of a typical surface burst from a nuclear explosion were applied. This procedure essentially reduced the problem to a free-field wave problem, whose solution was known.

Finally, sample problems have been solved to demonstrate the capability of the suspension system routine (Section 5.0) and to show results for a debonding and slip problem (Section 6.0).

1.3 Material Properties

Material properties for a large number of rock types were compiled and are presented in Section 7.0. Evaluation of these data for parameters required by digital computer analysis is illustrated. Properties of construction materials including backpacking are also given as well as estimates of friction factors between construction materials and earth media. Section 7.0 provides reference material only. The properties used for verification and design matrix computation are described in their respective sections.

II

COMPARISON WITH ANALYTICAL SOLUTIONS

A series of three cases was chosen to test the capability of the numerical method to reproduce results of analytical solutions to the wave-cavity interaction problem. All analytical cases dealt with plane elastic waves impinging on a cylindrical cavity. In one case the cavity was unlined, in the next it had a thin liner (thickness to radius ratio = 0.1) and finally it had a thick liner (thickness to radius ratio = 0.25). It was felt that if the interaction could be modeled correctly for an elastic wave, then confidence could be placed in the results for a plastic wave.

2.1 Interaction of Plane Stress Waves With A Cylindrical Cavity

Paul and Robinson (Ref.16) obtained an analytical solution to the interaction of plane dilational waves with a cylindrical cavity buried in an infinite, elastic, isotropic and homogeneous medium. The wave travels in a direction perpendicular to the axis of the cavity. The problem is a plane strain one.

The same problem was solved by the finite element method by using the plane strain program. A relatively crude finite element model (idealization A) was used as shown in Figures 2-1 and 2-2. The cavity boundary was approximated by twelve beam elements. These beam-elements were assigned the properties of the medium. Axial stresses in the beams were monitored and compared with the corresponding hoop stresses in the analytic solution. The dimensions of the model and the material properties used are as follows:

$$E = 2.5 \times 10^6 \text{ psi}$$

$$\rho = 200 \text{ lbs/ft}^3$$

$$\nu = 0.25$$

$$c_p = 100"/\text{msec}$$

$$\text{Radius of cavity} = 10 \text{ ft.}$$

$$\text{Element size} = 5' \times 5' \text{ (free field)}$$

$$\begin{array}{l} \text{Integration time} = \\ \text{step} \quad .25 \text{ msec} \end{array}$$

$$\begin{aligned}
 \text{Time of rise of} \\
 \text{pulse} &= 6 \text{ msec} = 5 \text{ radius transit times} \\
 &= 24 \text{ integration time steps}
 \end{aligned}$$

The input load was a stress pulse as shown in Figure 2-3. It was designed to provide both the transient and the steady state solution. The latter is equivalent to a static solution, as far as stresses are concerned. FEAT results are shown in Figures 2-3 through 2-5 along with corresponding analytic results.

The first results were compared at $\theta = 45^\circ$, and as Figure 2-3 shows, the comparison was excellent. Comparisons were also made for $\theta = 90^\circ$ and 0° and these are shown in Figures 2-4 and 2-5. It is clear that the results here are less satisfactory than at $\theta = 45^\circ$, particularly at $\theta = 90^\circ$ where FEAT under-estimates the peak value of the stress by about 16%. The orientation of the beam elements of Idealization A with respect to the incident wave front was suspected to be the major cause of this error. Consequently, another cavity idealization (B) was made as shown in Figures 2-1 and 2-6, with the "0°" beam element oriented parallel to the wave front. Peak stresses as a function of θ for both idealizations are presented in Figure 2-7, where it can be seen that no significant changes in the results have been made.

The accuracy of the results discussed above is governed primarily by the ability of the triangular elements of Figures 2-2 and 2-6 to represent the stress state around the cavity. In both cases these elements are deficient, since they are of relatively large size, especially normal to the cavity surface, and make use of a constant stress state in each element. Improved accuracy can be obtained with a finer idealization of the same basic form. However, still more improvement, and, in fact, very accurate problem solutions, can be obtained with a local structure-centered finite element mesh, using trapezoidal, linear stress, elements near the structure. Such a mesh is shown in Figures 2-10 and 2-11. It is the latter type of idealization which has been adopted for the final codes of the FEAT system.

2.2 Interaction of Plane Stress Waves With a Thin-Walled Cylinder

Garnet, Pascal, Isakson, and Pifko (Ref. 17) have obtained an analytic solution to the interaction of plane stress waves with a thin-walled cylinder buried in an isotropic, homogeneous and elastic medium. In the problem the wave travels perpendicular to the axis of the cylinder. The problem is therefore treated as one of plane strain.

The analytic solution was obtained by constructing a train of incident pulses from steady-state components, where each pulse represented the time history of the transient stress in the incident wave. One of the cases analyzed was an approximation of a concrete liner with a thickness-to-radius ratio of 0.1 embedded in porous sandstone and subjected to a plane stress wave with a triangular wave form. The incident stress time history and the time history of the hoop stress on the inner surface of the liner at $\theta = 90^\circ$ are shown in Figure 2-8.

To solve the problem by using the FEAT plane strain code, the structure-medium system was modeled by the idealization shown in Figures 2-1 and 2-6. For this case the properties used were the same as those used for the analytical solution.

The dimensions and material properties used are as follows:

	<u>Medium</u>	<u>Liner</u>
$E =$	$3.0 \times 10^6 \text{ psi}$	$2.5 \times 10^6 \text{ psi}$
$\rho =$	143 lbs/ft^3	145 lbs/ft^3
$\nu =$	0.20	0.20
$c_p =$	$124''/\text{msec}$	$113''/\text{msec}$
Element Size	$25'' \times 25'' \text{ (free field)}$	$25'' \text{ long (beam)}$

Radius of cavity = $50''$

Integration Time Step = 0.085 msec

Time of rise of pulse = $0.42 \text{ msec} = 1 \text{ Radius Transit Time}$

$= 5 \text{ Integration Time Steps}$

Results are presented in Figure 2-8 for the stress time history at $\theta = 90^\circ$, the point of maximum peak stress. The agreement is very good, but low by about 7%, with the maximum displaced in time by about two-thirds of a radius transit time. The oscillations displayed in the FEAT solution can be directly traced to the discretization of the problem by the finite elements.

The differences between the analytical solution and the solution obtained from the FEAT program can be attributed to dispersion - a phenomenon which is characteristic of the idealization process. Low frequency, long wavelength disturbances travel at approximately the group velocity in the continuum, but high frequency, short wavelength disturbances travel at reduced velocities. Because of this, the shape of the propagating disturbance changes in time and space.

The change in the shape of the stress time history in a FEAT solution relative to the corresponding time history of the incident stress is illustrated in Figure 2-9 for the case of a triangular stress pulse propagating through a homogeneous medium. Near the surface the FEAT solution closely approximates the incident stress except for the presence of high frequency oscillations. At greater depth the peak stress is reduced in magnitude and delayed in time relative to the incident stress.

In the FEAT analysis of the thin-walled cylinder problem, the cylinder was positioned far enough below the surface of the medium to permit the stresses to attain their steady state values before they were influenced by reflected stress waves. To satisfy this condition, the cylinder was placed at a position which was approximately ten radii below the surface. At this depth, the cylinder was exposed to a disturbance whose peak value was reduced in magnitude and delayed in time with respect to the disturbance considered in the analytical solution. This explains in part why the response obtained from the FEAT program is also reduced in magnitude and delayed in time with respect to the analytical solution.

2.3 Interaction of Plane Stress Waves With A Thick-Walled Cylinder

Paul, Robinson, and Ali-Akbarian (Ref. 18) have obtained analytical solutions to the interaction of plane stress waves with a thick cylinder embedded in an infinite, elastic, isotropic and homogeneous medium. The problem was solved by the same technique as described in Section 2.1. In essence, the thick liner of this plane strain problem was treated as a second medium in which waves propagate.

The analytic solution utilized superposition of cylindrical diverging and converging waves with the incident plane wave in such a way that the boundary conditions were satisfied at the interface between the two materials and at the free surface of the cavity. Solutions to the resulting integral equations were then calculated to obtain time histories of hoop stress in the liner and in the medium, at an angle of 90° from the crown. The incident plane wave was in the form of a ramp with a rise time equal to five times the transit time for the outer radius of the liner.

The idealizations used for this problem are shown in Figures 2-10 and 2-11. The dimensions and material properties used are as follows:

	<u>Medium</u>	<u>Liner</u>
$E =$	$3.0 \times 10^6 \text{ psi}$	832,000 psi
$\rho =$	143 lbs/cu. ft.	123 lbs/cu. ft.
$\nu =$	0.25	0.185
$c_p =$	130"/sec	77"/msec

Internal Radius = 40"

Liner Thickness = 10"

Time of rise of pulse = 1.925 msec = 5 Radius Transit Times

	<u>Medium</u>	<u>Liner</u>
<u>12 Element Liner</u>		
Element Size	25" x 25"	25" x 10"
Integration Time Step	.05 msec	.05 msec
<u>24 Element Liner</u>		
Element Size	50" x 50"	12-1/2" x 10"
Integration Time Step	.05 msec	.05 msec

The 24-element model shown in Figure 2-11 is a considerably more sophisticated model than the 12 element model, since it was developed to handle structures with and without backpacking. In addition to improvements in accuracy in the structure expected from the finer idealization in the structural region, better accuracy would be expected in the medium at the medium-liner interface. This is due to the use of trapezoidal elements adjacent to the liner allowing a linear strain across their thickness, as opposed to the constant strain triangular elements used for the medium adjacent to the 12 element liner.

The results are shown in Figures 2-12 through 2-14 for stress at $\theta = 90^\circ$ at the liner inner surface, liner outer surface, and medium inner surface. The accuracy obtained with the 12 element model is good, being low by about 8% for the peak stresses at the liner-medium interface, and 14% at the inner surface of the liner. The 24 element model gave excellent results.

2.4 Conclusions

Comparisons were made between analytic solutions and FEAT computations for three different problems involving the interaction of plane waves and cylindrical cavities in elastic media. The first problem considered an unlined cavity. The quality of the comparison for this case was mixed. At the 45° point excellent agreement was achieved while for the 0° and 90° points the FEAT results deviate from the analytic solution. It is possible that this deviation is a result of the discretization used, but no definite conclusion has been reached on this problem. The other two problems considered lined cavities; one used beam elements to represent a thin layer and the other used trapezoidal elements to represent a thick liner. Data for comparison were available only at the 90° point in both cases. For both problems, FEAT results showed excellent correlation with the analytic solution. For the thick liner, a more detailed model improved results slightly.

The comparative analysis effort shows that for plane wave interaction with cylindrical cavity, the FEAT code can compute accurate results. Similar capability for a variety of free field problems had been demonstrated previously as described in Reference 15.

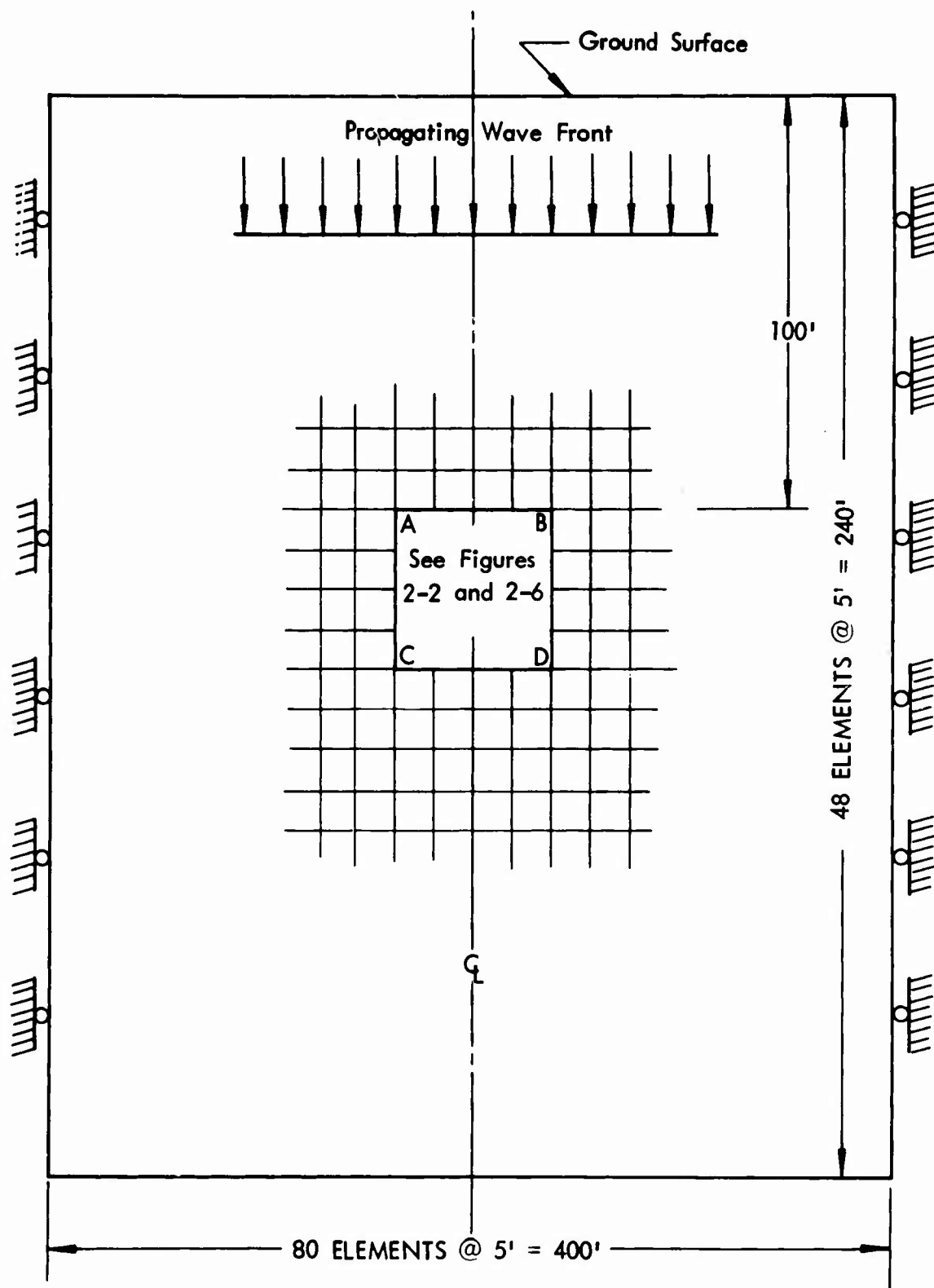


Figure 2-1: OVERALL LAYOUT - FREE-FIELD IDEALIZATION

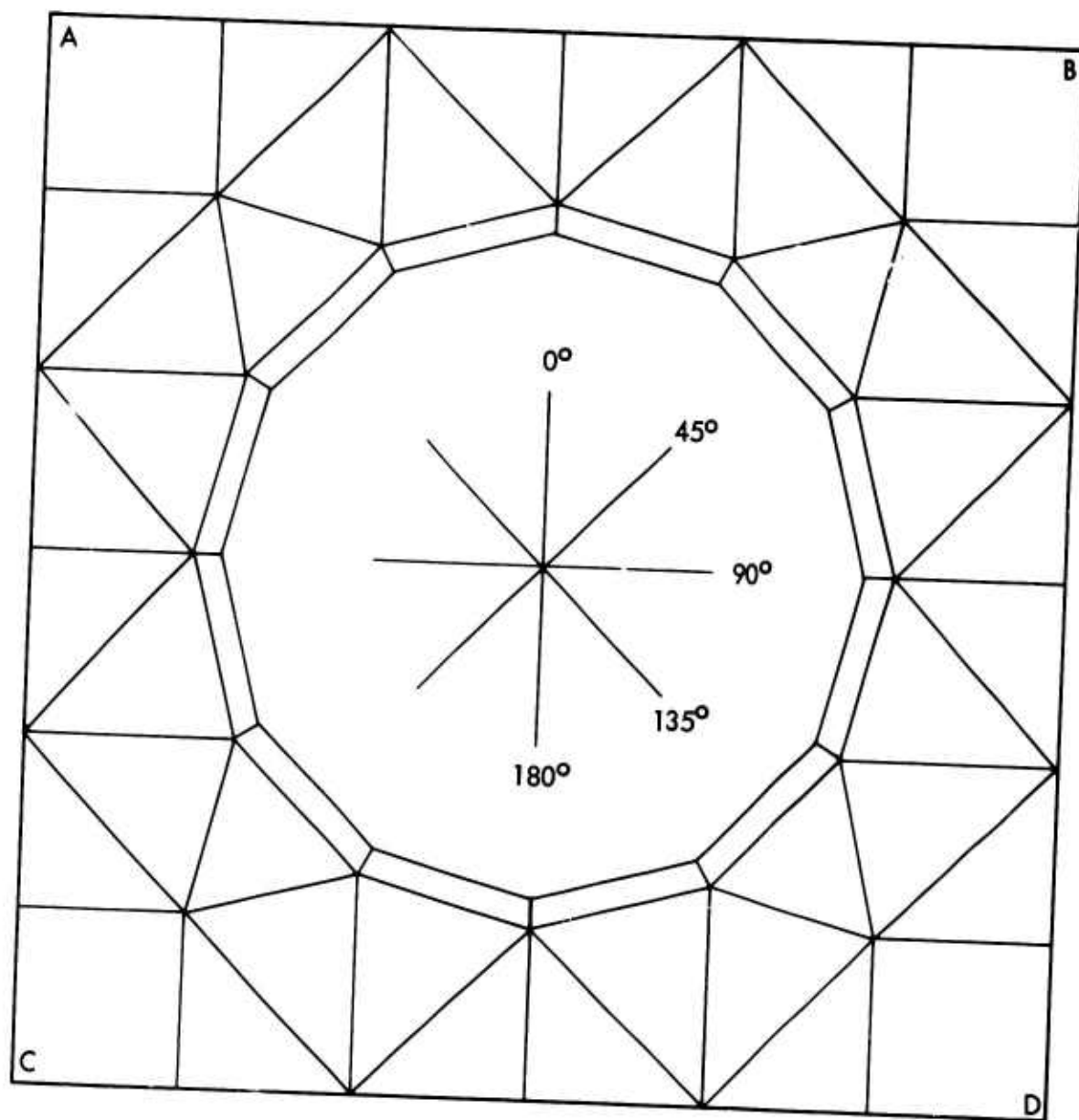


Figure 2-2: HORIZONTAL SECTION IDEALIZATION "A" (THIN LINER)

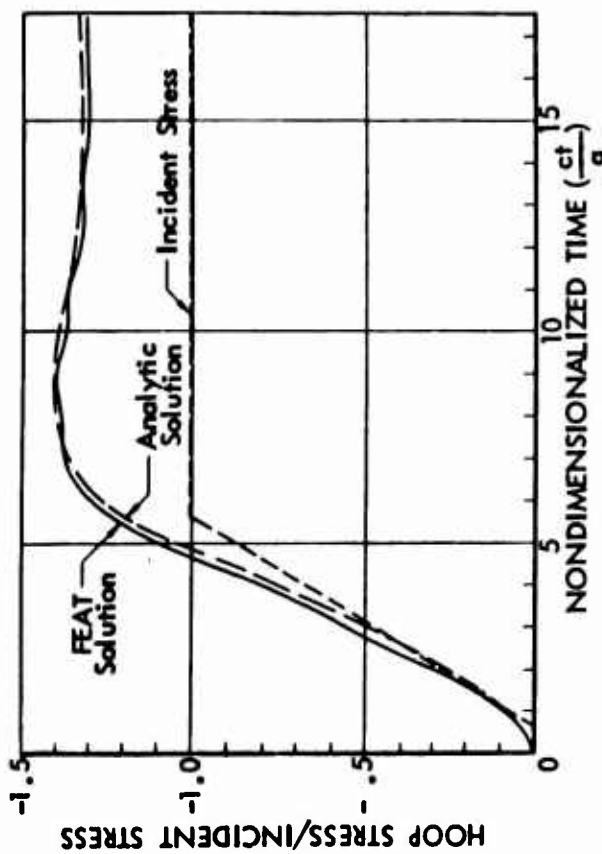


Figure 2-3: COMPARISON OF SOLUTIONS FOR UNLINED CAVITY, $\theta = 45^\circ$

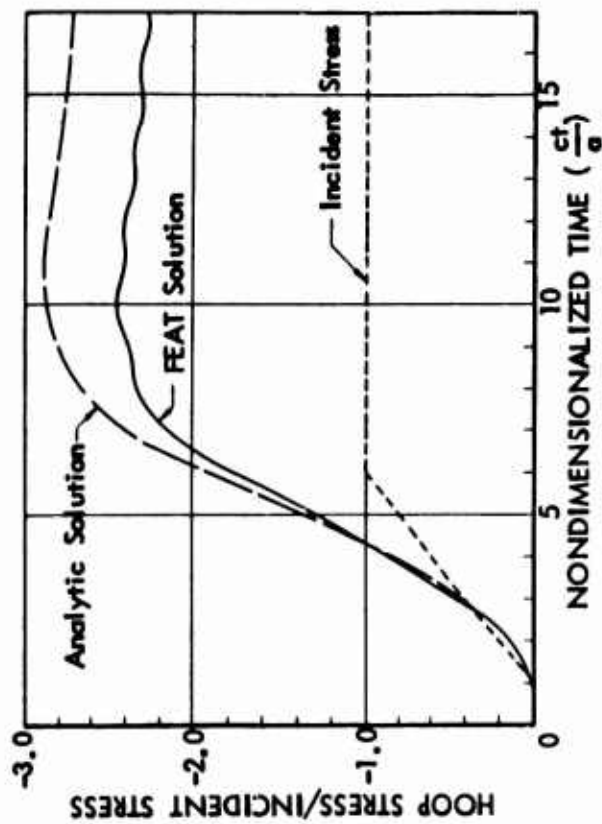


Figure 2-4: COMPARISON OF SOLUTIONS FOR UNLINED CAVITY, $\theta = 90^\circ$

Note:
 c is the Dilatational Wave Velocity
 t is Time
 a is the Cavity Radius

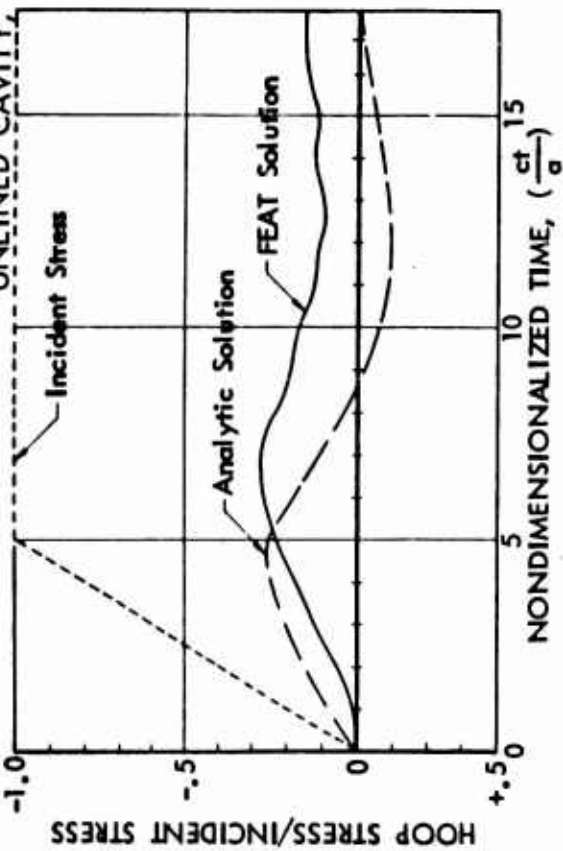


Figure 2-5: COMPARISON OF SOLUTIONS FOR UNLINED CAVITY, $\theta = 0^\circ$

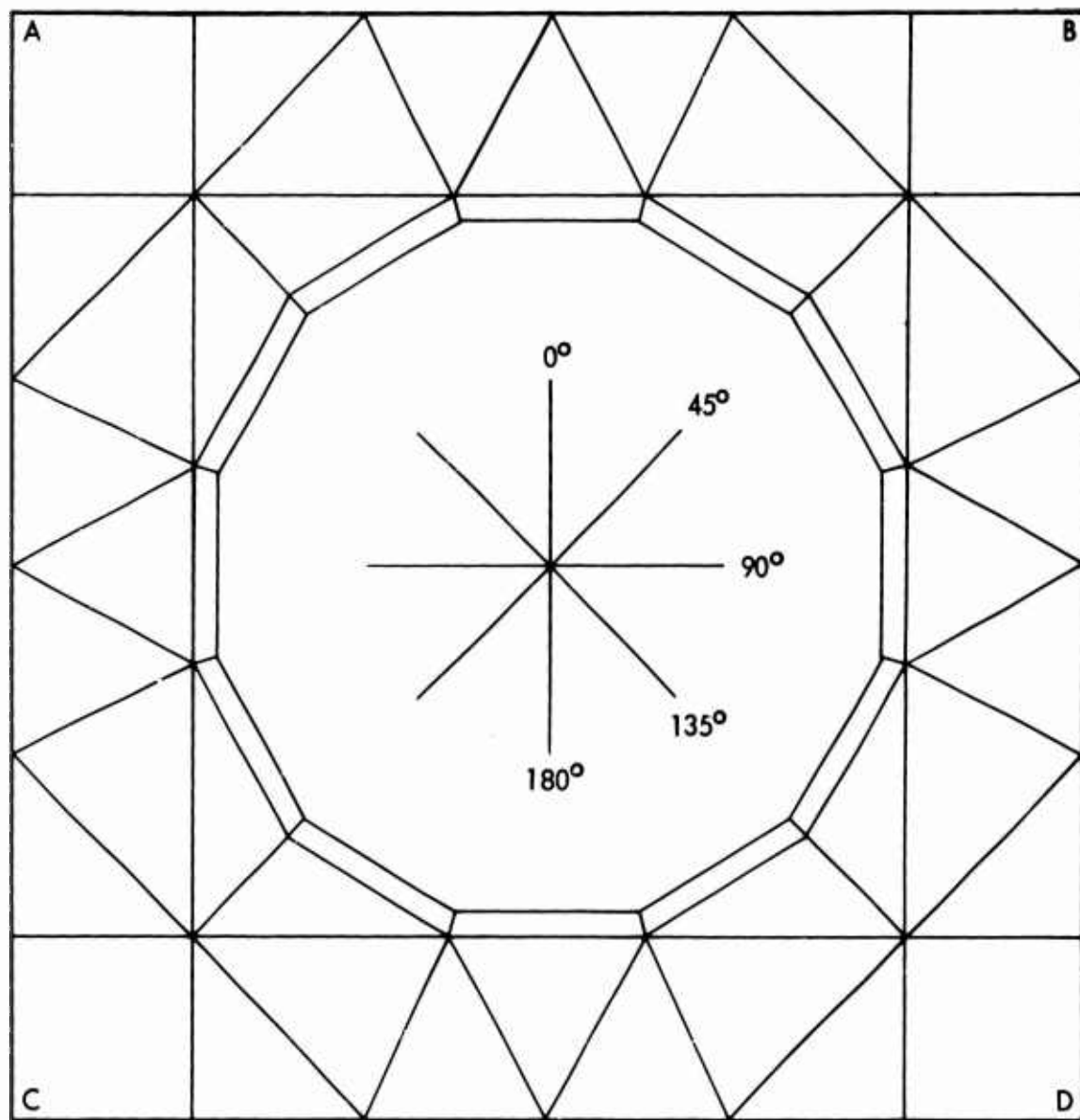


Figure 2-6: HORIZONTAL SECTION IDEALIZATION "B" (THIN LINER)

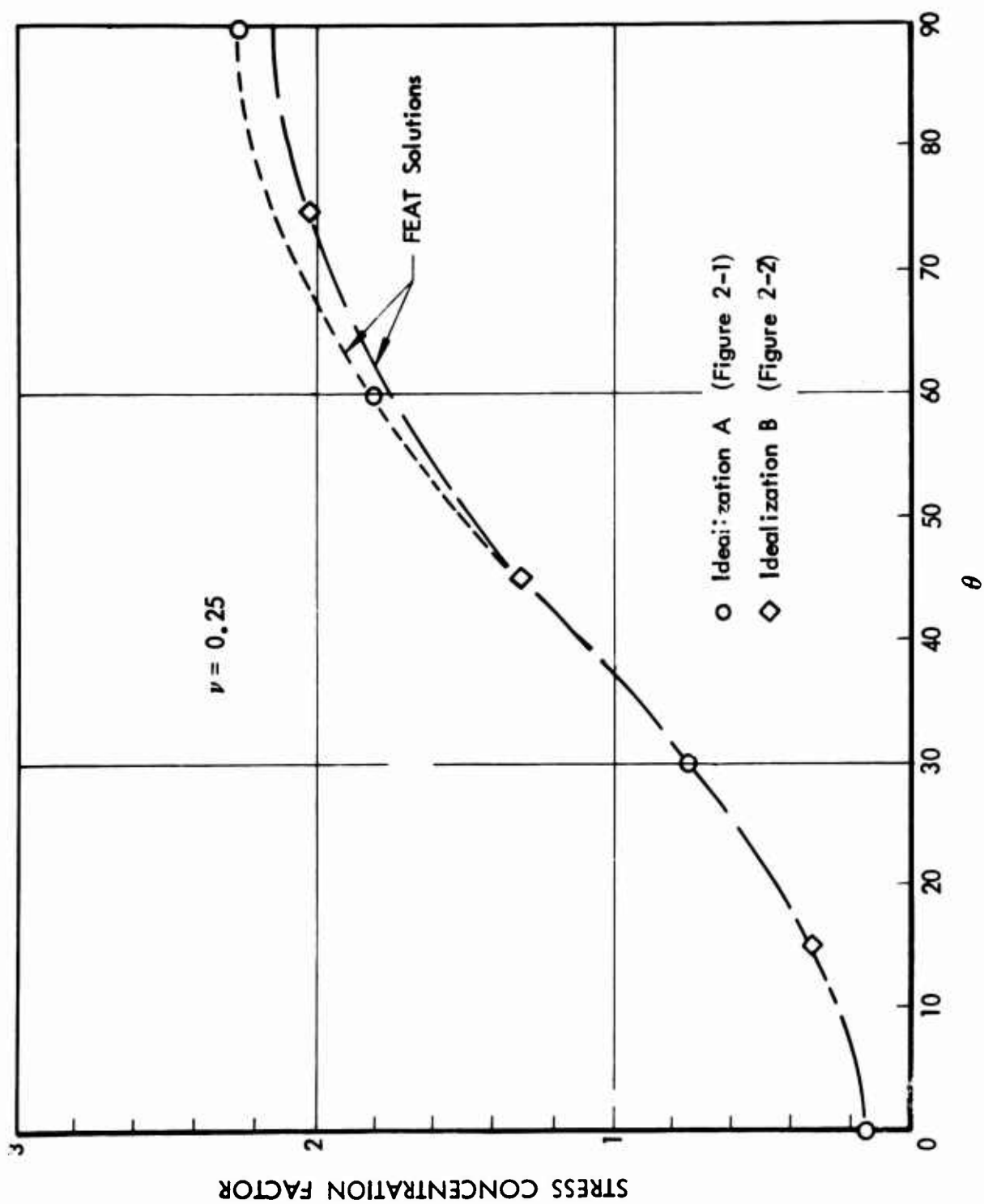


Figure 2-7: COMPARISON OF SOLUTIONS AS A FUNCTION OF θ FOR AN UNLINED CAVITY

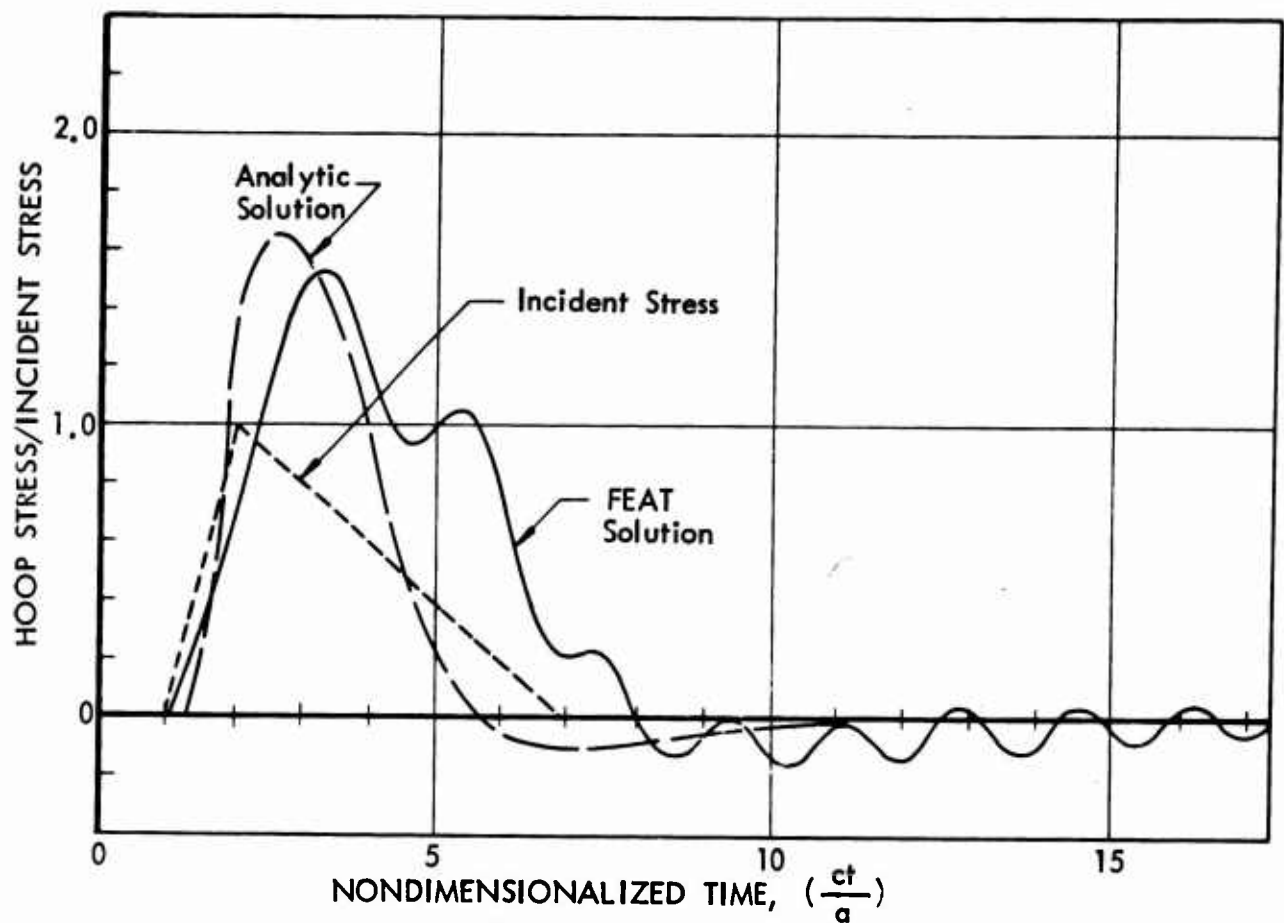


Figure 2-8: COMPARISON OF SOLUTIONS FOR THIN LINER, $\theta = 90^\circ$

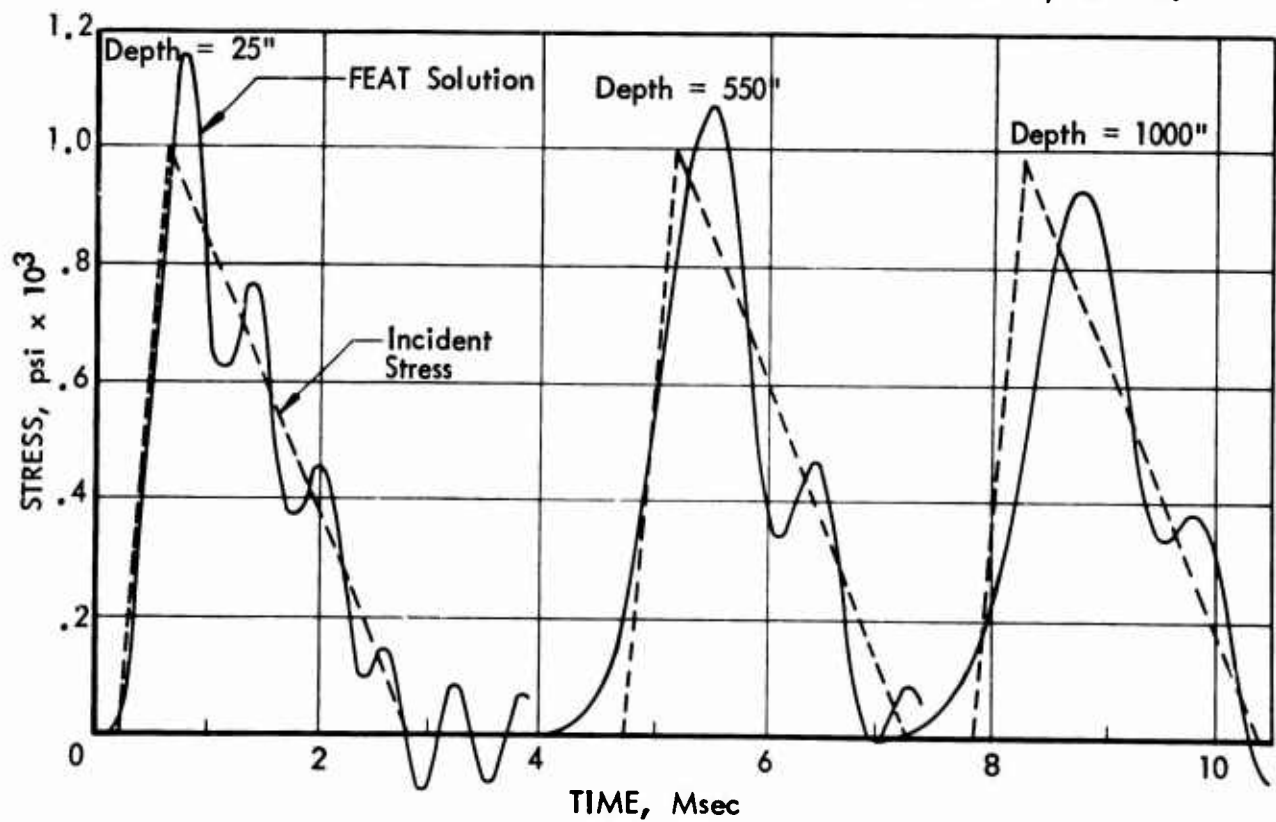


Figure 2-9: DISPERSION OF PULSE WITH DEPTH IN FINITE ELEMENT MESH

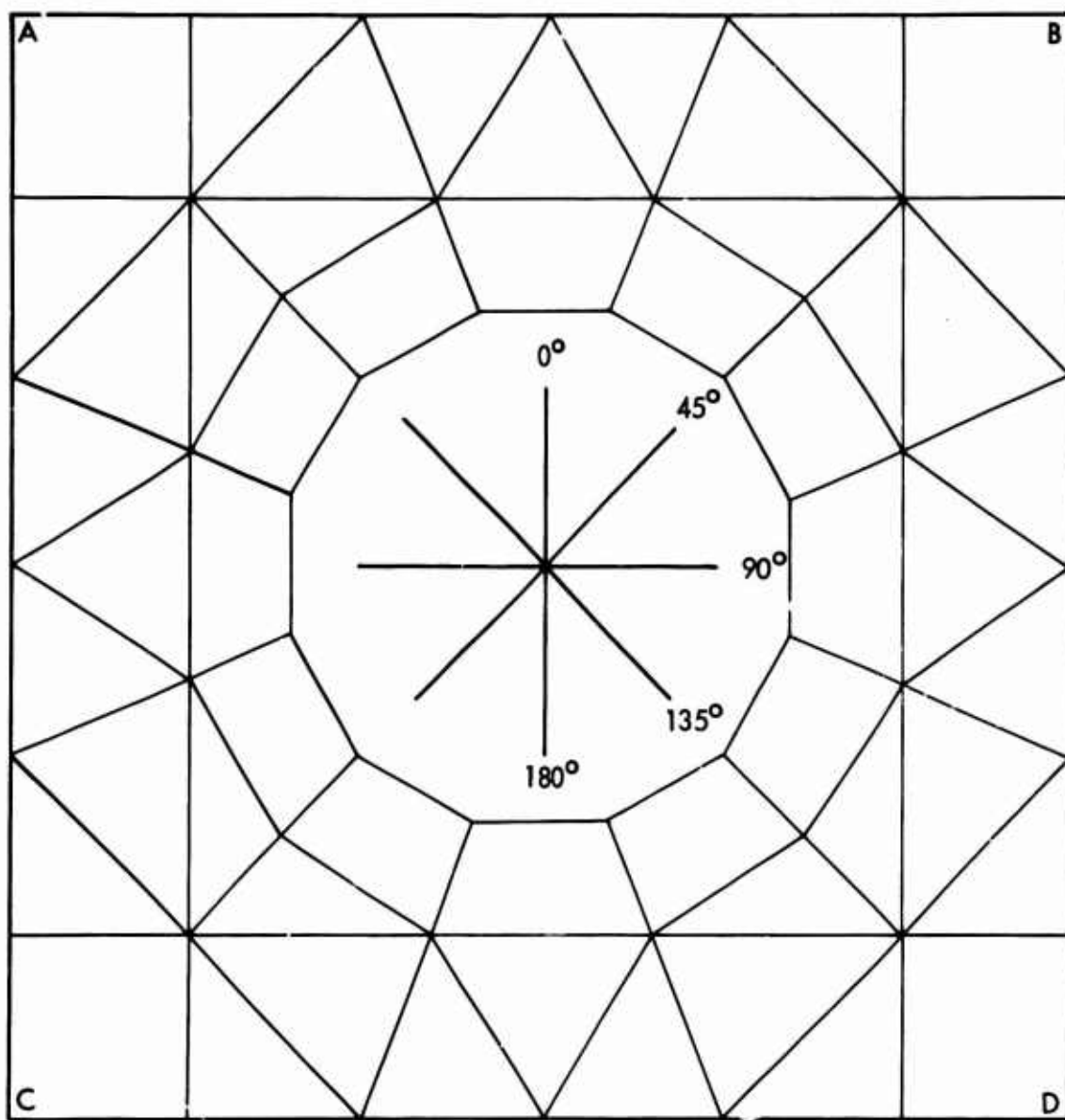


Figure 2-10: 12 ELEMENT IDEALIZATION SECTION (THICK LINER)

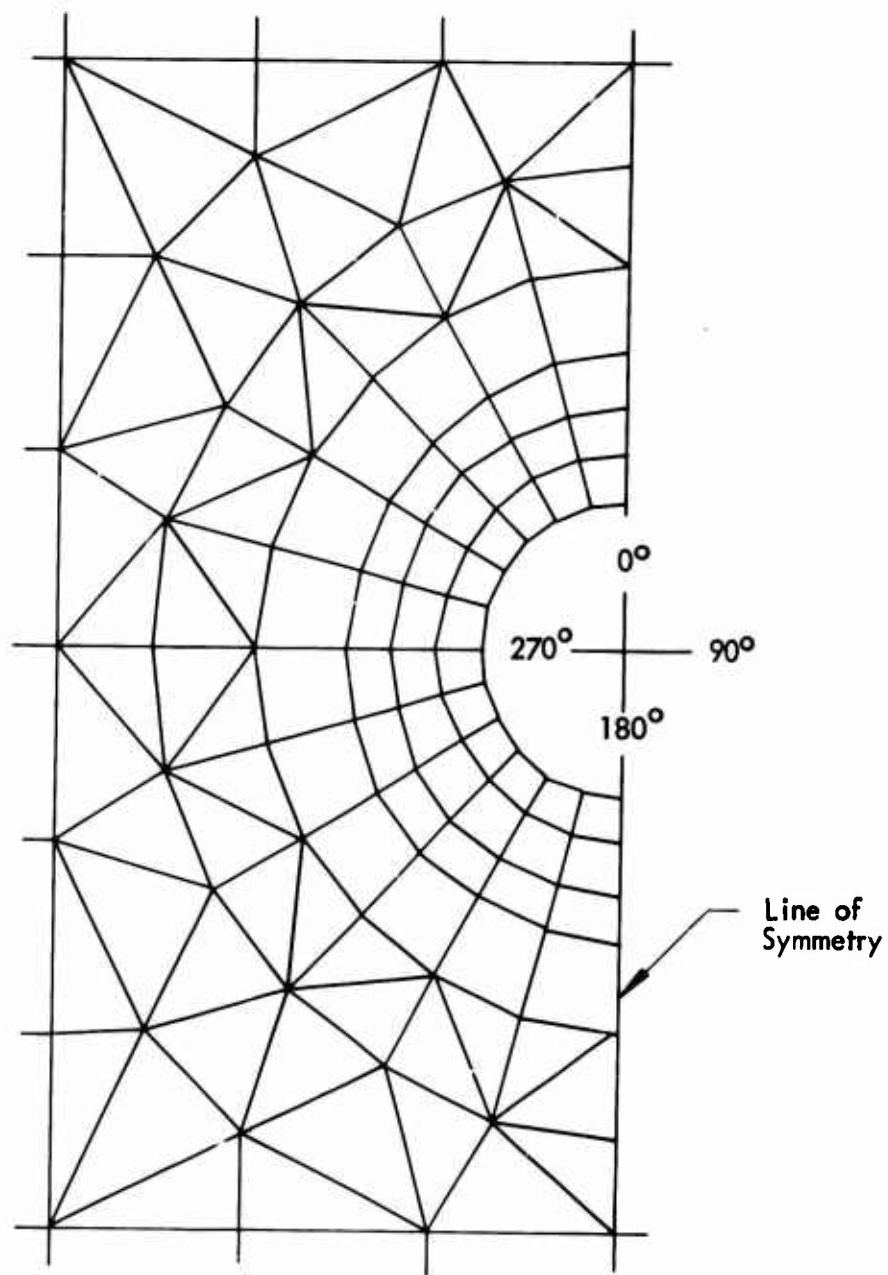


Figure 2-11: 24 ELEMENT IDEALIZATION THICK LINED CAVITY

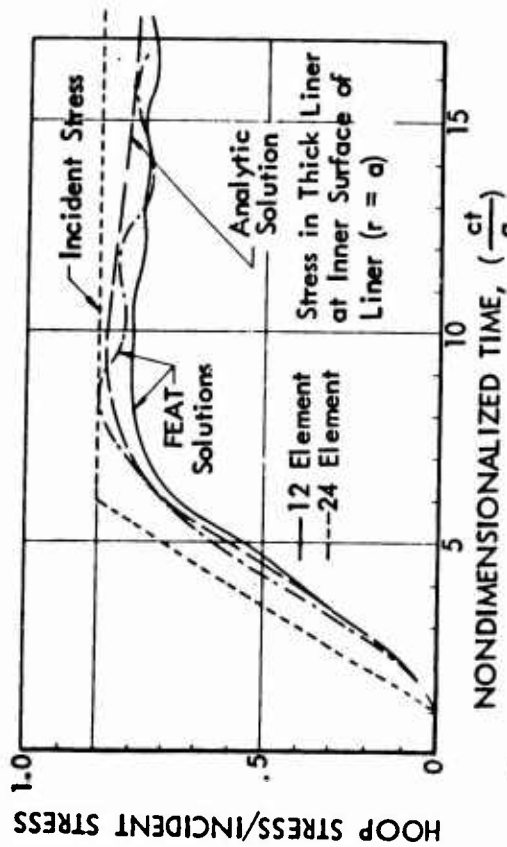


Figure 2-12: COMPARISON OF SOLUTIONS FOR THICK LINER, $\theta = 90^\circ$

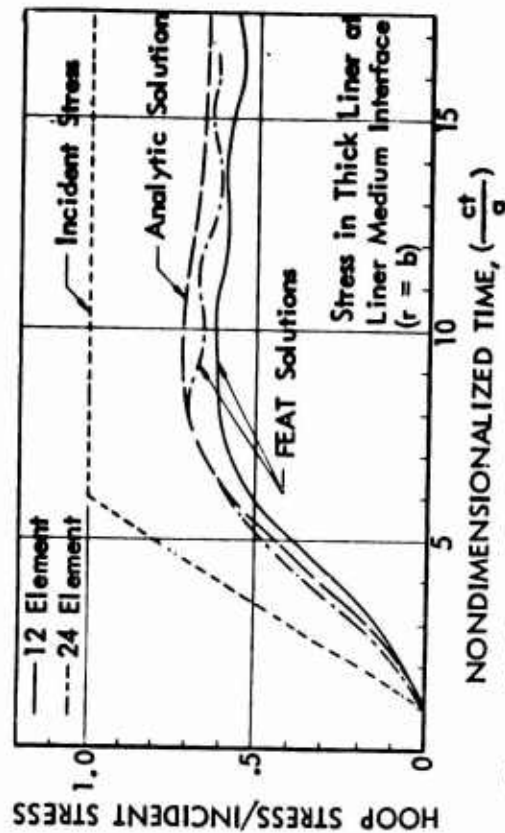


Figure 2-13: COMPARISON OF SOLUTIONS FOR THICK LINER, $\theta = 90^\circ$

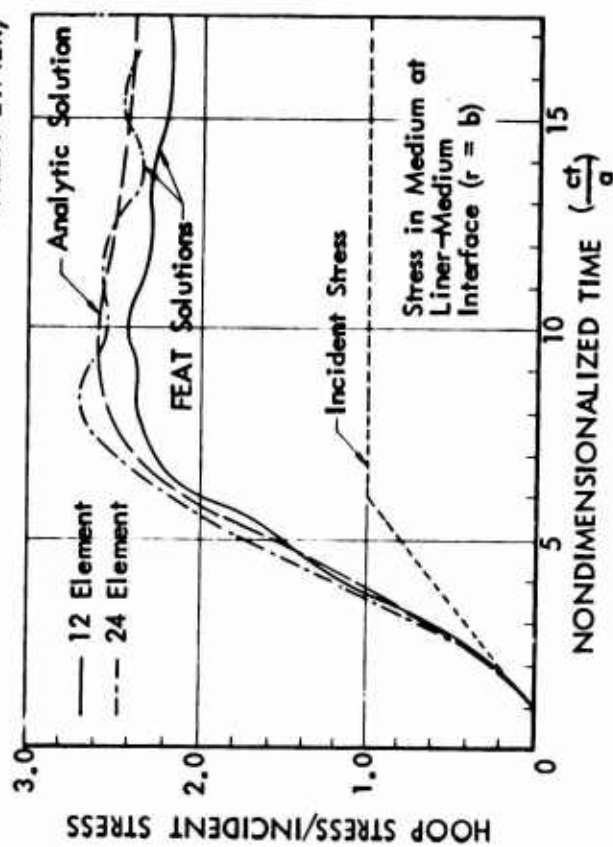


Figure 2-14: COMPARISON OF SOLUTIONS FOR THICK LINER, $\theta = 90^\circ$

III

COMPARISON WITH FIELD TESTS

In Section 2.0, the validity of the analysis using the plane strain FEAT code was demonstrated by comparing results obtained from this code with available analytic solutions. In this section the validity of the code solutions is further demonstrated by comparing results obtained with available experimental data. Two field tests were chosen for these comparisons. The selection of these tests was based on the quality and availability of test data and on the suitability of the test for comparison purposes, i.e., the type of structure, medium, and loading.

The two field tests were Hard Hat and Distant Plain 6. In the Hard Hat test a group of lined tunnels were subjected to stress waves of various intensities generated by an underground nuclear explosion in granite. In the Distant Plain 6 test a reinforced concrete cylinder buried in a layered medium was subjected to a surface explosion of TNT.

For each test case a finite element model was prepared representing the structure, the surrounding media, and the boundary conditions. Appropriate input data were derived from information contained in the test reports, and output data were reduced for comparison at points in the structures and the medium for which test data were available. The calculated results were compared with the test data and discussed in the following subsections.

In Section 2.0 it was shown that the finite element method predicts motions and transient stresses accurately when the problem is well defined. In the field tests, however, the definition of the properties of the media, the loading conditions and the test responses, were limited both in quality and quantity.

Due to the secret classification of the Hard Hat structural response results, it has been necessary to present these comparisons as a separate classified appendix to Volume II, but a description of the test and analysis model are presented in this section, together with some free-field results and an unclassified summary of the structural responses.

Each of the verification tests included non-linearly elastic, plastic, compacting material model. The code simulation of these materials was based upon a bulk modulus which was a function of hydrostatic pressure, and a shear modulus related to the bulk modulus by a constant Poisson's ratio. Such a simulation has widespread application in existing codes. Initial FEAT code runs based upon these properties were observed to produce erratic motions after a large number of time steps. The bases for the establishment of the elastic moduli were re-examined

and it was conclusively demonstrated that if the shear modulus is a function of hydrostatic pressure or dilational strain, alone, analytic calculations will always be potentially unstable. This condition exists when Poisson's ratio is held constant and bulk modulus is a function of pressure. This observation, based upon strain energy in an element as a function of time, is discussed in detail in the Appendix. It is applicable to any code investigating two-dimensional wave propagation in the elastic region.

3.1 Hard Hat

Hard Hat was an underground nuclear test conducted in granite at the Nevada Test Site to determine the response characteristics of the free field and a variety of tunnel linings. A plane strain FEAT code analysis of a specific tunnel section has been performed to show the applicability of the FEAT code to determine the response of cylindrical structures (with backpacking) to direct induced blast loads in rock.

3.1.1 Physical Problem

The test site layout is shown in Figure 3-1. The free-field stresses and motions were measured and are reported in Reference (19). Particle velocities of the structure wall (liner) and stresses at the interface of the structure and the backpacking were also measured. Specific details of the tunnel geometry, range from ground zero, materials used, etc., are presented in an appendix to Volume II of this Report. The properties of the rock at the test site were determined by Lawrence Radiation Laboratory (LRL) and are reported in References (20 & 21). The Hard Hat experiment test reports point out that the reported granite properties may vary by plus or minus 40%. In addition the material in situ experiences similar local variations. Therefore, correlation between calculated and test data was not expected to be as precise as for analytic solutions for which the medium is accurately described.

3.1.2 Mathematical Model

The three-dimensional Hard Hat test was idealized, for the FEAT code analysis, by using a two-dimensional plane strain theory. In addition, the solution was assumed to have polar symmetry about the burst point. As a consequence of the plane strain model the spherical wave radiating from the point source is represented by a cylindrical wave radiating from a line source.

The influence of other structures in the vicinity of the particular one under consideration was assumed negligible. Hence, only a single cylindrical structure was modeled for this analysis.

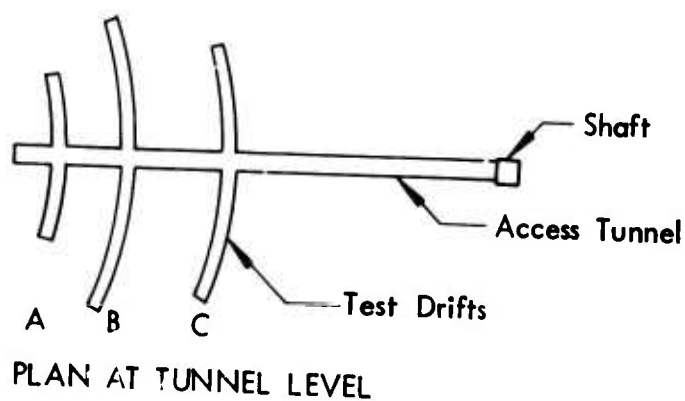
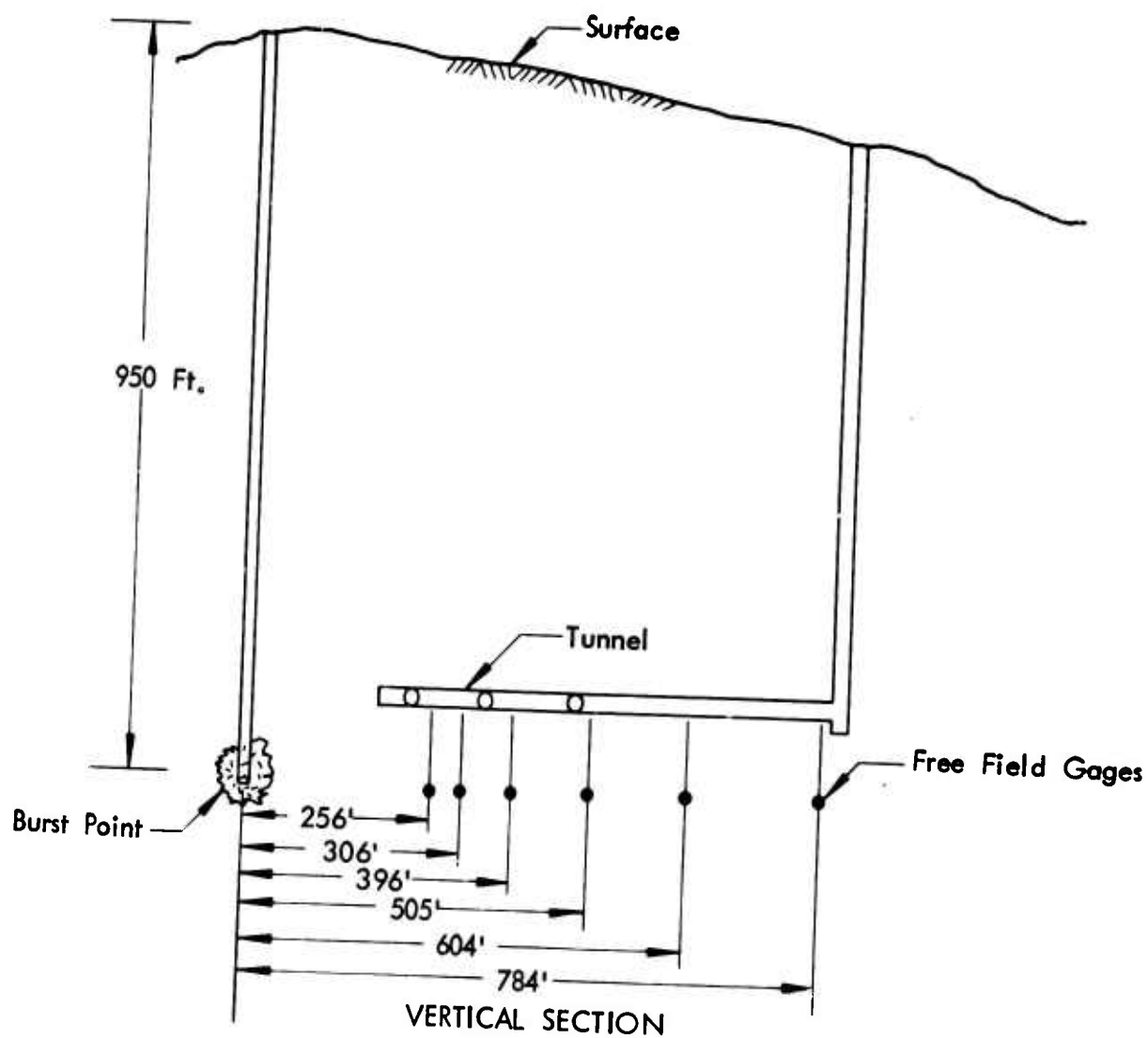


Figure 3-1: TEST SITE LAYOUT

The mathematical model of the Hard Hat test is composed of three basic elements. These are: first, the idealization of the geometry; second, the representation of the various material properties; and third, the loading pulse and boundary conditions.

Geometry

The structure-medium interaction was simulated by analyzing the behavior of a vertical section from an inner radius of 396 feet to an outer radius of 1232 feet. The free-field region was partitioned into trapezoidal elements - each with an incremental polar angle of 37.7 minutes. The radial increment of the trapezoidal elements was a constant five feet from the inner radius of 396 feet to a radius of 496 feet. From there to the outer radius of 1232 feet the radial increment increased by 10% with each successive element. The total polar angle was 6.3 degrees. This geometry is illustrated in Figure 3-2.

The "structure region" is shown in detail in Figure 3-3. It consists of a polar array of trapezoidal elements and a transition zone connecting these elements with the nodes of the "free-field" elements. The innermost ring represents the cylindrical structure and the adjacent ring of elements represents the backpacking material. The remaining elements in the "structure region" represent the rock medium.

Free-field analytic data were obtained from a FEAT Code run where the structure region of the model was replaced by uniform elements. The model was similar to that shown in Figure 3-2, except for element dimensions. The model was partitioned into trapezoidal elements with an incremental polar angle of 5 degrees. The radial increment of the trapezoidal elements was a constant 20 feet. The inner radius was 396 feet and the outer radius was 1816 feet. The total polar angle was 25 degrees.

Material Properties

Three types of materials are considered in the analysis model. The properties of the granite of the test site are given in Table 3-1. The stress strain data for the precast polyurethane foam were found in a Secret test report and are therefore included in the Classified Appendix to Volume II. The concrete liner was assumed to remain elastic. Its properties were taken as those of a composite section of concrete and reinforcing steel with a Young's Modulus of 3.45×10^6 psi, Poisson's Ratio of 0.23, and a density of 155 pcf.

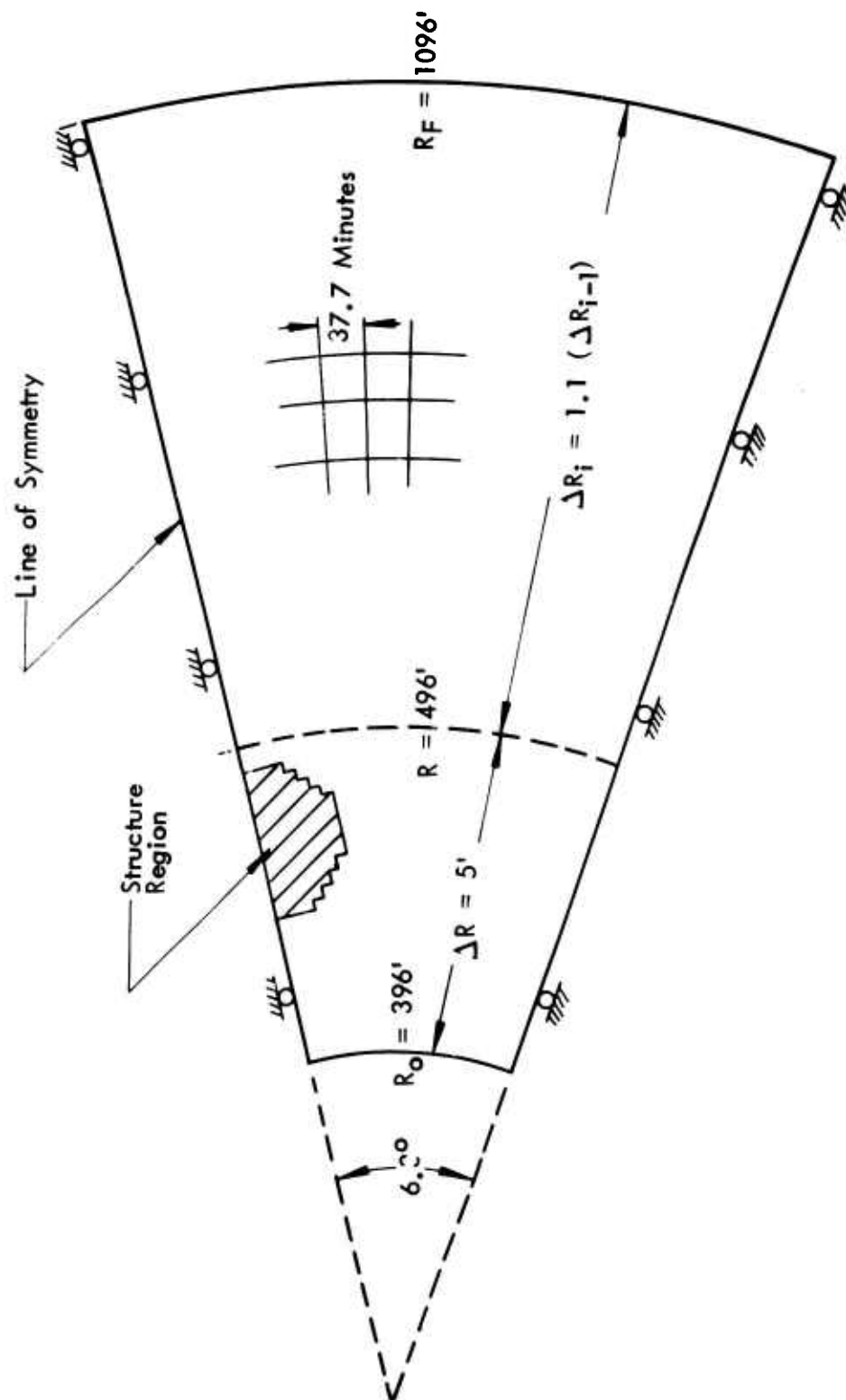


Figure 3-2: OVERALL LAYOUT - FREE-FIELD IDEALIZATION

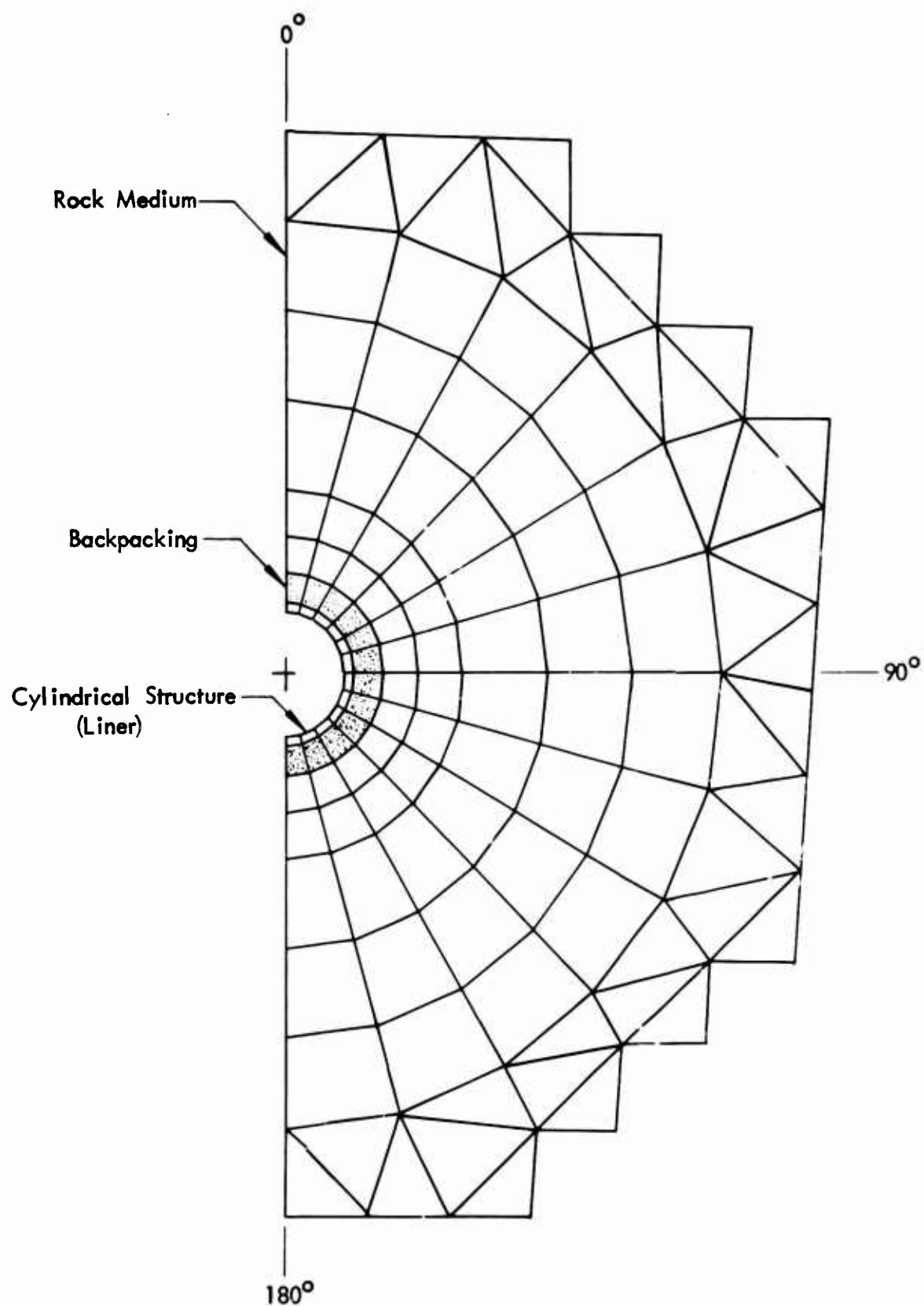


Figure 3-3: STRUCTURE REGION IDEALIZATION

TABLE 3-1

Hard Hat Granite Properties

Bulk Modulus, psi	8.1×10^6
Shear Modulus, psi	3.5×10^6
Drucker-Prager Yield Parameters	$\left\{ \begin{array}{l} \alpha \\ k, \text{psi} \end{array} \right.$
	.177
	4,000
Density, pcf	167.6
Poisson's Ratio	.311

Loading and Boundary Conditions

The radial displacement time history for all nodes on the inner radius of the model was specified. These displacement time histories were obtained, in digitized form, from integration of the velocity time history measured by Hard Hat transducer #8U. This displacement time history, shown in Figure 3-4, was applied at R=396 ft. (Boring 8 of Reference 19).

Due to the assumption of polar symmetry, the nodes along the radial edges of the model were constrained to radial motion. At the outer radius, the surface traction vector was set equal to zero, i.e., $\sigma_r = \tau_{r\theta} = 0$

3.1.3 Results

Comparisons were made between the experimental data and the FEAT code results for both the free field and structure responses. The free field comparisons are presented below while the structure comparisons are reported in the classified appendix to Volume II. The free field experimental displacement and velocity plots were taken from digitized data while the radial stress was extracted from the time history profile of Reference (19). The calculated radial displacements, velocities and stresses are compared with experimental data at ranges of 396 ft. and 505 ft. (Borings 8 and 9 of

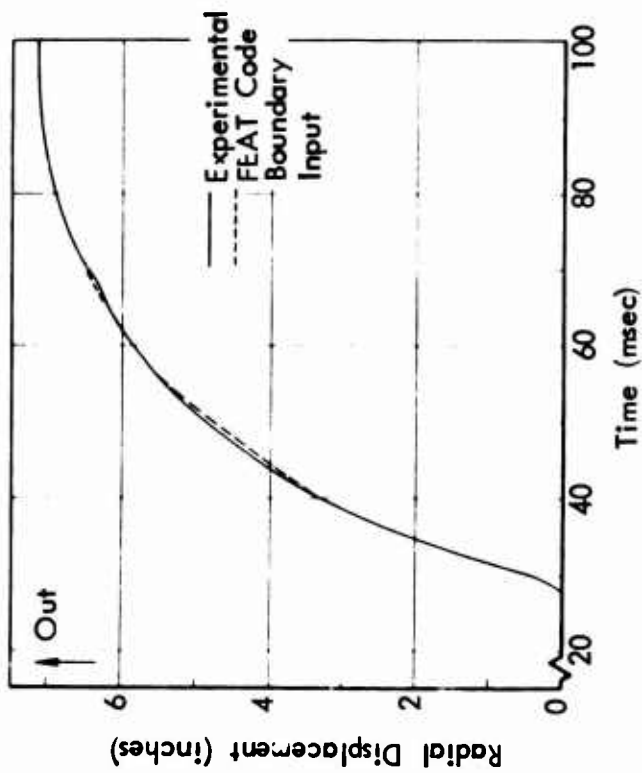


Figure 3-4: RADIAL DISPLACEMENT AT 396 FT.

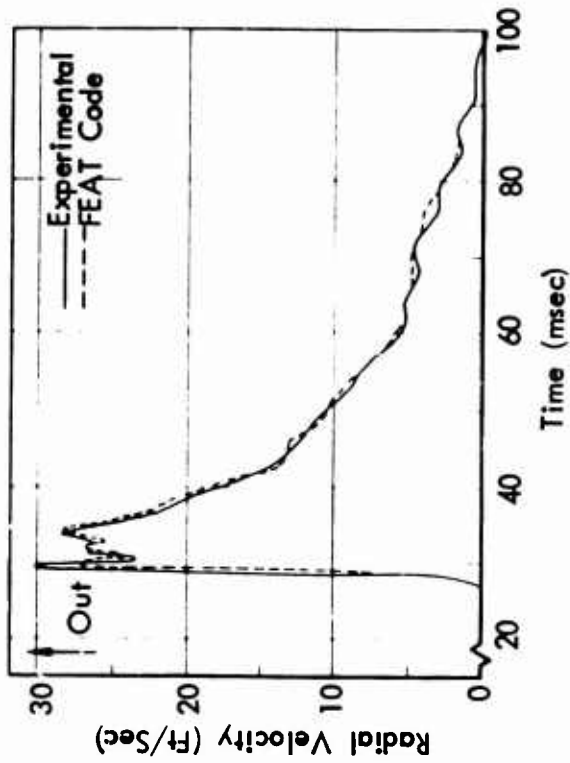


Figure 3-5: RADIAL VELOCITY AT 396 FT.

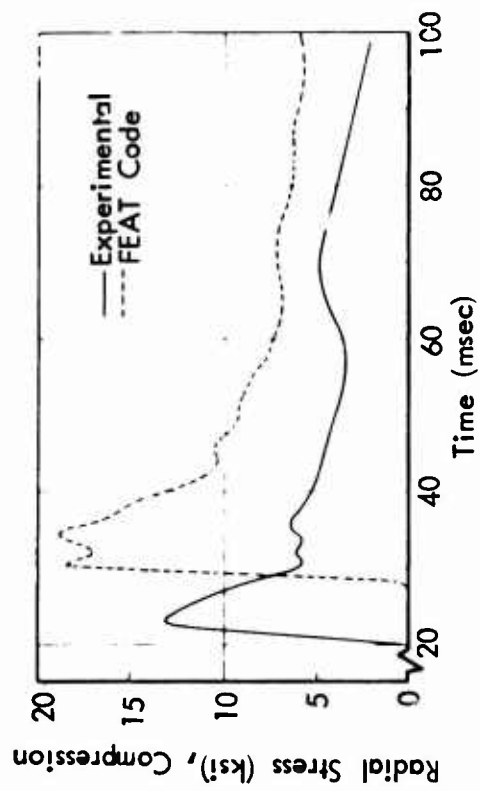


Figure 3-6: RADIAL STRESS AT 396 FT.

Reference 19). These results are presented in Figures 3-4 through 3-9.

The displacement comparisons in Figures 3-4 and 3-7 show excellent correlation between computed and measured data. Figure 3-7 for late times exhibits the difference in the cylindrical model attenuation of a spherical event.

Table 3-2 presents a comparison of velocity peaks and arrival times. Arrival times of the velocity front as well as the velocity peak are given for the 396', 496' and 596' ranges. The measured velocity front arrival times for those ranges are also presented.

Table 3-2, Velocity Pulse Comparisons

Range	FEAT Analysis		Experimental Data	
	Arrival	Peak	Arrival	Peak
396' (input)	.0266	27.03	.0231	30.0
496'	.0320	26.64	.0280	21.4
596'	.0378	24.74	.0346	11.0

The average computed propagation velocity of the front is 17,000 ft/sec while the measured velocity is 18,352 ft/sec based on interval times. It is apparent that the difference in the arrival times is nearly constant and hence the FEAT model exhibits the same propagation characteristics as the test site.

The difference in velocity peak attenuation rate can be related in the respective geometries. The test represented a spherical model, while the analysis considered a cylindrical model. In the FEAT data the velocity peaks decay as $r^{-.535}$ which is nearly the theoretical rate for cylindrical wave attenuation. Review of the computed data indicates that plastic flow in the granite does not occur until the peak stress has passed. The shapes of the measured and computed velocity pulses show similar character.

The computed radial stresses attenuate according to $r^{-.515}$ and can be shown to be consistent with the particle velocities by the momentum jump computation.

It is apparent that, over the range between the input boundary and 50 feet beyond the structure location, the pertinent responses are modeled well in the numerical model.

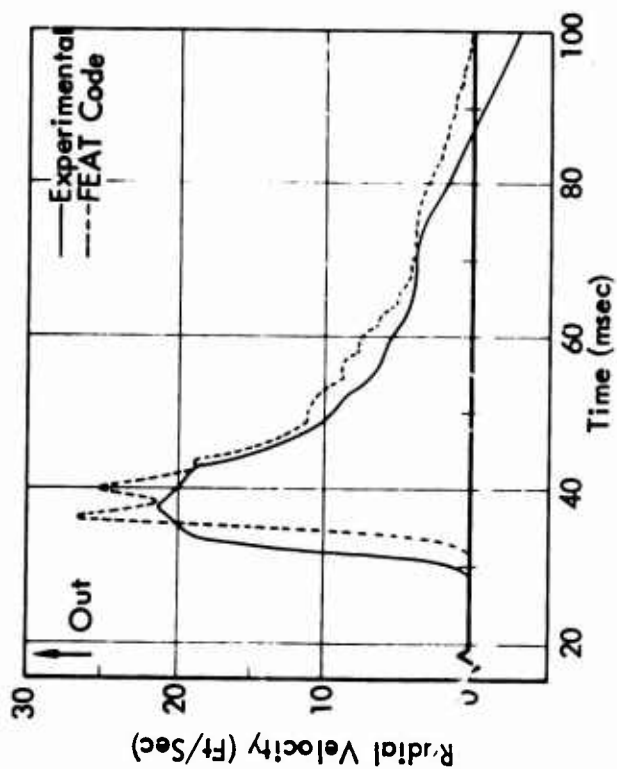


Figure 3-7: RADIAL DISPLACEMENT AT 505 FT.

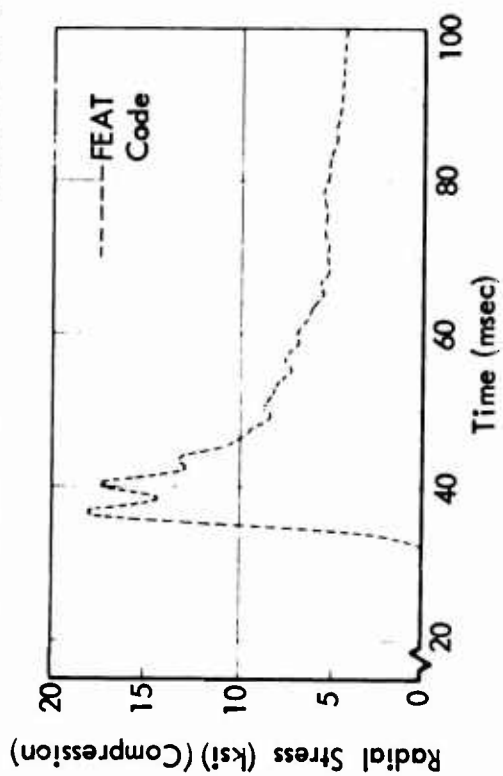


Figure 3-9: COMPUTED RADIAL STRESS AT 505 FT.

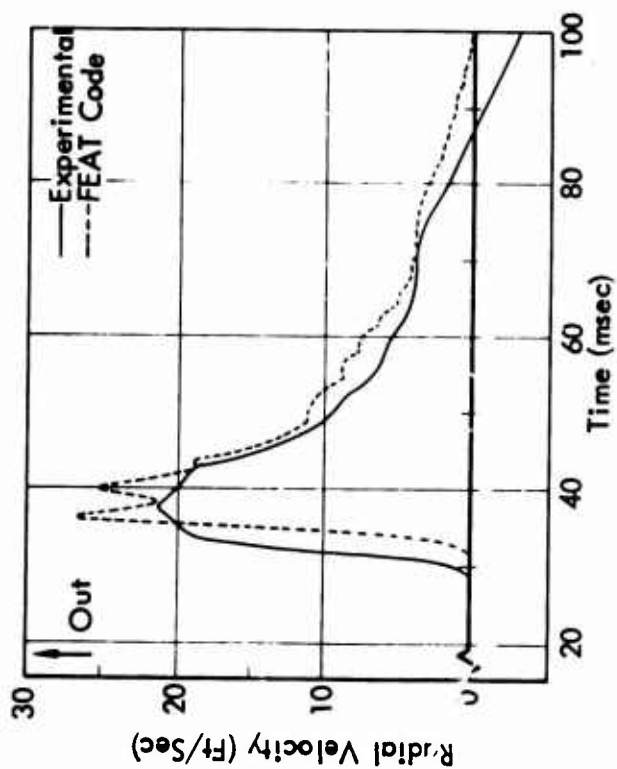


Figure 3-8: RADIAL VELOCITY AT 505 FT.

The amplitude of the computed pulse at the input station (Figure 3-6) is about 50% greater and it arrives 8 msec later than the observed pulse. The difference in amplitude is explained by a statement from Reference (19). "Observed stress at 396' is perhaps low by a factor of $1/3$." The discrepancy in arrival times relates back to a conflict in the test data between time of arrival of particle velocity and of stress at that range. The calculated input stress time history compares very well with the observed stress when the above factors are taken into consideration.

The results of the structure response calculations are presented in Appendix A. to the classified Volume II. They consist of data comparison for displacement and velocity of the structure at a point on the azimuth to the shot point. In addition the stresses, measured and computed, are presented for two locations in the backpacking material.

The FEAT solution for the displacement and velocity indicate that the structure as modeled in the analysis basically behaves as a simple oscillator. The displacement time history comparison shows that the computed solution compares well with the measured response. This solution oscillates about a mean which is nearly the experimental curve. The frequency of the response comparisons is best seen by examining the velocity comparison. This comparison shows that the period of the computed data is approximately 50% low with peak values and initial rise being too large. These two observations may be explained in the following manner. Either the stiffness of the backpacking material was too high or not all the material acted as indicated by the computed solution.

The later appears to be correct and use of the debonding and slip option of the FEAT code would yield a closer frequency comparison. In this way only approximately one quarter of the backpacking material will be affectively acting on the structure. The second item, the peak value and rise characteristic, is due to the lack of an adequate dissipative mechanism for the backpacking. To provide this in the code a special modification would be necessary.

The description of the backpacking stress data appears in the classified appendix.

3.1.4 Conclusions

The comparison of responses computed by a FEAT code analysis with measured responses indicates the capability of the structure - medium interaction code. The basic phenomena observed in the test were reproduced by the numerical analysis. Study of the data comparison indicates that better concurrence could be achieved by utilization of the debonding and slip capability of the computer code at the interface between the structure and the foam. This would decrease the stiffness of the suspension provided the structure by the foam, while modeling the suspension realistically.

In addition to that adjustment in the analysis model, it would be feasible to utilize a dissipative representation of the foam. This can, however, not be justified for this particular field test since insufficient foam data preclude determination of appropriate parameters.

3.2 Distant Plain 6

Shot Distant Plain 6 was a 100 ton high explosive surface burst test conducted at the Suffield Experimental Station, Alberta, Canada, during the summer of 1967. The Naval Civil Engineering Laboratory (NCEL) had responsibility for measuring the response of a buried concrete hollow cylinder. For this contract a plane strain FEAT code analysis of the buried cylinder response had been proposed to demonstrate the applicability of the code to analyze this type of problem which included a structure buried in a compacting, nonlinearly elastic, plastic, layered medium, with air overpressure, and direct induced loading.

However, the mathematical representation for earth material used by FEAT and other ground motion analysis codes proved to be inadequate for the solution of this problem. The inadequacy of the representation is discussed in the Appendix. An idealized version of the problem was analyzed under Navy contract N62399-67-C-0026 with a layered, nonlinearly elastic material model, the results of which are presented in the report submitted to NCEL entitled "Analysis of Buried Cylinder Response."

IV

AXISYMMETRIC PROGRAM

In the previous sections the capabilities of the plane strain version of the FEAT code were demonstrated. This section considers the verification of the axisymmetric version. Since no appropriate analytical solutions were available, verification of the FEAT code required comparisons with other computer code solutions to establish its credibility. The features of the code which were necessary to verify were 1) the ability to accept input displacements from another code and compute equivalent free-field results and 2) the ability to perform the structure region computations in a consistent manner.

Three problems were solved to demonstrate the capabilities of the axisymmetric code. The input used for the analysis was a combination of data generated by ATI-AJA, prescribing displacements of the soil island boundaries, and the corresponding airblast loading generated by a subroutine written for this analysis. In two of these problems only the free-field response was computed, while in the third the structure region was included in the model. However, earth media properties were input for all elements in the structure region.

4.1 Free Field Runs

The use of the "soil island" concept for the vertical section structure-medium interaction analysis was described in Part I of this report.

Driving forces applied to the "soil island" region were composed of an airblast loading precalculated for the interaction analysis and read from tape during the computations, and of free field displacements of points on the boundary of the "soil island" which were calculated by ATI-AJA and provided on data tapes.

Two computer runs were made to verify that with the given input it is possible to calculate the free-field motions and stresses which had previously been determined by ATI-AJA with their finite difference code. This was done for medium yield bursts on granite and limestone. Both cases considered the low overpressure region.

The comparison of the free field responses originally calculated by ATI-AJA for the granite case, with those calculated with the FEAT axisymmetric code is illustrated in Figure 4-1 through 4-5. Shown are vertical and horizontal displacements and particle velocities and horizontal stress for the low overpressure range at a point 80' below the ground surface. In Figures 4-6 through 4-10 the vertical and horizontal displacements and particle velocities, and the horizontal stress are shown for the same location but in limestone.

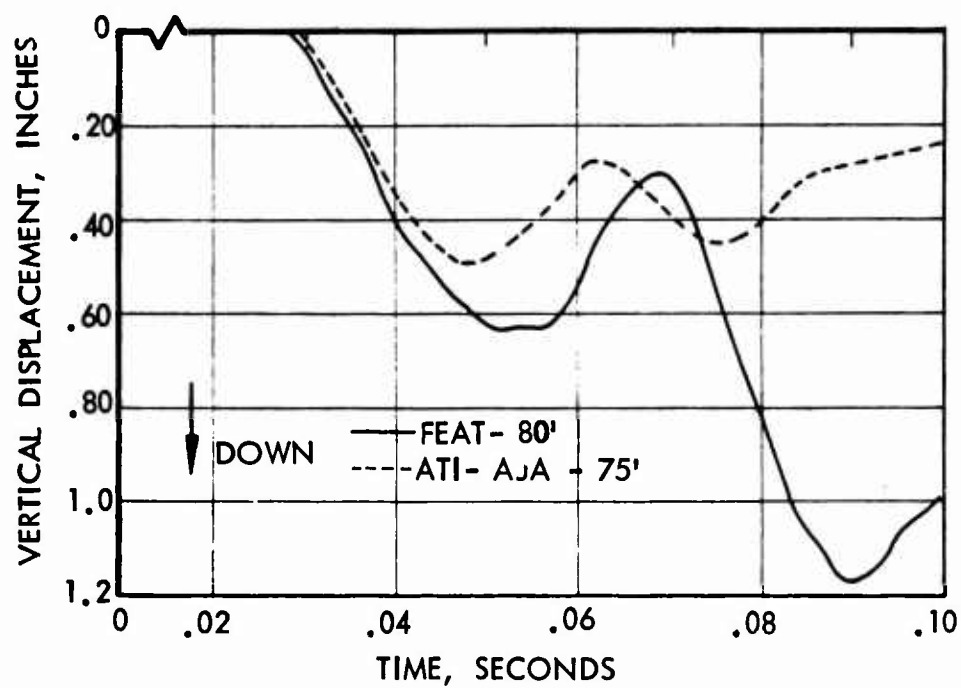


Figure 4-1: VERTICAL DISPLACEMENT GRAN-M LOW OVERPRESSURE FREE-FIELD RUN

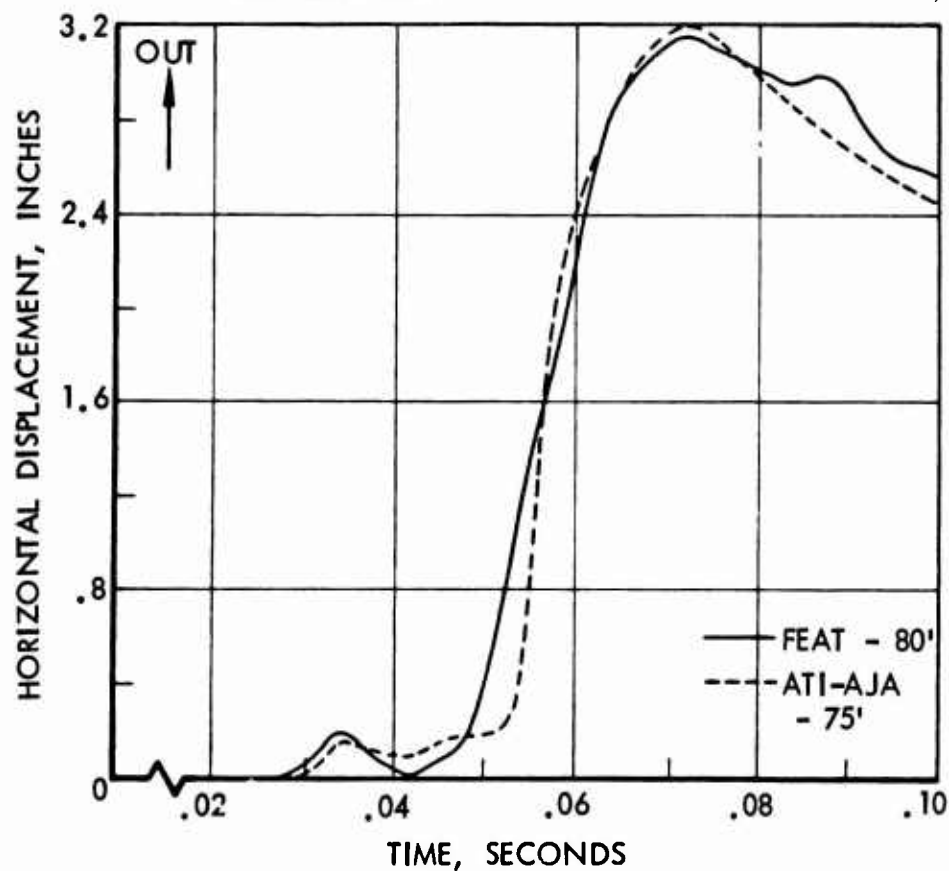


Figure 4-2: HORIZONTAL DISPLACEMENT GRAN-M, LOW OVERPRESSURE FREE-FIELD RUN

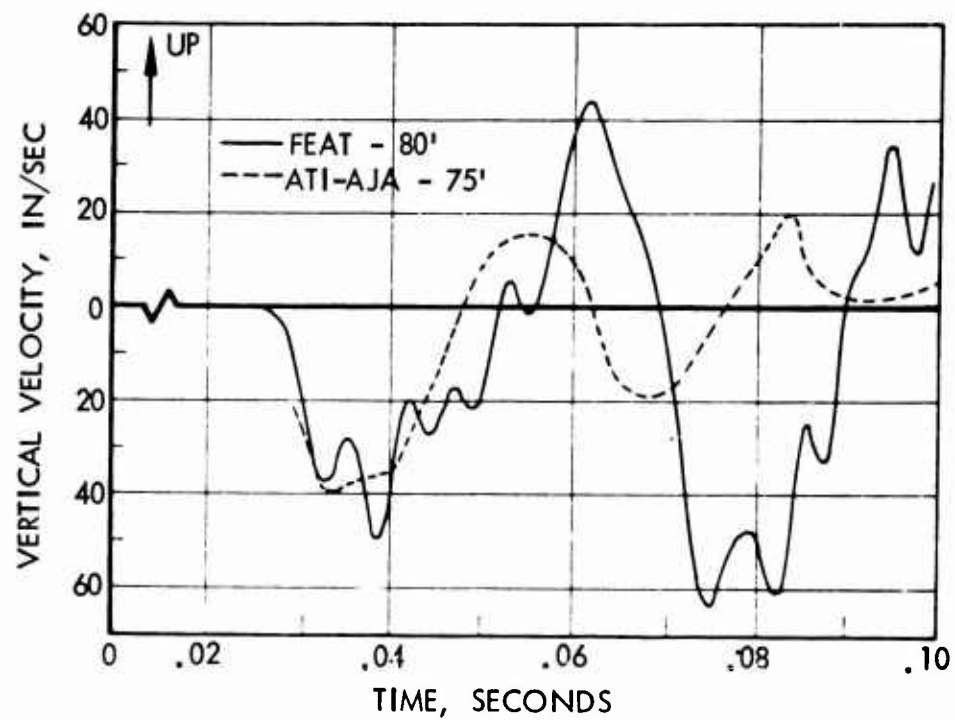


Figure 4-3: VERTICAL PARTICLE VELOCITY GRAN-M LOW OVERPRESSURE FREE-FIELD RUN

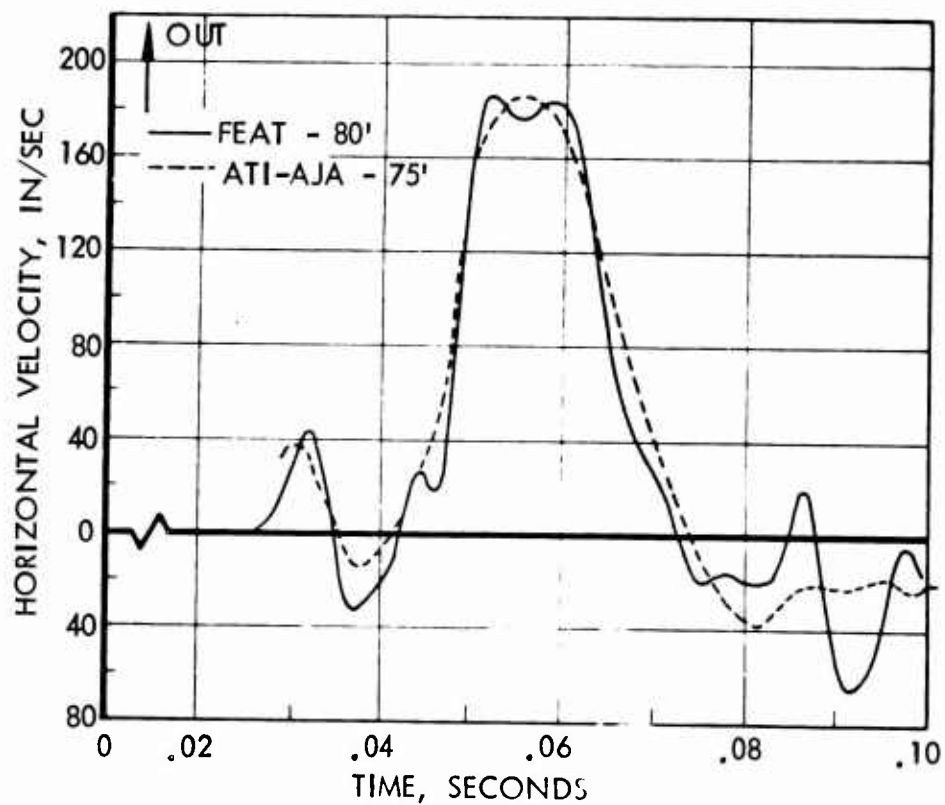


Figure 4-4: HORIZONTAL PARTICLE VELOCITY GRAN-M, LOW OVERPRESSURE FREE-FIELD RUN

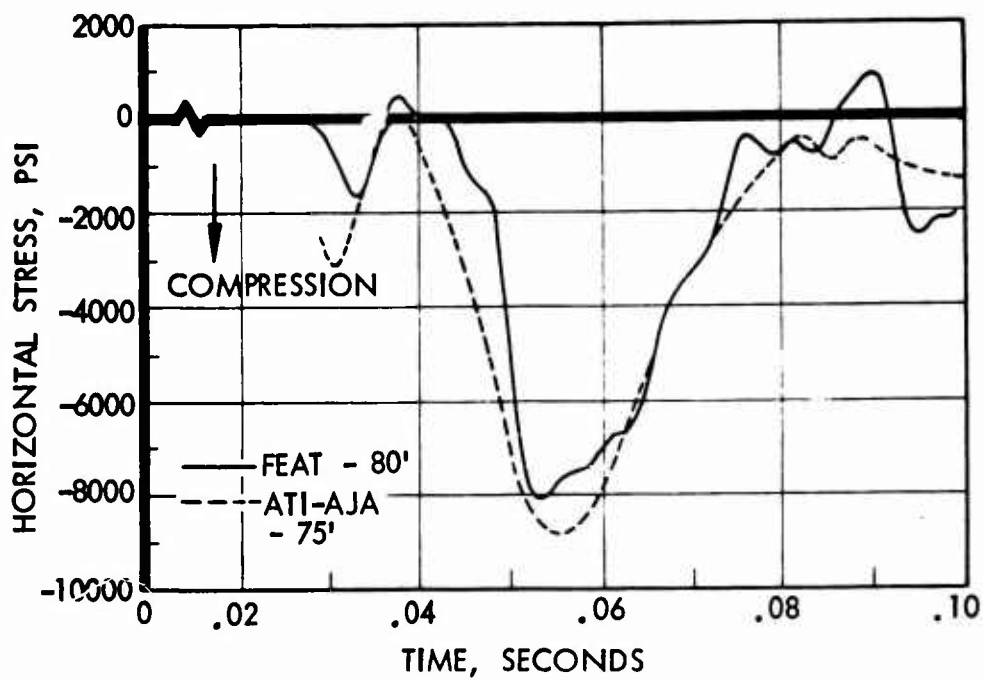


Figure 4-5: HORIZONTAL STRESS GRAN-M, LOW OVERPRESSURE FREE-FIELD RUN

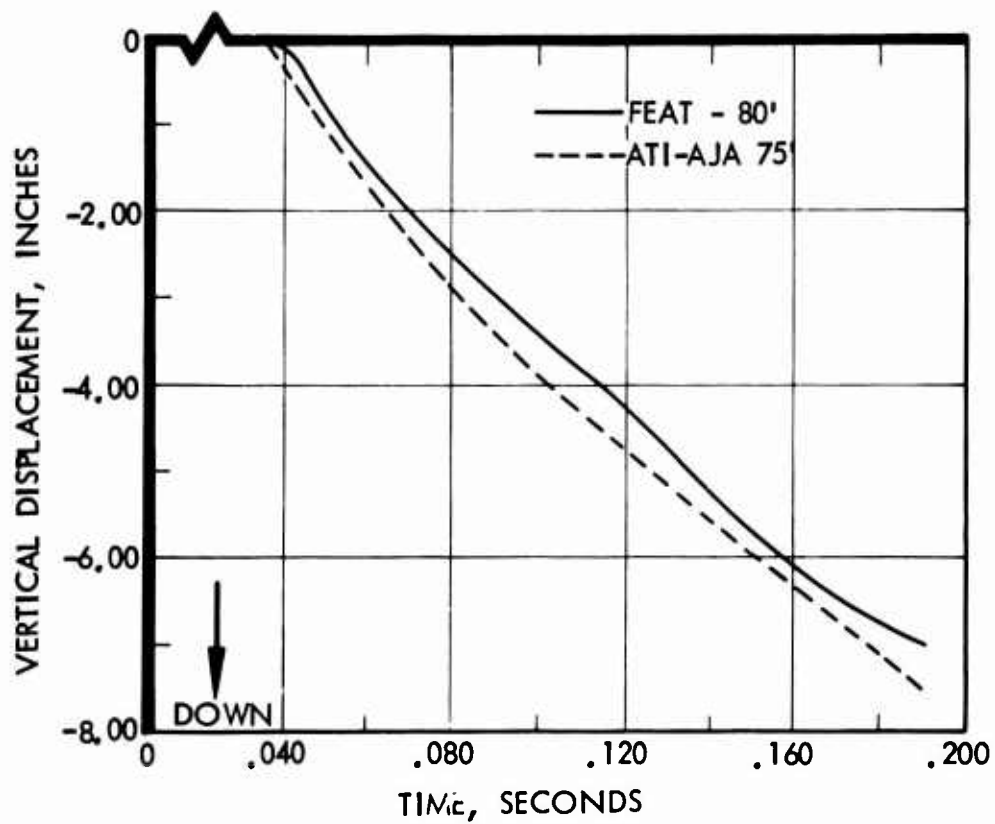


Figure 4-6: VERTICAL DISPLACEMENT LIME - M, LOW OVERPRESSURE FREE-FIELD RUN

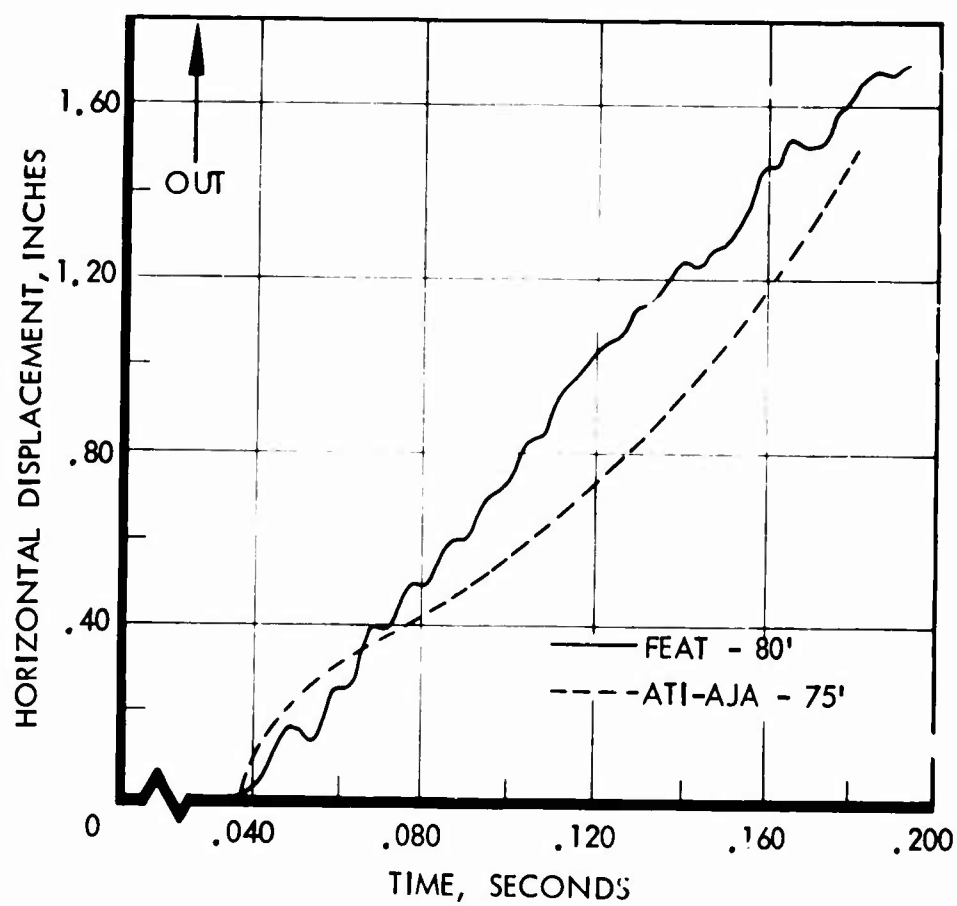


Figure 4-7: HORIZONTAL DISPLACEMENT TIME - M, LOW OVERPRESSURE
FREE-FIELD RUN

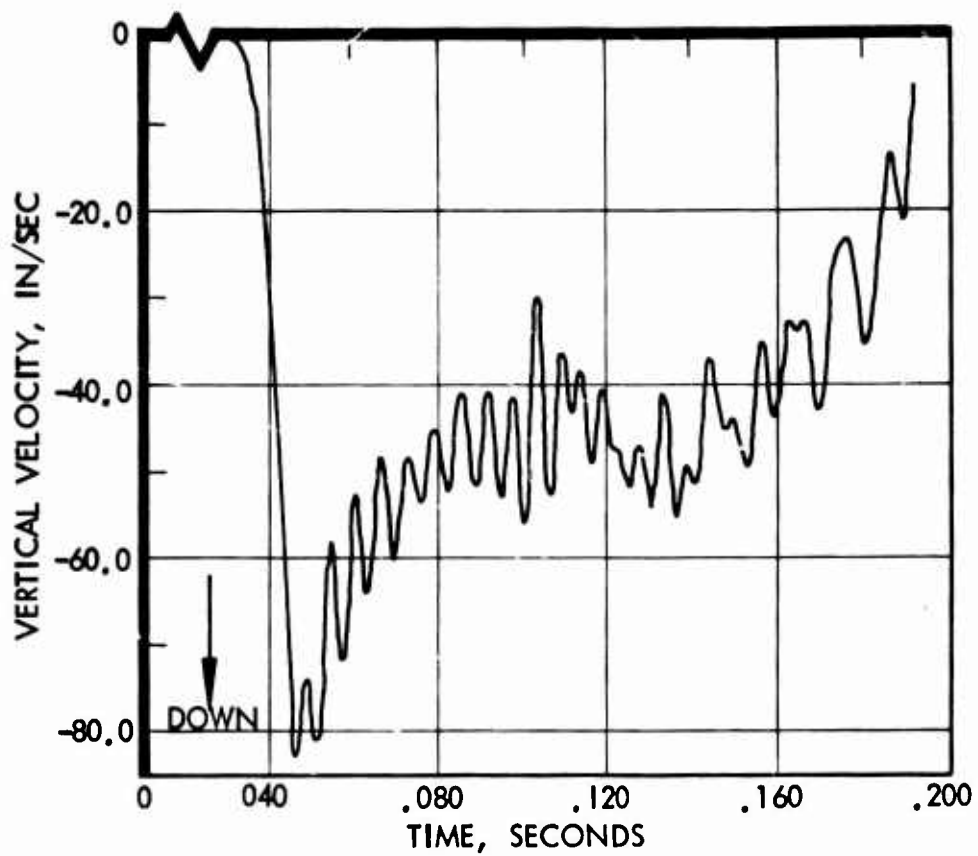


Figure 4-8(a): FEAT RESULTS VERTICAL PARTICLE VELOCITY LIME - M,
LOW OVERPRESSURE FREE-FIELD RUN

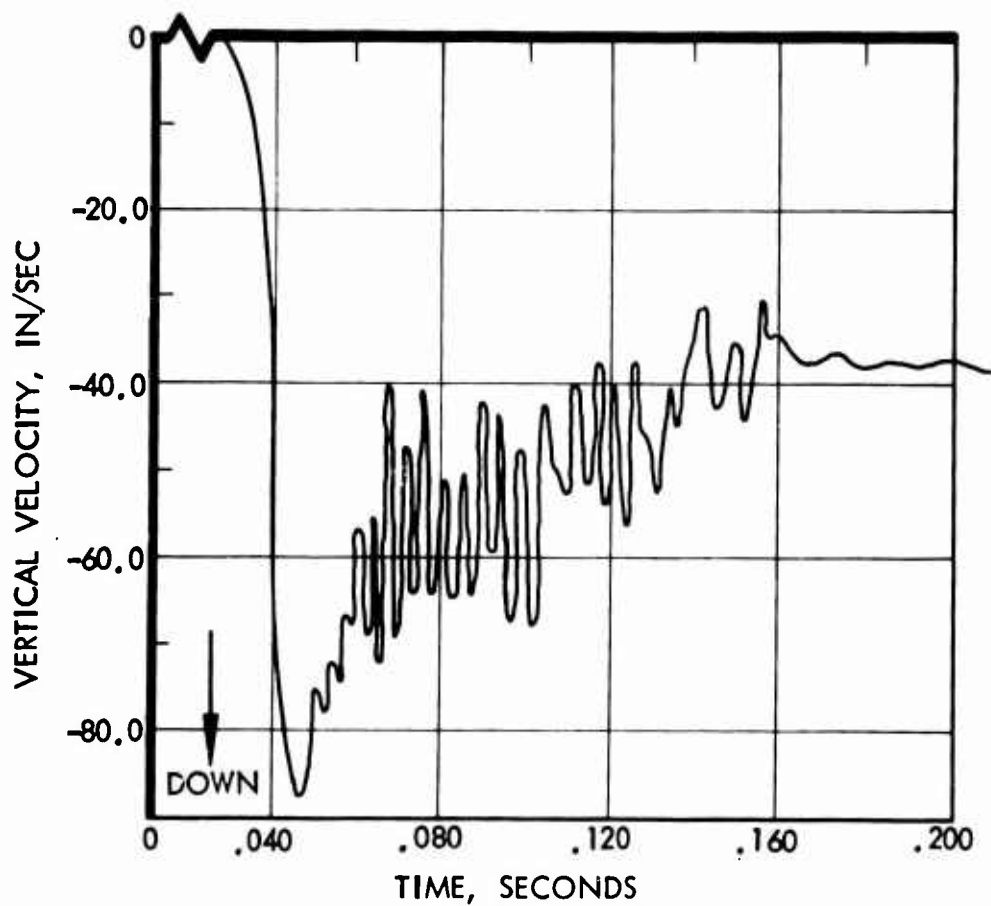


Figure 4-8(b): ATI-AJA RESULTS VERTICAL PARTICLE VELOCITY LIME - M,
LOW OVERPRESSURE FREE-FIELD RUN

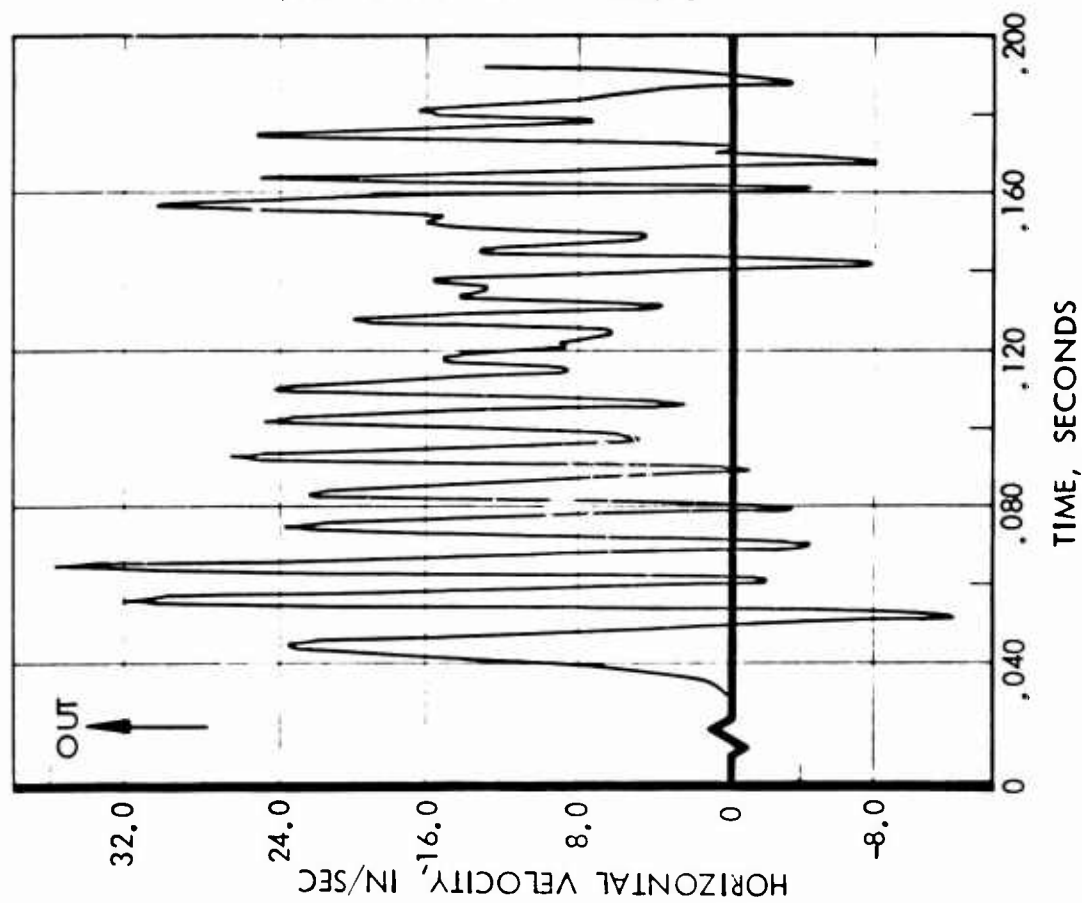


Figure 4-9(a): FEAT RESULTS HORIZONTAL PARTICLE VELOCITY
LIME - M, LOW OVERPRESSURE FREE-FIELD RUN

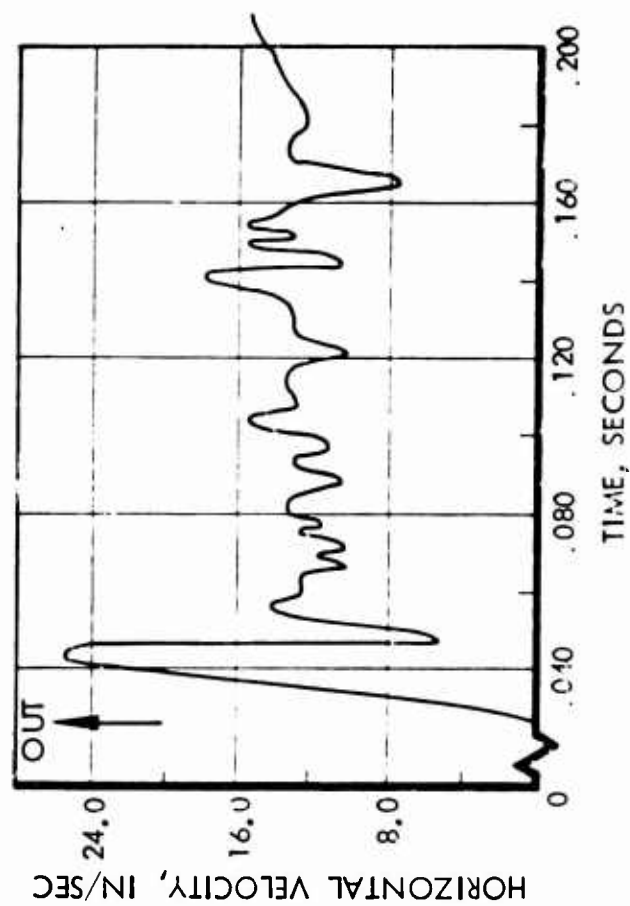


Figure 4-9(b): AT!-AJA RESULTS HORIZONTAL PARTICLE
VELOCITY LIME - M, LOW OVERPRESSURE
FREE-FIELD RUN

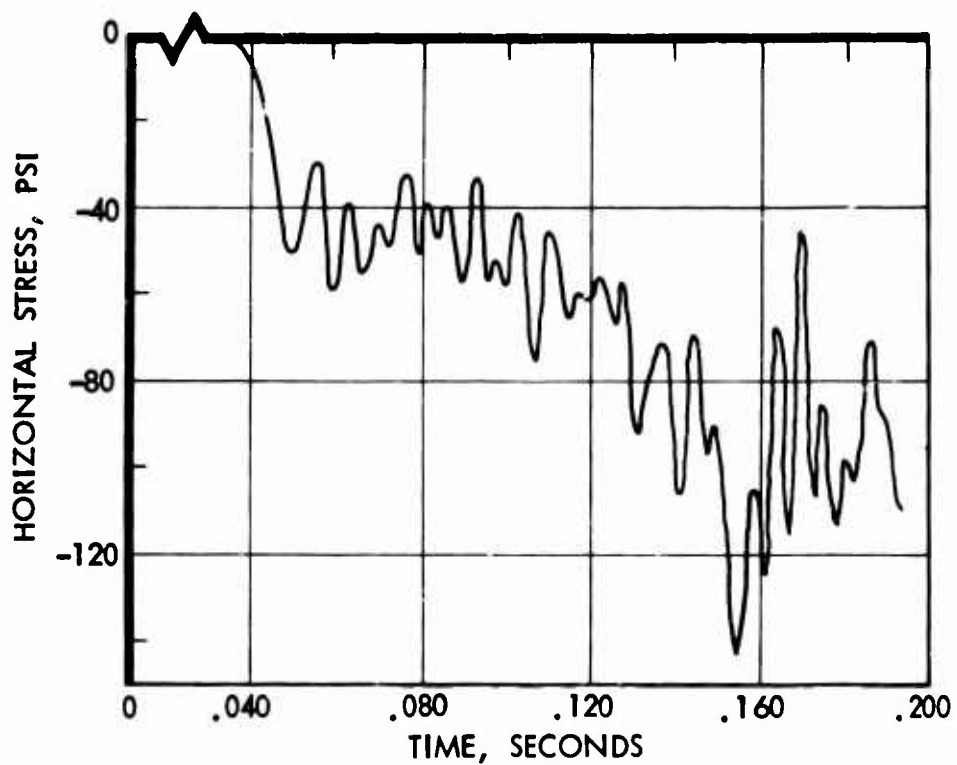


Figure 4-10(a): FEAT RESULTS HORIZONTAL STRESS LIME - M, LOW OVERPRESSURE FREE-FIELD RUN

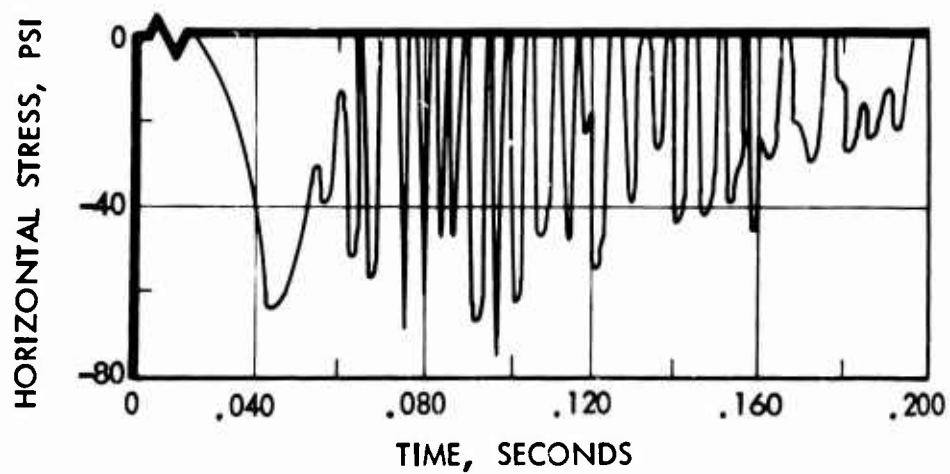


Figure 4-10(b): ATI-AJA RESULTS HORIZONTAL STRESS LIME - M, LOW OVERPRESSURE FREE-FIELD RUN

It can be observed that in general there is good agreement between the FEAT data and the calculations by ATI-AJA. Where the two results deviate it is possible to determine a number of plausible reasons for lack of agreement. It should suffice here to state some of the more pronounced reasons. The input data for the subsurface "soil island" boundaries is obtained by ATI-AJA by interpolation of their computed results in space and time. This procedure is not free of problems as is indicated by activity far ahead of the wave front, especially in the granite case. Another point is that the two programs treat the earth medium differently. For example, cracking is allowed to occur in the three normal stresses independently of each other in the ATI-AJA procedure, while in the FEAT code cracking of a region is enforced simultaneously for all stresses when the pressure in that region exceeds a certain specified level of hydrostatic tension. It is not at all clear which of the two approaches more accurately represents the behavior of an earth medium in tension. One can only state that the two codes consider this phenomenon in a different manner.

4.2 Structure Region Verification

It was necessary also to verify that the structure region subroutine is working properly. Since no suitable analytic solution was available for this checkout, a check against free-field calculations was made. For this purpose the inputs for a medium yield burst on granite in the low overpressure region were used. The structure region was placed into the soil island model, and all elements in it were assigned granite properties; this includes the structure path.

In Figures 4-11 through 4-15 the calculations are compared with previously determined free-field responses. This comparison is made for a point of the same range and depth as the data discussed in section 4.1. It is apparent that the results are not identical. However, they represent adequately the free-field behavior in character and amplitude. Since in the elements representing the structure material, the behavior is considered to be linearly elastic, this may account for the slight differences in response of the structure and overlay paths.

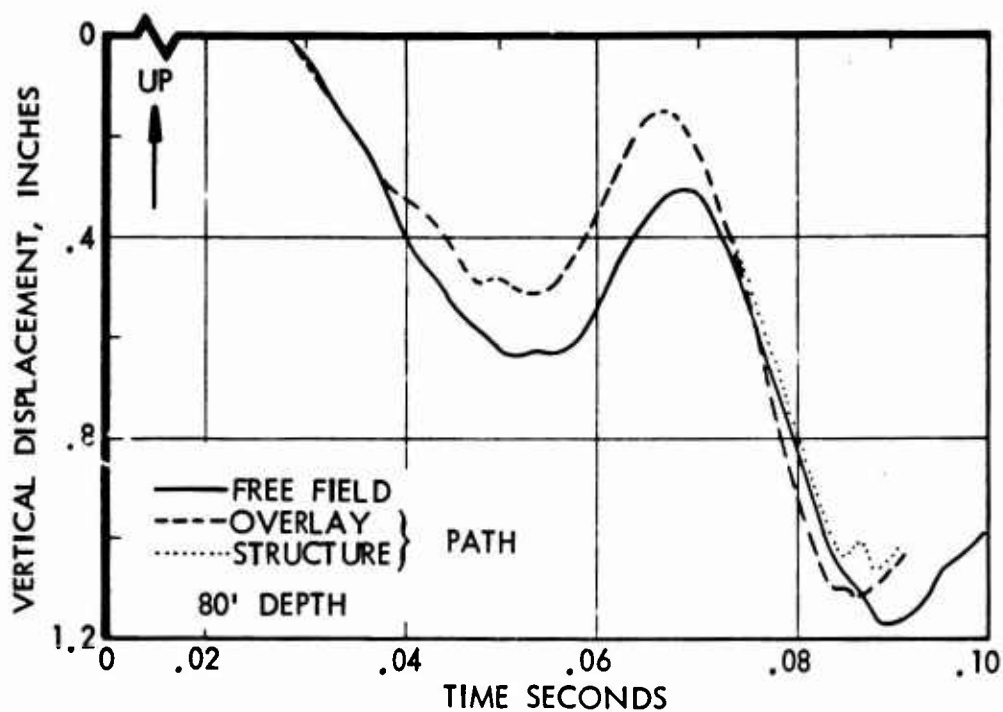


Figure 4-11: VERTICAL DISPLACEMENT STRUCTURE AND OVERLAY PATHS VS FREE-FIELD

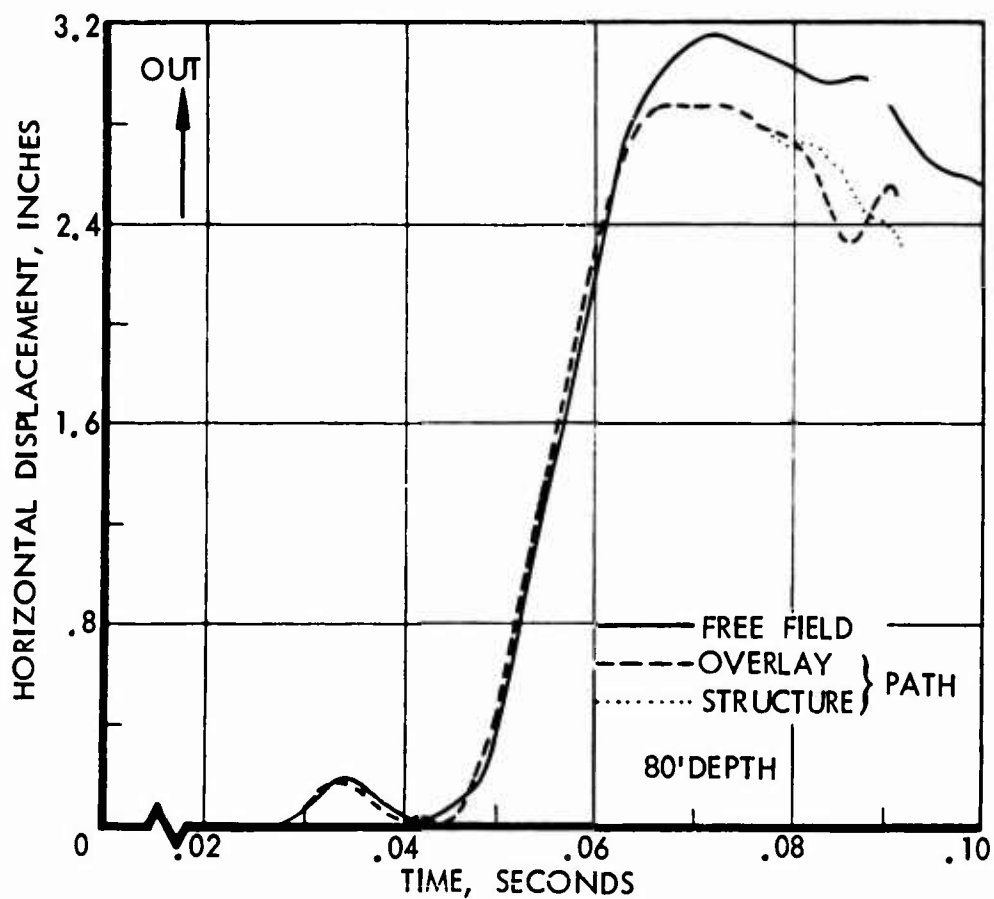


Figure 4-12: HORIZONTAL DISPLACEMENT STRUCTURE AND OVERLAY PATHS VS FREE-FIELD

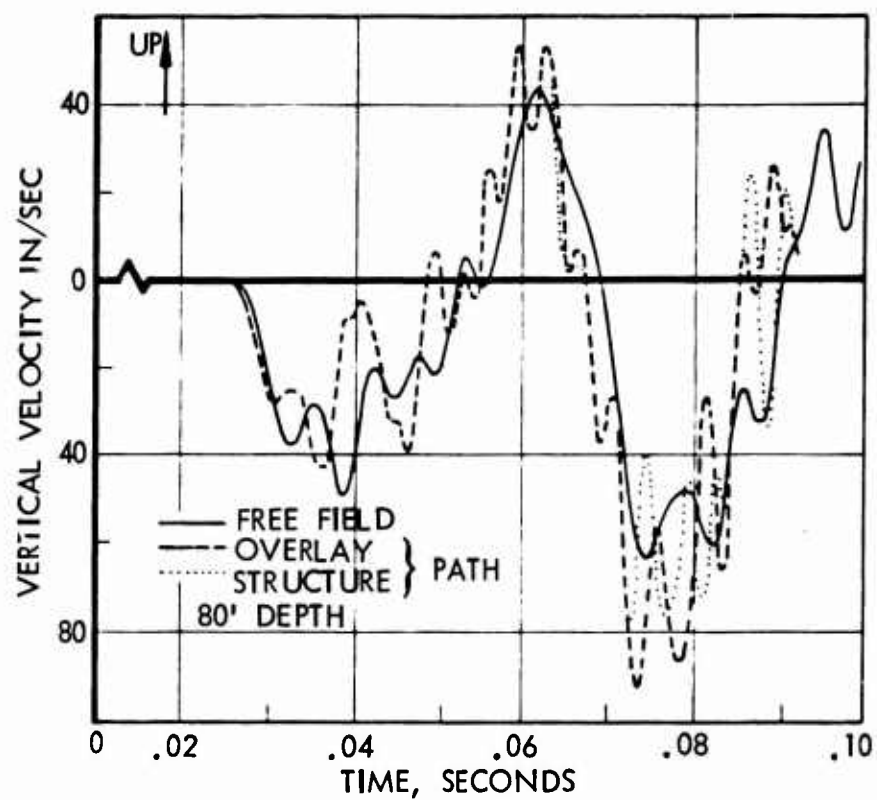


Figure 4-13: VERTICAL PARTICLE VELOCITY STRUCTURE AND OVERLAY PATHS VS FREE-FIELD

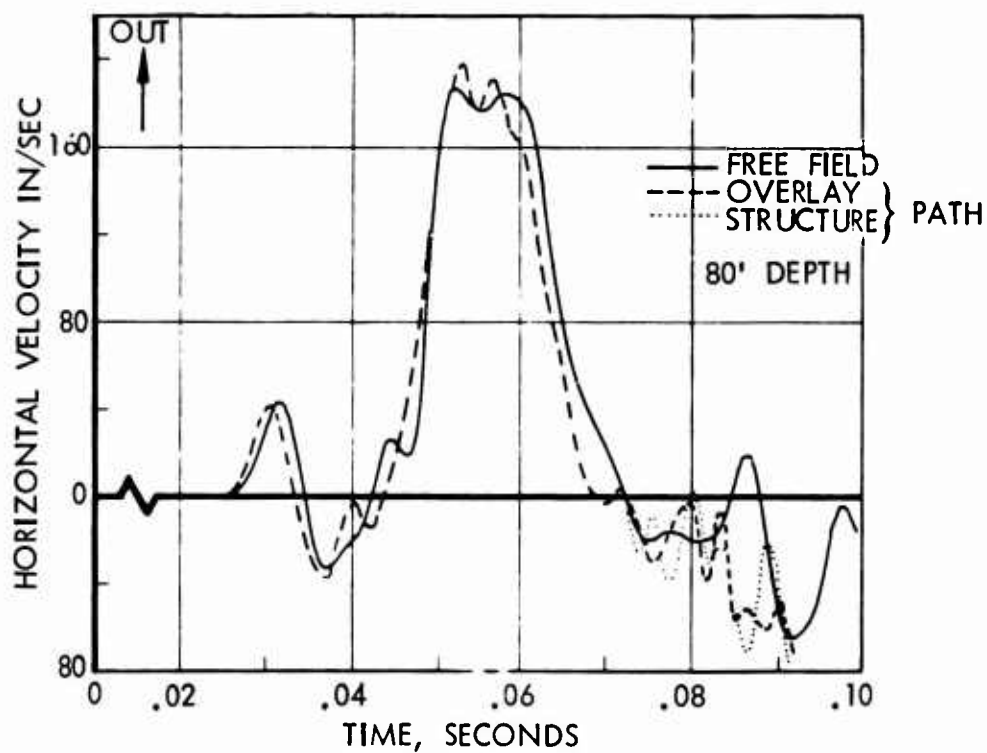


Figure 4-14: HORIZONTAL PARTICLE VELOCITY STRUCTURE AND OVERLAY PATHS VS FREE-FIELD

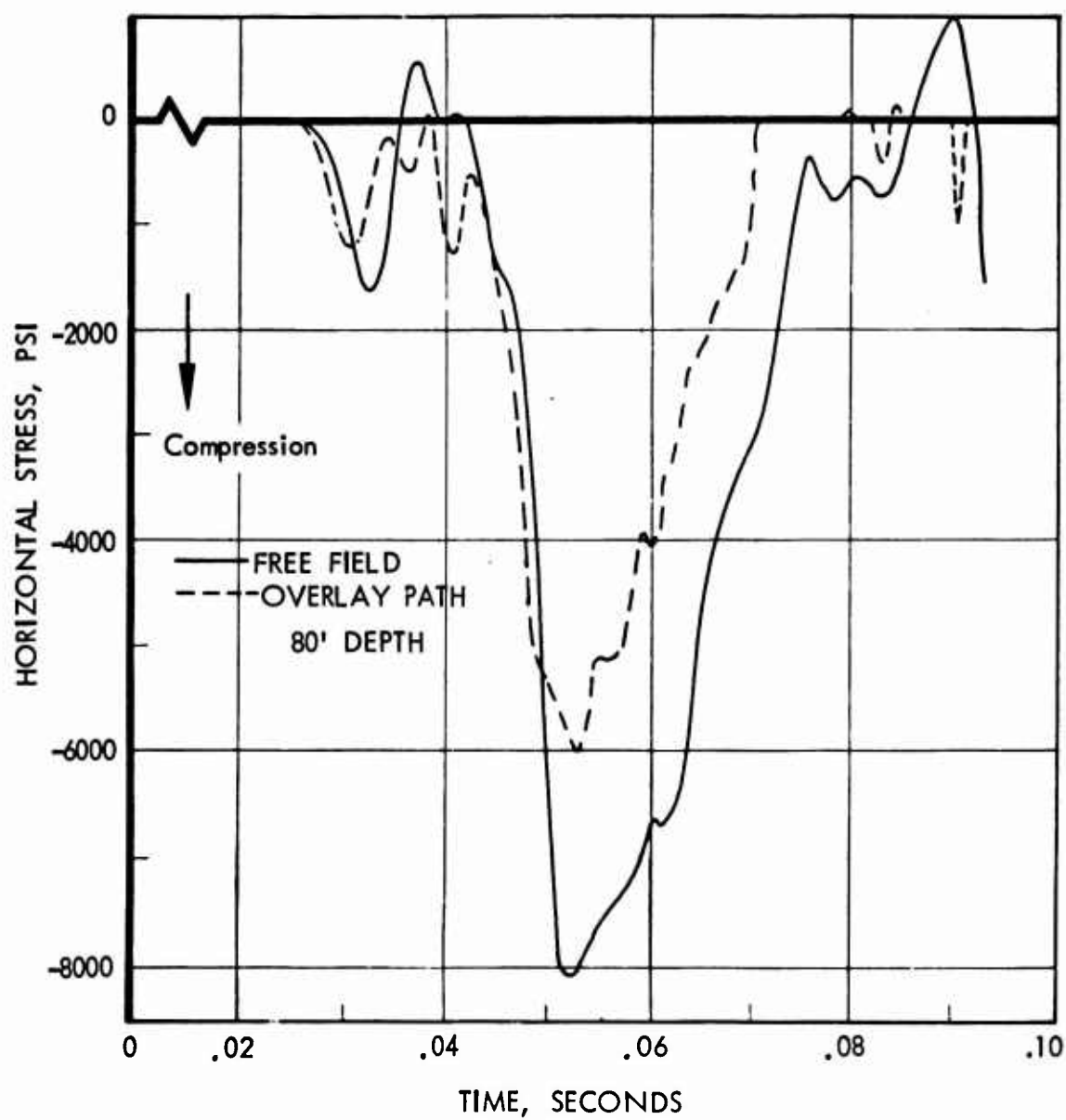


Figure 4-15: HORIZONTAL STRESS OVERLAY PATH VS FREE-FIELD

V

SUSPENSION SYSTEM TEST CASE

5.1 Problem Description

A sample problem has been run which demonstrates a part of the capabilities of the suspension system subroutine. This problem does not represent any proposed suspension system but, rather, illustrates some of the salient points of the program. It was assumed that the in-structure contents would be placed in a cavity with a cross-section 50 feet wide by 40 feet high. Three of the columns and 5 of the rows of the finite element structure representation were assumed to bound or terminate at the cavity as shown in Figure 5-1. The in-structure contents were assumed to be a rigid mass, although content flexibility could have been represented by one free-free bending mode. The rigid mass was assumed to be approximately centered in the cavity in the equilibrium position as indicated in Figure 5-1, with a gap of about 6 feet on all sides. The contents were assumed to have a mass of $1000 \text{ lb.} \cdot \text{sec}^2/\text{in}$ and a pitch moment of inertia of $10^7 \text{ lb.} \cdot \text{sec}^2\text{-in}$. The mass was assumed to be symmetric about a vertical axis and the c.g. was assumed to be 2 feet below the centroid of the body. (The subroutine is not limited to an assumption of symmetry, however).

As noted in the first volume of this report, the suspension elements can consist of any desired parallel combination of 1) nonlinear spring, 2) viscous damper, 3) Maxwell element, 4) linear spring and/or 5) Coulomb damper in series with a linear spring. The mass was assumed to be supported vertically by two suspension elements at opposite corners of the base. The vertical suspension elements consisted of a Coulomb-damper linear spring series in parallel with a linear spring. The mass was suspended horizontally between six suspension elements as shown in Figure 5-1. Each horizontal suspension element consisted of a viscous damper in parallel with a linear spring. Although no particular suspension system was modeled, a degree of realism was maintained so that responses would be representative of what might occur. The suspension system elements were sized as follows:

Vertical Suspension System Elements

The linear spring component of the vertical element shown in Figure 5-1 was sized to give an undamped natural frequency of 0.5 cps vertically.



Figure 5-1: SUPENSION SYSTEM SUBROUTINE, SAMPLE PROBLEM LAYOUT

$$\text{Total } K = (2\pi f)^2 M = \frac{(2\pi)^2}{4} \times 10^3 = 9860 \text{ lb/in.}$$

$$K_L = K/N = \frac{9.86 \times 10^3}{2} = 4930 \text{ lb/in.}$$

Where: K is the total stiffness of all vertical linear spring components (lb/in)

f is the natural frequency of the contents on the vertical linear spring components (cps)

M is the mass of the contents (lb-sec²/in.)

N is the number of vertical suspension elements

The Coulomb-damper linear spring series component was sized to slip at 0.1 Mg.

That is a slip force,

$$F_s = 0.1 \text{ Mg} = 0.1 (1000 \times 386) = 3.86 \times 10^4 \text{ lb.}$$

Where: M is the Mass of the contents (lb-sec²/in.)

g is the gravitation constant (386 in/sec²). This slip force was assumed to be developed at a deflection of 1.0 inch of the linear spring part of the series, giving a spring constant

$$K_F = \frac{F_s}{1.0} = 3.86 \times 10^4 \text{ lb/in.}$$

The static deflection of the vertical suspension system was approximately

$$S_s = Mg/K = 386 \times 10^3 / 9860 = 39.1 \text{ in.}$$

Therefore the free length of the vertical spring was input as

$$l_k = 120 + 39.1 = 159.1 \text{ in.}$$

which results in the desired 6 ft. gap between structure and contents at static equilibrium. All initial suspension element length projections were input to the program for a c.g. zero coordinate contents position 39.1 inches above (-39.1) the centerline of the cavity. The vertical suspension elements were initially at their free length. In the initialization phase, the computer program determined the actual equilibrium position which was found to be 39.1481 inches below the zero coordinate position as shown in Figure 5-2.

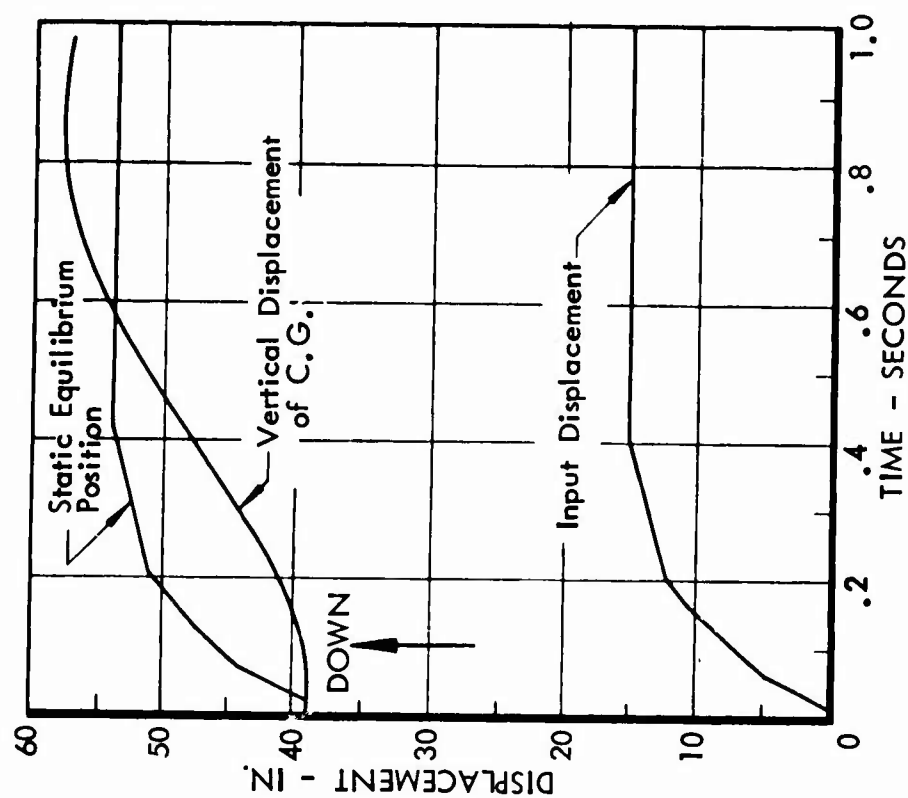


Figure 5-2: SUSPENSION SYSTEM CHECK CASE
VERTICAL DISPLACEMENT OF C.G.

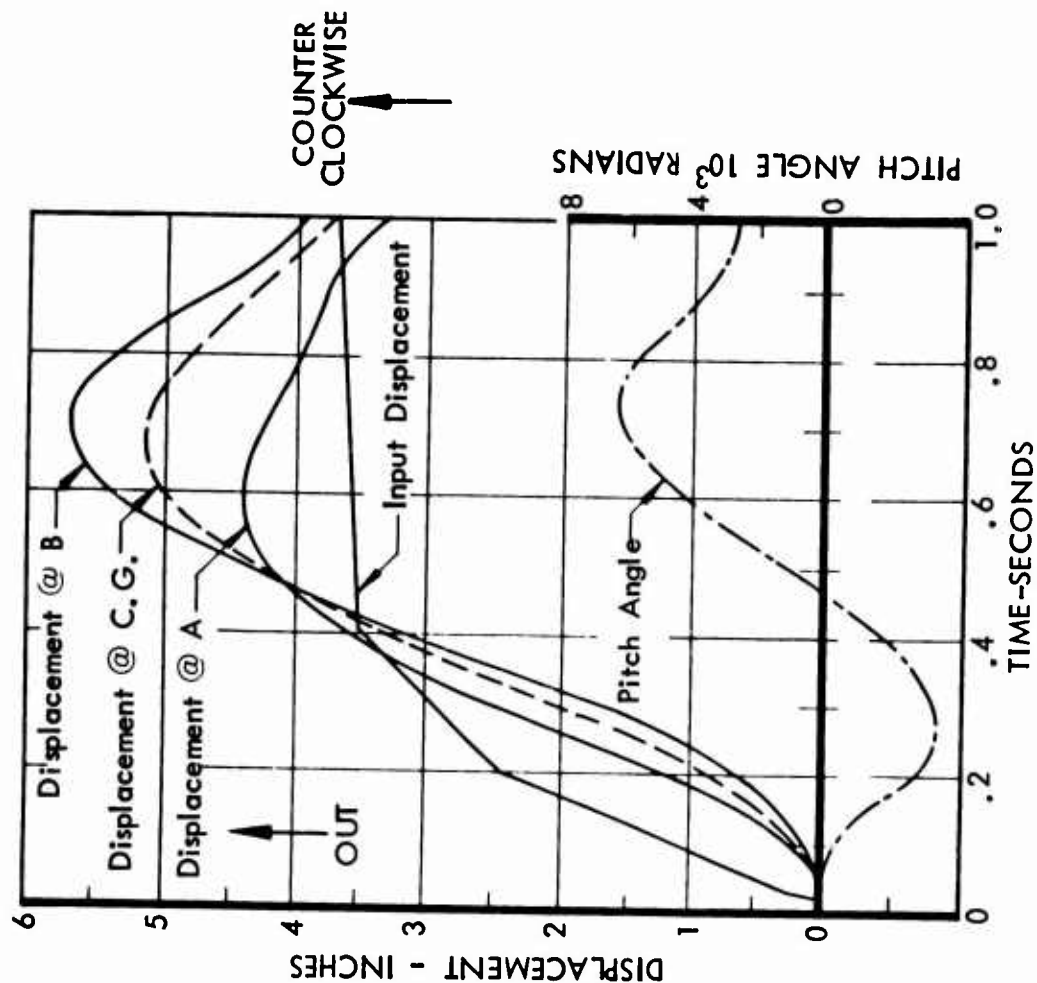


Figure 5-3: HORIZONTAL & PITCH DISPLACEMENT
OF SUSPENDED CONTENTS

Horizontal Suspension System Elements

All horizontal suspension system elements were assumed to be identical. The linear spring component on the horizontal element shown in Figure 5-1 was sized to give an undamped natural frequency of 1.0 cps horizontally.

$$\text{Total } K = (2\pi f)^2 M = 4\pi^2 \times 10^3 = 3.94 \times 10^4 \text{ lb/in.}$$

$$K_L = K/N = \frac{3.94 \times 10^4}{6} = 6.57 \times 10^3 \text{ lb/in.}$$

The viscous damper was sized to give 20% of critical damping for horizontal motion. The equivalent damping coefficient for all horizontal elements was given by

$$\begin{aligned} \text{Total } C &= 0.2C_c = 0.2 (2\sqrt{KM}) = 0.2 (2\sqrt{3.94 \times 10^4 \times 10^3}) \\ &= 2510 \text{ lb-sec/in.} \end{aligned}$$

$$C_v = C/N = \frac{2510}{6} = 418 \text{ lb/in/sec.}$$

Where: C_c is Critical Damping Coefficient (lb-sec/in.). The free length of the horizontal suspension elements was input as

$$l_k = 120 \text{ in.}$$

since they were to be relatively unstrained in the equilibrium position. They each had vertical projections of -39.1 inches in the contents zero coordinate position, indicating that they were stretched in this position.

Input Structure Motion

The motion of the structure was simulated for this example by positioning the ends of the suspension system elements with time histories of free-field displacement obtained from ATI for a large weapon at the 6000 psi range and a depth of 100 feet, Figures 5-2 and 5-3. These free-field motions were applied to the suspension system in the same order which structure wall motions would have been input had the subroutine been operated as part of the FEAT code. That is: (1) Motions were input to the suspension elements attached to column 4 and forces were calculated on column 4 from the elements (The left hand vertical suspension element was assumed attached to column 4 for the purpose of motion input); (2) Then the motions were input to the suspension elements attached to column 6 and forces were calculated on column 6 from the elements, and (3) The motions of the contents under the imposed loads were then calculated using the Acceleration Pulse Subroutine of the FEAT code. These motions were used

at the beginning of the next time step in calculating the forces of (1) and (2). A time step of 1 msec. was used in the calculations. The code was run to obtain a 1 sec time history of suspension element and in-structure contents response.

5.2 Results

The initial equilibrium position of the in-structure contents and the static forces in all suspension system elements were calculated by the code and printed out. Time histories of contents motions were output including c.g. horizontal acceleration and vertical acceleration and displacement, and the horizontal acceleration and displacement of the top and bottom of the contents. The responses of each suspension element were described by time histories of the incremental change in the gap between the contents attachment point and the structure attachment point, the incremental change in the element free length, force developed in each component of the suspension element, and the total force developed in a suspension element.

Typical time histories of suspension system/in-structure contents responses obtained are presented in Figures 5-2 to 5-8. The vertical displacement response of the in-structure contents c.g. to the input structure motions is shown in Figure 5-2. The horizontal displacement responses of the top and bottom of the contents (points A and B of Figure 5-1) are shown in Figure 5-3. The vertical and horizontal accelerations of the contents c.g. are given in Figures 5-4 and 5-5, respectively. The total forces developed in upper and lower horizontal, and a vertical suspension element (1, 3 and 4 of Figure 5-1) are given in Figures 5-6, 5-7 and 5-8, respectively.

5.3 Discussion

The contents c.g. responds to the input vertical displacement with the delayed "harmonic" motion shown in Figure 5-2. The large Coulomb friction included in the vertical suspension elements results in a highly damped motion whose "frequency" is much greater than that used to size the linear spring of the vertical suspension element (0.5 cps). A peak vertical relative displacement of 10.4 in. between contents and structure was developed at 0.20 seconds.

The difference in horizontal displacements at the top and bottom of the contents, shown in Figure 5-3, is proportional to the pitch response of the contents. Pitch displacement was excited primarily due to the eccentricity of the horizontal suspension system forces relative to the contents c.g. The initial facility displacements resulted in a clockwise torque about the content's c.g. with consequent clockwise acceleration. However, pitch response

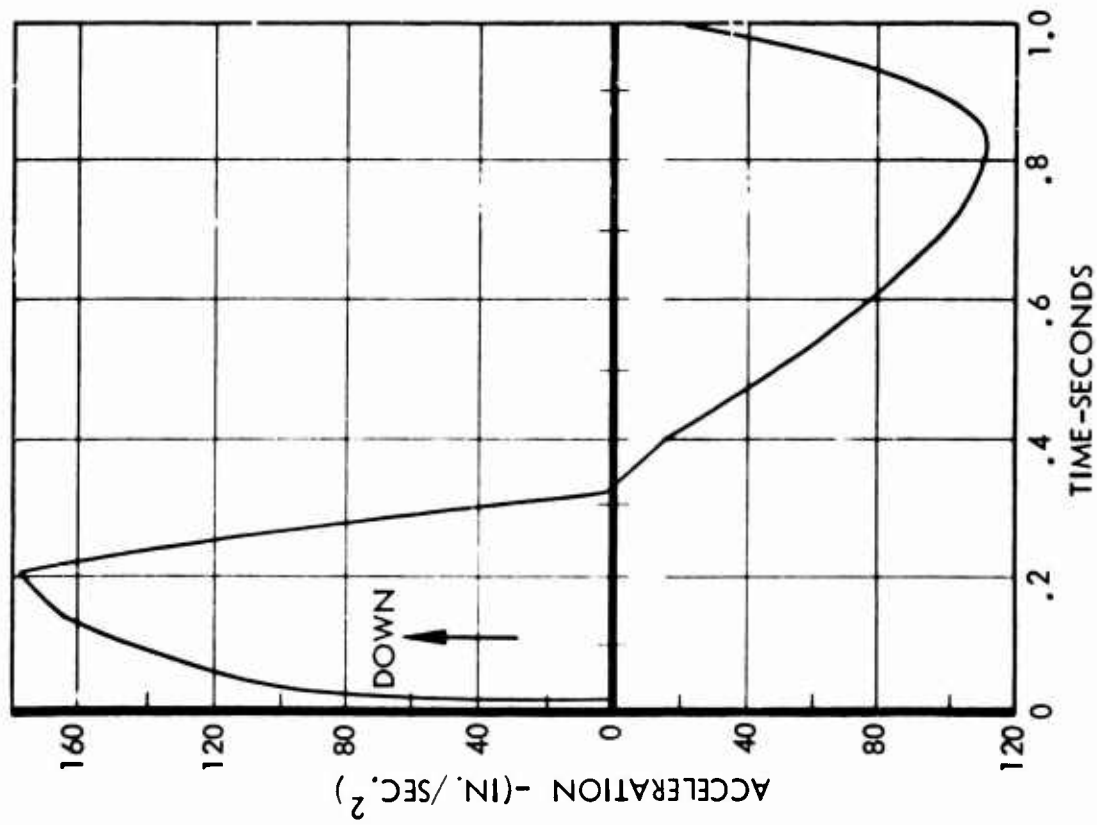


Figure 5-4: VERTICAL ACCELERATION OF C.G.

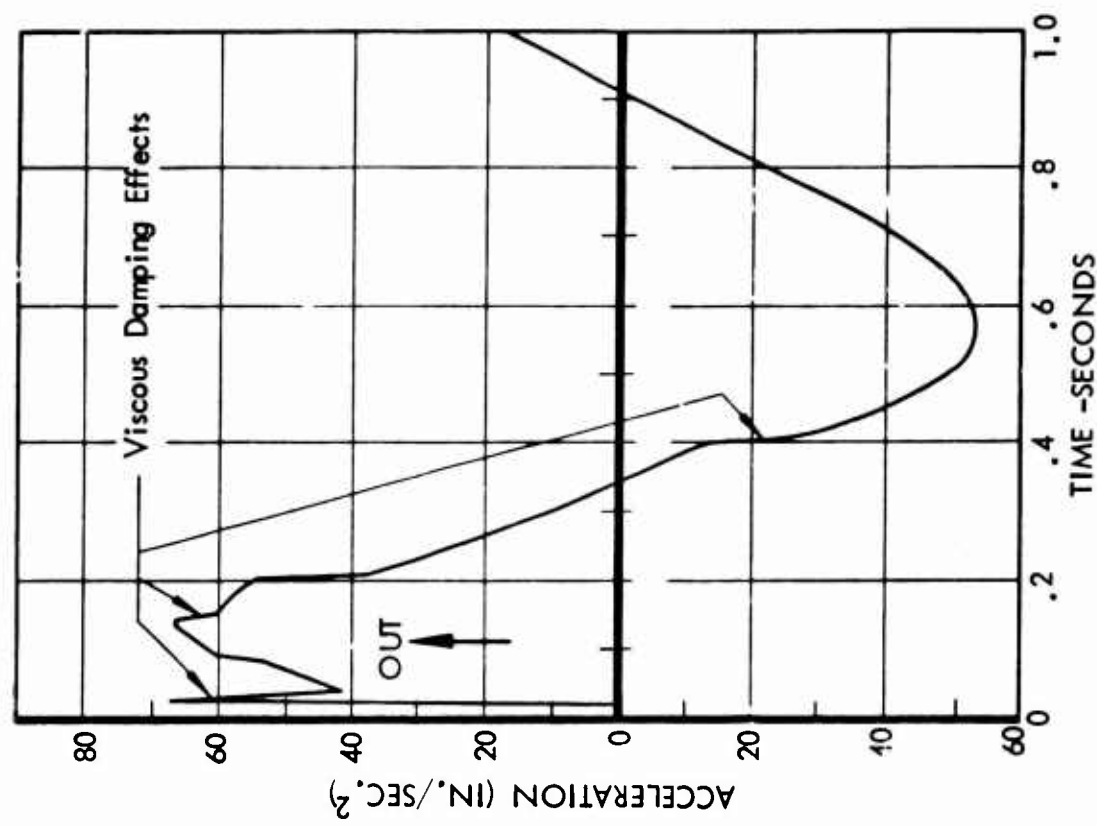


Figure 5-5: HORIZONTAL ACCELERATION OF C.G.

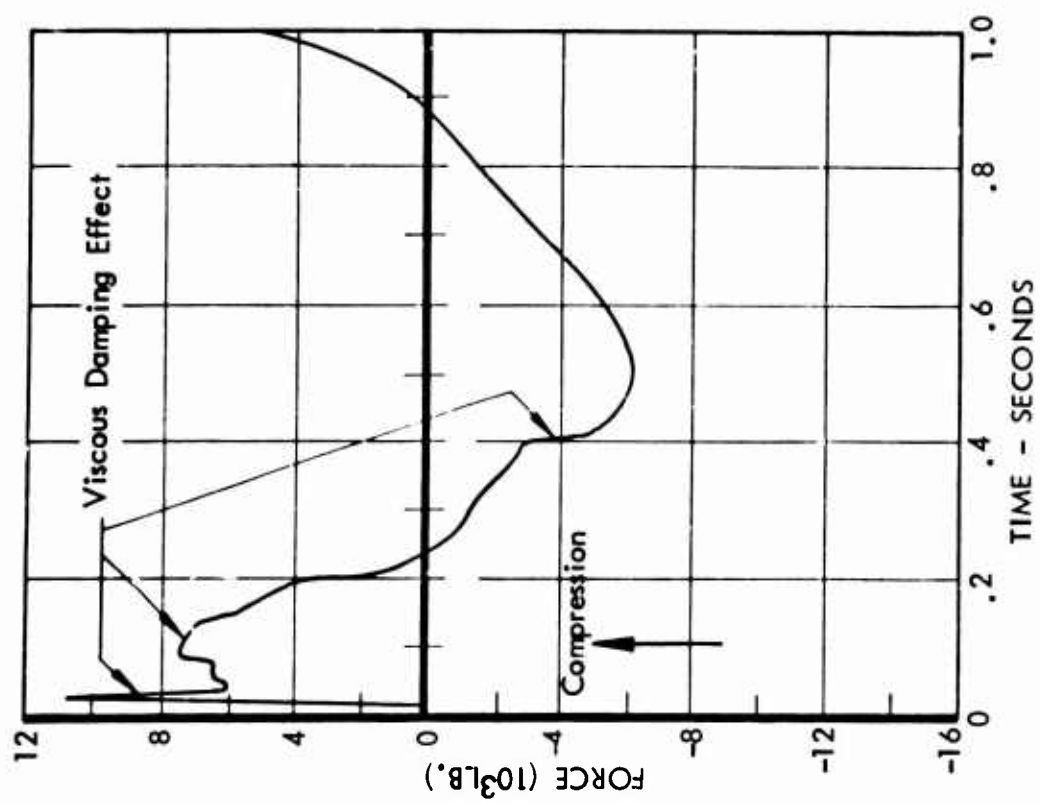


Figure 5-6: FORCE IN SUSPENSION ELEMENT (1)

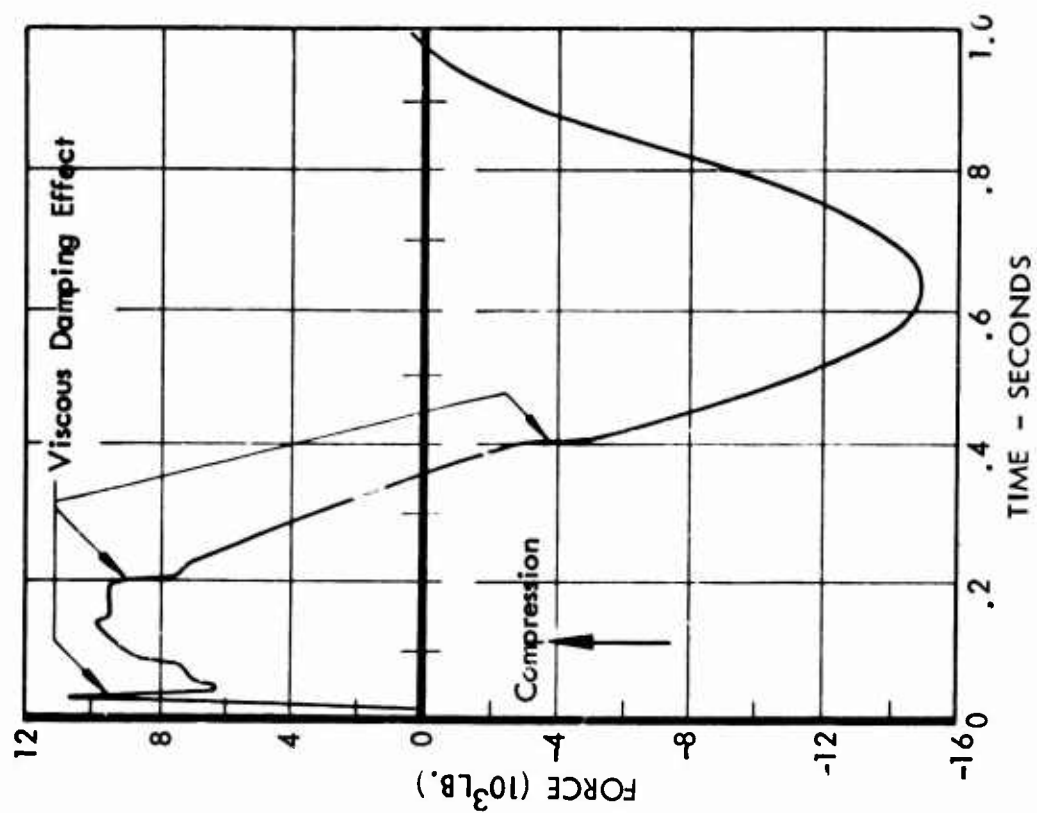


Figure 5-7: FORCE IN SUSPENSION ELEMENT (3)

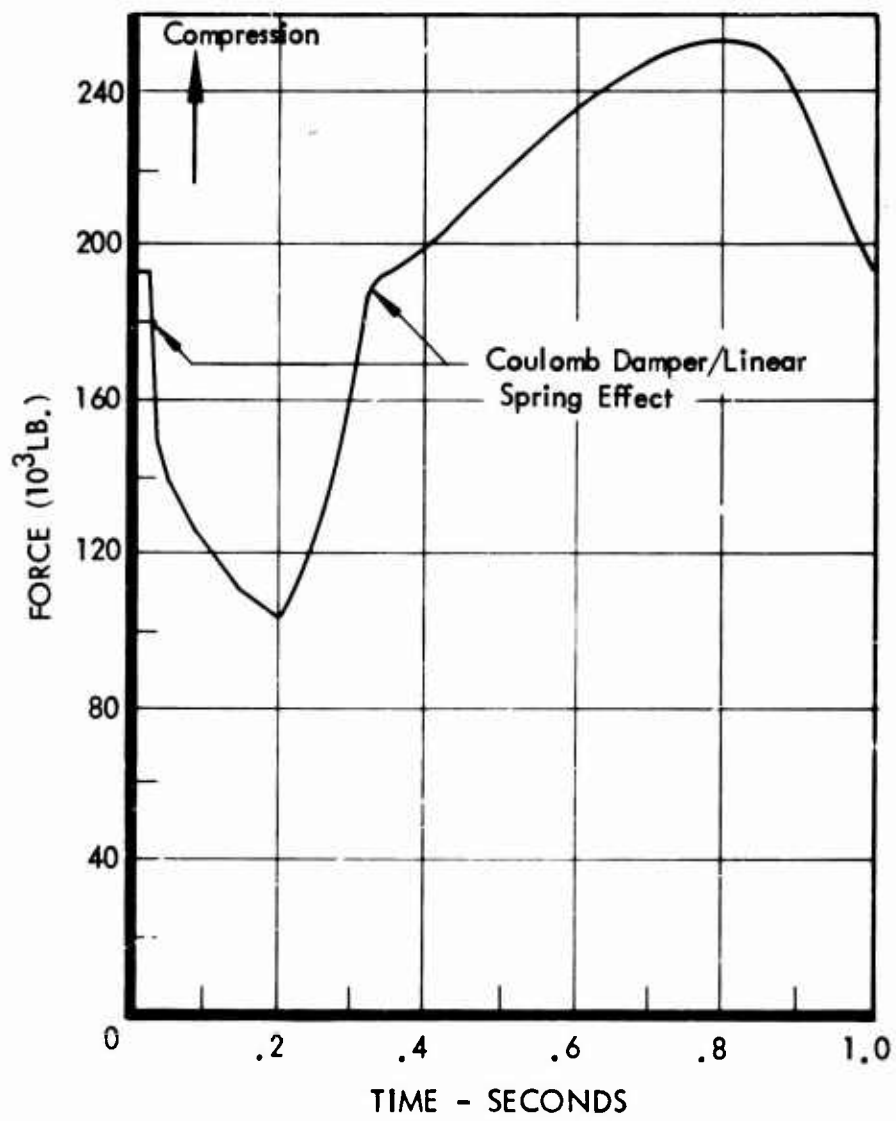


Figure 5-8: FORCE IN SUSPENSION ELEMENT (4)

frequency was such that pitch motions had reversed at the time of peak horizontal displacements. As a result the incremental displacement due to pitch tended to reduce the peak horizontal displacement at the top of the contents, and to increase that at the bottom.

The vertical acceleration of the contents c.g. shown in Figure 5-4 reflects the vertical suspension element relative deflections shown in Figure 5-2. The sharp breaks in acceleration at 0.02 and 0.32 sec. corresponds to the force limit of the Coulomb damper linear spring components of the vertical suspension elements. The peak downward incremental acceleration of 169 in/sec^2 is well within acceptable limits for shock isolation although no specific goals were established in this direction.

The horizontal acceleration of the contents c.g. shown in Figure 5-5, reflects the relative displacements of the horizontal suspension elements shown in Figure 5-3. The sharp breaks in acceleration occur at each of the changes of slope of the input structure displacement. Since the displacements were input as straight lines, each change in slope corresponds to a step change in velocity. A viscous damper component of a horizontal suspension element responds to a step change in velocity with a step change in force.

The forces developed in horizontal suspension elements 1 and 3 are shown in Figures 5-6 and 5-7, respectively. They substantiate the observations made on horizontal contents accelerations and displacements above. Horizontal forces at the top of the contents, Element 1, are smaller than those at the bottom, Element 3, due to the smaller motions. Viscous damper forces are apparent in both figures.

The force developed in a vertical suspension element (Element 4) is given in Figure 5-8. The Coulomb slip force (38600 lb) is responsible for the sharp change in slope at .02 and 0.32 sec. The sharp change in slope at 0.20 sec. reflects the change in slope of the input vertical structure displacement at the same time.

VI

DEBONDING AND SLIP TEST RUN

6.1 Pilot Program

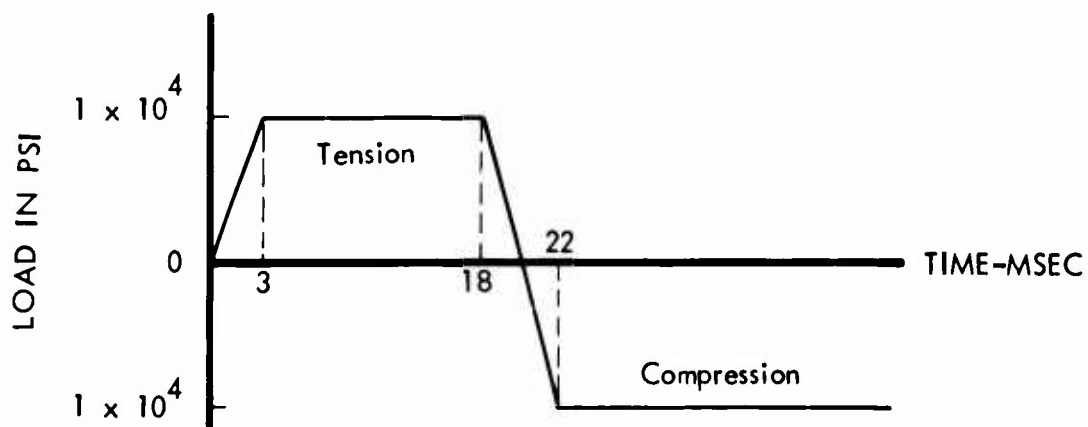
A pilot program was written and exercised to study the techniques for debonding and slip which are used in the main programs. This program used a plane strain model of the FEAT code; its layout and dimensions are shown in Figure 6-1.

During the development of the debonding and slip techniques for the FEAT programs a number of problems were solved, each with increased complexity. To illustrate the type of investigation which was conducted, the results of the so-called "Cork Problem" are presented.

6.2 "Cork Problem"

The purpose of this problem was to exercise all capabilities of the debonding and slip technique. The problem was posed so that certain specified nodes would experience the various phases of being joined, debonding or slipping. The model used is as described in Figure 6-1. The nodal locations of the data points can be identified from that layout.

The load pulse which was applied to the surface of the structure region is shown below.



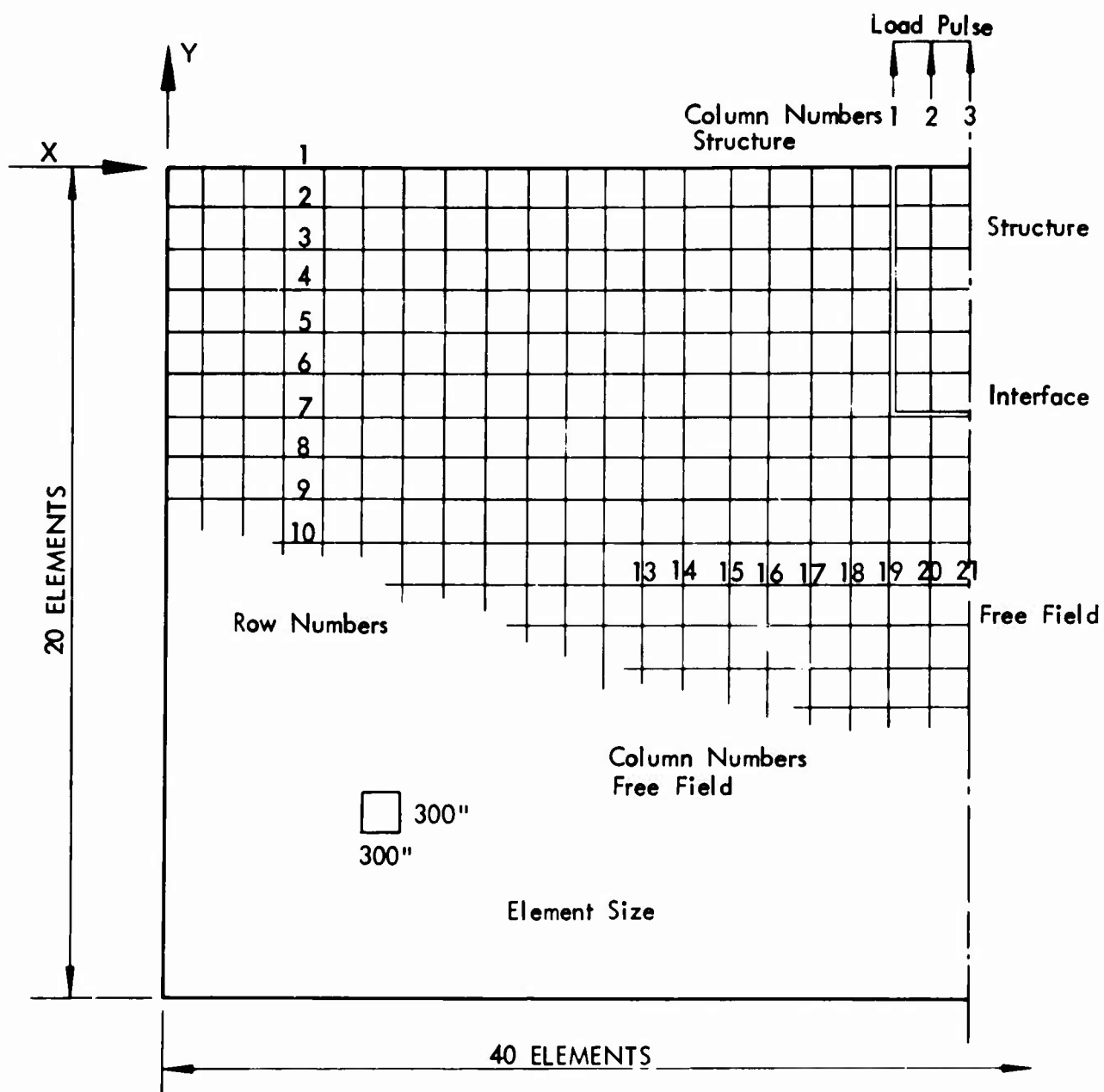


Figure 6-1: PILOT PROGRAM MODEL

The material properties used in this analysis are listed in Table 6-1. A detailed description of the technique used and identification of such special parameters as the velocity band are contained in Section 5.0 of Part I of this report.

TABLE 6-1

PILOT PROGRAM PARAMETERS

Parameter	Free Field	Interface	Structure
Density, $\frac{\text{lb} - \text{sec}^2}{\text{in}^4}$	2.497×10^{-4}		2.497×10^{-4}
Young's Modulus, psi	40.0×10^6		9.176×10^6
Poisson's Ratio	.25		.25
Cohesive Force, lb		3.75×10^5	
Velocity Band, in/sec		15.0	
Coefficient of Friction		.30	

6.3 Results

A number of displacement and stress time histories are presented to show the effect of allowing the interface between structure and earth medium to separate or slip. The displacement-time histories for three interface nodes are shown in Figures 6-2 through 6-7. Figures 6-2 and 6-3 refer to an interface node pair at the free surface, while 6-4 and 6-5 show displacements at a node pair half-way down the side of the structure. Figures 6-6 and 6-7 present the displacements of the bottom corner of the structure and of the surrounding medium.

Figures 6-8 through 6-13 show stress-time histories for the elements between rows 4 and 5 on the medium side of the interface as well as on the structure side. Horizontal, vertical, and shear stress plots are presented with comparison between solutions with and without debonding and slip.

The conclusion to be drawn from the performance of the pilot program, is that the techniques which were devised to handle this phenomenon in the finite element calculations are capable of providing the desired effects.

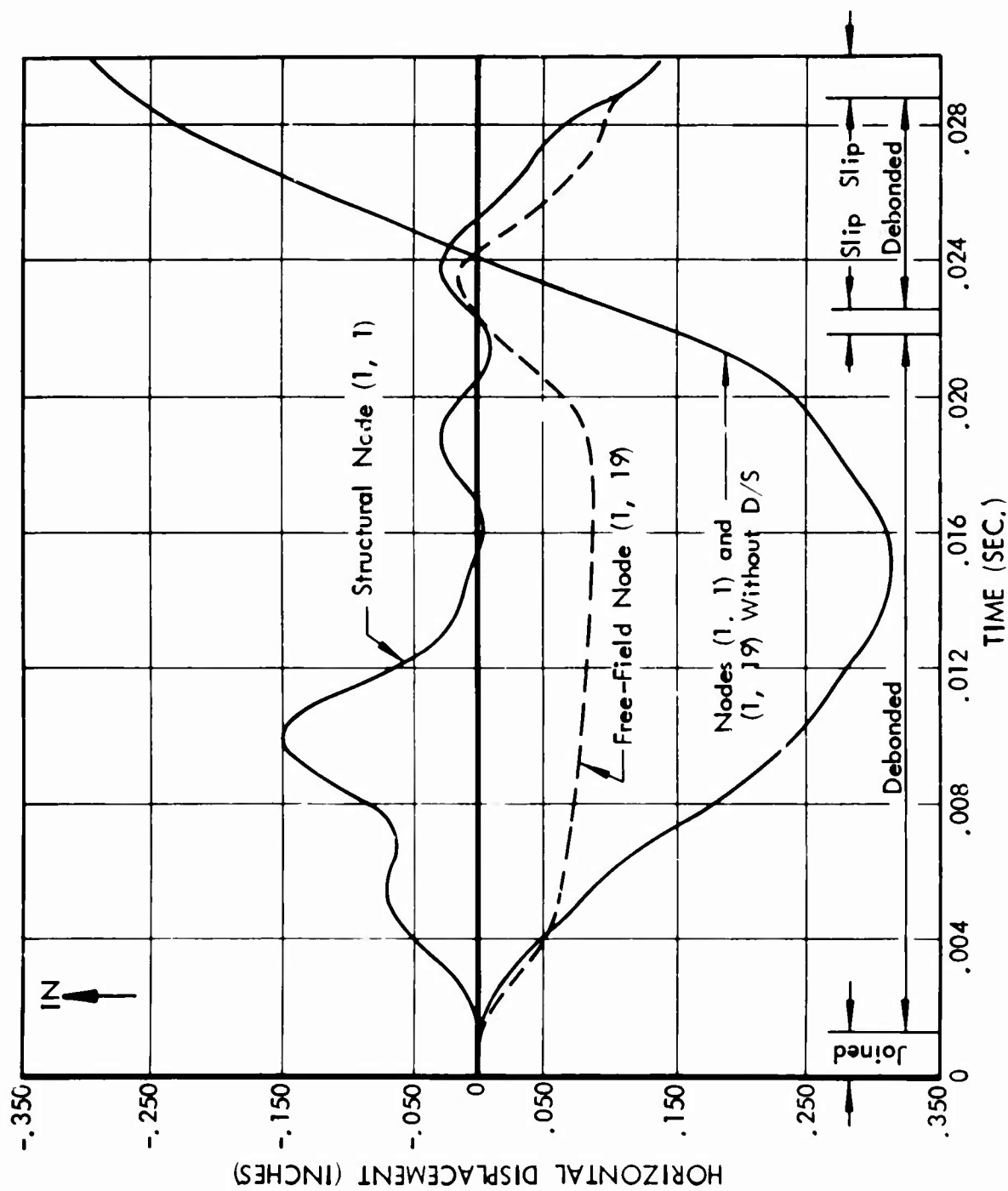


Figure 6-2: HORIZONTAL DISPLACEMENT - SURFACE NODE

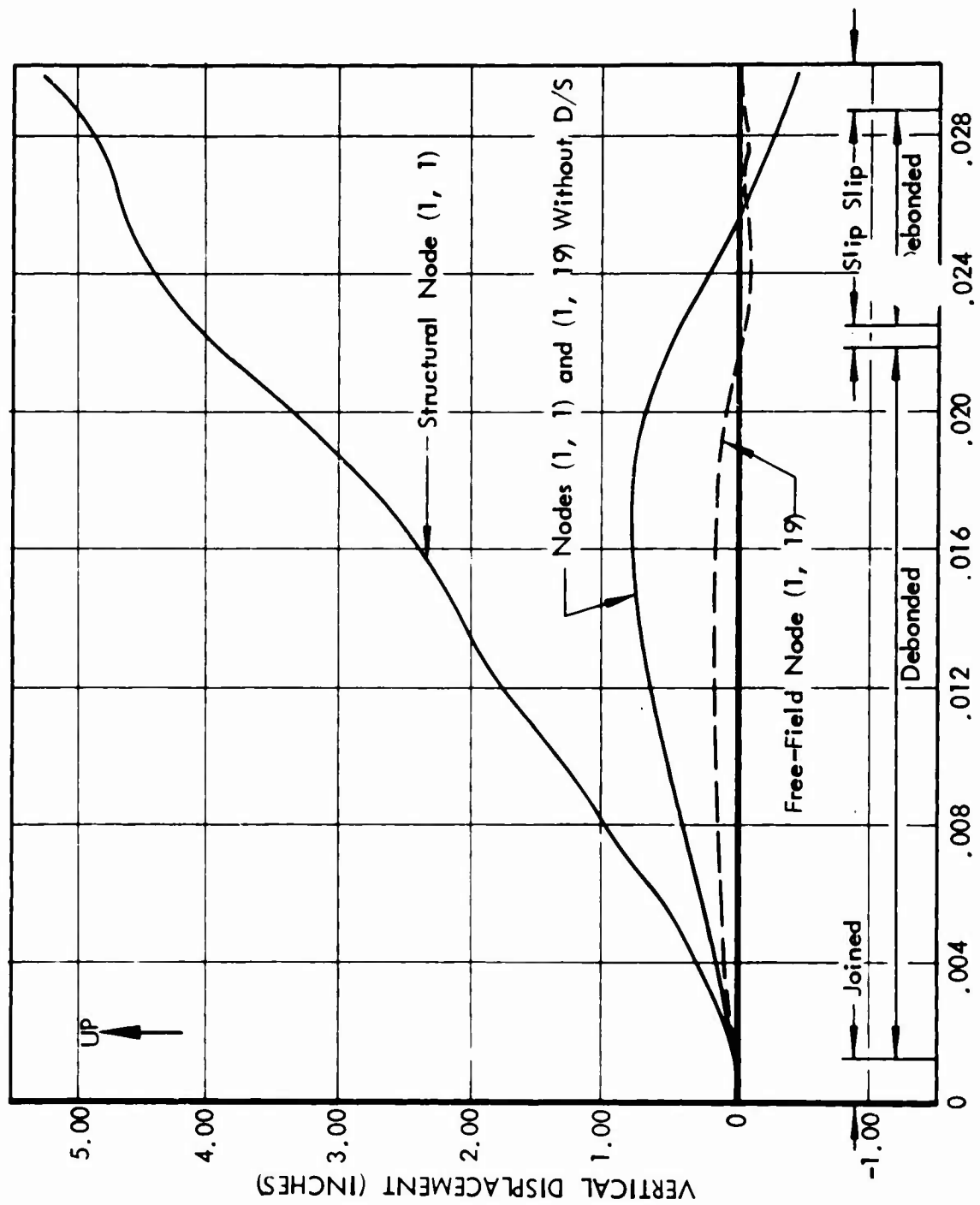


Figure 6-3: VERTICAL DISPLACEMENT - SURFACE NODE

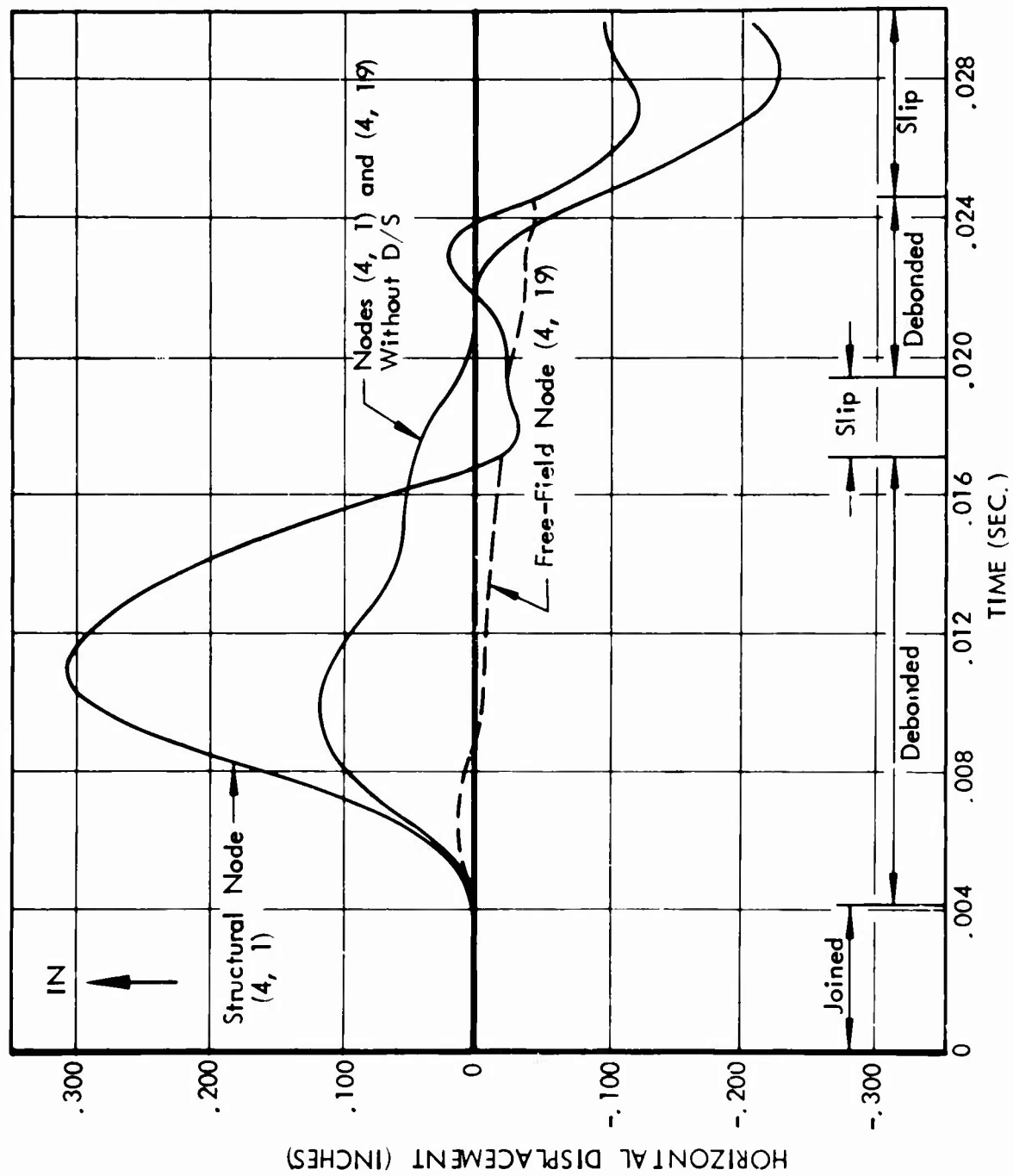


Figure 6-4: HORIZONTAL DISPLACEMENT - MID-POINT NODE

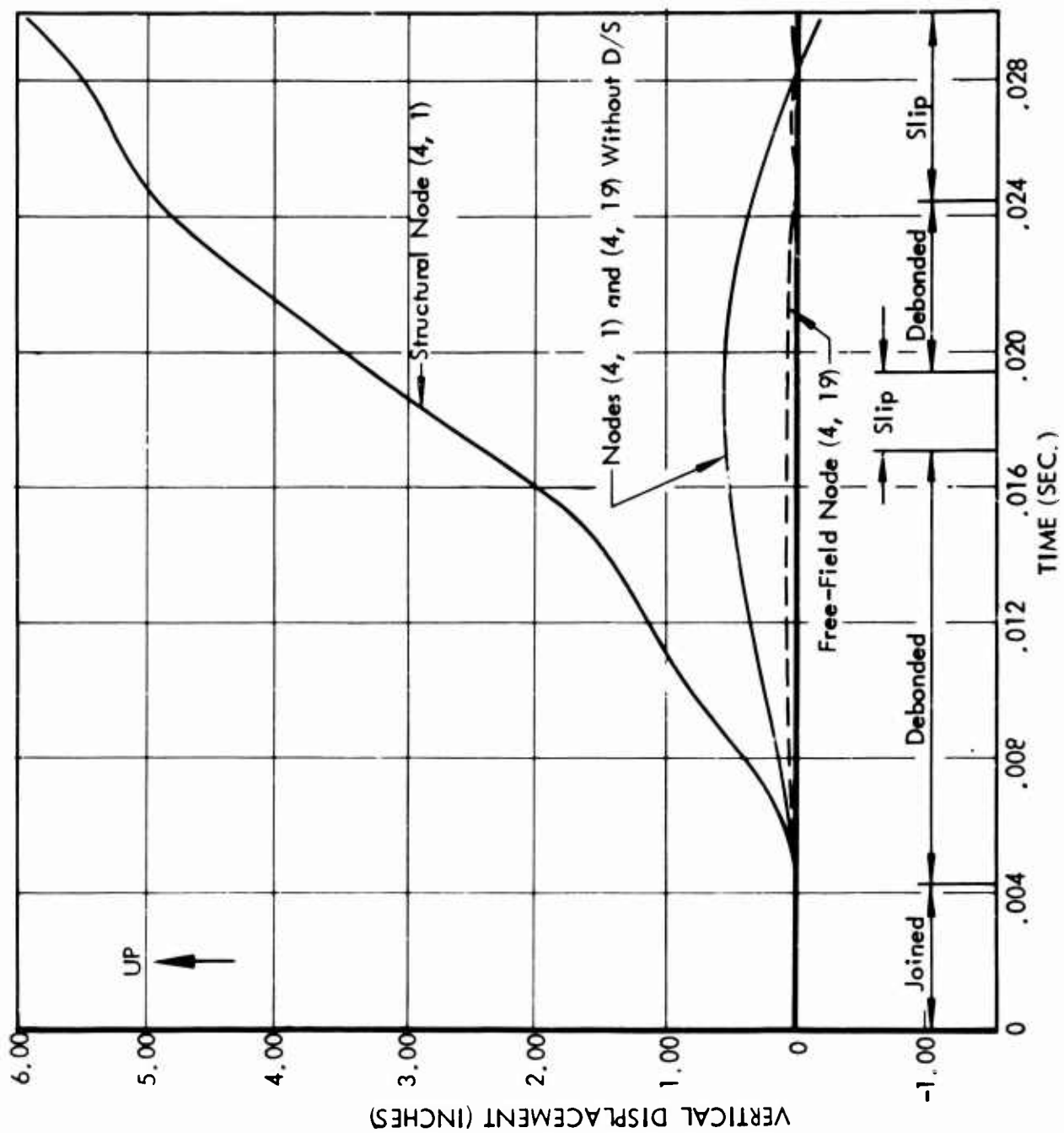


Figure 6-5: VERTICAL DISPLACEMENT - MID POINT NODE

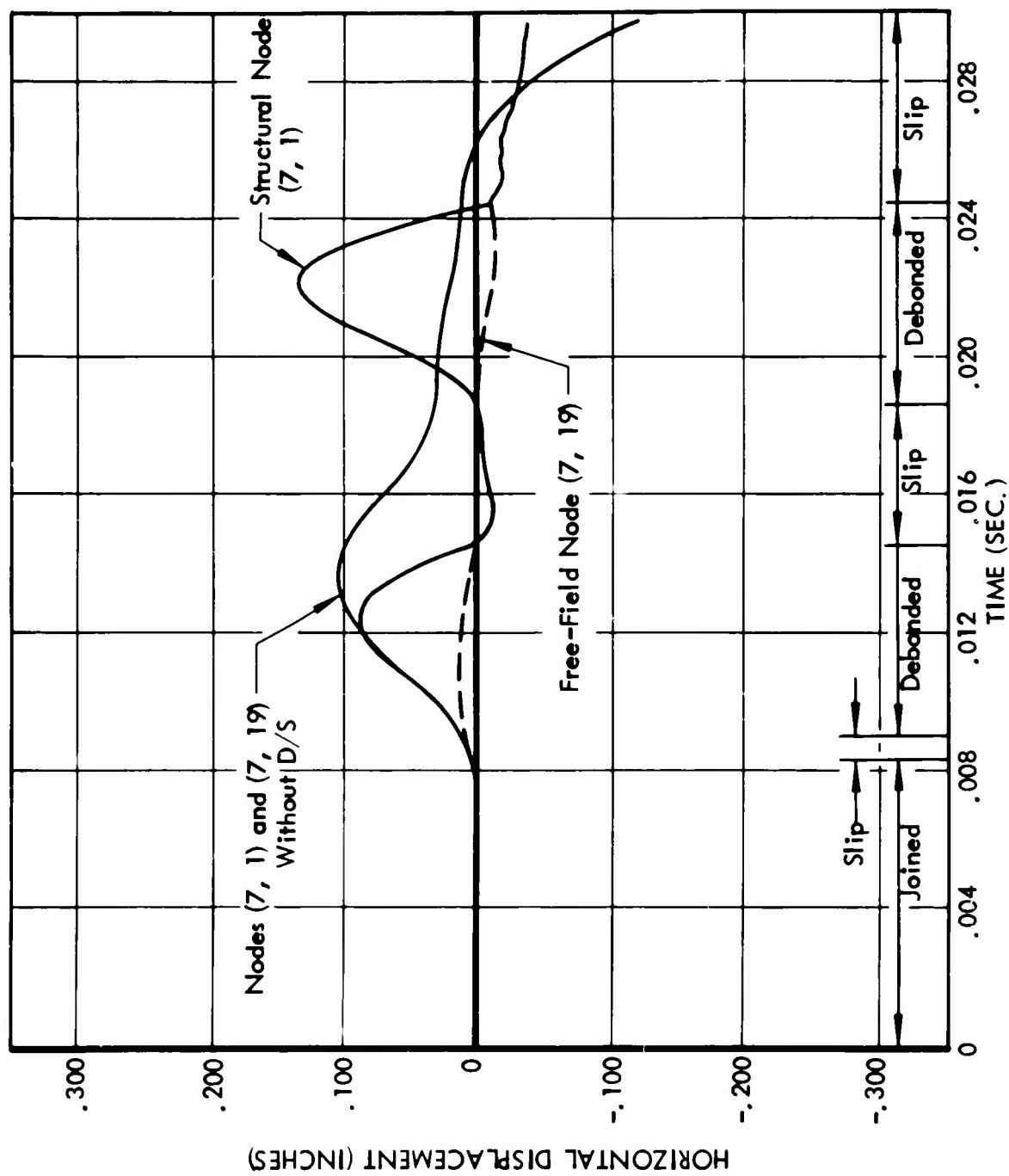


Figure 6-6: HORIZONTAL DISPLACEMENT - CORNER NODE

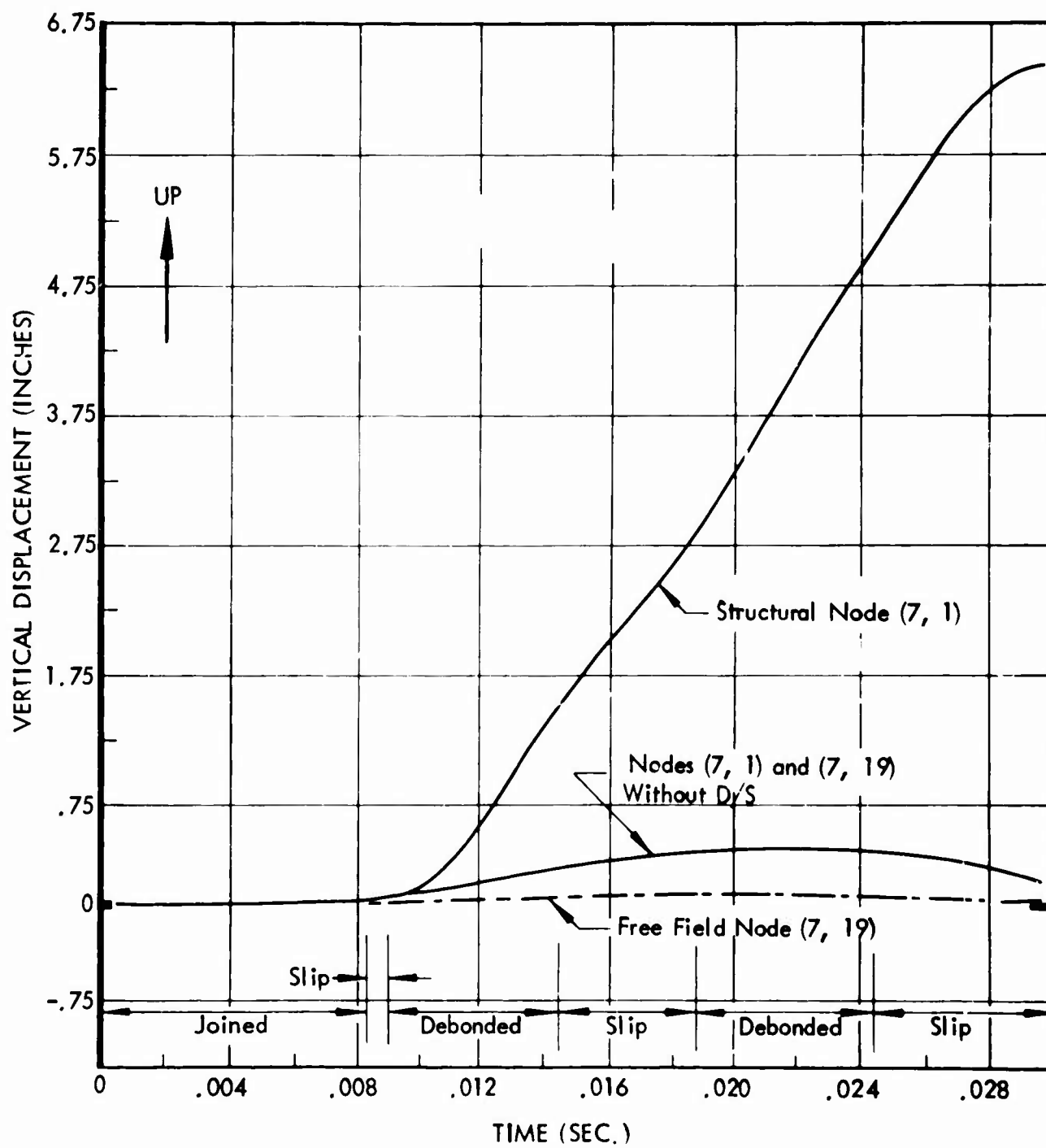


Figure 6-7: VERTICAL DISPLACEMENT - CORNER NODE

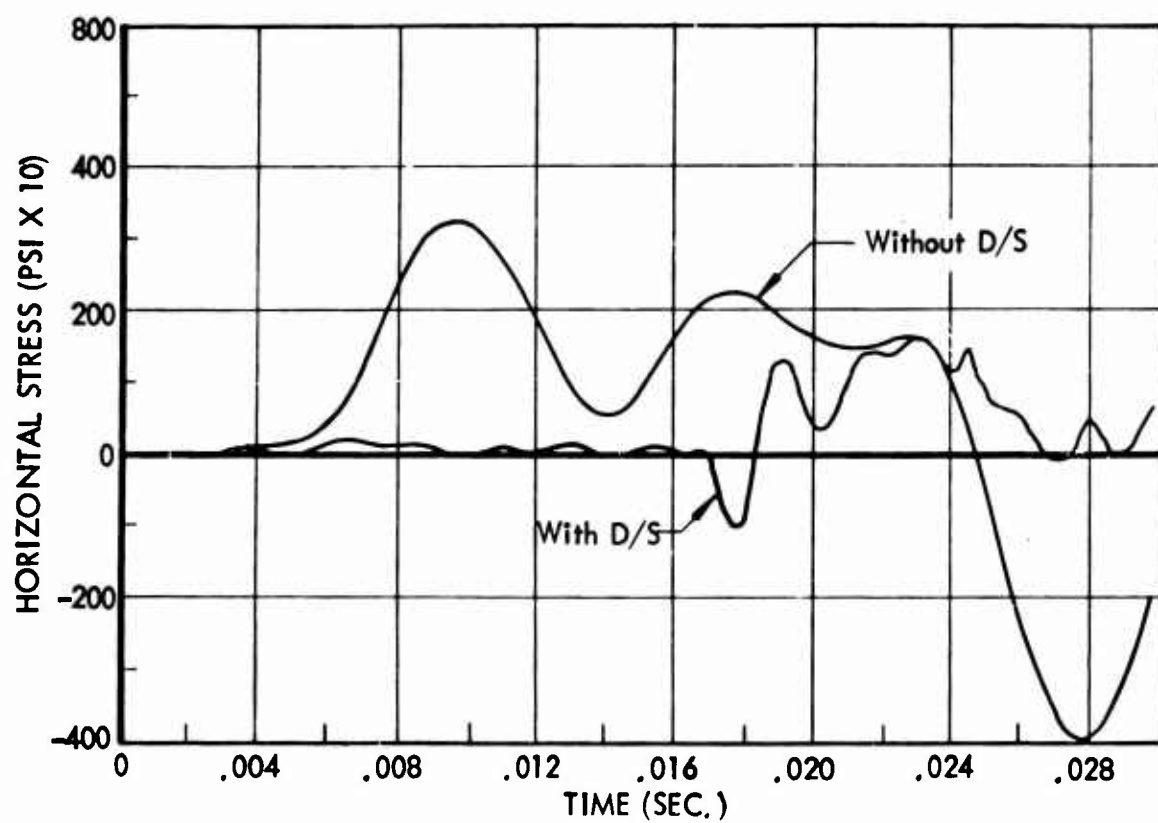


Figure 6-8: HORIZONTAL STRESS IN FREE-FIELD ELEMENTS (4, 18)

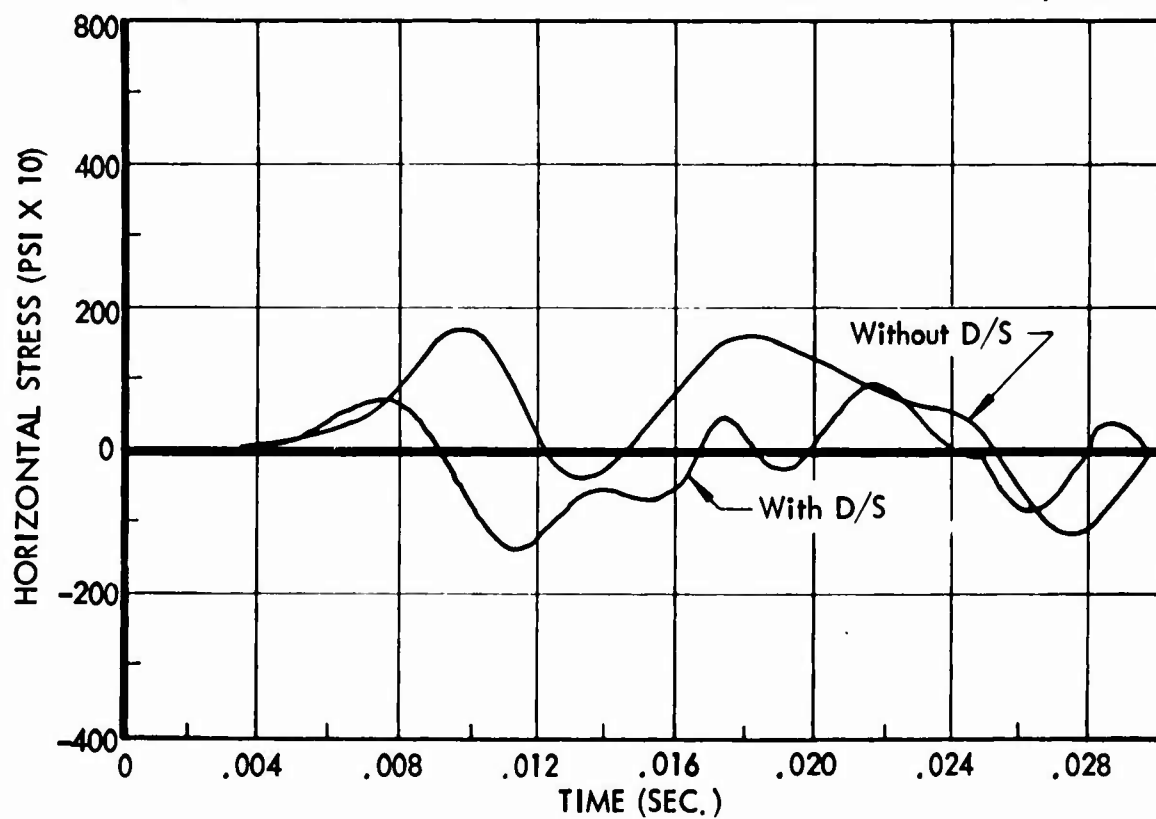


Figure 6-9: HORIZONTAL STRESS IN STRUCTURAL ELEMENT (4, 1)

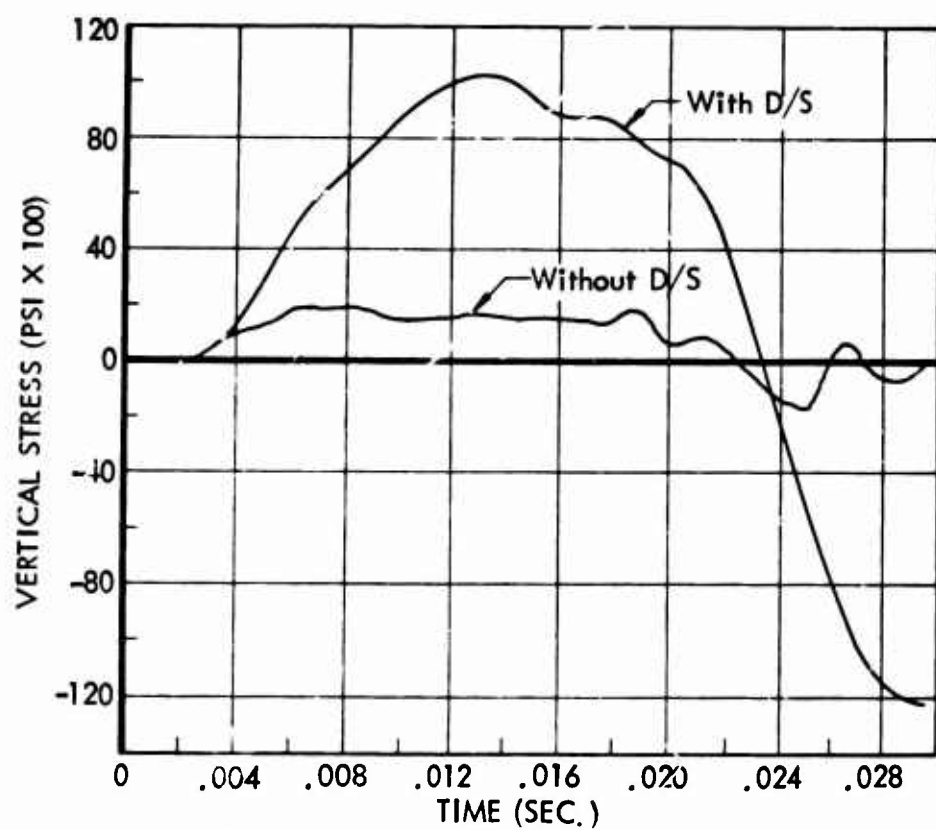


Figure 6-10: VERTICAL STRESS IN FREE-FIELD ELEMENT (4, 18)

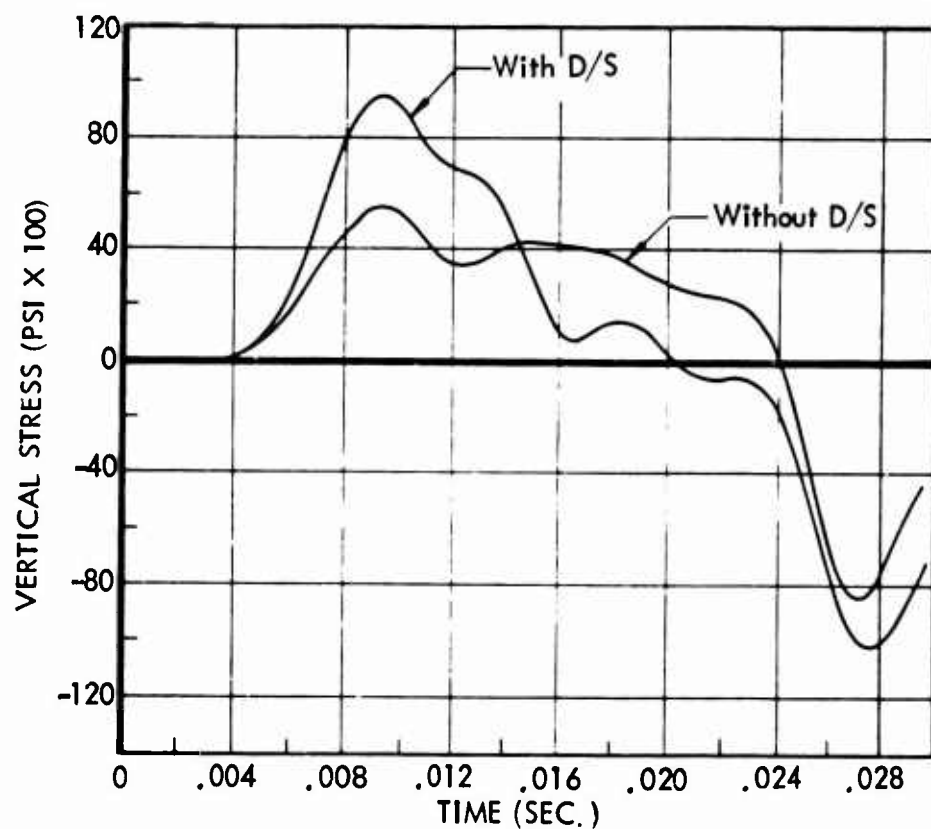


Figure 6-11: VERTICAL STRESS IN STRUCTURAL ELEMENT (4, 1)

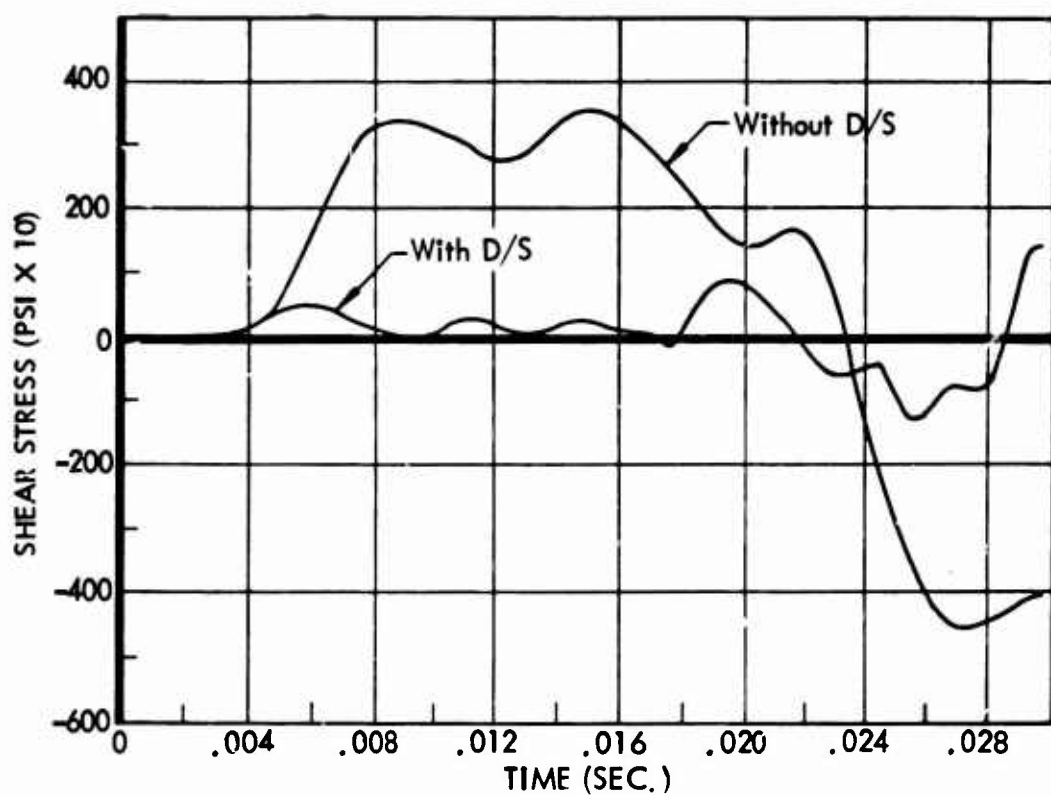


Figure 6-12: SHEAR STRESS IN FREE-FIELD ELEMENT (4, 18)

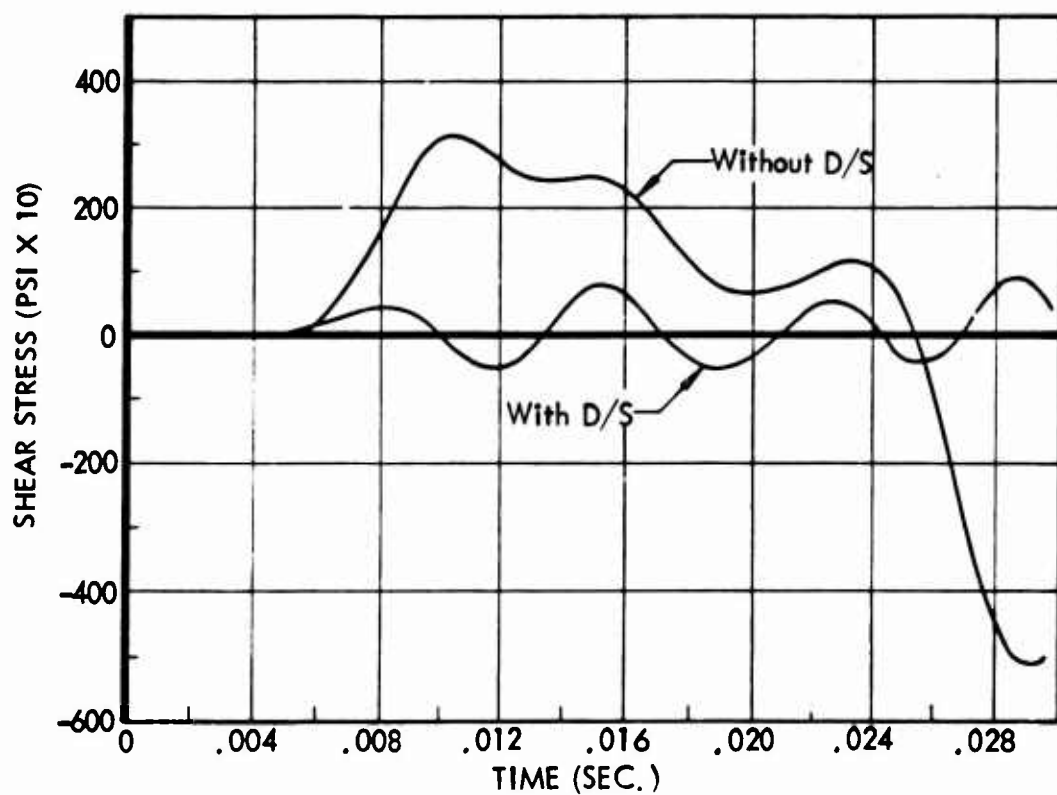


Figure 6-13: SHEAR STRESS IN STRUCTURAL ELEMENT (4, 1)

VII

COMPILATION OF MATERIAL PROPERTIES

This section presents the compilation of pertinent material property data for earth media (especially rock), construction and isolation materials.

7.1 Earth Media

There is a wide natural variation in the material properties of earth media. Furthermore existing soil and rock test data have been obtained, presented, and interpreted in a variety of ways. Apparently it will be some time before sufficient standardized test data become available to permit the material properties to be established on the basis of statistical analyses of data within standard geological classifications. In the interim, approximate material properties will be selected on the basis of existing data.

7.1.1 Yield Condition Parameters

The α and k parameters of the Drucker-Prager yield criterion (see equations 7-1 and 7-2) were determined by various investigators for 114 rock samples as shown in Table 7-1. The principal stresses during yielding were obtained from triaxial stress tests and one-dimensional (1-D) strain compression tests as the first step in the determination. In the case of triaxial testing, the axial stress and the confining pressure at the instant of specimen failure define one set of yield stresses, indicated by one point on the triaxial stress test yield path (See Figure 7-1). Additional samples of the same rock must be tested with different confining pressures to obtain additional sets of yield stresses sufficient to define the yield path. In the case of 1-D tests, a specimen is loaded axially while its lateral expansion is constrained. Throughout the test the axial stresses and constraining pressure are monitored providing a number of sets of yield stresses. At low levels of axial stress the data indicate essentially linear elastic behavior, with an abrupt change to plastic behavior as the stress level is increased as shown in Figure 7-1. Thus, in a triaxial test many samples are required to construct the yield path, but in a 1-D strain test only one sample is required. This is only possible for 1-D samples which do not exhibit work hardening, which was the case for all samples listed in Table 7-1.

Table 7-1: ROCK STRENGTH DATA

No.	Geological Classification	α	k	Confining Pressure psi (max)	Ref.
1	Granite (G-4), NTS	.202	7500	20,500	22
2	Granite (AFG-2), NTS	.177	4000	17,700	
3	Granite (AFG-5), NTS	.177	8800	22,000	
4	Granite (LG-2), NTS	.220	4280	22,000	
5	Rhyolite (R-2), NTS	.074	4025	24,500	
6	Rhyolite (R-3), NTS	.183	3940	21,500	
7	Rhyolite (R-4), NTS	.161	3740	18,500	
8	Rhyolite (R-7), NTS	.122	6800	24,000	
9	Rhyolite (R-8), NTS	.177	4000	24,000	
10	Rhyolite (R-9), NTS	.126	10400	23,300	
11	Rhyolite (R-10), NTS	.149	8560	23,800	
12	Rhyolite (R-11), NTS	.097	10600	20,500	
13	Basalt (B-1), NTS	.158	8380	18,500	
14	Basalt (B-2), NTS	.185	6700	22,200	
15	Basalt (B-3), NTS	.197	3040	24,200	22
16	Granite, origin unknown	.304	9600	12,000	23
17	Limestone, origin unknown	.105	3540	15,000	
18	Anhydrite, Blaine, Oklahoma	.206	5900	7,395	
19	Anhydrite (30% Gypsum) Alberta, Canada	.230	2100	10,000	
20	Basalt, Knippa, Texas	.210	14520	14,930	
21	Dolomite, Hasmark, Montana	.180	7930	29,000	
22	Dolomite, Luning, Nevada	.245	3570	74,675	
23	Dolomite, Glorieta, New Mexico	.175	4480	30,600	23
24	Dolomite, Clear Fork, Texas	.220	12000	29,290	24
25	Dolomite, Fusselman, Texas	.255	6490	29,290	
26	Dolomite, Blair, West Virginia	.155	20910	73,225	
27	Granite, Barre, Vermont	.345	4950	14,210	24

Table 7-1: (Continued)

<u>No.</u>	<u>Geological Classification</u>	<u>α</u>	<u>k</u>	<u>Confining Pressure psi (max)</u>	<u>Ref.</u>
28	Limestone, Alabama	.225	3000	29,435	24
29	Limestone, "Yule Marble", Leadville, Colorado	.170	3075	40,455	
30	Limestone, "Earthage Marble" Missouri	.150	3075	10,005	
31	Limestone, Becraft, New York	.130	6200	42,630	
32	Limestone, Wolfcamp (6A), Texas	.205	6100	29,290	
33	Limestone, Wolfcamp (3A), Texas	.180	4800	29,290	
34	Limestone, Fusselman, Texas	.180	2440	29,290	
35	Limestone, Devonian, Texas	.340	3920	29,290	
36	Limestone, Chico, Texas	.215	3923	10,005	
37	Limestone, Wells Station, Australia	.100	12608	14,500	
38	Limestone, Wombeyan Marble, Australia	.220	3736	3,045	
39	Limestone, "D-1 Formation," Alberta, Canada	.275	7020	14,935	
40	Limestone, Sobenhofren, Bavaria	.095	19680	16,240	
41	Limestone, "Carrara Marble," Italy	.100	9840	35,380	
42	Limestone, "White Dolomite," Origin unknown	.225	4800	14,935	
43	Pyrite, Utah	.285	5800	31,320	
44	Quartzite, Sioux, Minnesota	.230	37200	29,240	
45	Sandstone, Pico, California	.140	1853	29,000	
46	Sandstone, Berea, Ohio	.140	2779	29,000	
47	Sandstone, Bartlesville, Oklahoma	.150	2779	29,290	
48	Sandstone, Rush Springs, Oklahoma	.320	7345	14,790	
49	Sandstone, Barnes, Texas	.150	2768	29,290	

Table 7-1: (Continued)

<u>No.</u>	<u>Geological Classification</u>	<u>α</u>	<u>k</u>	<u>Confining Pressure psi (max)</u>	<u>Ref.</u>
50	Sandstone, Silty, Texas	.155	6150	14,790	24
51	Sandstone, Oil Creek, Texas	.345	3285	29,290	
52	Sandstone, Alberta, Canada	.120	3998	10,005	
53	Sandstone, Mutenberg, Germany	.175	3675	22,040	
54	Shale (muddy) Colorado	.125	2470	29,000	
55	Shale (calcareous) Colorado	.045	5100	29,290	
56	Shale (5900 Footsands) Texas	.070	5445	29,290	
57	Slate, Mettawee, Vermont	.080	6710	29,290	24
58	Siltstone, Permian "Red Beds," Texas	.125	3705	14,645	
59	Amphibolite (Fine to Medium grained), California	.477	4250	2,000	25
60	Andesite, Hypersthene I Palisades Dam	.365	4240	2,000	
61	Andesite, Hypersthene II Palisades Dam	.352	4275	2,000	
62	Basalt (low strength) Medord, Oregon	.343	4530	2,000	
63	Basalt (high strength) origin unknown	.375	6550	2,000	
64	Basalt (high strength) Idaho	.427	1470	2,000	
65	Basalt (medium strength) Idaho	.450	529	2,000	
66	Claystone (Silty) Texas	.362	38	3,000	
67	Claystone (silty and calcareous) Texas	.315	58	2,000	
68	Diorite, quartz, Idaho	.425	1850	2,000	
69	Diorite (low strength) origin unknown	.420	1550	2,000	
70	Diorite (high strength) origin unknown	.435	2280	2,000	
71	Granite, Grand Coulee, Washington	.452	2800	2,000	
72	Granite (coarse grained) Colorado	.445	1260	2,000	
73	Granite (slightly altered) Grand Coulee, Washington	.457	1180	2,000	

Table 7-1: (Continued)

No.	Geological Classification	α	k	Confining Pressure psi (max)	
74	Granite (pegmatite, group A) Thompson, Colorado	.456	865	2,000	25
75	Granite (pegmatite, group B) Thompson, Colorado	.426	1040	2,000	
76	Granite Wyoming, 1954	.447	3070	2,000	
77	Granite Wyoming, 1959	.445	3800	2,000	
78	Granite (altered) Wyoming	.435	1830	2,000	
79	Granite (Coarse grained, biolite) Arizona	.430	3430	2,000	
80	Graywacke, (sub-coarse-grained, high strength) California	.375	1760	2,000	
81	Graywacke, (sub-coarse-grained, low strength) California	.392	910	2,000	
82	Graywacke, (fine grained) California	.347	1765	2,000	
83	Graywacke, (medium grained) California	.360	1660	2,000	
84	Limestone (fine grained) Marble Canyon,	.460	1795	2,000	
85	Limestone (medium grained) Marble Canyon, Arizona	.272	6050	2,000	
86	Limestone (porous) Marble Canyon, Arizona	.380	2480	2,000	
87	Limestone (chaledonic) Marble Canyon, Arizona	.440	2500	2,000	
88	Limestone (stylolitic) Marble Canyon, Arizona	.460	1620	2,000	
89	Monzonite Porphyry (low strength) Wash.	.465	1960	2,000	
90	Monzonite Porphyry (high strength) Wash.	.488	2140	2,000	
91	Monzonite porphyry, Washington	.437	2870	2,000	
92	Phyllite, graphitic, Sly Park Dam, Calif.	.375	316	2,000	
93	Phyllite, quartzose, slightly weathered, California	.390	256	2,000	

Table 7-1: (Continued)

No.	Geological Classification	α	k	Confining Pressure psi (max)	Ref.
94	Phyllite, sericite, moderately weathered California	.383	285	2,000	25
95	Sandstone, (low strength), Wyoming	.380	1750	2,000	
96	Sandstone, (high strength), Wyoming	.389	2450	2,000	
97	Sandstone, (ferruginous, media) Arizona	.442	1990	2,000	
98	Sandstone, (quartzose), Arizona	.417	1815	2,000	
99	Sandstone, (medium grained, red), Arizona	.389	1250	2,000	
100	Schist (biotite with pegmatite,) Colorado	.230	2520	2,000	
101	Schist (high strength), Colorado	.480	969	2,000	
102	Schist (biotite - chlorite, low strength), Colorado	.467	304	2,000	
103	Schist (high strength), Colorado	.510	499	2,000	
104	Schist (biotite - sillimanite, low strength), Colorado	.415	460	2,000	
105	Schist (high strength), Colorado	.529	204	2,000	
106	Schist (quartz injection, low strength), Colorado	.375	206	2,000	
107	Schist (high strength), Colorado	.398	319	2,000	
108	Schist (sericite, quartzose), California	.432	320	2,000	
109	Schist, Fremont Canyon, Wyoming	.300	2610	2,000	
110	Shale (calcareous) Marble Canyon, Arizona	.430	1505	2,000	
111	Shale (quartzose) Marble Canyon, Arizona	.355	3600	2,000	
112	Siltstone, Monticello Dam, California	.400	706	2,000	
113	Siltstone, Texas	.425	699	2,000	
114	Tuff, Lithic, Oregon	.325	108	2,000	25

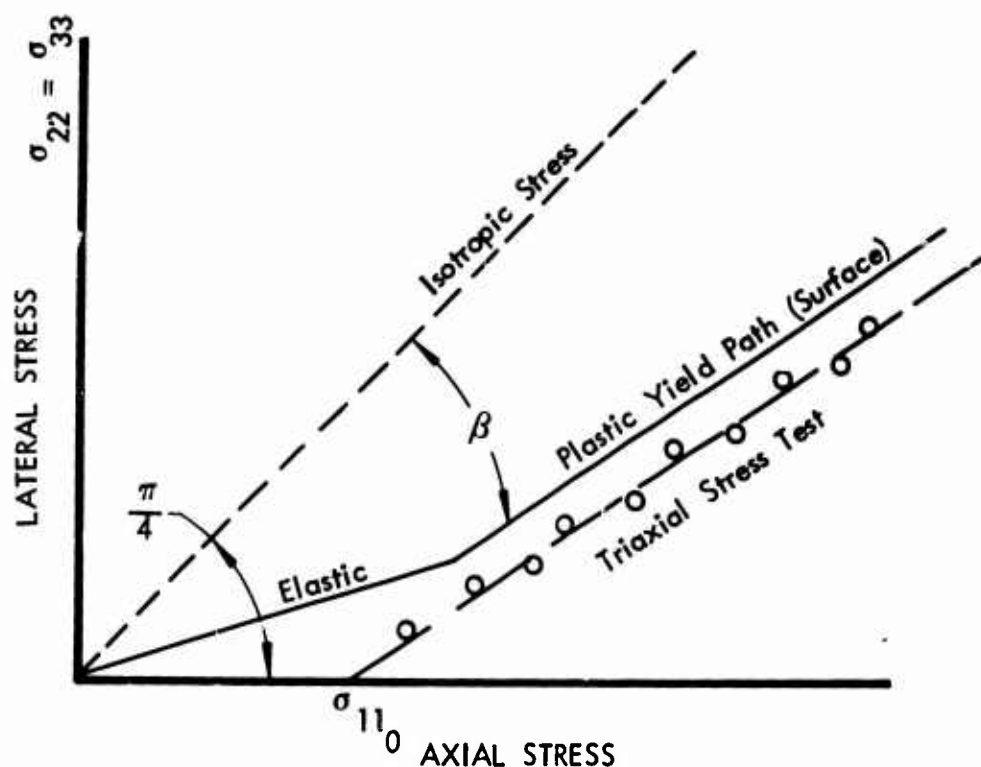


Figure 7-1: ELASTIC-PLASTIC YIELD PATHS

The intercept of the yield path with the axial stress axis is called the unconfined compressive strength, and is denoted here by σ_{110} . The angle between the yield path and the isotropic stress line (the isotropic stress line is inclined 45° to the axial stress axis) is denoted by β . The yield parameters are defined in terms of σ_{110} and β as follows:

$$\alpha = \frac{1}{\sqrt{3}} \frac{1 - \tan(\pi/4 - \beta)}{1 + 2 \tan(\pi/4 - \beta)} \quad (7-1)$$

$$k = (\alpha - 1/\sqrt{3}) \sigma_{110} \quad (7-2)$$

A plot of k versus α for the rock samples listed in Table 7-1 is presented in Figure 7-2. The values of α for the rock samples, tested under low confining pressure where the microcrack closing process is very pronounced, (the open symbols), lie mainly in the band between $\alpha = .3$ and $\alpha = .5$. The high values of α are due to the fact that the closing of the cracks causes an increase in the strength increments for given increments of confining pressure.

The values of α for the rock samples tested under high confining pressures (the solid symbols) lie mainly in the band between $\alpha = .1$ and $\alpha = .3$. These are more realistic of the actual confining pressure in the structure-medium interaction phenomenon. The value $\alpha = 0.177$ fits this data approximately, as shown in Figure 7-2. For this value of α , equation 7-2 becomes:

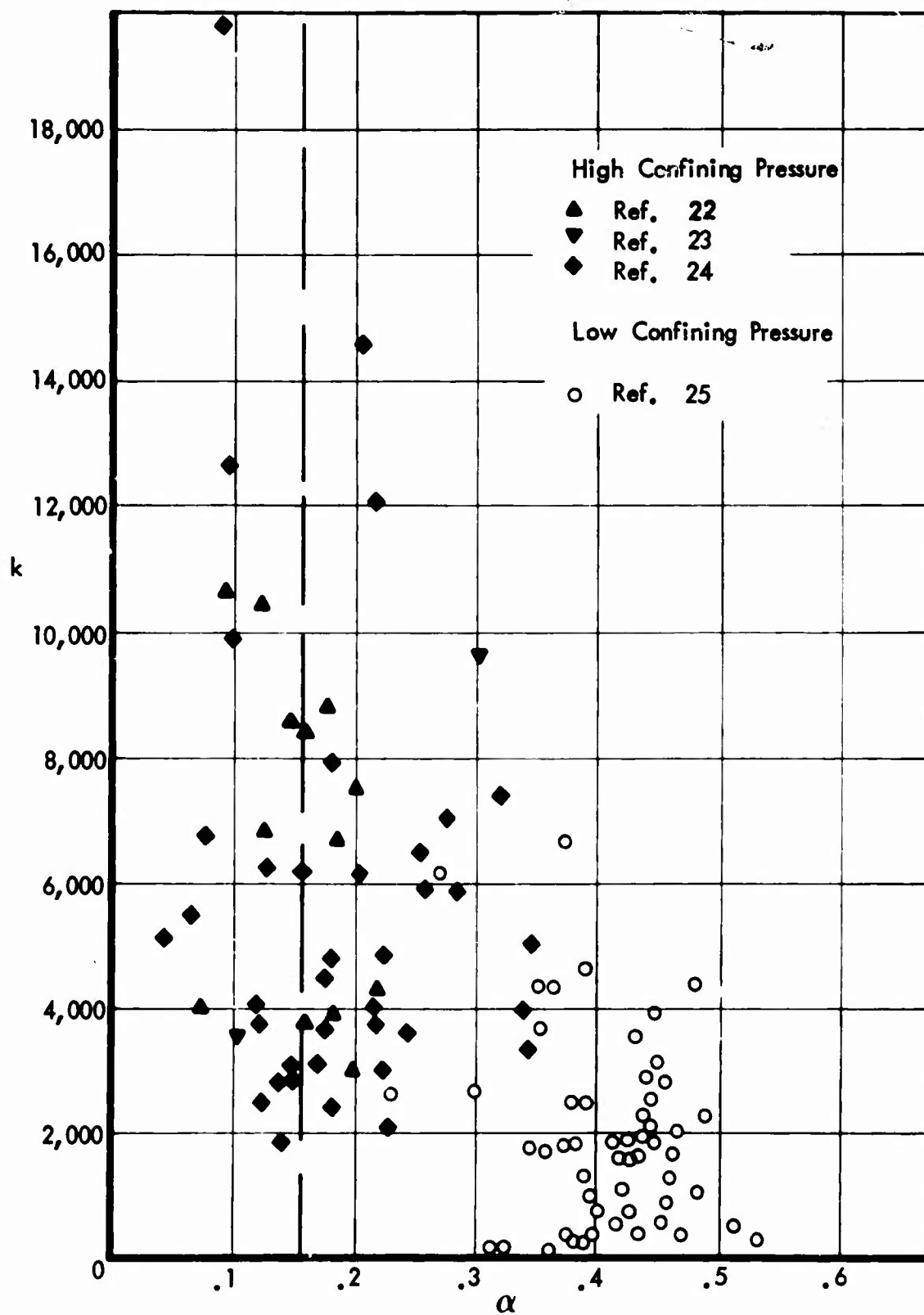


Figure 7-2: DRUCKER-PRAGER PARAMETERS FOR ROCKS

$$k \approx 0.4 \sigma_{110} \quad (7-3)$$

7.1.2 Poisson's Ratio

An examination of numerous test data (Ref. 26) shows that Poisson's ratio can vary for unconfined compression from about 0.1 to about 0.3 during loading and can approach 0.5 near ultimate load. Walsh (Ref. 27) has suggested that the increase in Poisson's ratio near ultimate load is due to crack closing initially and then crack sliding at high stress levels. The variation in Poisson's ratio presents difficulties in the evaluation and application of the confined compression test data.

Poisson's ratio can be determined from the following linear elasticity relationship:

$$\nu = \frac{K_o}{1 + K_o} \quad (7-4)$$

where K_o is the coefficient of earth pressure at rest. It is equal to the slope of the elastic portion of the lateral-axial stress plots for 1-D strain, as shown in Figure 7-3.

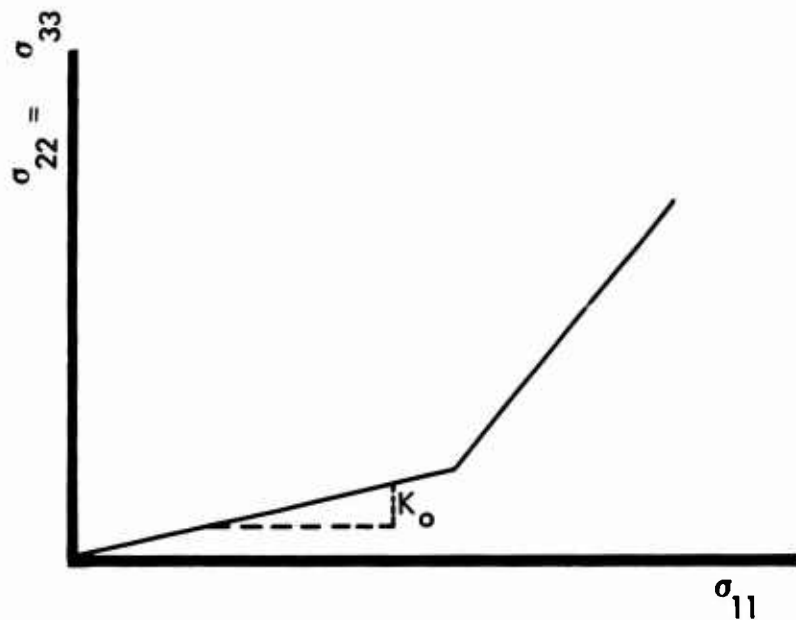


Figure 7-3: LATERAL-AXIAL STRESS PLOTS FOR 1-D STRAIN

Poisson's ratio was computed for the 14 rock samples tested in 1-D strain in Ref. 22. The results are shown in Table 7-2. The values of Poisson's ratio for the rocks listed range from .167 to .250, with the average for this group at .200.

7.1.3 Young's Modulus

A comprehensive test program in connection with the development of an engineering classification for intact rock is described in Ref. 26. A listing of the rock samples tested is presented in Table 7-3. Figure 7-4 is a plot of unconfined compressive strength versus Young's modulus at 50% of the unconfined compressive strength. At 50% of maximum load, crack closing has ceased. The moduli taken in this manner do not include the crack closing history and are considered to be appropriate for the high stress level response problem. The straight line fit shown on Figure 7-4 and given below is a reasonable expression for Young's Modulus:

$$E = 300 \sigma_{110} + .9 \times 10^6 \quad (7-5)$$

The solid square symbols in Figure 7-4 were added from Table 7-2 for comparison. It appears that equation 7-5 fits the 1-D strain data of Table 7-2 fairly well.

7.1.4 Unit Weight

The unit weight for intact rock is, of course, dependent upon its geological classification. The average unit weight for each group of rock samples listed in Ref. 26 is presented in Table 7-3. The sedimentary rocks have lower unit weights and more variation of unit weights than the igneous and metamorphic rocks. A representative value of unit weight for these rock samples is 166 pounds per cubic foot.

7.2 Construction Materials

Structural materials of particular interest to the designer of hardened facilities are Portland cement concrete, steel, and crushable backfill materials.

7.2.1 Concrete (Portland Cement)

Depending on the mix, concrete can be obtained commercially with a compressive strength from 2,500 psi to 6,000 psi. Values of up to 10,000 psi have been obtained under laboratory conditions (Ref. 28). Typical allowable stresses for concrete design according to the American Concrete Institute are shown in Table 7-4.

TABLE 7-2

ELASTIC PROPERTIES COMPUTED FROM 1-D STRAIN TESTS *

<u>Sample Number</u>	<u>Geological Classification</u>	<u>Elastic Properties **</u>		
		<u>σ_{110} psi</u>	<u>ν</u>	<u>E, psi</u>
1	Granite (G-4)	20,000	.167	9.6×10^6
2	Granite (AFG-2)	10,000	.167	8.7
3	Granite (LG-2)	12,000	.198	8.5
4	Rhyolite (R-2)	8,000	.198	6.8
5	Rhyolite (R-3)	10,000	.180	8.6
6	Rhyolite (R-4)	9,000	.211	1.3
7	Rhyolite (R-7)	15,000	.250	4.8
8	Rhyolite (R-8)	10,000	.230	5.0
9	Rhyolite (R-9)	23,000	.222	5.0
10	Rhyolite (R-10)	20,000	.207	8.4
11	Rhyolite (R-11)	22,000	.230	7.2
12	Basalt (B-1)	20,000	.222	4.7
13	Basalt (B-2)	18,000	.194	5.7
14	Basalt (B-3)	8,000	.207	5.6

* All samples taken from Ref. 22

** Elastic properties computed from the equations 7-5.

TABLE 7-3

ROCK SAMPLES USED FOR DETERMINATION OF
YOUNG'S MODULUS AND UNIT WEIGHT *

<u>Group Number</u>	<u>Rock Type (Name)</u>	<u>Location</u>	<u>Specimens</u>	<u>Density Lb/Ft³</u>
1.1	Basalt (lower granite)	Pullman, Washington	12	170.2
1.2	Basalt (little goose)	Walla Walla, Wash.	6	175.8
1.3	Basalt (John Day)	Arlington, Oregon	6	174.1
2.1	Diabase (Palisades)	West Nyack, New York	12	182.5
2.2	Diabase (Coggins)	Culpeper, Virginia	6	189.5
2.3	Diabase (French Crk.)	St. Peters, Penn.	6	190.8
3.1	Dolomite (Oneota)	Kasota, Minnesota	12	153.0
3.2	Dolomite (Lockport)	Niagara Falls, N.Y.	6	161.2
3.3	Dolomite (Bonne Terre)	Bonne Terre, Missouri	6	164.5
4.1	Gneiss (Dworshak)	Orofino, Idaho	12	174.5
5.1	Granite (Pikes Peak)	Colorado Springs, Colo.	6	166.8
5.2	Granite (Pikes Peak)	Colorado Springs, Colo.	6	164.6
5.3	Granite (Barre)	Barre, Vermont	12	165.2
6.1	Limestone (Bedford)	Bedford, Indiana	12	137.7
6.2	Limestone (Ozark Tavernelle)	Carthage, Missouri	12	165.6
6.3	Limestone (Solenhofen)	Solenhofen, Bavaria	6	163.6
7.1	Marble (Taconic White)	West Butland, Vermont	12	169.0
7.2	Marble (Cherokee)	Tate, Georgia	6	169.1
7.5	Marble (Imperial Danby)	West Rutland, Vermont	13	169.3
8.1	Quartzite (Baraboo)	Baraboo, Wisconsin	7	164.0
9.1	Rock Salt (Diamond Crystal)	Jefferson Island, La.	6	135.0
10.1	Sandstone (Berea)	Amherst, Ohio	12	136.2

TABLE 7-3 (Continued)

ROCK SAMPLES USED FOR DETERMINATION OF
YOUNG'S MODULUS AND UNIT WEIGHT *

<u>Group Number</u>	<u>Rock Type (Name)</u>	<u>Location</u>	<u>Specimens</u>	<u>Density Lb/Ft³</u>
10.2	Sandstone (Crab Orchard)	Crossville, Tenn.	9	157.0
10.3	Sandstone (Navajo)	Glen Canyon, Arizona	12	125.8
11.1	Schist (Luther Falls)	Unknown Origin	12	175.8
11.2	Schist (Luther Falls)	Unknown Origin	6	176.1
13.1	Siltstone (Hackensack)	Hackensack, N. J.	12	162.0
14.1	Tuff (NTS-E Tunnel)	Mercury, Nevada	12	100.7

* All samples taken from Reference 26.

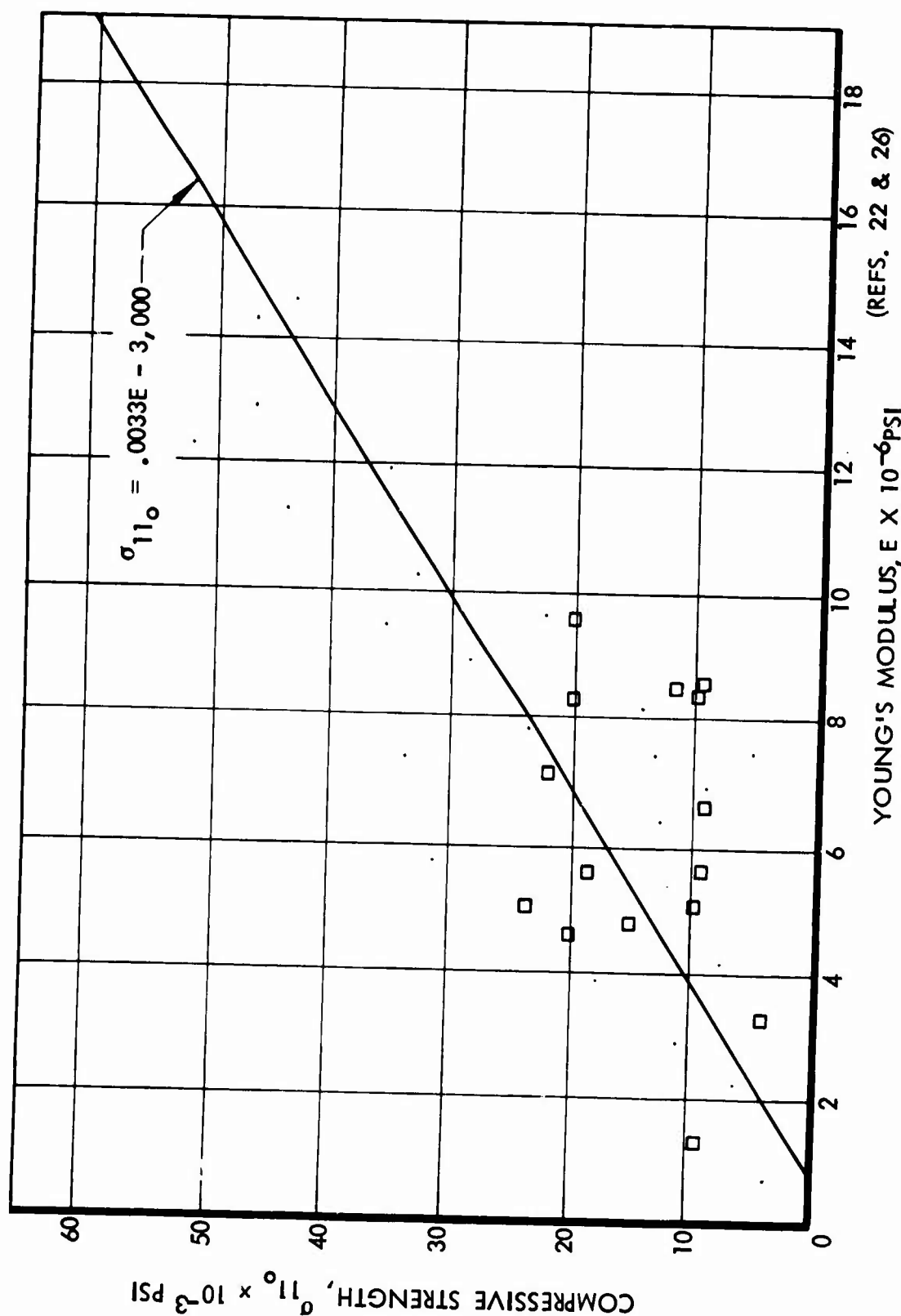


Figure 7-4: COMPRESSIVE STRENGTH VERSUS YOUNG'S MODULUS
(REFS. 22 & 26)

Table 7-4: ALLOWABLE STRESS IN CONCRETE

Description		Allowable Stresses				
		For any strength of Concrete in Accordance with Section 502	For Strength of Concrete Shown Below			
			$f_c' = 2500$ psi	$f_c' = 3000$ psi	$f_c' = 4000$ psi	$f_c' = 5000$ psi
Modulus of Elasticity		$\frac{29,000,000}{w^{1.5} 33 \sqrt{f_c'}}$				
Ratio: n						
For Concrete Weighing 145 lb per cu ft (See Section 1102)	n		10	9	8	7
Flexure: f_c						
Extreme Fiber Stress in Compression	f_c	$0.45f_c'$	1125	1350	1800	2250
Extreme Fiber Stress in Tension in Plain Concrete Footings and Walls	f_c	$1.6 \sqrt{f_c'}$	80	88	102	113
Shear: v (as a Measure of Diagonal Tension at a Distance d from the Face of the Support)						
Beams with no Web Reinforcement *	v_c	$1.1 \sqrt{f_c'}$	55 *	60 *	70 *	78 *
Joists with no Web Reinforcement	v_c	$1.2 \sqrt{f_c'}$	61	66	77	86
Members with Vertical or Inclined Web Reinforcement or Properly Combined Bent Bars and Vertical Stirrups	v	$5 \sqrt{f_c'}$	250	274	316	354
Slabs and Footings (peripheral Shear, Section 1207) *	v_c	$2 \sqrt{f_c'}$	100 *	110 *	126 *	141 *
Bearing: f_c						
On full Area		$0.25f_c'$	625	750	1000	1250
On One-third Area or Less		$0.375f_c'$	938	1125	1500	1875

* For shear values for lightweight aggregate concrete see Section 1208.

† This increase shall be permitted only when the least distance between the edges of the loaded and unloaded areas is a minimum of one-fourth of the parallel side dimension of the loaded area. The allowable bearing stress on a reasonably concentric area greater than one-third but less than the full area shall be interpolated between the values given.

The dynamic compressive strength of concrete increases with the rate of strain (Ref. 29). This is illustrated in Figure 7-5 which is reproduced from Reference 30.

The modulus of elasticity of concrete can be expressed in terms of the compressive strength and the mass density. The American Concrete Institute (Ref. 30) recommends the following relationship for estimating the modulus of elasticity.

$$E_c = W^{1.5} 33 \sqrt{f_c'} \quad (7-6)$$

where W is the density (lb/ft³) and f_c' is the compressive strength (psi).

Triaxial testing done at the University of Colorado (Ref. 31) indicates that concrete does not become plastic until confining lateral pressures of the order of 75,000 psi are applied. On the basis of this information, it would be reasonable to treat concrete as an elastic material for the overpressures considered in this study.

7.2.2 Steel

The group of steels that would be economically feasible for use in underground hardened structures include the structural carbon steels ASTM A7 and A36, the high strength steels ASTM A440, A441, and A242, the very high strength steels V50 through V65 and the construction alloy steels USS T1 or NA-X Tra 100 (Refs. 32, 33 and 34).

The yield point, tensile strength and percent elongation (ductility) of these steels are summarized in Table 7-5. The values given are the static mechanical properties.

The mechanical properties of steels, like most other materials, are actually a function of the strain rate. For example, the yield stress increases with increasing strain rate as shown in Figure 7-6, which was obtained from Reference 35.

7.2.3 Reinforced Concrete

A common configuration in hardened, buried facilities is a steel liner within a reinforced concrete structure. Because the modulus of steel is much higher than the modulus of concrete, it is reasonable to expect that the steel will develop its full yield strength as the concrete approaches its rupture strength.

7.3 Isolation Materials (Backpacking)

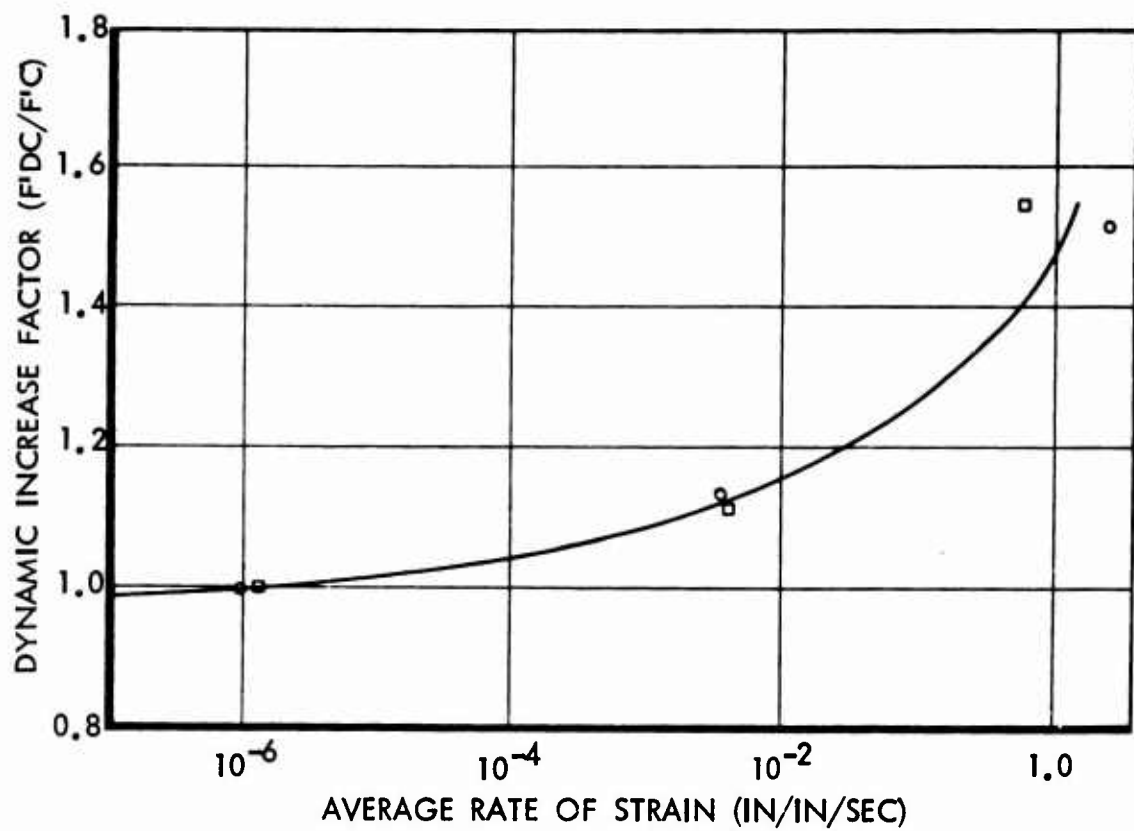


Figure 7-5: DYNAMIC INCREASE FACTOR FOR THE COMPRESSIVE STRENGTH OF CONCRETE (REF. 20)

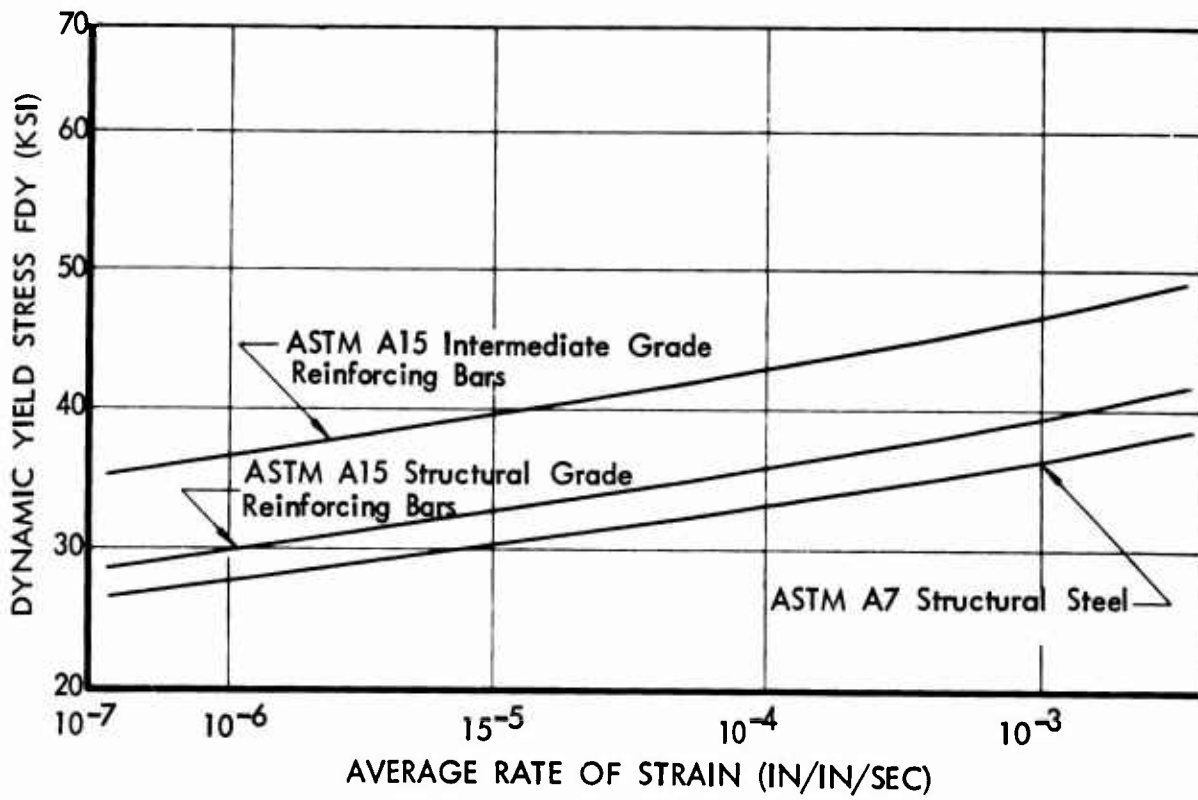


Figure 7-6: DYNAMIC INCREASE IN YIELD STRESS FOR STEEL (REF. 35)

Table 7-5: MECHANICAL PROPERTIES OF STRUCTURAL STEELS

CATEGORY	DESIGNATION	YIELD POINT MIN KSI	TENSILE STRENGTH MIN KSI	% ELONG. IN 8" MIN	% ELONG. IN 2" MIN
Structural Carbon Steel	ASTM A7 ASTM A36	33 36	60 58	21 20	24 23
Reinforcing Bars Structural Grade Intermediate Grade Hard Grade	ASTM A15	33 40 50	55 70 80		
Reinforcing Bars Reinforcing Bars Reinforcing Bars	ASTM A16 ASTM A61 ASTM A82	50 60 56-65*	80 90 70-75*		
High Strength Steel	ASTM A440, A441, A242 ASTM A440 ASTM A440	42* 46* 50*	63 67 70	16 19 18	24 22#
Very High Strength Steel	Bethlehem V45 or USS Ex-Ten 45 V50 or Ex-Ten 50 V55 or Ex-Ten 55 V60 or Ex-Ten 60 V65 or Ex-Ten 65	45* 50* 55* 60* 65*	65 70 70** 75** 80**	19 18 17 16 15	
Constructional Alloy Steel	USS T-1 or N-A-Xtra 100	90* 100*	105** 115**	11# 11#	17 18

* Check ASTM Specification or Vendor Specification for thickness range

** Min Tensile Strength Varies with Vendors

These values not covered by ASTM or Vendor Specification

Steel Density = 0.283 lb/in³ Modulus of Rigidity = 11×10^6 psi

Modulus of Elasticity = 29×10^6 psi Poisson's Ratio (ν) = 0.32

7.3.1 Objectives

Backpacking materials are placed between the medium and the structure. The purpose of the backpacking materials is to limit the stress levels imposed on the structure.

7.3.2 Types

Backpacking materials are of two basic types. The first type is the so-called elastic material and the second type is the so-called crushable material. The elastic materials are designed to return to their original shape and capability after exposure to a shock.

Reinforced concrete is the most commonly employed elastic backpacking material. Depending upon the mix (the water to cement ratio, the cure and type of aggregate, etc.) its static mechanical properties can vary within the following ranges:

W	(density)	- 90 to 225 lb/ft ³
E	(modulus of elasticity)	- 1.26×10^6 to 7.0×10^6 psi
F_c	(compressive strength)	- 2000 to 8000 psi
ν	(Poisson's ratio)	- 0.2 to 0.3

A listing of crushable materials is given in Table 7-6. It can be seen that density and compressive strength can be varied over a wide range for a given material. Beyond these two basic properties very little further information is available in general concerning detailed behavior of backpacking materials under load.

Another form of crushable material, polyurethane foam could be considered for scale testing. The idealized form of the one-dimensional stress-strain relationship for polyurethane foam is shown in Figure 7-7 but the actual values for E_1 , yield strength, and E_2 would have to be determined by test for each formulation of foam used.

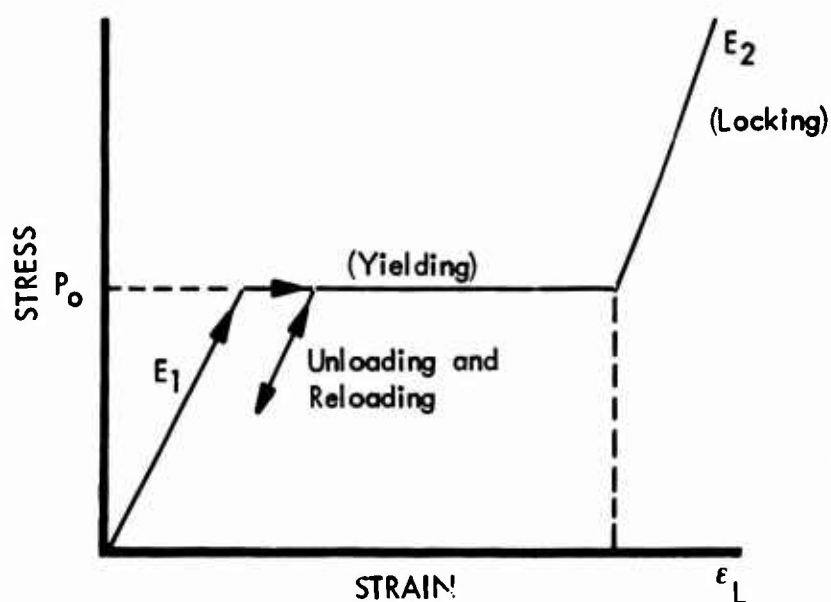


Figure 7-7: TYPICAL STRESS-STRAIN CURVE FOR POLYURETHANE FOAM

7.4 Debonding and Slip

Essentially no information was discovered that was directly appropriate to the problem of debonding and slip at the interface between earth and a buried facility. Some friction coefficient values are given in Table 7-7 but their applicability to the current problem is doubtful. Due to the lack of any credible values for debonding strengths it is recommended to take the normal tensile capability as zero at the appropriate boundary.

TABLE 7-6
CRUSHABLE BACKFILL MATERIALS

I Concrete (Crushable Foamed)

Density; 20 to 120 lbs/ft³

Crush stress levels of 100 to 4000 psi

Trade Names; Marlecrete, Surox and Haydite

II Other Crushable Materials

1. "FLUFTROX" by Fluftrox Expanded Obsidian mixed with 10% (Granitic volcanic glass) - Portland Cement.
2. Fuller Earth Bricks - Johns-Mansville Co.
25-30¢/board foot, 3.60#/cu.ft.
3. Foamed Aluminum, Foamalum Co.
4. Foamed Zinc, Foamalum Co.
5. "CALICEL" by Keasbey & Mattison Co.

TABLE 7-7
COEFFICIENTS OF FRICTION*

<u>Material</u>		<u>Static</u>	<u>Dynamic</u>
Smooth Mortar on	20-30 sand	0.52 - .65	
Teflon	"	0.31 - .43	
Graphite	"	0.30 - .42	
Plain Steel on	20-30 sand	0.34 - 0.35	
Plain Smooth Mortar	"	0.32 - 0.36	0.67
Plain Rough Mortar	"	0.70 - 0.79	0.82
Teflon Coated Steel	"	0.32 - 0.33	0.56
Teflon Coated Smooth Mortar	"	0.33 - 0.35	0.58
Graphite Coated Steel	"	0.22 - 0.26	
Graphite Coated Smooth Mortar	"	0.31 - 0.32	0.44
Plain Steel on	60-80 sand	0.49 - 0.51	0.63
Plain Smooth Mortar	"	0.99 - 1.06	
Plain Rough Mortar	"	1.04 - 1.26	
Teflon Coated Steel	"	0.51 - 0.66	
Graphite Coated Steel	"	0.37 - 0.42	
Teflon Coated Smooth Mortar	"	0.51 - 0.69	
Graphite Coated Smooth Mortar	"	0.53 - 0.73	
Stone Masonry on Concrete		0.76	
Dry Masonry on Brickwork		0.6 - 0.7	
Iron on Stone		0.3 - 0.7	

*References 36, 37

APPENDIX

Energy Implications of Inter-Related Bulk and Shear Moduli

This discussion is limited to the circumstance that the shear tangent modulus, G is determined solely on the basis of the bulk deformation and deformation rate. The specific set of material properties in question involves a bulk tangent modulus, K , which is a nonlinear function of the pressure, P , and which may exhibit compaction i.e., a large K value, on unloading. The shear modulus is constrained by a constant value of Poisson's ratio to be proportional at all times to the bulk modulus. Stated very briefly, the discussion is aimed at all nonlinear, constant Poisson's ratio material descriptions.

It has been found that for such a material description, the mathematical model may create or destroy energy during the response being computed. In either case, a seriously incorrect solution is likely to result. Whether the model creates or destroys energy depends on the nature of the response; specifically, it depends on the sequence of occurrence of dilatational and deviatoric deformations. If energy is created, unrealistically large stresses and velocities may occur at late times; if it is destroyed, unrealistically large permanent deformations may occur at late times. In any problem having a complex wave response, if the calculation is run long enough, eventually a loading sequence for some region of the model will occur which will activate this energy violation. In Distant Plain 6, the phenomenon was encountered at relatively short time.

Consider a simple, bilinear, elastic relationship between the pressure P and the volumetric strain, e .

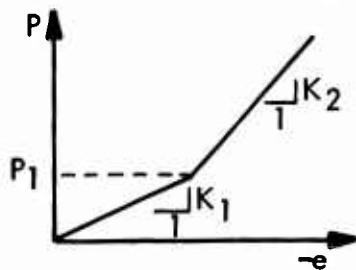
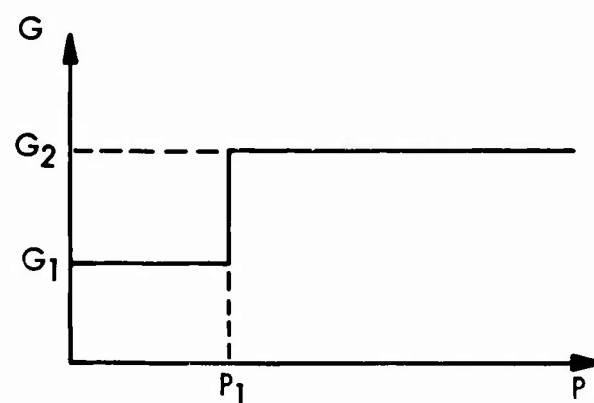


Figure 1: TYPICAL PRESSURE - VOLUME RELATION

If Poisson's ratio is constant, then G can be plotted as a function of P . For $P < P_1$, G has a relatively low value, and for $P > P_1$ it has a higher value. The two moduli are proportional to the slopes of the two segments of the P vs. e plot, as shown in Figure 2.



That is $G_1/G_2 = K_1/K_2$

Figure 2: SHEAR MODULUS VS PRESSURE FOR BI-LINEAR MEDIUM

Suppose that on the P versus e plot, an advancing sequence of times is denoted by successive letters as shown in the Figure 3. Loading takes place during abcde and unloading during efghij.

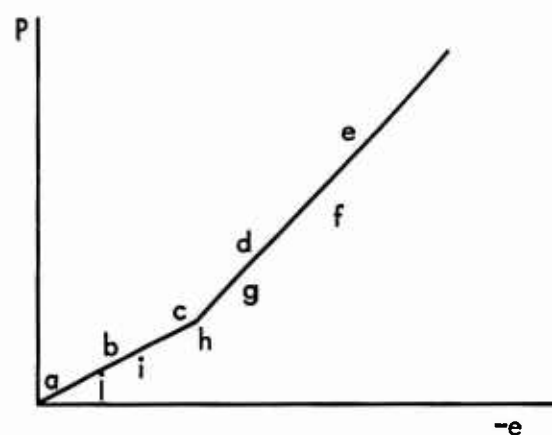


Figure 3: LOAD HISTORY FOR BI-LINEAR MEDIUM

If a time history of shear (or deviatoric) strain, γ , occurs such that γ increases from a through h and decreases from h through i, and if very little strain is accumulated during abc, then the shear (or deviatoric) stress versus strain plot as shown in Figure - 4.

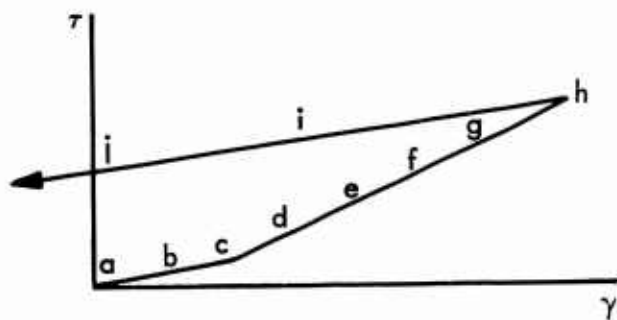


Figure 4: HISTORY OF SHEAR STRESS VS SHEAR STRAIN (BI-LINEAR MEDIUM)

Since the deformation is still continuing, a final accounting of the energy cannot be made. It is still possible, by means of a rather complicated τ - γ path to obtain a final state with energy conserved. However, as far as it is shown, the region of material which undergoes this γ history has been a source of energy. That is, the work integral has a negative value.

$$\int \tau d\gamma < 0$$

The material in question has started from the undeformed state, undergone deformation, and has not absorbed energy, but instead has done work on the surrounding medium. The source of this work has been the continuing large shear stresses which were not reduced sufficiently by the reduction of the shear strain. No matter what subsequent γ path is followed, this behavior is unacceptable.

By means of a different sequence of bulk and shear loadings, the τ - γ plot can be made to show a loss of energy. This could be interpreted as damping or plasticity, since a permanent deformation is implied. However, this situation is also unacceptable, because at the outset the intention has been to describe an elastic, though bilinear, material.

In the case of a compacting material, whose P-e plot is shown below, an even more striking energy violation can be obtained. Again, the letters on the plot indicate the loading sequence. The problem in question is the earth response to combined airblast and direct induced blast loadings.

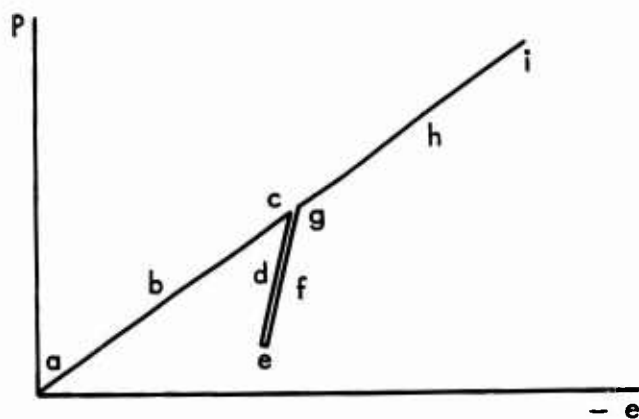


Figure 5: LOAD HISTORY FOR COMPACTING MEDIUM

The period abc is intended to describe the rise of the overpressure, the period cde the decay of the overpressure, and the period efghi the compression due to the direct induced ground motion. The letters do not indicate equally spaced times. The downward displacement of the earth surface occurs mostly after the peak overpressure has passed; i.e., a large γ increase takes place during the period cde. The arrival of the direct induced motion causes a reduction and in some cases a reversal of γ . The γ value reduces significantly during the period efghi. The result is as shown below.

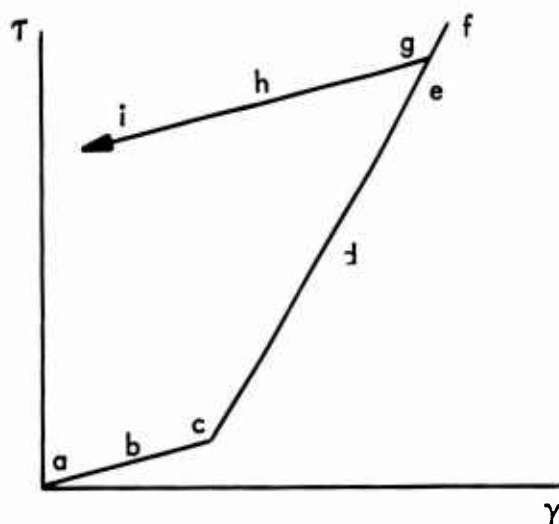


Figure 6: HISTORY OF SHEAR STRESS VS SHEAR STRAIN (COMPACTING MEDIUM)

Again, the earth region with this $\tau - \gamma$ history has done work on the surrounding medium. This work has resulted from a residual high shear stress which has not been removed by the shear strain reduction. It is seen that a positive τ will accompany a negative γ .

It is easily seen that the energy created by the earth material at the surface tends to drive the upper layers of earth toward ground zero. The shear deformation due to the airblast is as shown below. The motion is predominantly vertical.

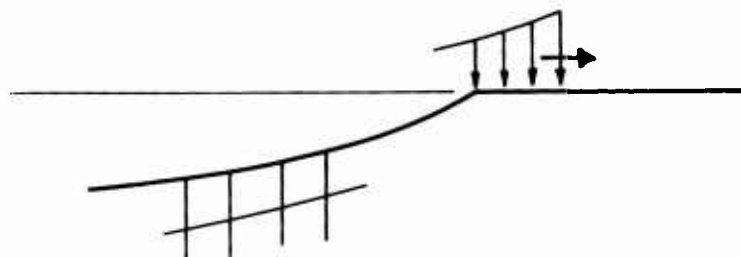


Figure 7: SURFACE DEFORMATION FROM AIR BLAST

A typical surface node experiences forces from the elements on either side as shown below. These forces account for the early tendency of the earth surface to move

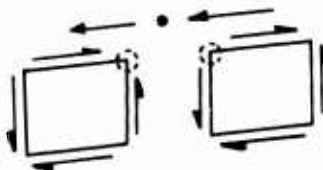


Figure 8: SURFACE NODE FORCES

back toward ground zero relative to the motion of the deeper material. However, with the material properties postulated, the resulting motion is unable to cause a significant reduction of the stresses. The shears continue to act and hence the inward velocities continue to increase with roughly constant acceleration.

This description is somewhat oversimplified. It is to be expected that some erratic model velocities will occur in calculations, because the oscillations which accompany the finite element solution affect the sequence of bulk and shear strains to some extent. However, the calculated data for Distant Plain

6 show the essential features as described.

It is noted that in many of the current numerical solutions to ground motion problems a significant relative inward motion of the earth surface is observed. These responses appear to be subject to some question, therefore, if they were obtained with a constant Poisson's ratio material description.

The above discussion has dealt with the shear stress and strain. It applies equally to all deviatoric stresses and strains. Therefore, it applies to those components of the vertical and horizontal stresses which occur due to deviatoric strains. This indicates, for example, that the stress σ_r , may take larger compressive values than it should under the condition that the vertical stress or the lateral horizontal stress are relatively small, so that a deviatoric state exists.

Relative to the bulk and shear stiffness relationship, the plasticity theory of the Mohr-Coulomb type requires mention. This theory has the potential to produce an energy violation because of the inter-relationship between plastic strain and the pressure. Energy violations in this case are avoided by the requirement that the plastic strain rate be normal to the yield surface. The motivation for this requirement actually is similar to the difficulty between K and G which has been discussed above.

It is concluded from the above discussions that any material description in which shear and bulk tangent moduli are inter-related is likely to give rise to energy violations in calculations. The use of a constant Poisson's ratio is just such a case. For nonlinear bulk elastic behavior and for compactive bulk elastic behavior, an energy violation is guaranteed in these cases. Such material properties cannot be expected to produce reasonable results in problem solutions. The use of a constant shear modulus, or one dependent only on the shear behavior itself, will eliminate this difficulty.

PART III.

Summary and Design Procedure Discussion

TABLE OF CONTENTS

PART III.

	PAGE
1.0 INTRODUCTION	217
1.1 Program Capability	217
1.2 Design Procedures	218
1.3 Method Extension	218
2.0 CURRENT CAPABILITIES	219
2.1 Geometric Representation	219
2.2 Material Representation	222
2.3 Structure - Medium Interface	223
2.4 Input Loading	224
2.5 Output	226
3.0 APPLICATIONS TO DESIGN PROCEDURES	227
3.1 Trade Studies	227
3.2 Design Environment	228
3.3 Design Verification	230
4.0 CONCLUSIONS AND RECOMMENDATIONS	231
4.1 Current Status of FEAT Codes	231
4.2 Recommended Improvements	231
4.3 Recommendations	232
REFERENCES	233

INTRODUCTION

In this part of the Report, the current capabilities of the FEAT code are summarized and where limitations exist, they are described. The application of the method to the development of design procedures is presented. Particular emphasis is given here to the design problems of an advanced missile system silo. Since the FEAT method is a complex first generation system of computer programs, a list of suggested improvements is given which will lead to extended usefulness and accuracy of the technique. These include, improved material representation, extended configuration capability, and improved efficiency of computation.

1.1 Program Capability

Three basic codes comprise the FEAT system. The axisymmetric (A/S) version of the FEAT codes constitutes the heart of the system. It models the structure and a portion of the surrounding earth medium to compute the interaction between them, a technique referred to as the "soil island" concept. Two supplemental programs are used for parametric and interpretive studies. These are a one layer ("thin layer" or TL) version of the axisymmetric code, and a plane strain (FAN) program, modeling a circular structure in a fan shape region of earth medium. These two programs consider only plane cylindrical wave propagation. (See Figure 1-1 for model layouts).

Each one of the programs is capable of modeling the earth's medium and back-packing as non-linearly elastic, compacting, plastic materials with limited tensile capability. They consider for structure representations a linearly elastic material, and permit debonding and slip between the earth and the structure. Simple input loading descriptions are required for the thin layer and fan models, while the axisymmetric version admits airblast loading on its top surface and free-field displacement-time histories along the other three "soil island" boundaries.

The computer programs yield information about motions and stresses in the structure and the surrounding medium, providing the basis for evaluation of structure, site, and interface condition effects as required for design decisions.

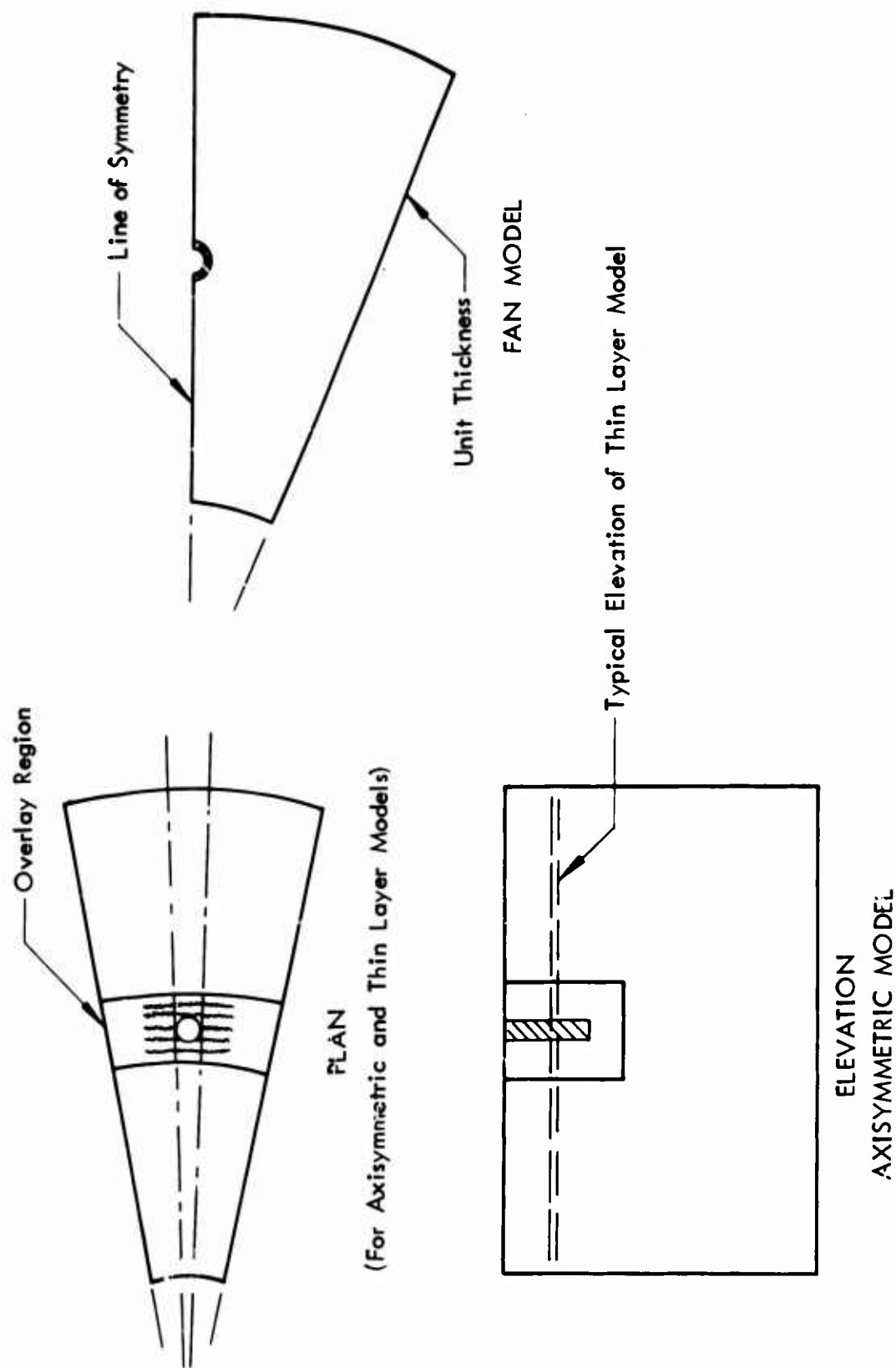


Figure 1-1: FEAT MODEL LAYOUT

1.2 Design Procedures

The objective of this study is to provide a tool which will assist in the establishment of a hardened facility design and to assure high confidence in the survivability of the end item. The application of the FEAT codes to the development of design procedures is presented. This includes their use in trade studies which consider site effects, structure size and configuration, and attack levels, to establish critical design conditions.

The second phase of the design information study concerns the computation of structure loads and motions for design sizing. This requires the usual iterative process of design development. The final contribution of the analysis procedure is the verification of the design. This requires an analysis of the final configuration for all considered attack environments and site configurations.

To assure the necessary confidence in this verification, a parallel program of pre-test predictions and post-test verification must be conducted with the FEAT system in conjunction with field tests. Only when this correlation is accomplished satisfactorily, can extrapolation to realistic nuclear attack environments be made with confidence.

1.3 Method Extension

In their current form the FEAT codes can consider structures buried tangent to the ground surface, represented as right circular cylinders as well as completely buried cylinders in sections normal to their longitudinal axis. For extended usefulness it is necessary to broaden the scope of the structure modeling to include such characteristics as variations of outside diameters over the length of the structure, side-by-side arrangement of silos, and horizontal capsules. This will require improvements of structure representations now in use.

Studies of earth media properties must be performed to provide the basis for more realistic mathematical models for the numerical analyses. The behavior of real earth-structure interfaces must be investigated to establish better modeling concepts for debonding and slip.

II

CURRENT CAPABILITIES

The FEAT code system for interaction analysis in its current configuration must be considered a first generation tool. Its capability to solve interaction problems has exceeded the initial anticipations. These capabilities are discussed in some detail in this section. However, the current version of the system has limitations. Where appropriate these limitations are identified. A thorough description of the FEAT interaction analysis scheme has been given in PART I of this Report, and the reader desiring knowledge of specific derivations and discussion of concepts is referred to that section.

The extent to which the models are representing realistically the problem geometry is discussed, as well as the material representations used in the codes. The description of the concepts of modeling structure-medium interface separation and slipping contains also a discussion of the need for testing to determine the realistic behavior of such interfaces. The input loading for each of the models is discussed with emphasis on compatibility between computational procedure used for the free-field input to the axisymmetric model. The volume of data generated by these numerical analyses is enumerated.

2.1 Geometric Representation

The FEAT code system consists of three basic codes. Each one of them uses finite elements to represent structures and earth media. It is quite apparent that the structure-medium interaction problem is a three-dimensional problem in space. However, since current computers are forcing a limitation upon the size of problem solution which can reasonably be considered, a three-dimensional analysis is not yet feasible. In order to solve interaction problems in an accurate and useful manner, a set of two dimensional models has been developed.

The main program, the axisymmetric version of FEAT, basically models structure and earth in cylindrical coordinates with a significant extension beyond the two dimensions of the cylindrical system. This extension is referred to in this study as the overlay path. The essence of this conceptual advance is that it provides the axisymmetric model with the capability to represent the phenomenon of arching, by providing a dual path in the immediate vicinity of the structure which affords the choice of two main stress paths. This model is limited in physical size to a region several hundred feet upstream, downstream and below the structure. This is the essence of the so called "soil island" concept.

It is necessary, for the current version of the FEAT axisymmetric structure-medium code, to provide free-field displacement time histories for every boundary node, except those on the top surface which are subject to the airblast loading. The existing version of this code can consider several horizontal layers of different earth media.

To assist in parametric and interpretive studies required for the use of the pseudo three-dimensional axisymmetric version of the FEAT code, it was necessary to set up two supplementary codes. The first is a single layer model of the axisymmetric version with the same structure and overlay paths representation as the main version. This is referred to as the "thin layer" (TL) model. To afford the capability for horizontal section analysis, a plane strain model was developed which can consider the appropriate geometry. This is referred to as the FAN model because it represents a sector of a plan view of the axisymmetric model, having thereby a fan shape planform. The latter version can model the ring shape of a section through a vertical cylinder very accurately.

The two supplementary programs, using the same geometric limits as the main version, can provide parametric investigation results which are required to provide three specific sets of parameters for the axisymmetric program. These parameters are the ratio of overlay path extent to that of the structure path, i.e., it determines the effects of arching for a specific site and structure, in addition there are the crushing stiffness of the structure and the shear connection between the two paths in the axisymmetric model. Again, it is essential that the reader wishing exact details of the overlay concept refer to PART I of this Report, particularly section 4.0.

The thin layer and fan models have a further task in the overall analysis. For a suitable pulse shape of a cylindrical wave input and the parameters used in the axisymmetric version solution of a specific design case, they provide the essential data for wall circumferential bending stress. That means they establish a relationship between the radial crushing observed in the thin layer model structure, and the ring deformation of the fan model structure. For the fan model, it is also possible to compute wall stresses in the structure, so that a link can be established between the deformations observed in the axisymmetric model and the corresponding tensile stresses in the cylinder cross-section.

Two definite recommendations can be made for essential improvements necessary for the interaction analyses required for generation of design information. It is necessary to develop structure representations which are not limited to right circular cylinders, i.e., allowing variations in outside diameter along the length of the structure. This requires extensions to the finite element models of the structure region as well as to the concept of interface behavior.

2.2 Material Representation

The FEAT codes consider very complex material behavior for the earth media representation. They also model the interface between the earth to the extent that they allow separation of the materials as well as slipping along the interface. Structure materials are represented with linearly elastic properties, allowing some detail in the modeling of such characteristics as steel inside of concrete walls.

Throughout this study earth materials have been considered to exhibit a constant Poisson's ratio. This assumption relates the medium's shear stiffness to its bulk stiffness. Earth material properties were given in form of hydrostats i.e., hydrostatic pressure versus volume relationships, and a reference density as well as a Poisson's ratio. Separate loading and unloading hydrostats were given for the limestone type of material specified for use in the demonstration problems. The interpretation given to this input as it applies to the FEAT codes was to compute from the hydrostats the bulk tangent moduli for a set of hydrostatic pressure levels. On the basis of the prescribed Poisson's ratio shear tangent moduli were computed to correspond to the bulk modulus tabulation. In the computational process of FEAT each element is interrogated at every time step to determine its current state of hydrostatic stress. On the basis of that current value, each element is assigned an instantaneous value of bulk and shear modulus. Not until the final weeks of this contract effort did it become apparent that this method of material representation violates conservation of energy. This fact is taken to be responsible for instabilities which occurred in several verification runs which had to be terminated until this problem is clearly identified and more realistic material descriptions are established.

The representation of plastic behavior of earth materials is accomplished in an incremental fashion. Yield conditions are determined by the Drucker-Prager yield criterion, i.e., the medium's shear strength is a function of hydrostatic stress. Above a certain level of hydrostatic pressure, this increase of shear strength is taken to become negligible, and the von Mises yield criterion is adopted for pressure states above that limiting value.

The limited tensile strength of earth media is modeled in the codes in an approximate fashion. The state of hydrostatic stress in each element is monitored constantly as described above. A limiting value for hydrostatic tension is chosen for each type of earth material used in the model. At the instant, when an element exceeds this limit in the tensile direction, that element is considered pulverized, i.e., it exerts no more force on the surrounding regions. At the instant of cracking, the value of volumetric strain in that element is computed and stored. During subsequent computation cycles, the volumetric strain in that element is monitored, and the element remains in a cracked state

until it has recompacted in excess of the volumetric strain it had at the time of cracking. At this point, it resumes its role as a normal earth element with modified elastic and plastic parameters.

There are several improvements which must be made in the material representation currently used to obtain more realistic models of earth media. As described above, it is necessary to derive material models which describe independently the bulk and shear behavior of earth media. An interim solution to that problem would be to select a single value for the shear modulus. However, it appears advantageous to plan implementation of the variable moduli models for future use of the codes, thus removing the ambiguity of combinations of non-linear elasticity, compaction and plasticity.

Realistic cracking behavior of earth materials must also be determined to assess the validity of cracking procedures used in the FEAT codes.

2.3 Structure - Medium Interface

In order to model as realistically as possible the characteristics of the interface between the structure and the surrounding medium, the FEAT codes have been provided with special subroutines capable of considering debonding and slip at appropriate locations in the model. This is accomplished by providing the nodes (points of intersection of finite element boundaries) along the interface with the capability to split into the earth and structure portions to pursue separate motions.

The ability of nodes to debond is determined by the tensile force across the interface and the normal force on the interface exerted by the over-burden. The latter varies with depth of burial of the nodes. These partial nodes are not permitted to move past one another, i.e., earth elements may not penetrate the structure elements or vice versa. When such a condition is observed, a crossover point is determined and nodes are considered to be joined at that position.

A similar approach is used in representing slip along the interface. Slipping of partial nodes is admitted when the shear force along the interface at a particular location exceeds the friction force determined by the normal force at that point and a specified friction coefficient plus some initial bond strength. After the first incidence of slipping or debonding this bond strength is assumed lost. Slipping is considered ceased when the relative velocity of the partial nodes falls below a small specified value.

In the demonstration problems described in the Volume II of this Report it was shown that the debonding and slip greatly affects the loads introduced into the structure. While it reduces axial loading in most instances by eliminating the effect of negative skin friction, for slip in the circumferential direction it appears to introduce momentary high stresses into the structure walls which heretofore had not been anticipated. It has not yet been possible to show conclusively that this is a real phenomenon. In order to complete the understanding of the debonding and slip implications on structural design, further work is necessary. This includes tests on realistic models to assess the parameters controlling separation and sliding in actual structures.

In addition, an assessment of the mathematical representations of debonding and slip behavior along the earth-structure interface must be made. It is impossible to determine whether the high stress oscillations observed the horizontal ring section, when slip occurs, are realistic. It is conceivable that what is observed here is an actual case of physical instability analogous to brake chatter for example. Conceptual studies and tests are also required to ascertain the effects of over-burden and aging of interfaces on bond and friction.

2.4 Input Loading

The finite element models of earth and structure regions which are used in the FEAT code accept a variety of prescribed boundary conditions. These input loadings and restraints may be established to meet model requirements. The complete flexibility in boundary load specification has not yet been exercised since only very definite requirements existed.

For the axisymmetric model two types of boundary loading are considered. Along the top surface of this model air blast forces are applied to the appropriate nodes. For this purpose a so called loads tape is generated on which are stored the external vertical forces to be applied to the surface nodes at discrete time steps. The forces are computed with a set of empirical equations providing arrival time, peak pressure and pressure decay for air blast waves from nuclear surface bursts. The equations used for this purpose were supplied by Aerospace Corporation.

Along the earth boundaries of the "soil island" model, i.e., the two vertical boundaries and the horizontal bottom, each node is prescribed a vertical and horizontal displacement at discrete time intervals. These displacements are obtained by the computer program during the computations from a data tape. This magnetic data tape is generated by execution of free-field analysis of an appropriate site and attack problem. For the demonstration problems analyzed in this study the free-field displacement inputs were generated with the AFTON-2A code by ATI-AJA under Contract FO4694-67-C-0120.

An additional admissible input to the axisymmetric model derives from simultaneous execution of the suspension system subroutine which was developed for that purpose under this study. That subroutine models the response of a flexible package suspended inside the structure from specified attachment points. The routine is executed simultaneously with the axisymmetric program. It derives incremental displacement changes of the attachment points from the axisymmetric program and in turn computes reaction forces to be applied to the attachment points of the structure.

The "thin layer" and "FAN" programs accept either prescribed forces or displacements along their inner boundary. These inputs may be time dependent describing particular pulse shapes. For both models it is possible to prescribe either motion or stress conditions on the outer boundaries, or, if desired, specify that the outer boundaries are either fixed or free. For the fan model additional constraints must be specified for the radial boundaries. In general this is accomplished by restricting the boundary nodes to radial motions.

One specific problem relative to the establishment of input loadings has become apparent. The generation of free-field motions for "soil island" boundaries should be accomplished with a compatible earth medium model. The free-field computer code must treat all material characteristics in the same manner as the interaction code using the free-field motions as input.

If the two procedures are not identical, interference will occur between the driven boundaries and the signal propagated through the "soil island" region. A specific example of such incompatibility can be cited since it occurred in the demonstration cases. AFTON-2A admits cracking of the individual stress components while FEAT cracks elements based on their level of hydro-static tension. This leads to somewhat greater outward motions in AFTON-2A computations because hoop tension develops in radial waves causing a break in hoop strength, while at a comparable instant in the FEAT computation hoop tension can develop for some time.

2.5 Output

The FEAT codes produce large volumes of numerical data for interpretation. Time dependent responses for many points in the models must be studied for evaluation of their significance in the analysis. Peak responses occur at varying time at different locations in the model, making careful scanning of all data imperative for adequate interpretation.

The data analysis pursued in analysis of FEAT results has essentially four separate phases. The first segment concerns the limiting output provided by the on-line printer while the computations are in progress. Motions and stresses for a few select locations in the structure and the free-field are called out, together with space plots at select times displaying particle velocity levels for every node in the model, and stress state for every element. These data provide sufficient information for assessment of successful execution of the problem.

For determination of loads and motions of the structure, displacements of all points in the structure region for every time point are stored on magnetic tape. This tape is interrogated subsequently by an interpretation routine which computes gross motions of the structure, bending moments, axial and shear forces, cross-section deformation, etc.

The processed data are usually presented as time plots for the pertinent locations. Examination of the plots allows evaluation of the structure's response to the applied environment. A further analysis involves the correlation between horizontal section analysis performed with the thin layer and the fan models, and the cross-sectional deformation observed of the structure in the axisymmetric model. This allows determination of wall stresses in the structure.

The fourth phase of data analysis involves an in-depth study of the computed responses for assessment of the results. This will lead to understanding of the influences of the site (medium and layering), the structure (stiffness and size), the interface conditions (debonding and slip), and where appropriate the suspended contents and a summary evaluation provide the knowledge required to determine either that a suitable design has been achieved, or that changes in design parameters are required.

The most clearly identifiable improvement necessary in this data analysis effort is the development of better data presentation methods. These will be in the form of scanning devices, multidimensional displays which afford fast identification of significant response parameters which can then be selected for detailed study.

III

APPLICATIONS TO DESIGN PROCEDURES

The design of hardened underground facilities will likely evolve from an iterative procedure. Design requirements are established and an initial estimate of the facility configuration is made. Trade studies concerned with basic configurational concept, structural material selection, siting medium, nuclear weapon threat, and subsystem concepts must be conducted to identify key facility design parameters.

Design data from the trade studies is used to modify the initial configuration to the extent that detailed analyses can be made. The detailed analyses identify facility structural stress and motion and these are used to determine if the design does or does not satisfy all design requirements. Required modifications are made to the design keeping in mind that overdesign can be as important as underdesign.

Verification of the facility design that evolves is achieved through a process of analysis and test. A test environment corresponding to, say, a HEST/DIHEST test is predicted; analysis is conducted to predict the facility response in terms of stress and motion; the test is run, measuring both the input environment and facility response; the analysis technique is used to compute responses to the measured environment; and measured and computed responses are compared. If the analysis technique can adequately predict facility response to a known input environment some confidence can be placed in using these techniques to predict the response to a criteria environment.

3.1 Trade Studies

The principal objectives of the analyses to be conducted in support of design trade studies are:

- (1) Develop data showing the effects of site medium response characteristics on the loads imposed on the facility and resulting stresses in and motions of the facility, leading to identification of acceptable and unacceptable site characteristics.
- (2) Develop data showing the effects of facility configuration variables (size, shape, materials, thicknesses of protective back-packing) on the stresses in and motions of the facility, leading to selection of a facility configuration for detail design.

(3) Develop data showing the variation of facility loads, stresses, and motions with attack conditions (weapon yield, orientation relative to facility, etc.) leading to identification of critical conditions for which design environments must be determined.

(4) Develop preliminary design environment data on facility motions sufficient to permit trade studies and analyses leading to selection of suspension systems and other internal subsystems (hard mounted equipment, etc.)

These objectives can be achieved for, say, a hardened launch facility, by conducting parametric analyses on a relatively simple geometric shape. Selecting, for example, a right circular cylinder as the initial geometry, the influence on facility stress and motion of design parameters such as length, diameter, wall construction, site description, weapon yield, and over-pressure (range) can be established.

An example of such a series of analyses is shown in Table 3-1.

Cases 1 and 2 determine the effect of wall thickness variation while 2 and 3 determine the influence of concrete stiffness. The effects of length variation are examined between 3 and 4, while 5 through 7 consider the use of steel liner inside the concrete wall. At this point in the analysis a choice of a structural configuration is made, and that is then examined in 8 through 11 for different site and attack conditions. The effects of different strength backpacking between the structure and the earth are examined in 12 through 15 for two site and attack conditions.

It is clear from this suggested plan that a much more extensive investigation could be made. However, judgement will have to be used by the investigating engineer at each step of this procedure to assure that the next case actually studied will provide the most useful information. This implies a continuous review of the analyses and will lead to variations from the initially chosen plan of cases.

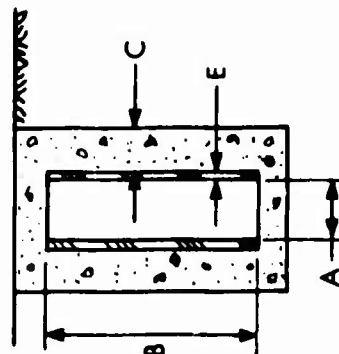
The same process of developing design information can be applied to other geometric shapes, differently oriented, and for both surface and buried locations.

3.2 Design Environment

The design information from the trade studies is used to define facility designs to the extent that detail analyses can be conducted. These analyses result in a definition of the critical design environments for the facility and its subsystems.

Table 3-1: ANALYSIS PLAN FOR DESIGN INFORMATION

ANALYSIS CASE	SITE & ATTACK CONDITION	STRUCTURE DESCRIPTION											
		DIMENSIONS				LINER 1				LINER 2			
		D	L	Material	Ex10 ⁻⁶	ν	ρ	Material	Ex10 ⁻⁶	ν	ρ		
1	1	A	B	--	--	--	--	Concrete	3	.33	C		
2	1	"	"	--	--	--	--	"	"	"	2C		
3	1	"	"	--	--	--	--	"	5	"	"		
4	1	"	2B	--	--	--	--	"	"	"	"		
5	1	"	"	Steel	30	.3	E	"	"	"	"		
6	1	4/3A	"	"	"	"	"	"	"	"	"		
7	1	"	"	"	"	"	2E	"	"	"	"		
8	2	Select one of the above structural configurations.											
9	3												
10	4												
11	5												
12													
13		Select one of the above structural configurations and two site & attack conditions and add 5 feet of Backpacking of 150 and 450 psi crushing strength.											
14													
15													



This environmental data is in the form of loads, both external (pressure and shears applied to the facility); internal (bending moments, axial forces, etc., at critical locations in the facility); and motions (acceleration, velocity, displacement) at key locations on the inside of the facility.

The loads are used for detail sizing of the facility structure and the motions for detail design of shock isolation systems and hard mounted equipment. With siting in rock, the design environments are probably dependent on the design itself and an iterative procedure is required to establish the combination of design and design environments that satisfy all design requirements.

3.3 Design Verification

The problem of design verification of hardened ground facilities designed to resist nuclear weapon attack is that direct test verification is not practical without resorting to atmospheric nuclear explosions. Hence verification must be accomplished by a combination of tests that partially simulate attack conditions and extrapolation of measured responses from these tests to design conditions by analysis. Looked at another way, verification of the design is achieved by verification of the analyses used in the course of the design.

The analysis and test procedure to achieve design verification could be as follows:

- (1) Use analysis techniques to predict facility response to a predicted test environment. This step is necessary to design an instrumentation system for the test. At this time analysis should also be conducted to identify facility responses that are particularly sensitive to variations in the input environment.
- (2) Conduct the test and measure facility responses and all the environmental quantities that are required as input to the prediction techniques.
- (3) Conduct post-test analyses, using the measured test environment as input, to compute facility response, for comparison of measured and predicted values.
- (4) The analysis method is modified if necessary to achieve correlation of computed responses and measured data.
- (5) Using the verified analytical technique, the response of the system to the various nuclear attack criteria conditions are computed. These responses are compared to the capability of the system to provide the required confidence in the design.

IV

CONCLUSIONS AND RECOMMENDATIONS

4.1 Current Status of FEAT Codes

The FEAT codes represent the only currently available method for realistic analysis of structure-medium interaction. The codes are capable of considering realistic representations of earth materials, backpacking, simple structure configurations, debonding and slip on the structure-medium interface, and the three-dimensional wave diffraction in the vicinity of the structure. Earth materials are modeled as layered, non-linearly elastic, compacting, plastic media with limited tensile strength. Backpacking is modeled in the same fashion. Structures are represented as right circular cylinders of composite construction, i.e., steel liner inside of concrete wall. All structure materials are considered linearly elastic. The interface between the structure and the earth medium is permitted to gap or slide when an initial bond strength and the shear resistance are exceeded. Wave diffraction or arching are modeled by means of the overlay concept.

The current version of the FEAT codes can be used immediately for design trade studies using a specified, simple structure configuration. In these studies the combinations of structure materials (concrete and steel), the structure size (wall thickness, diameter and length), site and attack conditions can be analyzed, and their relative importance determined.

Computation of free-field input to the axisymmetric model should be accomplished with a computer code using the same material representation and grid zones as the FEAT codes. This will avoid interference between input and propagated responses, a phenomenon which was observable in the demonstration problems.

4.2 Recommended Improvements

Several specific recommendations can be made at this time for improvements of the FEAT code system as well as recommended studies for improved analysis wave propagation in earth media in general.

Problems resulting from use of inappropriate material models have been discussed in considerable detail in the two preceding reports. The need for accurate description of the behavior of earth materials is apparent from the computational difficulties encountered in this study. A clear definition of concepts of cracking, compaction, and plasticity, and their applicability to the description of earth material behavior must be obtained. This is a need which exists for all currently operational computer codes for calculation of wave propagation in earth media.

Specific improvements recommended for the FEAT codes are as follows:

- a) Conduct investigation into the debonding and slip characteristics of earth-structure interfaces to assure realistic modeling of those phenomena. Such investigation must be supported by tests designed to assess how debonding and slip occur in real situations. A clear understanding of the phenomena is essential.
- b) to utilize fully the capabilities of the FEAT codes, structure representations must be extended to include models of vertical cylinders whose outside diameter varies along the length. A further feasible extension of the techniques must include models of side-by-side arrangement of vertical silos, as well as horizontal capsules. This requires programming and checkout of specific structure region subroutines using essentially available technology.
- c) for complete analysis of all pertinent data computed for interaction problems, sub-programs must be developed for three-dimensional display of data, facilitating data scanning in space and time coordinates simultaneously. This will permit rapid evaluation of pertinent items in large volumes of data.
- d) extension of structure modeling to include inelastic deformation of materials. This requires development and extension of the concepts used to represent ring deformation of the structure, and coupling of this mode with axial compression, bending and shear.

Items (a) and (d) can be categorized as major modifications while the other two items require only minor modifications.

4.3 Recommendations

The FEAT codes provide a unique capability for design trade studies for hardened missile silos currently under consideration, and for the prediction and verification of field tests. It is recommended that they be utilized for those purposes immediately.

It is further recommended that work be started immediately on the improvements of the codes listed above. This will assure a broadened capability for design studies and evaluation in a timely fashion.

REFERENCES

1. Warren, D. S., Castle, R. A., and Gloria, R. C., "An Evaluation of the State of the Art of Thermodynamical Analysis of Structures," Wright Air Development Division, TR 61, 1961.
2. Turner, M. J., Clough, R. W., Martin, H. C., and Topp, L. J., "Stiffness and Deflection Analysis of Complex Structures," Jour. Aero. Sci., Vol. 23, No. 9, September, 1956.
3. Clough, R. W., "The Finite Element Method in Structural Mechanics," pp 85-119 in "Stress Analysis," edited by O. C. Zienkiewicz and G. S. Holister, John Wiley, 1965.
4. Chang, G. C. and Fair, G. S., "Finite Element Approach to Wave Motions in Elastic-Plastic Continua," American Institute of Aeronautics and Astronautics Paper No. 68-145, 1968.
5. Shipley, S. A., Leistner, H. G., and Jones, R. E., "Elastic Wave Propagation-A Comparison Between Finite Element Predictions and Exact Solutions," Boeing Document D2-125404-1, May, 1967, also in Proceedings of the Symposium on Wave Propagation and Dynamic Properties of Earth Materials, Albuquerque, 1967.
6. Norris, C., et al, "Structural Design for Dynamic Loads", McGraw-Hill, 1959.
7. Nelson, I., and Bacon, M.L., "Investigation of Ground Shock Effects in Nonlinear Hysteretic Media", Paul Weidlinger, Consulting Engineer, Contract Report S-68-1, U.S. Army Waterways Experiment Station, March, 1968.
8. Terzaghi, K., "Theoretical Soil Mechanics," John Wiley, New York, 1943.
9. Drucker, D. C., and Prager, W., "Soil Mechanics and Plastic Analysis of Limit Design," Quarterly Applied Mathematics, Vol. 10, No. 2, pp. 157 - 165, 1952.
10. Christian, J. T., "Plane-Strain Deformation Analysis of Soils," MIT Contract Report No. 3-129 to DASA DA-22-079-eng-471, December, 1966.

REFERENCES (Cont.)

11. Prager, W., and Hodge, P. G., "Theory of Perfectly Plastic Solids," John Wiley, New York, 1951.
12. Hill, R., "Mathematical Theory of Plasticity," Oxford University Press, London, 1950.
13. "Analytic Approximation to the Brode Airblast Function," Aerospace Corporation, transmitted by letter 67-3750-NFK-260, N. F. Kfoury to S. L. Strack, October, 1967. (Secret-RD).
14. Martin, H. C., "Introduction to Matrix Methods of Structural Analysis," McGraw-Hill, 1966.
15. Shipley, S. A., Leistner, H. G., and Jones, R. E., "Elastic Wave Propagation - A Comparison Between Finite Element Predictions and Exact Solutions," Boeing Document D2-125404-1, May, 1967 and Proceeding of Symposium on Wave Propagation & Dynamic Properties of Earth Materials, Albuquerque, 1967.
16. Paul, S. L., and Robinson, A. R., "Interaction of Plane Elastic Waves with a Cylindrical Cavity," AFTDR-63-3021, June, 1963.
17. Garnet, H., Crouzet-Pascal, J., Isakson, G., and Pafko, L. N., "Dynamic Stresses in a Thick Elastic Cylinder Subject to Transient Pressure Loadings," Vol. 1, AFWL-TR-65-20, September 1965.
18. Paul, S. L., Robinson, A. R., and Ali-Akbarian, M., "Interaction of Plane Stress Waves with a Thick Cylindrical Shell," AFWL-TR-65-31, University of Illinois, June 1965.
19. Perret, W. R., "Free Field Ground Motion Studies in Granite, (U)," Operation Nougat, Shot Hard Hat, POR-1803, Sandia Corporation 1960. For Official Use Only.
20. Giardini, A. A., et. al., "Triaxial Compression Data on Nuclear Explosion Shocked, Mechanically Shocked, and Normal Granodiorite from the Nevada Test Site" pp. 1305-1320 Vol. 73, No. 4, J. Geophysical Research, February 15, 1968.

REFERENCES (Cont.)

21. Stephens, D. R., and Lilley, E. M., "Static PV Curves of Cracked & Consolidated Earth Materials to 40 Kilo Bars" - UCRL Preprint 14711, Also in the Proceedings of the Conference on Shock Metamorphism of Natural Materials, Greenbelt, Maryland, April 1966.
22. Brown, W. S., Devries, K. L., and Smith, J. L., "Properties of Rocks Tested in One-Dimensional Compression," AFWL-TR-66-124, University of Utah, January 1967.
23. Serata, S., "Principles of Stress Fields in Underground Formations: Continuous Medium Analysis of Elastic, Plastic, and Viscoelastic Behavior of a Model Salt Cavity" - Progress Report No. 5, Projects 9-19791 and GP-2696, National Science Foundation, 1964.
24. Handin, J., "Strength and Ductility," Geological Society of America Memoir No. 97, pp. 244-270.
25. Clark, G. B., and Caudle, R. D., "Geologic Structure Stability and Deep Protection Construction," AFSWC-TDR-61-93, University of Missouri, School of Mines and Metallurgy, November 1961.
26. Deere, D. A., and Miller, R. P., "Engineering Classification and Index Properties for Intact Rock," AFWL-TR-65-116, University of Illinois, December 1966.
27. Walsh, J. B., "The Effect of Cracks on Poisson's Ratio" - Journal of Geophysical Research, Vol. 70, No. 20, October 15, 1965.
28. Saucier, K. L., et. al., "High Compressive Strength Concrete," AFWL-TR-65-16, September 1965.
29. Watstein and Boresi, "The Effect of Loading Rate on the Compressive Strength and Elastic Properties of Plain Concrete," National Bureau of Standards Report No. 1523, Washington, D. C., March 1952.
30. American Concrete Institute, "Building Code Requirements for Reinforced Concrete", ACI 318-63, June 1963.

REFERENCES (Cont.)

31. University of Colorado, "Concrete Under Various High Triaxial Compression Conditions", WL-TR-64-163, August 1965.
32. American Institute of Steel Construction, "Manual of Steel Construction", Sixth Edition, 1963.
33. Bethlehem Steel Corporation booklet, "Bethlehem V Steels", 1961.
34. United States Steel folders, "USS Man-Ten, USS Cor-Ten, USS Tri-Ten, USS Ex-Ten, USS T-1 and F-1 Type A."
35. Corps of Engineers, U. S. Army, "Design of Structures to Resist the Effects of Atomic Weapons", EM 1110-345-414, March 1957.
36. Leonards, G. A., "Experimental Study of Static and Dynamic Friction Between Soil and Typical Construction Materials," AFWL-TR-65-161, December 1965.
37. Mark's Mechanical Engineer's Handbook and Engineering Technical Handbook-McNeece and Hoag.

UNCLASSIFIED

Security Classification

DOCUMENT CONTROL DATA - R&D		
(Security classification of title, body of abstract and indexing annotation must be entered when the overall report is classified).		
1. ORIGINATING ACTIVITY (Corporate author) THE BOEING COMPANY P.O. Box 3999 Seattle, Washington - 98124		2a. REPORT SECURITY CLASSIFICATION UNCLASSIFIED
		2b. GROUP
3. REPORT TITLE Structure-Medium Interaction and Design Procedures Study, Volume I - Analysis Method, Theory, Verification and Applicability		
4. DESCRIPTIVE NOTES (Types of report and inclusive dates) Final Report, Study Period, April 16, 1967 - October 27, 1969.		
5. AUTHORS (First name, middle initial, last name) Mr. H. G. Leistner, Dr. R. E. Jones, Mr. W. J. Walker, et. al.		
6. REPORT DATE October 27, 1969	7a. TOTAL NO. OF PAGES 245	7b. NO. OF REFS 37
8. CONTRACT OR GRANT NO. F04694-67-C-0084 Project: 672A Program	9a. ORIGINATOR'S REPORT NUMBERS D2-121409-1	
	9b. OTHER REPORT NO(S) (Any other numbers that may be assigned to this report) SAMSO TR 69-313, Volume I.	
10. DISTRIBUTION STATEMENT This document is subject to special export controls and each transmittal to foreign Governments or foreign nationals may be made only with prior approval of SAMSO (). The distribution of this report is limited because it contains technology restricted by mutual securities acts.		
11. SUPPLEMENTARY NOTES	12. SPONSORING MILITARY ACTIVITY The Dept. of the A.F., Space & Missile Sys. Org. Air Force Systems Command Norton Air Force Base, California	
13. ABSTRACT <p>This report contains a detailed description of the analysis method developed for this structure - medium interaction study. The material properties representation and the structure modeling concepts used in the analysis models are presented. Results of analyses performed for verification of the method and compilations of typical earth media and construction material physical properties are included.</p> <p>A summary section presents a description of capabilities of the FEAT computer codes developed for the analysis of structure - medium interaction. It also includes discussion of the application of the analysis method to the development of design information for advanced, hardened missile facilities. Recommended uses for the method are presented, together with suggested extensions for the enhancement of its capabilities.</p>		

UNCLASSIFIED

Security Classification

UNCLASSIFIED

Security Classification

14.	KEY WORDS	LINK A		LINK B		LINK C	
		ROLE	WT	ROLE	WT	ROLE	2 T
	Structure-Medium Interaction						
	Analysis						
	Finite Element Method						
	Non-Linearly Elastic						
	Plastic						
	Compacting						
	Overlay Model						
	Debonding and Slip						
	Suspension System						
	Verification						
	Design Information						
	"FEAT" Code						